Investigation of the Transverse and Longitudinal Beam Parameters at the TESLA Test Facility Linac

Dissertation
zur Erlangung des Doktorgrades
des Fachbereichs Physik
der Universität Hamburg

vorgelegt von
Marc Alexander Geitz
aus Hagen

Hamburg

1999

Gutachter der Dissertation:	Prof. Dr. P. Schmüser Priv. Doz. Dr. M. Tonutti
Gutachter der Disputation:	Prof. Dr. P. Schmüser Priv. Doz. Dr. A. Gamp
Datum der Disputation:	5. November 1999
Dekan des Fachbereichs Physik und Vorsitzender des Promotionsausschusses:	Prof. Dr. F. W. Büßer

Abstract

The operation of a free electron laser in the VUV regime puts stringent demands on the beam quality of an electron linear accelerator. That is why beam diagnostic techniques have been developed to determine the transverse phase space density and the longitudinal charge distribution of the electron bunches with the required precision. The transverse phase space distribution is determined from beam intensity profiles using tomographic image reconstruction techniques. Measurements at the TESLA Test Facility linac yield a normalized transverse emittance of $\gamma\epsilon_x = 5.5 \cdot 10^{-6}\,\mathrm{m}$ und $\gamma\epsilon_y = 9.5 \cdot 10^{-6}\,\mathrm{m}$ with a bunch charge of 1 nC. The longitudinal bunch charge distribution is determined by frequency– and time-resolved methods. Fourier– and Hilbert-transform spectroscopy of coherent transition radiation belong to the former techniques. Longitudinal phase space rotations to determine the longitudinal bunch charge distribution and streak camera measurement using optical synchrotron radiation are applications of time-resolved methods. The different techniques yield consistent results and hint at a minimum electron bunch length of $\sigma_z = 250\,\mu\mathrm{m}$.

Zusammenfassung

Der Betrieb eines Freien Elektronen Lasers im ultravioletten Wellenlängenbereich stellt hohe Anforderungen an die Strahlqualität eines Elektronenlinearbeschleunigers. Daher wurden Strahldiagnoseinstrumente entwickelt, die eine Messung der transversalen Phasenraumverteilung und der longitudinalen Ladungsverteilung der Elektronenpakete mit der erforderlichen Präzision ermöglichen. Die transversale Phasenraumverteilung wird unter Verwendung von tomographischen Rekonstruktionmethoden aus Strahlintensitätsverteilungen bestimmt. Die Messungen an der TESLA Test Anlage ergeben, bei einer Ladung der Elektronenpakete von 1 nC, eine transversale Emittanz von $\gamma\epsilon_x = 5.5 \cdot 10^{-6}\,\mathrm{m}$ und $\gamma\epsilon_y = 9.5 \cdot 10^{-6}\,\mathrm{m}$. Zur Bestimmung der longitudinalen Ladungsverteilung werden frequenz– und zeitaufgelöste Methoden angewendet. Zur Ersteren gehört die Fourier– und die Hilbert-Transformations Spektroskopie kohärenter Übergangsstrahlung. Die Ausnutzung definierter longitudinaler Phasenraumrotationen zur Bestimmung der Elektronenpaketlänge und Streak Kamera Messungen optischer Synchrotronstrahlung sind Anwendungen zeitaufgelöster Methoden. Die verschiedenen Messungen ergeben konsistente Ergebnisse und weisen auf eine minimale Elektronenpaketlänge von $\sigma_z = 250\,\mu\mathrm{m}$ hin.

Contents

1 Introduction **1**

2 TESLA Test Facility Linac **3**
2.1 Injectors . . . 3
2.1.1 Thermionic Injector . . . 3
2.1.2 RF Photo Injector . . . 6
2.1.3 Matching and Dispersive Section . . . 10
2.2 Linac . . . 11
2.2.1 General Linac Layout . . . 11
2.2.2 Linac Optics . . . 12
2.2.3 Bunch Compression Scheme . . . 14

3 Properties of Transition Radiation **21**
3.1 Transition Radiation as a Tool for Beam Diagnostics . . . 21
3.2 Optical Transition Radiation . . . 21
3.2.1 Ginzburg-Frank Equation . . . 21
3.2.2 Radiated Energy . . . 22
3.2.3 Polarization . . . 23
3.2.4 Angular Distribution . . . 24
3.2.5 Oblique Incidence . . . 25
3.3 Far Infrared Transition Radiation . . . 26
3.3.1 Source Dimension . . . 26
3.3.2 Huygens-Fresnel Principle . . . 32
3.4 Coherent Transition Radiation . . . 35
3.4.1 Radiation Power . . . 36
3.4.2 Investigation of the Longitudinal and Transverse Form Factor . . . 37

4 Transverse Phase Space Tomography **41**
4.1 Theory of Phase Space Tomography . . . 41
4.1.1 The Radon Transform . . . 41
4.1.2 The Filtered Backprojection Algorithm . . . 43
4.1.3 Discrete Implementation of the Filtered Backprojection Algorithm 48
4.1.4 Reconstruction Artifacts . . . 51
4.1.5 Application of the Filtered Backprojection Algorithm to Transverse Beam Dynamics . . . 52
4.1.6 Determination of the Beam Parameters . . . 56
4.1.7 Incorporation of Space Charge Effects . . . 56

4.2 Parabola Fit Analysis . . . 57

5 Determination of the Transverse Beam Parameters 59
5.1 Experimental Setup . . . 59
5.2 Measurements with the Photo Injector Beam . . . 60
5.2.1 Data Processing . . . 61
5.2.2 Tomographic Reconstruction . . . 63
5.2.3 Transverse Beam Parameters and Emittance . . . 64
5.2.4 Discussion of the Systematic Errors . . . 65
5.2.5 Further Emittance Studies using the Photo Injector Beam . . . 69
5.3 Measurements with Thermionic Injector Beam . . . 71
5.3.1 Parabola Fit Analysis . . . 73

6 Time Domain Techniques for Bunch Length Measurements 75
6.1 Streak Camera . . . 75
6.1.1 Experimental Setup . . . 75
6.1.2 Bunch Length Measurements . . . 77
6.2 Longitudinal Phase Space Rotations . . . 78
6.2.1 Theory and Simulation . . . 78
6.2.2 Bunch Length and Energy Distribution Measurements . . . 81

7 Fourier Transform Spectroscopy 85
7.1 Description of the Martin-Puplett interferometer . . . 85
7.2 Working Principle of the Interferometer . . . 88
7.3 Frequency-dependent Acceptance Function . . . 91
7.3.1 Spectral Transmission and Reflectivity of Wire Grids . . . 91
7.3.2 Spectral Acceptance of the Wire Grid Beam Divider . . . 94
7.3.3 Diffraction in the Interferometer . . . 96
7.3.4 Detector Acceptance . . . 99
7.3.5 Transmission of the Quartz Window . . . 101
7.3.6 Aluminum Foils of Finite Thickness . . . 101
7.3.7 Spectral Acceptance of the Martin-Puplett Interferometer . . . 104
7.3.8 Systematic Error of the Acceptance Function . . . 105
7.4 The Autocorrelation Function . . . 106
7.5 Reconstruction of the Longitudinal Charge Distribution . . . 109
7.6 Determination of the Bunch Length . . . 113
7.6.1 Analysis of the Autocorrelation . . . 113
7.6.2 On-line Monitoring of the Bunch Length . . . 114
7.7 Bunch Length Measurements . . . 115
7.7.1 Measurements with the Photo Injector Beam . . . 116
7.7.2 Measurements at the TTF Thermionic Injector . . . 121
7.8 Possible Improvements of the Interferometer . . . 122

8 Hilbert Transform Spectroscopy 123
8.1 Electric Properties of a Josephson Junction . . . 123
8.1.1 The Josephson Effect . . . 123
8.1.2 DC Characteristic of the Josephson Junction . . . 124

8.1.3 Josephson Junction with Incident Radiation . . . 125
8.1.4 Hilbert Transform Spectrometry . . . 126
8.2 The Josephson Junction . . . 127
8.3 Bunch Length Measurements . . . 129
8.3.1 The Intrinsic Parameters of the Junction . . . 129
8.3.2 The Spectroscopic Measurement . . . 130
8.3.3 Data Analysis . . . 132

9 Conclusion and Outlook **133**

A Beam Dynamics and Parameters **135**
A.1 The Transfer Matrix Formalism . . . 135
A.2 Beam Transfer Matrices . . . 136
A.3 First Order Beam Matrix Formalism . . . 137
A.3.1 Beam Transfer . . . 140
A.3.2 Beam Emittance . . . 140

B Derivation of the Ginzburg-Frank formula **141**

C Electromagnetic Fields of Relativistic Electron Bunches **149**

D Space Charge Forces **159**

E Hilbert Transform Spectroscopy **163**
E.1 Current-Voltage Characteristic without Radiation . . . 163
E.2 Current-Voltage Characteristic with Radiation . . . 165
E.3 The Hilbert Transform . . . 168

F Acceptance Measurement of the Pyroelectric Detectors **171**

Chapter 1

Introduction

Electron-positron colliders are essential instruments to investigate the structure of matter and the understanding of the fundamental forces in nature. The presently largest collider LEP at CERN stores electrons and positrons with an energy of about 100 GeV per beam and is energy-limited by synchrotron radiation losses. A possible way to go beyond the energy limit of storage rings is the concept of two linear accelerators in collision. The higher center-of-mass energies are necessary to increase the resolution of high energy physics experiments and to investigate smaller structures of matter. Detailed studies of the top quark and the Higgs particle, the last missing constituent of the standard model, will be a major task of a particle physics experiment at a future linear collider. The detection of supersymmetric particles would hint at a unification of the strong, weak and electromagnetic interaction and at physics beyond the standard model.

The TESLA collaboration proposes a superconducting linear accelerator design to reach a center-of-mass energy of 500 GeV in its first stage. The accelerating structures consist of nine-cell niobium cavities with a field gradient of 25 MV/m and a quality factor of 10^{10}. The advantage of the superconducting 1.3 GHz cavities is the high conversion efficiency between the primary and the beam power of about 17%. The perturbing effects of cavities, like wake fields transforming part of the energy gain into transverse beam oscillations, are weaker than in conventional, normal-conducting accelerators of higher frequency. The high quality factor of the superconducting resonators facilitates the acceleration of highly-charged electron bunches of sub-picosecond length to drive an X-ray free-electron laser based on the principle of self-amplified spontaneous emission (SASE).

The goal of the TESLA Test Facility (TTF) is to validate the technology of superconducting niobium cavities with the TESLA specifications and to demonstrate the acceleration of an electron beam of 8 mA average current, up to 8 nC bunch charge, over a macropulse length of 800 μs. The beam of the TTF linac will be used to drive a SASE free-electron laser in the VUV wavelength regime.

The measurement of the transverse and longitudinal beam quality is a key ingredient of the TTF experimental program and the achievement of the design beam parameters is essential for the success of the test facility. Beam diagnostic techniques have been developed and commissioned to determine the transverse beam emittance, bunch length and energy spread. The transverse phase space distribution is derived from beam intensity

profiles using tomographic image reconstruction techniques. The transverse beam intensity distribution is recorded using optical transition radiation. Phase space tomography produces an image of the entire transverse phase space distribution without making any assumptions on the charge distribution. The longitudinal charge distribution is measured with time- and frequency-resolved methods. Streak camera measurements using optical synchrotron radiation and longitudinal phase space rotations imposed by rf cavities and a magnetic dipole chicane have been applied to measure the longitudinal bunch charge distribution. Frequency-resolved techniques using coherent transition radiation detected by a Martin-Puplett interferometer and a Josephson junction have been developed and used for bunch length measurements.

Chapter 2

TESLA Test Facility Linac

The TESLA Test Facility (TTF) linac can be subdivided in three major sections: the injector, the main superconducting linear accelerator and the experimental area. A description of these accelerator sections, including the transverse and longitudinal beam dynamics, will be outlined.

2.1 Injectors

The TTF linac has been operated with two types of injectors, a thermionic injector and an rf photo injector. The thermionic gun has been used to produce a high quality beam of moderate bunch charge to permit a successful operation of the superconducting accelerating sections. In a second step, an rf gun photo injector has been installed to produce a high charged, high quality beam such as required for the TESLA collider and a VUV free electron laser. Both injectors achieve the TTF design average beam current of 8 mA over a macropulse length of 800 μs and a repetition rate of 10 Hz.

2.1.1 Thermionic Injector

The thermionic injector [1] consists of a triode gun with a heated cathode of 8 mm diameter (on ground potential), a grid (typically -3 V voltage) and an anode providing 30 kV of accelerating voltage. The gun produces short electron pulses, $\sigma_t < 1$ ns, of $2.3{\cdot}10^8$ electrons by a fast 216.7 MHz modulation of the cathode voltage from 0 V to about -100 V. The micropulse repetition is a 1/6 sub-harmonic multiple of the linac accelerating frequency of 1.3 GHz. The average beam current is 8 mA and extends over a macropulse length of 800 μs. The thermionic injector timing scheme [2] is displayed in Fig. 2.1.

The beam is pre-accelerated by a 1 m long 220 kV electro-static column consisting of a series of field gradient rings separated by glass insulating discs [2]. The 250 keV energy electron pulses are then injected into a copper cavity operating at 216.7 MHz with a moderate voltage of about 100 kV. The so-called "sub-harmonic buncher cavity" is used for the longitudinal compression of the electron bunches. Following the sub-harmonic buncher the beam passes a superconducting, 9 cell, 1.3 GHz cavity for further bunching and acceleration to an energy of at least 10 MeV. The resulting bunch length is $\sigma_z = 0.5$ mm.

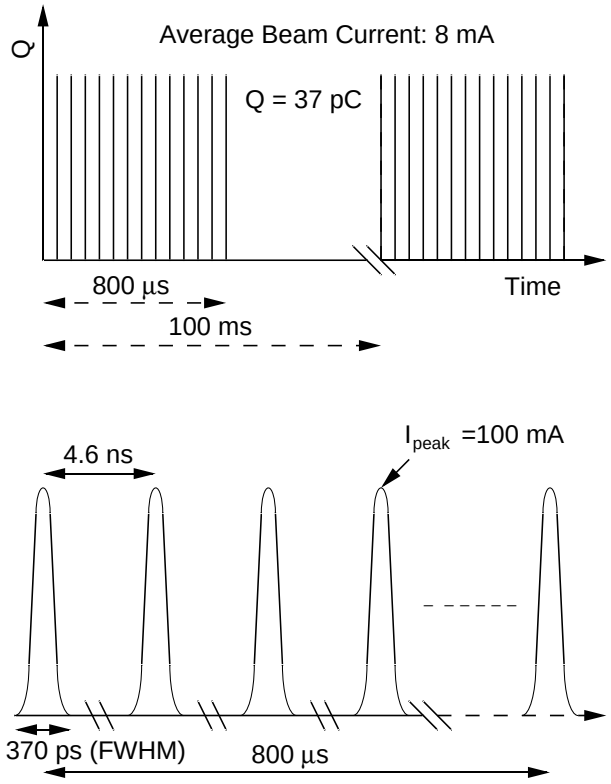


Figure 2.1: Bunch timing structure of the TTF thermionic injector. Pulses of $2.3 \cdot 10^8$ electrons are emitted with a repetition rate of 216.7 MHz over a macropulse length of 800 μs. The macropulse repetition rate is 10 Hz.

Beam Parameters: The beam parameters at the exit of the capture cavity, predicted by the PARMELA [3, 2] program are listed in Tab. 2.1 for a 10 MeV beam.

Beam Parameter	Prediction by PARMELA
$\gamma \cdot \epsilon_{\mathrm{rms}}$ $[10^{-6}\,\mathrm{m}]$	4.8
σ_{11}, σ_{33} $[10^{-6}\,\mathrm{m}^2]$	0.24
σ_{12}, σ_{34} $[10^{-6}\,\mathrm{m}]$	0.23
σ_{55} $[10^{-6}\,\mathrm{m}^2]$	0.24
σ_{66} $[10^{-6}]$	53.3

Table 2.1: Design beam parameters of the TTF thermionic injector as determined by the code PARMELA. The beam energy is $E = 10\,\mathrm{MeV}$ and the bunch charge is $Q = 37\,\mathrm{pC}$.

The beam parameters are understood as elements of the beam matrix (σ-matrix) [4], which is the covariance matrix of the bunch charge distribution. The diagonal elements denote the square of the horizontal and vertical rms beam width (σ_{11} and σ_{33}), the square of the horizontal and vertical rms angular divergence (σ_{12} and σ_{34}), the square of the bunch length (σ_{55}) and the square of the fractional energy deviation (σ_{66}). The off-

diagonal elements denote the covariance, hence the coupling, among the respective phase space coordinates. The beam matrix formalism, which is used throughout this thesis, is outlined in appendix A.

Bunch Compression:

The 1-cell sub-harmonic buncher cavity is used to compress the longitudinal bunch charge distribution at a low beam energy of $E = 250\,\mathrm{keV}$. The buncher cavity induces a head-tail energy modulation on the bunch, hence a velocity modulation since $\beta = v/c$ is only about 0.55, where the faster electrons trail the slower electrons. In a following drift section of 2.66 m length, the trailing electrons catch up with the leading electrons and a longitudinal bunch compression is achieved. The phase of the buncher cavity has to be optimized to obtain the minimum bunch length within the first cell of the nine-cell capture cavity, where the beam energy is increased rapidly into the MeV range ($\beta \to 1$). The capture cavity has a non-negligible influence on the optimum bunching because of the low injection energy. Above 10 MeV the longitudinal beam dimension is invariant in a linear accelerator since $\beta \approx 1$.

To evaluate the optimum phase of the sub-harmonic buncher cavity, let us consider one electron at the head, at the center and at the tail of the bunch. The energy of the electrons after passing the buncher is

$$\gamma_f^{(k)} = \gamma_i^{(k)} + \frac{eU}{mc^2}\cos\left(\phi^{(k)} + \phi_0\right) \tag{2.1}$$

where γ denotes the relativistic Lorentz factor, U the accelerating gradient, ϕ the accelerating phase and m the electron mass. The index f denotes the final, i the initial beam

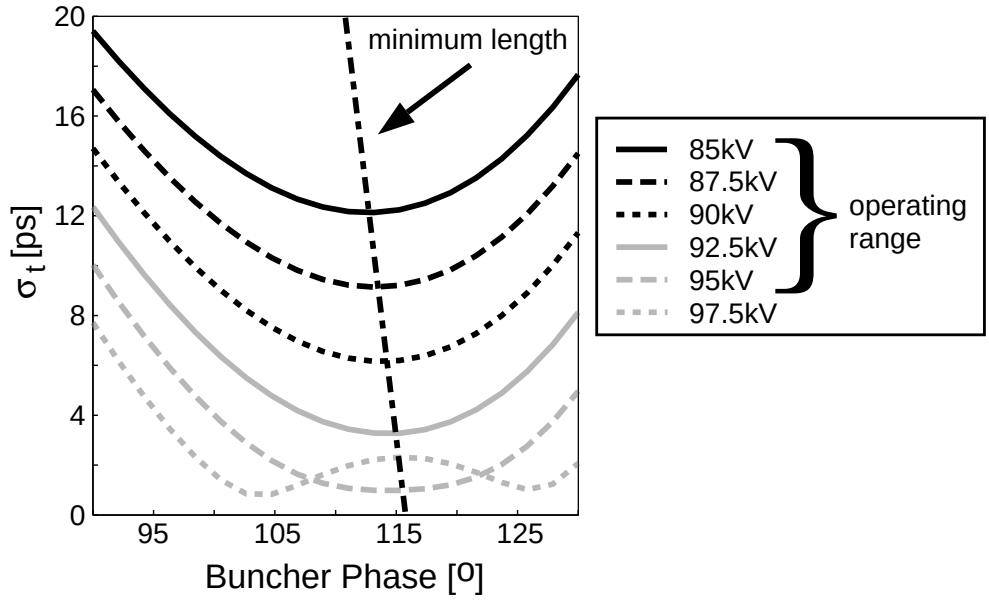


Figure 2.2: Bunch length as a function of the buncher cavity phase for various settings of the buncher voltage. The initial bunch length is $\sigma_t = 300\,\mathrm{ps}$ [2]. Notice that the buncher phase yielding the minimum bunch length varies linearly with the voltage.

energy. The superscript (k) indicates either of the three electrons, ϕ_0 the rf phase of the center electron. The energy gain yields a particle velocity $\beta = v/c$ of

$$\beta_f^{(k)} = \sqrt{\frac{\left(\gamma_f^{(k)}\right)^2 - 1}{\left(\gamma_f^{(k)}\right)^2}} = \frac{\sqrt{\left(\gamma_i^{(k)} + \frac{eU}{mc^2}\cos(\phi^{(k)} + \phi_0)\right)^2 - 1}}{\gamma_i^{(k)} + \frac{eU}{mc^2}\cos(\phi^{(k)} + \phi_0)}\,. \tag{2.2}$$

The particles experience a repelling electromagnetic force as they approach each other. The longitudinal electric field of a single particle at the longitudinal position ζ_0 traveling with velocity βc along a straight line is (see appendix C)

$$E_z = \frac{e}{4\pi^2\epsilon_0\gamma^2}\frac{1}{(\zeta - \zeta_0)^2} \tag{2.3}$$

where $\zeta = z - \beta ct$. The single particle electric field is weighted with a Gaussian charge distribution to describe the space charge forces of the entire particle bunch. Figure 2.2 shows the bunch length in the first cell of the capture cavity as a function of the buncher cavity phase for different settings of the buncher voltage. The initial bunch length is $\sigma_t = 300\,\mathrm{ps}$ [2]. Higher buncher voltages yield shorter bunches. The minimum obtainable bunch length, however, is restricted by longitudinal space charge forces, causing the deviation from the parabolic characteristic of σ_t versus ϕ_0 at voltages $U \leq 95\,\mathrm{kV}$. At these operating voltages the minimum achievable bunch length depends linearly on the phase of the buncher cavity. At voltages $U > 95\,\mathrm{kV}$, the space charge forces tend to (longitudinally) de-focus the bunch before reaching the capture cavity. The minimum bunch length is obtained at buncher phases other than indicated by the line of minimum length.

2.1.2 RF Photo Injector

The electron bunches are produced by the photo-electric effect using a UV laser pulse interacting with a Cs_2Te photo cathode. The electron bunch is accelerated rapidly by strong electromagnetic fields ($E_{\mathrm{acc}} = 35$–$50\,\mathrm{MV/m}$, $f = 1.3\,\mathrm{GHz}$) in the gun cavity yielding a beam energy of 4 MeV. The rf power ($P \approx 3\,\mathrm{MW}$) is fed into the gun cavity by a side-coupled waveguide. The required focusing is provided by two solenoid coils surrounding the gun cavity. The primary solenoid focuses the beam envelope close to the cathode at low beam energies. The secondary solenoid applies further focusing on the beam at the downstream end of the gun cavity. A third solenoid is used to compensate the magnetic field on the cathode. An advantage of the twin coil arrangement is the possibility to correct alignment errors. Figure 2.3 shows a sketch of the 1 1/2 cell, room-temperature gun cavity. The rapid acceleration, the fringe field focusing and the helical path of the electrons in the solenoid field counteract the emittance blowup by space charge forces. The electron beam is then injected into the superconducting capture cavity to increase the beam energy to 16 MeV [5].

The UV laser of the rf photo injector is driven by a mode-locked Nd:YLF oscillator ($\lambda = 1.47\,\mu\mathrm{m}$) producing a 3 ms long output pulse train of 18.5 ns spaced bunches. A Pockels cell selects laser pulses with a repetition rate of 1 MHz and transmits these pulses into three linear Nd:YLF amplifiers. The pulses of up to $200\,\mu\mathrm{J}$ energy are frequency converted twice to green light by a LPO crystal and to UV by a BBO crystal. The UV

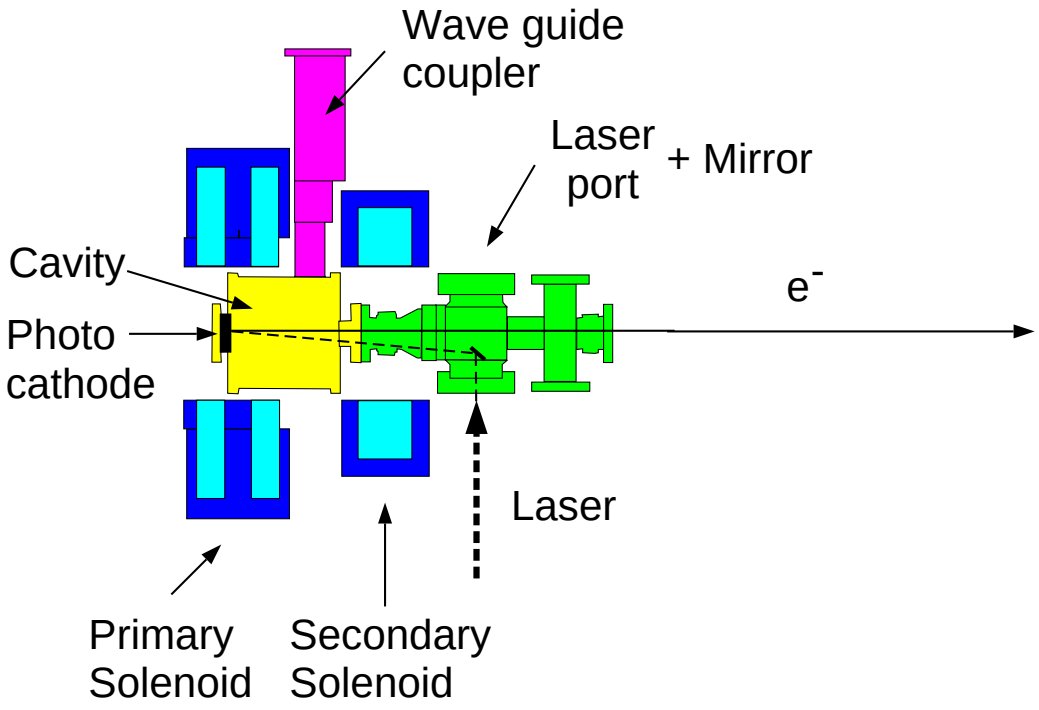


Figure 2.3: The 1-1/2-cell rf gun copper cavity surrounded by three solenoid coils. The rf feed, the photocathode and the UV laser beam is indicated.

beam is sent to the photo cathode in the rf gun to produce the electron bunches [6, 7]. The design laser pulse length in the resonator is about $\sigma_z = 10$ ps. The frequency conversion reduces the pulse length by a factor of 2 yielding a UV laser pulse length of $\sigma_z = 5$ ps, 262 nm wavelength and up to 25 μJ energy [8]. The Cs_2Te photo cathode has a quantum efficiency of about 0.5 % which is stable over months [9]. The laser pulse energy, focused onto a spot of 10 mm diameter on the cathode, is sufficient to produce bunch charges of about 10 nC [5] well above the design bunch charge of 8 nC. The macropulse length is 800 μs.

Figure 2.4 [7] shows the timing scheme for the two operating modes of the rf gun photo injector. The collider mode (left) requires a bunch charge of 8 nC at 1 MHz repetition rate and a FWHM bunch length of 18 ps. The macropulse length is 800 μs with a repetition rate of 10 Hz. The timing parameters are similar to the parameters of a future high energy physics collider based on the TESLA design. The free electron laser mode (right) requires a bunch charge of 1 nC at 9 MHz repetition rate and a FWHM bunch length of 10 ps. Macropulses of 800 μs length repeat with a rate of 10 Hz. The beam produced in the free electron laser mode is a high quality, low emittance electron beam to demonstrate the SASE principle at a VUV free electron laser.

Beam Parameters: The PARMELA [3, 7] program has been used to optimize the gun parameters to obtain the collider- and free electron laser mode beam parameters at the exit of the capture cavity. The results are listed in Tab. 2.2.

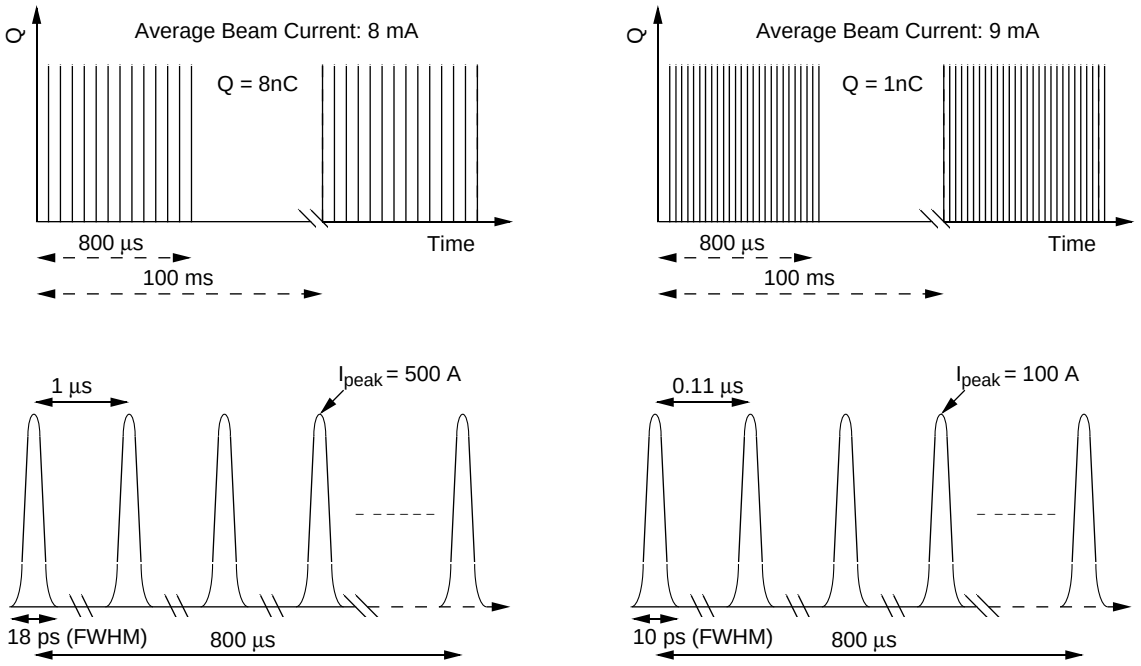


Figure 2.4: Timing structure for the two modes of the TTF photo injector operation. Left: collider mode. Right: free electron laser mode. Pulses of $5 \cdot 10^{10}$ / $6.3 \cdot 10^{9}$ electrons are emitted with a repetition rate of 1 MHz / 9 MHz over a macropulse length of 800 μs. The macropulse repetition rate is 10 Hz.

Beam Parameter	Collider (PARMELA)	FEL (PARMELA)
$\gamma \cdot \epsilon_{\mathrm{rms}}$ $[10^{-6}\,\mathrm{m}]$	15	1
σ_{11}, σ_{33} $[10^{-6}\,\mathrm{m}^2]$	to be determined	to be determined
σ_{12}, σ_{34} $[10^{-6}\,\mathrm{m}]$		
σ_{55} $[10^{-6}\,\mathrm{m}^2]$	4	4
σ_{66} $[10^{-6}]$	< 4	< 4

Table 2.2: Design beam parameters of the TTF photo injector as determined by the code PARMELA. The beam energy behind the capture cavity is $E = 18.2\,\mathrm{MeV}$ and the bunch charge is $Q = 8\,\mathrm{nC}$ for the collider mode and $Q = 1\,\mathrm{nC}$ for the free electron laser mode.

Emittance Conservation Scheme

The transverse emittance dilution of an electron beam in an rf gun is caused by space charge forces and effects of the gun rf field. For convenience, the space charge field of a particle bunch can be separated in linear and higher-order terms. Carlsten [10] demonstrated that the correlated emittance growth due to the linear part of the transverse space charge field can be compensated by appropriate linear focusing close to the rf gun. The phase advance of a longitudinal slice of charge is larger at the center than at the head of the bunch because of the larger charge density. The result is the opening of a "phase space fan", where each longitudinal slice of charge has rotated by a different angle in

phase space. The projected emittance along the bunch is hence larger than the emittance of the individual slices [11]. Using a lens of appropriate strength, the front slice of charge can be made more convergent than the center slice. During the following drift section, the front slice is focused to a smaller waist than the center slice and is therefore subject to stronger space charge forces. It experiences a larger phase space rotation and catches up with the rotation of the center slice. The result is a closure of the phase space fan and a compensation of the correlated emittance growth.

The residual transverse emittance of the rf gun beam, other than the thermal emittance, is determined by the following mechanisms which cannot be compensated. Non-linear space charge forces become non-negligible for tightly focused, divergent and convergent beams. Non-linearities of radial rf field components in the gun cavity cause an emittance dilution for large radius beams. Lastly, the time dependence of the accelerating rf field leading to energy and focusing strength variations over the bunch length, causes a non-reversible emittance growth [12, 7].

The emittance conservation scheme is based on the focusing of the primary and the secondary solenoid coil. The strength of the solenoids was adjusted experimentally to minimize the emittance produced at the end of the injector. Secondly, the focusing influences the emittance growth caused by non-linear space charge forces, which are strong for small beam sizes, and by non-linear radial rf fields, which are strong for large beam sizes. There is a significant dependence of the emittance on the laser spot size at the

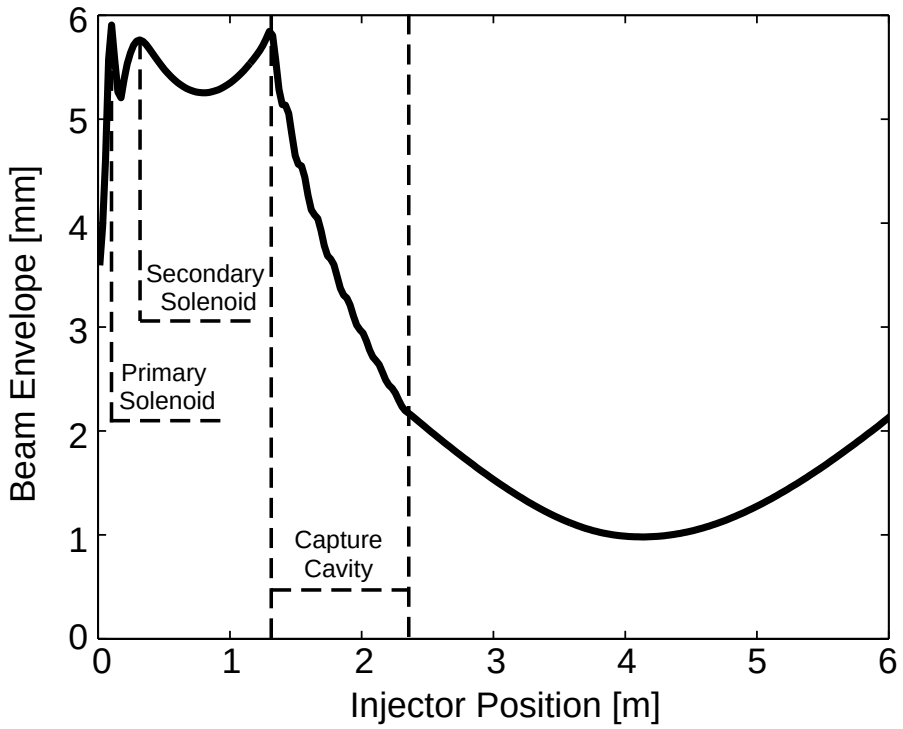


Figure 2.5: The normalized beam emittance along the TTF photo injector as predicted by the PARMELA program.

photo cathode and on the laser pulse length. A large laser spot yields a large electron bunch size and therefore a large emittance dilution due to non-linear rf fields but low space charge forces. A long laser pulse yields a long electron bunch and therefore a large energy and focusing difference along the electron bunch.

The envelope of the photo injector beam as simulated by the PARMELA [3] program is shown in Fig. 2.5. The beam is focused by the gun solenoids and the envelope reaches a maximum in front of the capture cavity at $z = 1.3\,\mathrm{m}$. The beam is accelerated and focused in the cavity, $z = 1.3\,\mathrm{m}$ to $z = 2.3\,\mathrm{m}$, yielding a convergent envelope in the matching section, $z > 2.3\,\mathrm{m}$.

Bunch Compression

The bunch length produced by the rf gun depends on the laser pulse length and the compression caused by the rf field within the first centimeters of the gun cavity. By proper choice of the rf phase a velocity modulation can be impressed on the electrons in the bunch leading to a reduction of its length within the gun cavity. Leading electrons must see a lower electric field than trailing electrons to obtain pulse compression. Very short bunches can be obtained at the price of sacrificing a large fraction of the bunch charge. This, however, is not desirable for the TTF linac because of the peak current required for the FEL. After passing the capture cavity, the beam energy has increased to 16 MeV and the longitudinal extension of the charge distribution remains invariant because β approaches unity.

2.1.3 Matching and Dispersive Section

The beam is transfered from the capture cavity to the first acceleration section of the main linac through a room-temperature beam line consisting of a quadrupole doublet (Q1-INJ) and two quadrupole triplets (T1-INJ, T2-INJ). The lattice of the matching section can be seen in Fig. 2.7 for the beam produced by the thermionic injector and Fig. 2.8 for the beam produced by the rf gun. A dipole magnet between the capture cavity and the main linac can be used to deflect the beam into a dispersive section in order to adjust the injector

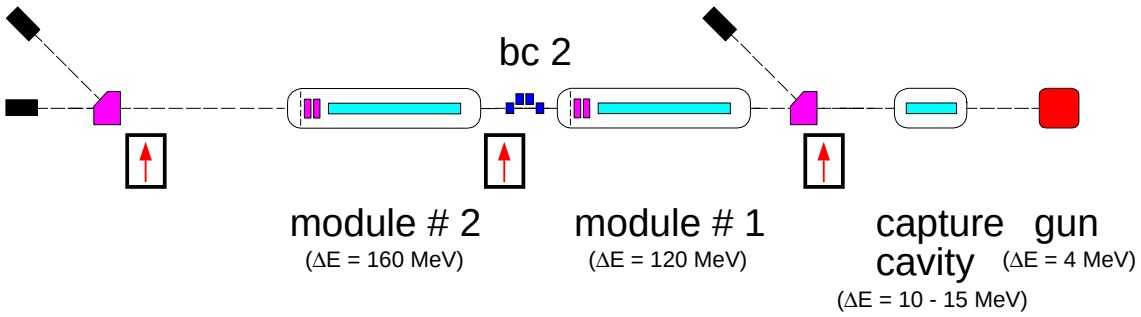


Figure 2.6: Schematics of the TTF linac showing the injector, the accelerating module #1, the magnetic bunch compressor, module #2 and the high energy analysis area. The arrows indicate three diagnostic stations used for emittance measurements. The energy increase in the accelerating sections is shown.

parameters to produce a beam of minimum energy spread. Several diagnostic stations equipped with transition radiation screens are used together with a focusing quadrupole multiplet, either in the straight section (emittance measurement) or in the dispersive section (energy profile measurement) to determine the beam parameters experimentally. The last triplet of the matching section is used to match the beam to the design optics of the main linac. A schematics of the TTF linac, including the matching and the dispersive section, is shown in Figure 2.6.

2.2 Linac

2.2.1 General Linac Layout

In its present configuration the main linac consists of two modules of accelerating cavities (ACC1 and ACC2). The superconducting niobium cavities consist of nine cells with a resonant frequency of 1.3 GHz. Eight cavities form an accelerating module. The cavities are installed in a cryostat which serves as vacuum insulation, heat shield and mechanical support structure. The cavities installed in cryostat #1 and #2 achieve an average gradient of 15 MV/m and 20 MV/m respectively with a loaded quality factor of about $Q = 2.2 \cdot 10^6$. The rf power (about 160 kW per cavity at 20 MV/m) is supplied by a single klystron and fed into the cavities by coaxial input couplers. After a field filling time of 400 μs, the rf field is kept stable in gradient and phase for 800 μs [13]. The cavity electric fields are measured by a pick-up probe inside the cavity resonator. The field gradient is proportional to the amplitude of the probe signal and the phase information is obtained by frequency down-conversion (mixing) of the signal using a frequency-stabilized local oscillator. Focusing is applied by a superconducting quadrupole doublet (D1-ACC1 and D1-ACC2) at the end of each rf module.

A magnetic bunch compressor section (BC2) is installed between the two accelerating modules. The section consists of a quadrupole triplet (T1-BC2), four dipole magnets deflecting the beam through a symmetric chicane and a second quadrupole triplet (T2-BC2). Diagnostic stations are used to display either the energy and energy spread of the beam (screen in the dispersive section of the chicane compressor) or the transverse emittance (screen in front of module #2) together with the second focusing triplet [14].

Behind the second accelerating module, the beam is passed to the end of the linac through a room-temperature transfer line. The transfer line has been replaced by a collimation section [15] and an undulator magnet [16] during the construction period in summer 1999. The experimental area at the end of the linac consist of a quadrupole triplet (T1-EXP), and several diagnostic stations equipped with transition radiation screens to perform transverse emittance scans. A spectrometer dipole magnet deflecting the beam horizontally into a dispersive section is used to produce synchrotron radiation. The TTF spectrometer, consisting of the dipole magnet and a transition radiation screen, yields a resolution of $\Delta E/E = 2 \cdot 10^{-4}$ and allows an absolute determination of the beam energy with an accuracy of about 1%. Two de-focusing quadrupole magnets in the dispersive section are used to increase the transverse beam size before sending the beam into the beam dump.

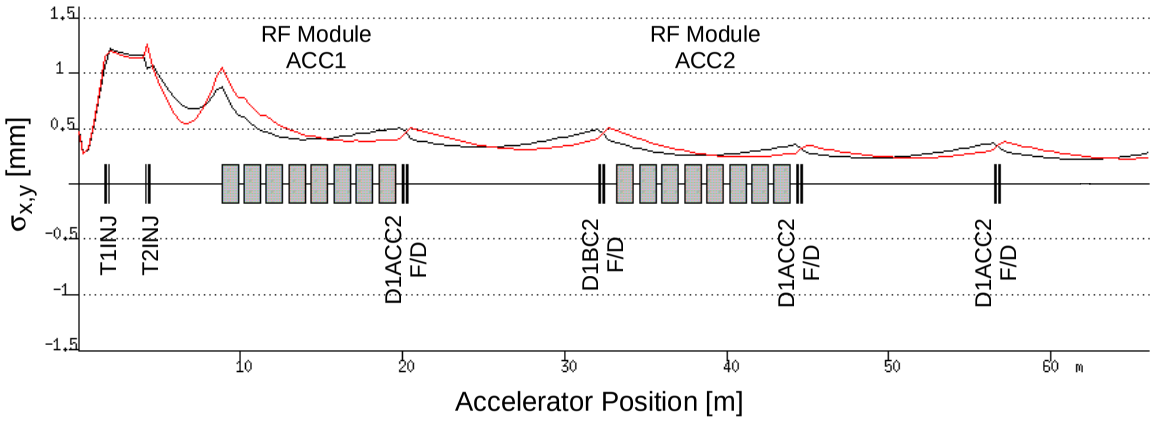


Figure 2.7: Horizontal and vertical beam envelopes along the TTF linac in stage 1. The design beam parameters of the TTF thermionic injector are matched to the linac FIDA lattice by the matching quadrupole triplets. The phase advance of the linac lattice is 90°. The accelerating cavities ($E_{\mathrm{acc}} = 15\,\mathrm{MV/m}$) are indicated by the gray boxes, the quadrupole multiplets by the black lines.

2.2.2 Linac Optics

The linac lattice has a FIDA structure: focusing quadrupole, interleave, de-focusing quadrupole and an accelerating section. The period length is 12.2 m.

Stage 1: Optics with the Thermionic Injector Beam

Figure 2.7 shows the matching and the linac section. The matching section consists of two quadrupole triplets T1-INJ and T2-INJ. The linac section is composed of the accelerating rf modules ACC1 and ACC2. Focusing is applied by the superconducting quadrupole doublets D1-ACC1 and D1-ACC2. A quadrupole doublet (D1-BC2) and a drift section is located between the rf modules. Behind the second rf module, space is left for a third accelerating section ACC3. Presently there is a beam line with a room-temperature quadrupole doublet D1-ACC3. The beam envelope $\sqrt{\sigma_{11}}$ and $\sqrt{\sigma_{33}}$ is computed with the XBEAM [17] program. The design beam parameters behind the capture cavity (Table 2.1) are matched to the linac lattice by the last two quadrupole triplets. The FIDA lattice is adjusted to a phase advance of 90° in both planes yielding a symmetric oscillation of the beam envelopes [18]. Notice the reduction of the beam size due to the energy gain of the beam. The reduction is due to the fact that the momentum ratio of transverse and longitudinal momentum is decreased by the acceleration. Additional focusing is applied by the standing wave cavities [19]. The quadrupole gradients are scaled with beam energy. The beam is transfered to the end of the linac through a beam line without acceleration. The bunch compressor chicane was not installed during the operation of the thermionic injector.

Stage 2: Optics with the RF Gun Beam

Figure 2.8 shows the matching and the linac section operated with the rf gun beam. The magnetic lattice is identical to the lattice shown in Fig. 2.7 except for the bunch compres-

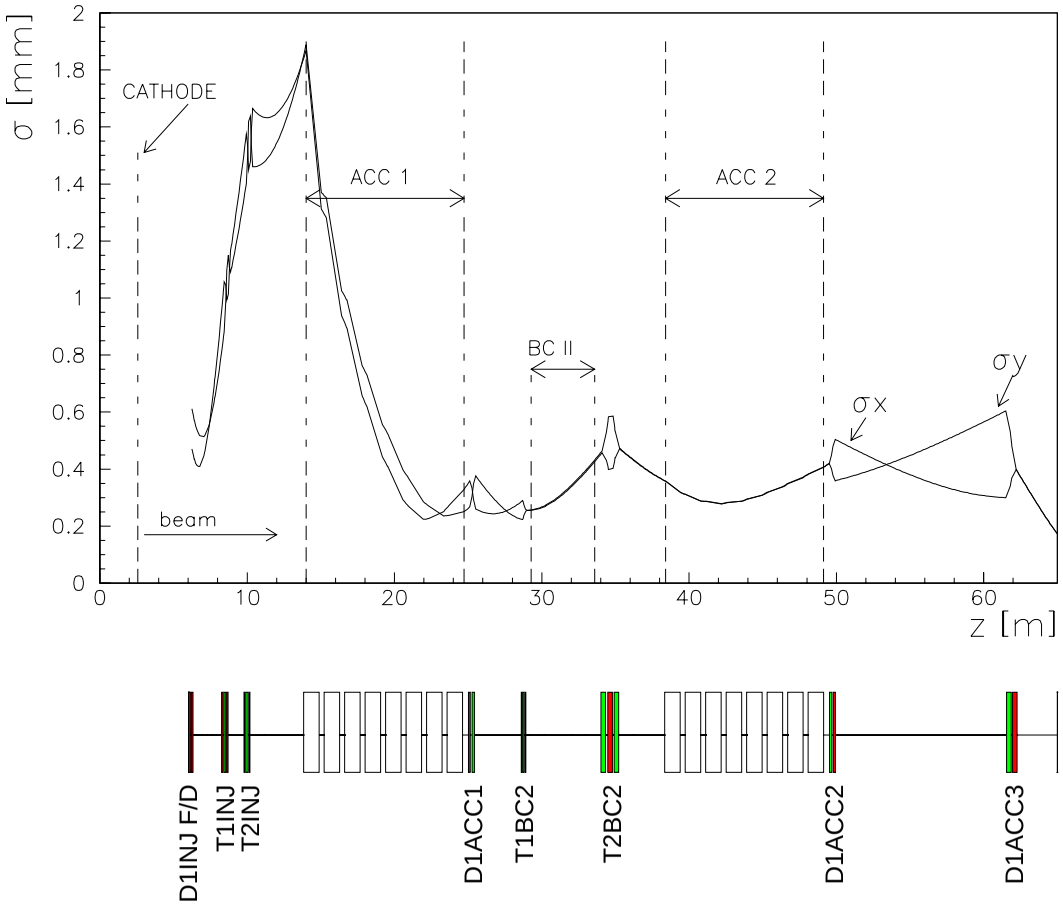


Figure 2.8: Horizontal and vertical beam envelopes along the TTF linac in stage 2. The initial beam parameters used for the presented computation have been determined by transverse phase space tomography outlined in this report. These parameters are matched to the linac lattice by the matching quadrupole triplets [21].

sor (BC2) section. The quadrupole doublet D1-BC2 is replaced by two quadrupole triplets T1-BC2 and T2-BC2 in front of and behind the magnetic chicane, which is not included in the present computation. The chicane dipole magnets would cause additional vertical focusing due to the edge focusing of the fringe magnetic dipole fields. The computation of the linac lattice is based on the first-order beam transfer code COMFORT [20] including linearized space charge forces (see appendix D). The linac lattice has been developed [21] by considering a set of constraints. A small beam envelope in the bunch compressor section is needed to transfer the beam through the narrow gap inside the dipole magnets. In front of the collimating section ($z > 60\,\mathrm{m}$), the envelopes have to be convergent and of equal horizontal and vertical size to insure the proper functioning of the collimator. The beam parameters in front of D1INJ,

$\gamma \cdot \epsilon_x$ $[10^{-6}\,\mathrm{m}]$	5.5	$\gamma \cdot \epsilon_y$ $[10^{-6}\,\mathrm{m}]$	9.5
σ_{11} $[10^{-7}\,\mathrm{m}^2]$	3.3	σ_{33} $[10^{-7}\,\mathrm{m}^2]$	3.9
σ_{12} $[10^{-8}\,\mathrm{m}]$	5.2	σ_{34} $[10^{-8}\,\mathrm{m}]$	1.3

obtained by measurement, have been used. The phase advance of the FIDA lattice is as close as possible to 90°.

2.2.3 Bunch Compression Scheme

Longitudinal compression of relativistic electron bunches can be obtained by an off-crest acceleration in a cavity followed by a magnetic chicane bunch compressor. The off-crest acceleration produces a correlated energy spread in the bunch with the higher energy electrons trailing the lower energy electrons. The higher energy electrons then travel on a shorter path through the magnetic chicane than the lower energy electrons yielding a bunch length reduction. The compressor section and the longitudinal phase space distributions of the electron bunch along the compressor section is shown in Fig. 2.9.

Off-Crest Acceleration:

The off-crest acceleration in an rf cavity is described by a longitudinal transfer matrix M_A

$$M_A = \begin{pmatrix} 1 & 0 \\ M_{65} & M_{66} \end{pmatrix} \quad \text{acting on the vector} \quad \begin{pmatrix} l \\ \delta \end{pmatrix} \tag{2.4}$$

where l is the longitudinal position and δ the fractional energy deviation of an electron. Let Φ_0 be the rf phase corresponding to the reference electron located at the center of the bunch and Φ the rf phase of an electron located σ_z behind the center. If the cavity operates with a voltage U_{acc}, the energy deviation σ_E^f between the two electrons behind the accelerating section will be

$$\sigma_E^f = eU_{\mathrm{acc}} \left(\cos\Phi - \cos\Phi_0\right) + \sigma_E^i \tag{2.5}$$

where σ_E^i denotes the initial energy deviation. For $\Phi = \Phi_0$, the Taylor expansion of Eq. (2.5) yields

$$\sigma_E^f = \sigma_E^i - eU_{\mathrm{acc}} \sin\Phi_0 \left(\Phi - \Phi_0\right) - \frac{1}{2} eU_{\mathrm{acc}} \cos\Phi_0 \left(\Phi - \Phi_0\right)^2 \tag{2.6}$$

The fractional energy deviation at the final location is derived by dividing Eq. (2.5) with the final energy $E_f = E_i + eU_{\mathrm{acc}} \cos\Phi_0$ (E_i denotes the initial beam energy). We obtain

$$\begin{aligned} \frac{\sigma_E^f}{E_f} = \frac{\sigma_E^i}{E_i + eU_{\mathrm{acc}}\cos\Phi_0} - \frac{eU_{\mathrm{acc}}\sin\Phi_0}{E_i + eU_{\mathrm{acc}}\cos\Phi_0}\left(\Phi - \Phi_0\right) - \\ \frac{1}{2}\frac{eU_{\mathrm{acc}}\cos\Phi_0}{E_i + eU_{\mathrm{acc}}\cos\Phi_0}\left(\Phi - \Phi_0\right)^2 + \mathcal{O}\Big(\left(\Phi - \Phi_0\right)^3\Big) \ . \end{aligned} \tag{2.7}$$

The transfer matrix elements M_{65} and M_{66} can be associated with the zeroth and first order term of Eq. (2.7), hence

$$M_{66} = \frac{E_i}{E_i + eU_{\mathrm{acc}}\cos\Phi_0} \quad \text{and} \quad M_{65} = \frac{-eU_{\mathrm{acc}}\sin\Phi_0}{E_i + eU_{\mathrm{acc}}\cos\Phi_0}\frac{2\pi}{\lambda} \tag{2.8}$$

where the relation $(\Phi - \Phi_0) = 2\pi l/\lambda$ has been used. The second order term of the Taylor expansion (2.7) accounts for the non-linearity of the rf wave within the dimension of

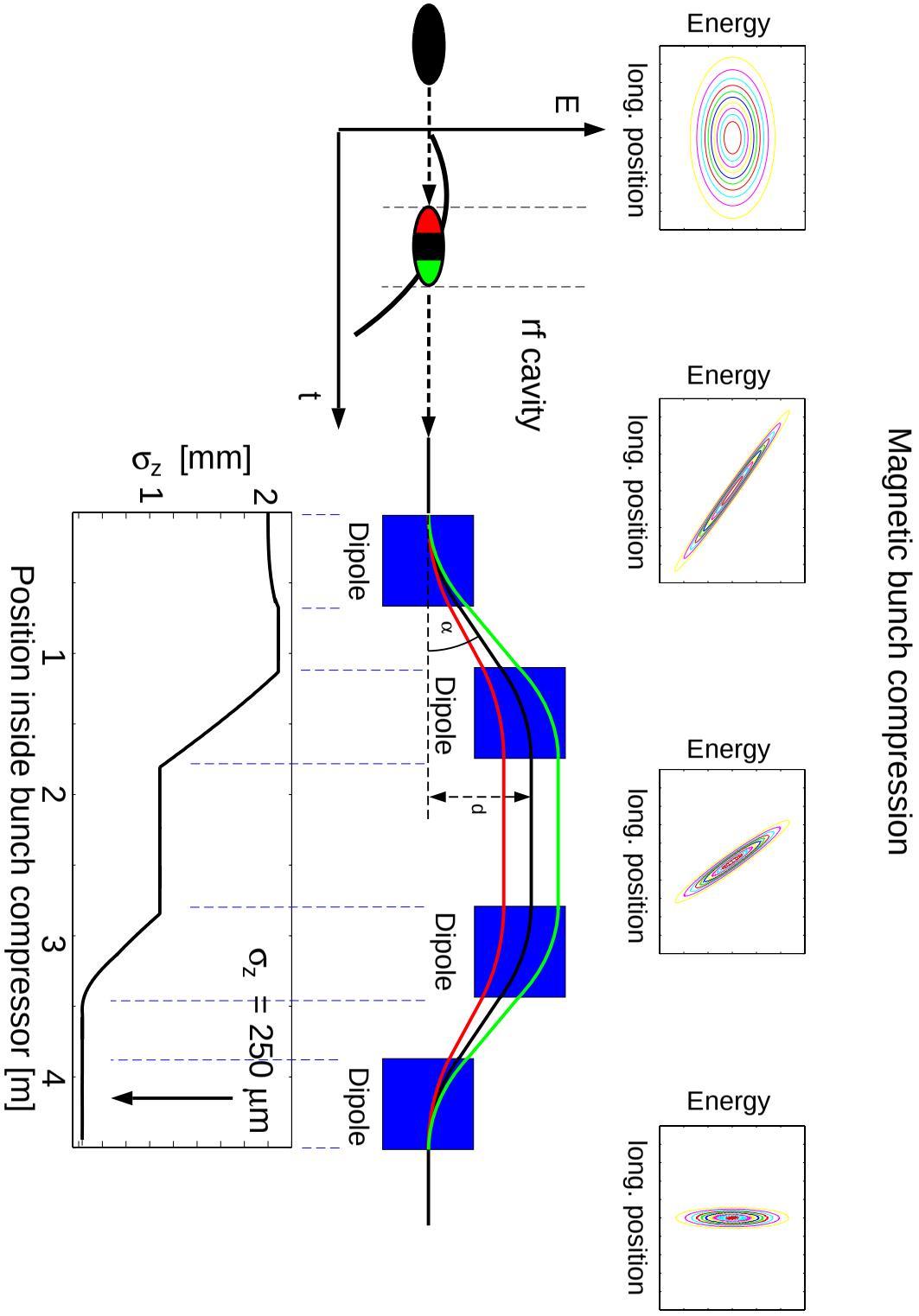


Figure 2.9: Longitudinal bunch compression by an off-crest acceleration in an rf cavity followed by a magnetic chicane compressor. The imposed energy-position correlation (higher energy electrons trailing lower energy electrons) and the dispersion of the chicane account for the bunch compression. Shown is the evolution of the longitudinal phase space distribution along the beam line and the rms bunch length along the chicane.

the particle bunch. This effect can be included into the transfer matrix formalism by expanding the transfer matrix to

$$\tilde{M} = \left(\begin{array}{c|c} M_A & S_A \\ \hline 0 & T_A \end{array} \right) \tag{2.9}$$

such that the linear transfer matrix M_A forms the upper left square matrix of $\tilde{M}$,

$$S_A = -\frac{1}{2} \frac{eU_{\mathrm{acc}} \cos \Phi_0}{E_i + eU_{\mathrm{acc}} \cos \Phi_0} \frac{2\pi}{\lambda} \tag{2.10}$$

denotes the second order contribution mapping l on the σ_E^f / E_f and $T_A = M_{65}^2$. $\tilde{M}$, expressed in the basis of $(l, \Delta E/E, l^2)$, yields a 3×3 square matrix and can be used for the beam matrix formalism outlined in appendix A.

The photo injector is adjusted to produce a beam of minimum energy before injection into the first accelerating rf module. Then there is no correlation between l and δ and the longitudinal part of the beam matrix can be expressed as a diagonal matrix as

$$\sigma_i = \begin{pmatrix} \sigma_{55} & 0 & 0 \\ 0 & \sigma_{66} & 0 \\ 0 & 0 & \sigma_{55}^2 \end{pmatrix} \tag{2.11}$$

where the term σ_{55}^2 accounts for the non-linearity of the rf field in the cavity. The beam matrix is transformed by

$$\sigma_f = \tilde{M} \cdot \sigma_i \cdot \tilde{M}^T \tag{2.12}$$

hence

$$\begin{aligned} \sigma_f &= \begin{pmatrix} 1 & 0 & 0 \\ M_{65} & M_{66} & S_A \\ 0 & 0 & M_{65}^2 \end{pmatrix} \cdot \begin{pmatrix} \sigma_{55} & 0 & 0 \\ 0 & \sigma_{66} & 0 \\ 0 & 0 & \sigma_{55}^2 \end{pmatrix} \cdot \begin{pmatrix} 1 & M_{65} & 0 \\ 0 & M_{66} & 0 \\ 0 & S_A & M_{65}^2 \end{pmatrix} \\ &= \begin{pmatrix} \sigma_{55} & M_{65}\sigma_{55} & 0 \\ M_{65}\sigma_{55} & M_{65}^2\sigma_{55} + M_{66}^2\sigma_{66} + S_A^2\sigma_{55}^4 & S_A M_{65}^2 \sigma_{55}^2 \\ 0 & S_A M_{65}^2 \sigma_{55}^2 & M_{65}^4 \sigma_{55}^2 \end{pmatrix} . \end{aligned} \tag{2.13}$$

The inspection of the matrix (2.13) shows that the off-diagonal elements $(\sigma_f)_{56}$ and $(\sigma_f)_{65}$ do not vanish for $M_{65} \neq 0$, yielding a correlated longitudinal phase space distribution after an off-crest acceleration in an rf cavity. The bunch length $\sqrt{\sigma_{55}}$ does not vary during the off-crest acceleration. The final energy deviation receives contributions from the initial energy spread $M_{66}^2 \sigma_{66}$, the initial bunch length $M_{65}^2 \sigma_{55}$ and the non-linear term $S_A^2 \sigma_{55}^4$ which are added quadratically. Figure 2.9 shows the correlated phase space distribution yielding an optimum bunch compression in the following chicane section.

Magnetic Chicane

The magnetic chicane consists of four rectangular dipole magnets deflecting the beam in the horizontal plane. The dipole magnets are of the same strength but the polarity of the second and third dipole is inverse to the polarity of the first and the fourth. Dipole 1 deflects the beam by an angle of $\alpha = 18°$. After passing the second dipole magnet the beam axis is transposed 35 cm parallel to the axis of the accelerator – magnets 3 and 4 deflect

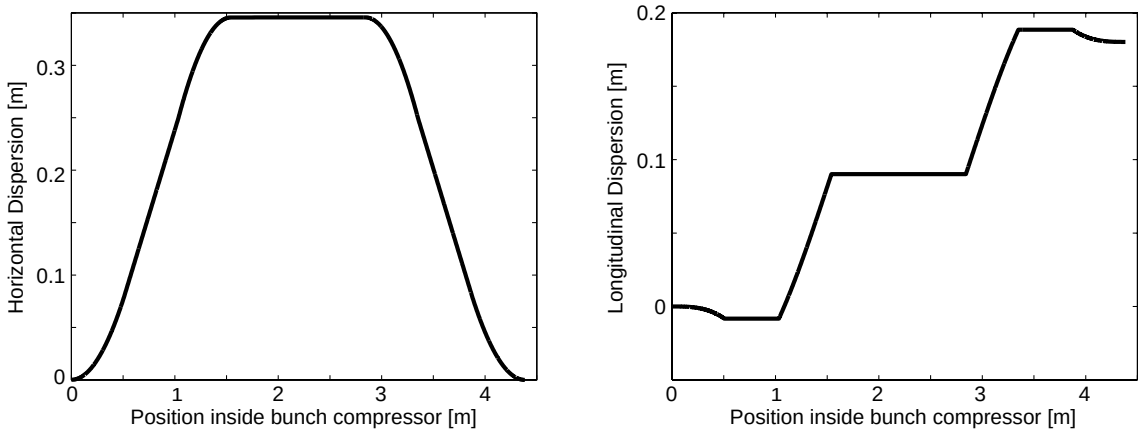


Figure 2.10: Left: horizontal dispersion of the magnetic chicane compressor. The maximum dispersion is $D_x = 0.35\,\mathrm{m}$ in the center of the chicane. Right: longitudinal dispersion of the magnetic chicane compressor. The maximum longitudinal dispersion is $M_{56} = 0.18\,\mathrm{m}$.

the beam back to the axis (see Fig. 2.9). Figure 2.10 shows the horizontal dispersion as a function of the position inside the bunch compressor. The dispersion is increasing towards the middle of the compressor reaching a maximum value of $D_x = 35\,\mathrm{cm}$. The transverse dispersion has to be entirely suppressed behind the compressor to avoid that electrons of different energy travel on different trajectories through the accelerating module #2 yielding a blow-up of the transverse emittance.

The transfer matrix $\tilde{M}_C$ of the magnetic chicane is given by

$$\tilde{M}_C = M_R(\alpha,\psi)\cdot M_D(L_1)\cdot M_R(-\alpha,\psi)\cdot M_D(L_2)\cdot M_R(-\alpha,\psi)\cdot M_D(L_1)\cdot M_R(\alpha,\psi)\ . \quad (2.14)$$

where $M_R(\alpha,\psi)$ and $M_D(L_{1,2})$ denote the transfer matrices of a rectangular bending magnet with bending angle α and pole face rotation angle ψ and a drift space of length $L_{1,2}$ respectively. The definition of these transfer matrices is given in appendix A. The longitudinal part of $\tilde{M}_C$ yields

$$M_C = \begin{pmatrix} 1 & M_{56} \\ 0 & 1 \end{pmatrix} \quad (2.15)$$

where the matrix element M_{56} denotes the longitudinal dispersion of the chicane compressor. M_{56} is shown as a function of the position in Fig. 2.10. Significant variations of M_{56} take place in the second and third dipole magnet. M_{56} describes the compression strength of the magnetic chicane since it maps the initial energy spread onto the final longitudinal position with respect to the reference particle.

The beam matrix (2.13) can be transformed through the magnetic chicane yielding in the basis of $(l, \Delta E/E)$

$$\tilde{\sigma}_f = \begin{pmatrix} 1 & M_{56} \\ 0 & 1 \end{pmatrix}\cdot\begin{pmatrix} \sigma_{55} & M_{65}\sigma_{55} \\ M_{65}\sigma_{55} & M_{65}^2\sigma_{55} + M_{66}^2\sigma_{66} + S_A^2\sigma_{55}^2 \end{pmatrix}\cdot\begin{pmatrix} 1 & 0 \\ M_{56} & 1 \end{pmatrix} \quad (2.16)$$

where

$$\tilde{\sigma}_{55}|_f \;=\; \sigma_{55}(1 + M_{56}M_{65})^2 + \sigma_{66}M_{56}^2M_{66}^2 + \sigma_{55}^2S_A^2M_{56}^2 \quad (2.17)$$

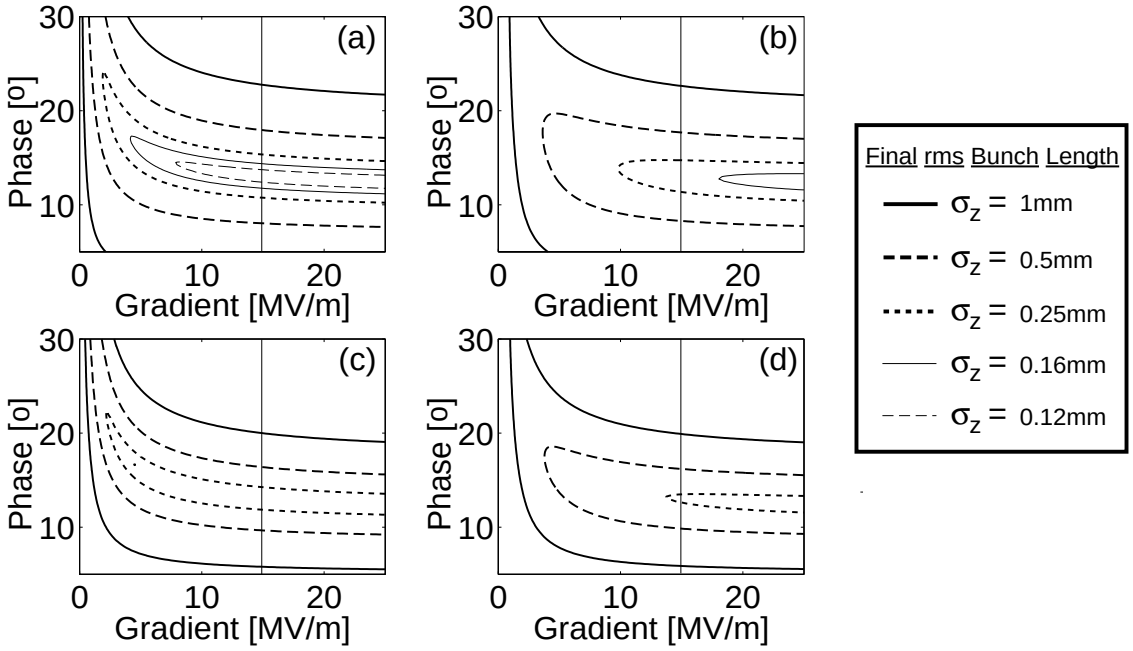


Figure 2.11: Lines of constant rms bunch length σ_z behind the bunch compressor as a function of the gradient and phase of the rf acceleration in Module #1. The four subplots depict the optimum phase gradient setting for different injector beam parameters. (a) $\sigma_z^i = 1.25$mm, $\sigma_E^i = 2 \cdot 10^{-3}$. (b) $\sigma_z^i = 1.25$mm, $\sigma_E^i = 8 \cdot 10^{-3}$. (c) $\sigma_z^i = 1.75$mm, $\sigma_E^i = 2 \cdot 10^{-3}$. (d) $\sigma_z^i = 1.75$mm, $\sigma_E^i = 8 \cdot 10^{-3}$.

$$\tilde{\sigma}_{56}|_f = \sigma_{55}\left(M_{65} + M_{65}^2 M_{56}\right) + \sigma_{66} M_{66}^2 M_{56} + \sigma_{55}^2 S_A^2 M_{56} \tag{2.18}$$

$$\tilde{\sigma}_{66}|_f = M_{65}^2 \sigma_{55} + M_{66}^2 \sigma_{66} + S_A^2 \sigma_{55}^2 \tag{2.19}$$

The final bunch length $\tilde{\sigma_z}$ therefore is

$$\tilde{\sigma_z} = \sqrt{\sigma_{55}(1 + M_{56} M_{65})^2 + \sigma_{66} M_{56}^2 M_{66}^2 + \sigma_{55}^2 S_A^2 M_{56}^2}\,. \tag{2.20}$$

The linear contribution of σ_{55} can be minimized by choosing M_{65} such that $M_{56} M_{65} + 1 \to 0$. The contribution of the initial energy spread σ_{66} to the final bunch length can be decreased by using stronger accelerating field gradients, hence an higher energy gain, yielding a smaller M_{66}. The term $\sigma_{55}^2 S_A^2 M_{56}^2$ can be decreased only be choosing a smaller initial bunch length $\sqrt{\sigma_{55}}$. The latter contribution limits the achievable longitudinal compression in the magnetic chicane.

Figure 2.11 shows a contour plot of the achievable bunch length as a function of the gradient and the phase of the rf cavities in front of the magnetic chicane. Injector bunch lengths of $\sigma_z^i = 1.25\,\mathrm{mm}$ and $\sigma_z^i = 1.75\,\mathrm{mm}$ and injector energy spreads of $\sigma_E^i = 2 \cdot 10^{-3}$ and $\sigma_E^i = 8 \cdot 10^{-3}$ are considered. The rf de-phasing to obtain optimum bunch compression is decreasing with increasing field gradient. The vertical lines indicate the nominal operating gradient of the TTF linac, which is $15\,\mathrm{MeV/m}$. At this field gradient, a bunch length of (a) $\sigma_z = 110\,\mu$m, (b) $\sigma_z = 200\,\mu$m, (c) $\sigma_z = 190\,\mu$m and (d) $\sigma_z = 250\,\mu$m can be obtained.

Acceleration by RF Module #2

The energy spread at the experimental area can be evaluated by transforming the beam matrix through the second rf module. We obtain the beam matrix

$$\begin{aligned}\bar{\sigma}_f &= \begin{pmatrix} 1 & 0 & 0 \\ R_{65} & R_{66} & U_A \\ 0 & 0 & R_{65}^2 \end{pmatrix} \cdot \begin{pmatrix} \tilde{\sigma}_{55} & \tilde{\sigma}_{56} & 0 \\ \tilde{\sigma}_{56} & \tilde{\sigma}_{66} & 0 \\ 0 & 0 & \tilde{\sigma}_{55}^2 \end{pmatrix} \cdot \begin{pmatrix} 1 & R_{65} & 0 \\ 0 & R_{66} & 0 \\ 0 & U_A & R_{65}^2 \end{pmatrix} \qquad (2.21) \\ &= \begin{pmatrix} \tilde{\sigma}_{55} & R_{65}\tilde{\sigma}_{55}+R_{66}\tilde{\sigma}_{56} & 0 \\ R_{65}\tilde{\sigma}_{55}+R_{66}\tilde{\sigma}_{56} & R_{65}(R_{65}\tilde{\sigma}_{55}+R_{66}\tilde{\sigma}_{56})+R_{66}(R_{65}\tilde{\sigma}_{56}+R_{66}\tilde{\sigma}_{66})+U_A^2\tilde{\sigma}_{55}^2 & U_A^2R_{65}^2\tilde{\sigma}_{55}^2 \\ 0 & U_A^2R_{65}^2\tilde{\sigma}_{55}^2 & R_{65}^4\tilde{\sigma}_{55}^2 \end{pmatrix}\end{aligned}$$

The final energy spread $\sqrt{\bar{\sigma}_{66}}$ can be expressed in terms of the initial beam parameters

$$\begin{aligned}\bar{\sigma}_{66} &= R_{65}^2\tilde{\sigma}_{55} + 2R_{65}R_{66}\tilde{\sigma}_{56} + R_{66}^2\tilde{\sigma}_{66} + U_A^2\tilde{\sigma}_{55}^2 \qquad (2.22) \\ &= R_{65}^2\Big\{\sigma_{55}(1+M_{56}M_{65})^2 + \sigma_{66}M_{56}^2M_{66}^2 + S_A^2M_{56}^2\sigma_{55}^2\Big\} + \\ &\quad 2R_{65}R_{66}\Big\{\sigma_{55}\Big(M_{65}+M_{65}^2M_{56}\Big) + \sigma_{66}M_{66}^2M_{56} + S_A^2M_{56}\sigma_{55}^2\Big\} + \\ &\quad R_{66}^2\Big\{\sigma_{55}M_{65}^2 + \sigma_{66}M_{66}^2 + S_A^2\sigma_{55}^2\Big\} + \qquad (2.23) \\ &\quad U_A^2\Big\{\sigma_{55}(1+M_{56}M_{65})^2 + \sigma_{66}M_{56}^2M_{66}^2 + S_A^2M_{56}^2\sigma_{55}^2\Big\}^2 \ .\end{aligned}$$

The second accelerating module is generally operated at an rf phase $\Phi_0 = 0°$ yielding the maximum energy gain. In this case we obtain $R_{65} = 0$ and Eq. (2.23) reduces to

$$\begin{aligned}\bar{\sigma}_{66} = R_{66}^2\Big\{&\sigma_{55}M_{65}^2 + \sigma_{66}M_{66}^2 + S_A^2\sigma_{55}^2\Big\} + \\ &U_A^2\Big\{\sigma_{55}(1+M_{56}M_{65})^2 + \sigma_{66}M_{56}^2M_{66}^2 + S_A^2M_{56}^2\sigma_{55}^2\Big\}^2 \ .\end{aligned} \qquad (2.24)$$

$\sqrt{\bar{\sigma}_{66}}$ is obtained by scaling the the rms energy deviation behind the magnetic chicane with R_{66}. The non-linear contribution of the rf acceleration is added quadratically.

A measurement of the longitudinal bunch charge distribution can be performed by rotating the longitudinal phase space distribution using the magnetic chicane and the second rf acceleration. In particular, the longitudinal phase space distribution is rotated by $\pi/2$ transforming a temporal slice in front of the chicane into a slice of constant energy behind the second rf module. This condition is fulfilled for $M_{56}R_{65} + R_{66} \to 0$ [22] and Eq. (2.23) reduces to

$$\begin{aligned}\bar{\sigma}_{66} &= \sigma_{55}R_{65}^2 + U_A^2\Big\{\sigma_{55}(1+M_{56}M_{65})^2 + \sigma_{66}M_{56}^2M_{66}^2 + S_A^2M_{56}^2\sigma_{55}^2\Big\}^2 \qquad (2.25) \\ &\approx \sigma_{55}R_{65}^2 \ . \qquad (2.26)\end{aligned}$$

Equation (2.26) is a linear relation between the longitudinal bunch charge distribution and the bunch energy deviation and is the basis for the bunch length measurement. The parameters of the second rf module R_{65} and R_{66} have to fulfill $M_{56}R_{65} + R_{66} \to 0$. Details will be presented in chapter 6.

Chapter 3

Properties of Transition Radiation

3.1 Transition Radiation as a Tool for Beam Diagnostics

Transition radiation is emitted whenever a charged particle passes from one dielectric medium into another. In either medium the charge carries an electromagnetic field distribution, which changes rapidly at the boundary because of the different permittivities. In this process, part of the field traveling with the charge is radiated away as transition radiation. The radiation is emitted both into the forward and the backward hemisphere of the boundary.

This chapter is dedicated to outline the basic properties of transition radiation, such as the radiation spectrum, angular distribution, polarization and the radiation source dimension. Attention will be drawn to optical transition radiation (OTR), $400\,\mathrm{nm} \leq \lambda \leq 800\,\mathrm{nm}$, and far-infrared transition radiation, $0.1\,\mathrm{mm} \leq \lambda \leq 10\,\mathrm{mm}$.

Optical transition radiation can be used to record the transverse and the longitudinal charge distribution of an electron bunch. The light emitted at the boundary is imaged onto a CCD. The radial intensity distribution is a direct measure of the transverse bunch charge distribution. The temporal distribution of the light pulse can be used to determine the longitudinal bunch charge distribution.

Far-infrared transition radiation is a powerful tool to measure the longitudinal bunch charge distribution of electron bunches in the pico- and sub-picosecond range. The bunch length and the radiation wavelength are of equal magnitude and coherent transition radiation is emitted. The coherent transition radiation power spectrum carries information about the bunch length and the shape of the longitudinal bunch charge distribution.

3.2 Optical Transition Radiation

3.2.1 Ginzburg-Frank Equation

Figure 3.1 shows a bunch of particles in medium 1 with permittivity ϵ_1 approaching a boundary to medium 2 with permittivity ϵ_2. The particle bunch moves on a straight line

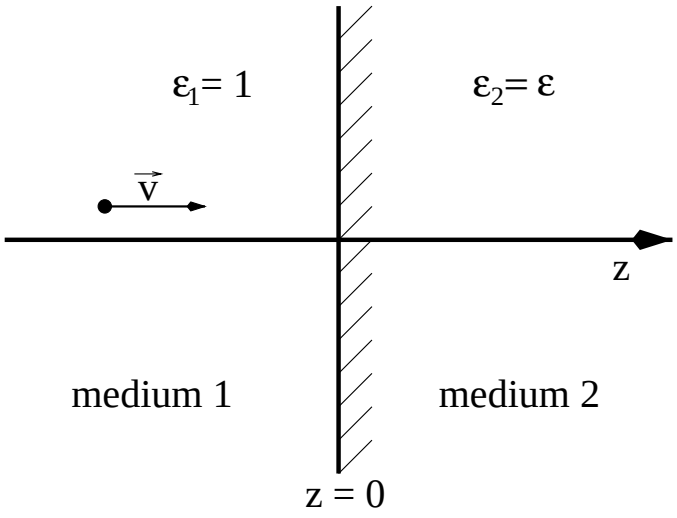


Figure 3.1: Configuration for the derivation of the Ginzburg-Frank Equation.

with uniform velocity $\vec{v}$, directed perpendicular to the boundary. The boundary itself is assumed to be of infinite extent. The radiation energy U emitted into the backward hemisphere when a single electron of charge $-e$ crosses the boundary between vacuum ($\epsilon_1 = 1$) and a medium ($\epsilon_2 = \epsilon$) is described by the Ginzburg-Frank formula

$$U = \int_0^\infty \int_0^{2\pi} \int_0^\pi d\omega\, d\phi\, \sin\theta\, d\theta\, U_1(\omega,\theta) \quad \text{with} \tag{3.1}$$

$$U_1 = \frac{e^2}{4\pi^3\epsilon_0 c} \frac{\beta^2 \sin^2\theta \cos^2\theta\, (\epsilon-1)^2 \left(1-\beta^2+\beta\sqrt{\epsilon-\sin^2\theta}\right)^2}{(1-\beta^2\cos^2\theta)^2 \left(1+\beta\sqrt{\epsilon-\sin^2\theta}\right)^2 \left(\epsilon\cos\theta-\sqrt{\epsilon-\sin^2\theta}\right)^2}\,. \tag{3.2}$$

$U_1(\omega,\theta)$ denotes the spectral energy distribution, ω the angular frequency and θ the polar angle of the radiation. The velocity of the electron is given by $\beta = v/c$. Note that U_1 does not depend on the radiation frequency ω. This feature makes transition radiation an excellent tool for beam imaging, since no frequency-dependent correction for the emitted radiation power is necessary. For metallic screens we let $\epsilon \to \infty$, which is a valid approximation for frequencies well below the plasma frequency of the metal, yielding

$$U_1 = \frac{e^2}{4\pi^3\epsilon_0 c} \frac{\beta^2 \sin^2\theta}{(1-\beta^2\cos^2\theta)^2}\,. \tag{3.3}$$

Equation (3.3) is the Ginzburg-Frank formula as it is commonly applied to describe transition radiation for optical beam diagnostics. The derivation of Eq. (3.3) [23] is outlined in appendix B.

3.2.2 Radiated Energy

The total energy per unit frequency emitted from a metallic screen is determined by integration of Eq. (3.3) over the solid angle $d\Omega = \sin\theta d\theta d\phi$

$$\frac{dU}{d\omega} = \int d\theta\, d\phi\, \sin\theta\, U_1(\theta) \tag{3.4}$$

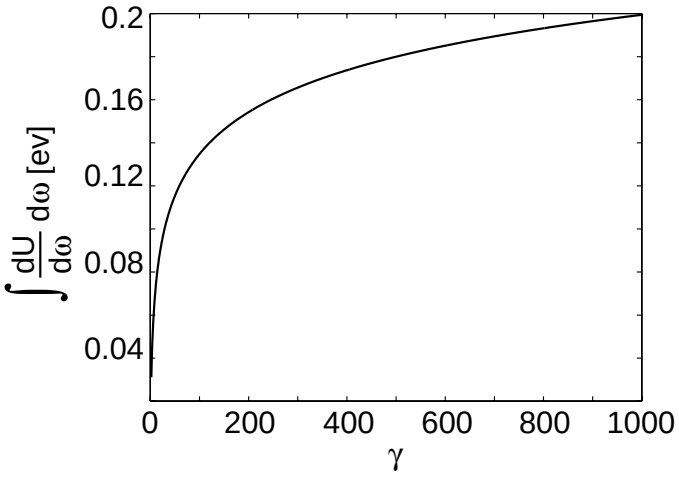


Figure 3.2: Energy in the visible range emitted by single particle transition radiation as a function of the Lorentz factor γ.

$$= \frac{e^2\beta^2}{2\pi^2\epsilon_0 c}\int_0^\pi d\theta\,\frac{\sin^3\theta}{\left(1-\beta^2\cos^2\theta\right)^2} \tag{3.5}$$

$$= -\frac{e^2}{8\pi^2\epsilon_0 c}\left(4+\frac{(1+\beta^2)}{\beta}\log\frac{(1-\beta)^2}{(1+\beta)^2}\right). \tag{3.6}$$

The emitted energy by a single electron in the visible wavelength band $400-800\,\mathrm{nm}$ is shown in Fig. 3.2 as a function of the relativistic Lorentz factor γ. The total radiated energy is increasing with increasing electron energy, however, the increase is most significant below $\gamma \approx 100$. The emitted radiation energy per electron is evaluated by

$$U = \int_{opt}\frac{dU}{d\omega}\,d\omega \tag{3.7}$$

where frequencies in the optical range are taken into account ($4.7\cdot 10^{15}1/\mathrm{s} \geq \omega \geq 2.4\cdot 10^{15}1/\mathrm{s}$). For $\gamma = 100$, the total emitted radiation energy is $U = 0.13\,\mathrm{eV}$ per electron. The photon energy corresponding to $\omega = 3.8\cdot 10^{15}\,1/\mathrm{s}$ is $E_\gamma = \hbar\omega = 2.5\,\mathrm{eV}$, hence the number of photons can be approximated by 0.05 per electron, i. e. twenty electrons are needed to produce one photon. A bunch of $5\cdot 10^{10}$ electrons generates therefore $5\cdot 10^8$ photons in the visible range, a number which is easily detectable with standard CCD devices [24].

3.2.3 Polarization

The polarization of transition radiation can be understood in terms of its generation process. Part of the charge field configuration in vacuum is transfered to the radiation field while the bunch is undergoing transition. The field configuration is polarized in the so-called "radiation plane", which is defined by the radiation momentum $\vec{k}$ and the direction of particle motion $\vec{z}$. The polarization of the electric field $\vec{E}^R$ emitted with momentum $\vec{k}$ is shown in Fig. 3.3.

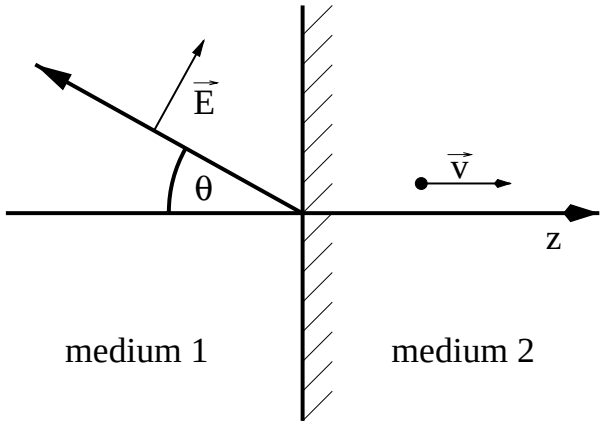


Figure 3.3: Polarization of transition radiation.

3.2.4 Angular Distribution

The angular distribution of backward transition radiation is shown in Fig. 3.4. The maximum energy is radiated at an angle of $\theta_0 = 1/(\beta\gamma)$. This result is obtained by the differentiation of the Ginzburg-Frank formula with respect to θ yielding

$$\frac{dU_1}{d\theta} = \frac{\rho^2_{q,\omega}(0)}{4\pi^3\epsilon_0} \frac{\beta^4 c \sin 2\theta}{\left(1-\beta^2\cos^2\theta\right)^3} \left\{1-\beta^2-\beta^2\sin^2\theta\right\} . \tag{3.8}$$

Equation (3.8) vanishes for the maximum energy radiated, hence

$$\sin^2\theta_0 = \frac{1-\beta^2}{\beta^2} \quad \Rightarrow \quad \theta_0 = \frac{1}{\beta\gamma} . \tag{3.9}$$

No energy is emitted at $\theta = 0$, because of the radial polarization of the fields traveling with the electron bunch. Notice, however, that a significant part of the energy is radiated

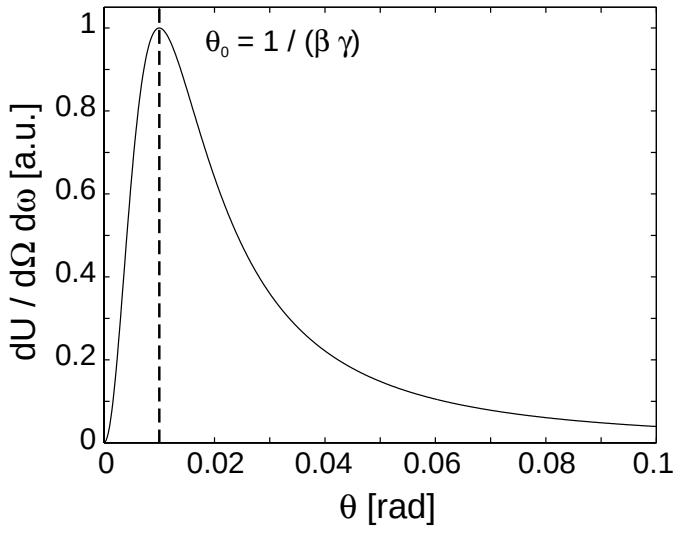


Figure 3.4: Angular distribution of single particle transition radiation.

at angles larger than θ_0. The optical system used for the imaging of optical transition radiation therefore has to have a larger aperture to collect sufficient intensity.

3.2.5 Oblique Incidence

The transition radiator at the TESLA Test Facility is a thin 40 nm aluminum layer evaporated onto a 25 μm Kapton foil stretched in a frame. The foil is mounted at an angle of 45° with respect to the accelerator axis so that the backward lobe of transition radiation is reflected at 90° out of the vacuum chamber. The theoretical description of transition radiation has to be extended to describe this situation.

(1) Oblique Incidence

The particle is moving on a straight line with uniform velocity in the xz-plane, as shown by Fig. 3.5. ψ is the angle between the electron trajectory and the z axis. The derivation of

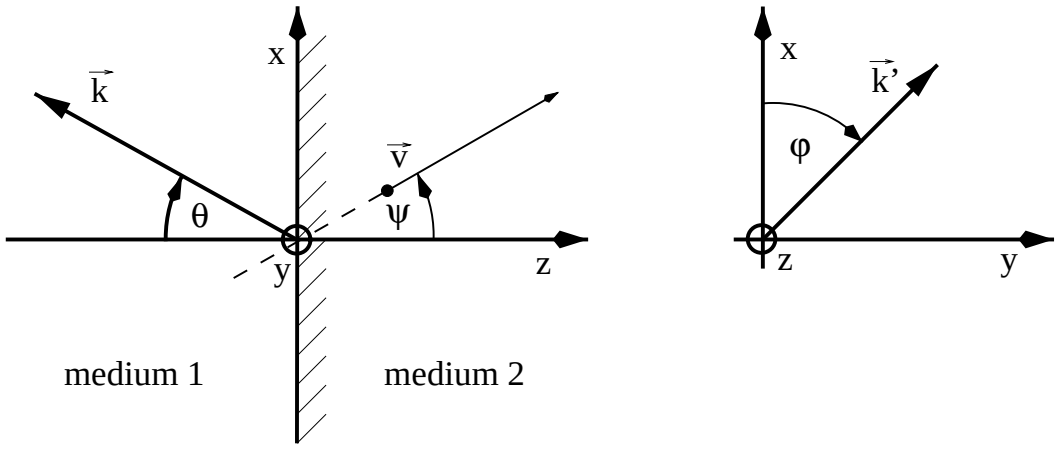


Figure 3.5: Coordinates for oblique incidence of the particle bunch. ψ denotes the angle between the particle velocity $\vec{v}$ and the z-axis in the xz-plane, $\pi - \theta$ the angle between the backward lobe of the transition radiation and z. The azimuthal angle of $\vec{k'}$ (projection of $\vec{k}$ in the xy-plane) with respect to the x-axis is denoted by ϕ.

the radiation field is more elaborate than for normal incidence. The more general situation requires the introduction of a polar angle θ and an azimuthal angle ϕ. The "radiation-plane" which is defined by $\vec{k}$ and $\vec{v}$ becomes the preference plane. Radiation polarized parallel and orthogonal to the radiation plane is denoted by $E_{\parallel}$ and $E_{\perp}$ respectively.

(2) Metallic Interface

The formulae describing the spectral energy distribution radiated by a single electron of charge $-e$ are [25]

$$U_1^{\parallel} = \frac{e^2}{4\pi^3\epsilon_0 c}\left(\frac{\beta\cos\psi\,(\sin\theta - \beta\cos\phi\sin\psi)}{(1-\beta\sin\theta\cos\phi\sin\psi)^2 - \beta^2\cos^2\theta\cos^2\psi}\right)^2 \tag{3.10}$$

$$U_1^{\perp} = \frac{e^2}{4\pi^3\epsilon_0 c}\left(\frac{\beta^2\cos\psi\cos\theta\sin\phi\sin\psi}{(1-\beta\sin\theta\cos\phi\sin\psi)^2 - \beta^2\cos^2\theta\cos^2\psi}\right)^2 \tag{3.11}$$

where $U_1^{\parallel}$ and $U_1^{\perp}$ denote the radiated spectral energy density of the field component polarized parallel and perpendicular to the radiation plane and $\beta = v/c$. The metallic interface is of infinite permittivity ($\epsilon \to \infty$). The Ginzburg-Frank formula (3.3) can be recovered from Eq. (3.10) and (3.11) for normal incidence $\psi = 0$. $U_1^{\parallel}$ then agrees with the Ginzburg-Frank formula, whereas $U_1^{\perp}$ vanishes. Note that transition radiation vanishes for a grazing incidence angle of $\psi \approx \pi/2$.

Figure 3.6 shows the angular distribution of $U_1^{\parallel}$ (left column) and $U_1^{\perp}$ (right column) as a function of the polar angle θ. The beam is incident at an angle of $\psi = 45°$. The subplots show the distribution for different azimuthal angles ϕ. The lobe is centered at $\theta = \psi$. The energy density of $U_1^{\parallel}$ is decreasing rapidly for larger azimuthal angles ϕ indicating that $U_1^{\parallel}$ contributes mostly in the reference plane defined by $(\vec{v}, \vec{z})$. $U_1^{\perp}$, on the other hand, vanishes for $\phi = 0$, rises to the magnitude of $U_1^{\parallel}$ at $\phi = 1/\gamma$ and decreases for larger azimuthal angles. The angular distribution of $U_1^{\perp}$ contains only a single maximum.

3.3 Far Infrared Transition Radiation

The description of transition radiation in the millimeter- and sub-millimeter wavelength range needs a modification of the Ginzburg-Frank formula. The size of the transition boundary is no longer large compared to the transverse extension of the electromagnetic fields. Diffraction at a transition screen of finite size leads to a widening of the angular distribution and a reduction of the spectral acceptance of the detection system.

3.3.1 Source Dimension

The transverse source size of transition radiation is the projection of the electromagnetic fields carried by the charge distribution onto the transition boundary. The Maxwell equations can be solved using a Fourier transformation of the longitudinal coordinate $\zeta = z - ct$ to the longitudinal wave number k

$$E_{r,z}(\zeta, r) = \int_{-\infty}^{\infty} \tilde{E}_{r,z}(k, r) \exp(ik\zeta) dk \tag{3.12}$$

while the transverse coordinates are not transformed. This procedure permits a description of the transverse field as a function of the wave number k.

The frequency domain description of the electric and magnetic fields, $\tilde{E}_z$, $\tilde{E}_r$ and $\tilde{B}_\theta$ (the other components vanish for reasons of symmetry) is evaluated as the bunch of charges passes by the observer. A ring charge distribution of radius a modulated with a longitudinal distribution whose Fourier transformation is denoted as $\tilde{\lambda}(k)$ is evaluated. The fields have to obey boundary conditions at the surface of the beam pipe with radius b, which is assumed to be perfectly conducting. The following results can be derived [26, 27]

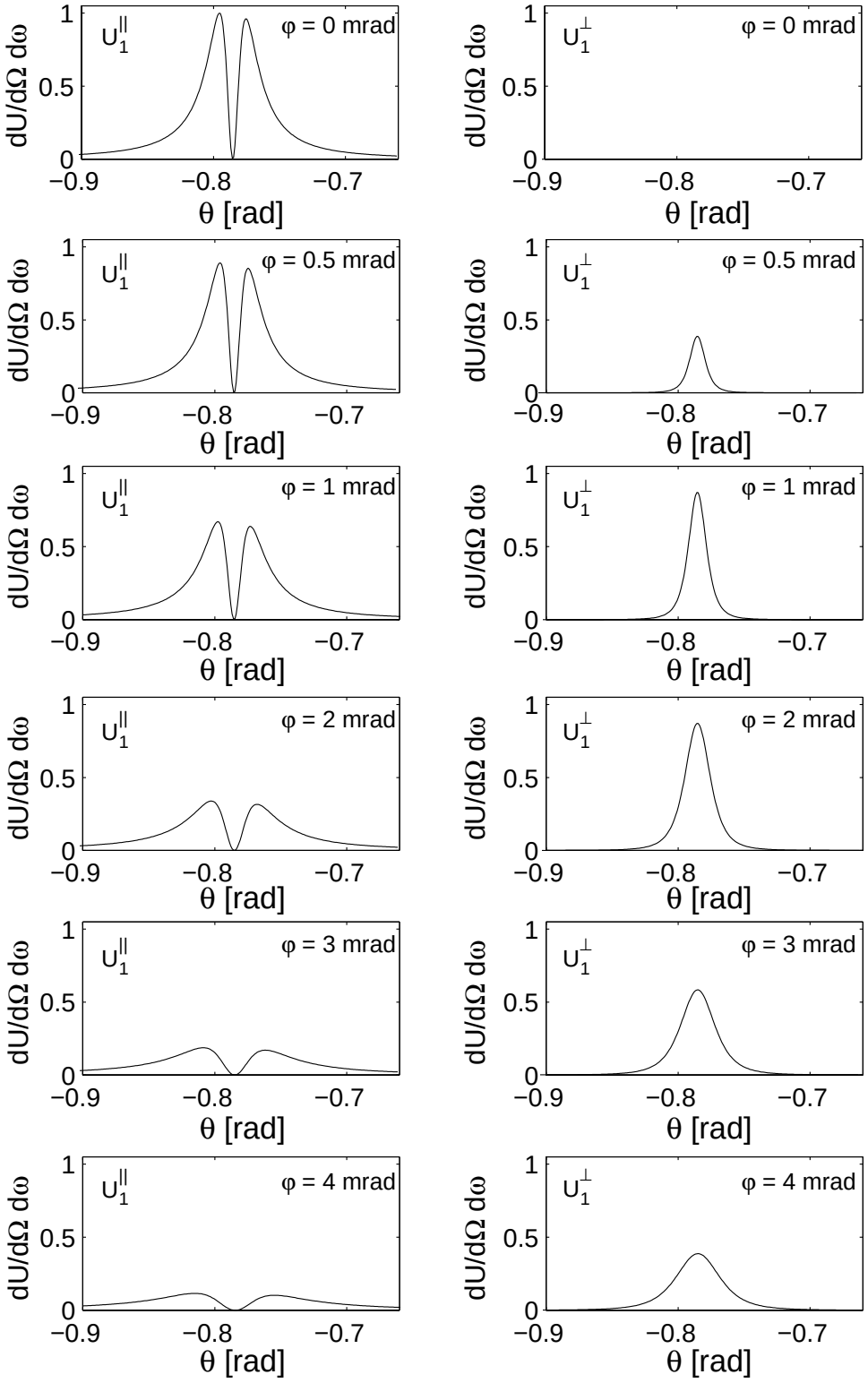


Figure 3.6: Transition radiation $dU/d\Omega d\omega$ as a function of the polar angle θ for the oblique incidence angle of $\psi = \pi/4$. The left column shows the polarization component parallel, the right column orthogonal to the radiation plane. The subplots show $dU/d\Omega d\omega$ for a set of azimuthal angles ϕ.

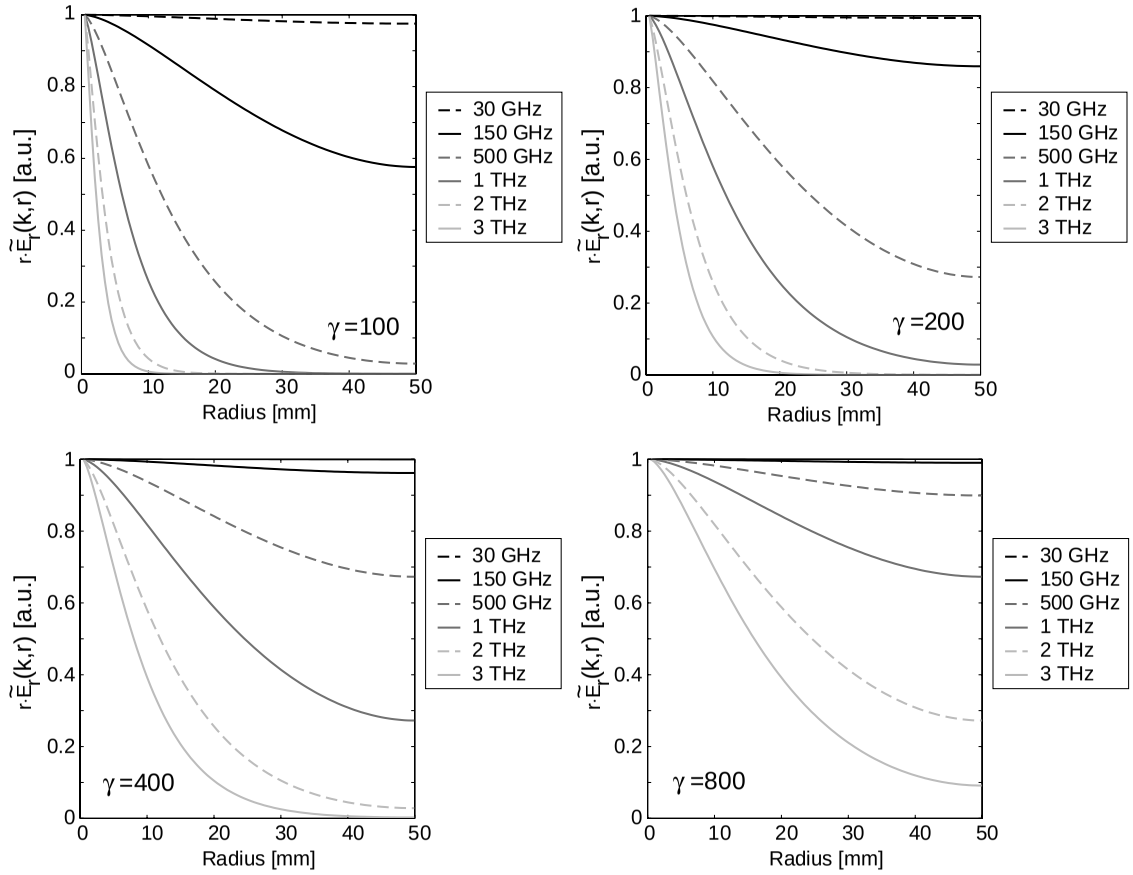


Figure 3.7: Fourier components of the radial electric field $r\tilde{E}_r$ as a function of radius for frequencies between 30 GHz and 3 THz. The field distributions are normalized to 1 at $r = 0$.

$$\tilde{E}_z(k,r) = \frac{ik}{2\pi\epsilon_0\gamma^2} q\tilde{\lambda}(k) \left[\left\{ \begin{array}{ll} -K_0\left(\frac{ka}{\gamma}\right) I_0\left(\frac{kr}{\gamma}\right) & , \quad r < a \\ -I_0\left(\frac{ka}{\gamma}\right) K_0\left(\frac{kr}{\gamma}\right) & , \quad r > a \end{array} \right\} + I_0\left(\frac{ka}{\gamma}\right) \frac{K_0\left(\frac{kb}{\gamma}\right)}{I_0\left(\frac{kb}{\gamma}\right)} I_0\left(\frac{kr}{\gamma}\right) \right] . \tag{3.13}$$

$$\tilde{E}_r(k,r) = \frac{k}{2\pi\epsilon_0\gamma} q\tilde{\lambda}(k) \left[\left\{ \begin{array}{ll} -K_0\left(\frac{ka}{\gamma}\right) I_1\left(\frac{kr}{\gamma}\right) & , \quad r < a \\ I_0\left(\frac{ka}{\gamma}\right) K_1\left(\frac{kr}{\gamma}\right) & , \quad r > a \end{array} \right\} + I_0\left(\frac{ka}{\gamma}\right) \frac{K_0\left(\frac{kb}{\gamma}\right)}{I_0\left(\frac{kb}{\gamma}\right)} I_1\left(\frac{kr}{\gamma}\right) \right] . \tag{3.14}$$

and $\tilde{B}_\theta = \beta/c\tilde{E}_r$. I_0, K_0, I_1 and K_1 denote the modified Bessel-functions of zeroth and first order, γ the relativistic Lorentz factor. The bunch charge is given by q. Details of the derivation are outlined in appendix C, where a solution of the problem including a vacuum chamber of finite conductivity is presented as well. The fields are rising propor-

tional to I_0 and I_1 inside the ring charge but are decreasing proportional to K_0 and K_1 outside. The second term denotes the contribution of the cylindrical beam pipe to the total field configuration. If we assume a line charge distribution ($a = 0$), the primary fields will drop with $K_0(kr/\gamma)$ or $K_1(kr/\gamma)$, while the beam pipe causes a rise of the fields with $I_0(kr/\gamma)$ or $I_1(kr/\gamma)$. Notice that the contribution of the vacuum chamber can be neglected for Fourier components corresponding to the optical range ($k \approx 10^7\,1/\mathrm{m}$), because it is entirely suppressed by the factor $K_0(kb/\gamma)$. For further considerations, it is sufficient to consider the radial component of the electric field. The longitudinal electric field component can be neglected compared to the transverse electric field, because $\tilde{E}_z \sim \tilde{E}_r/\gamma$. The azimuthal magnetic field is related to the radial electric field by the factor of β/c.

Figure 3.7 shows the Fourier components of the radial electric field multiplied with $2\pi r$ (Jacobian of cylindrical coordinates) for frequencies between 30 GHz and 3 THz. The expressions are normalized to 1 at $r = 0$ to permit a comparison of the radial dependences. The screens at the TTF linac have a diameter of $d = 35\,\mathrm{mm}$. The field components propagating at larger distances from the charge distribution miss the screen and do not contribute to the radiation. Therefore the radiated energy decreases towards lower frequencies, because an increasing fraction of the field misses the screen. The radius b of the beam pipe is also of influence; the low frequency field components do not vary significantly within the beam pipe, hence the minimum acceptance is $\pi(d/2)^2/\pi b^2$. The fraction of the field components contributing to the radiation process can be evaluated by

$$D = \frac{\int_0^{d/2} dr\, 2\pi r \tilde{E}_r}{\int_0^{b} dr\, 2\pi r \tilde{E}_r}\,. \tag{3.15}$$

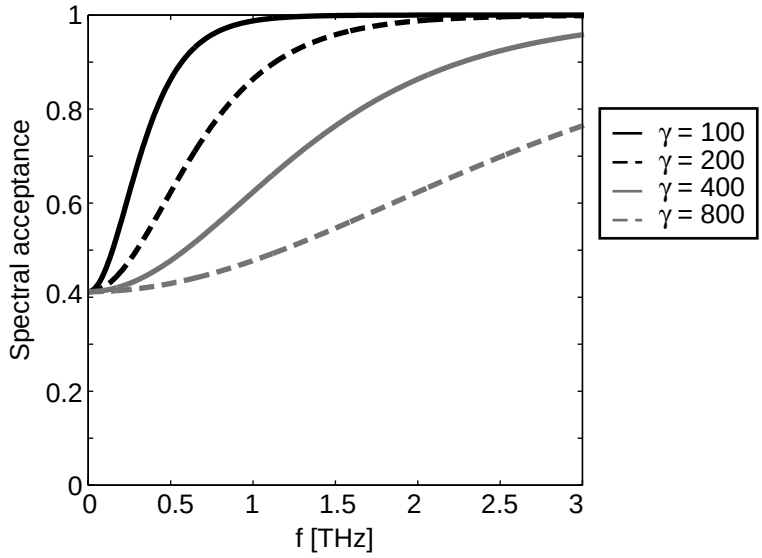


Figure 3.8: Spectral acceptance $D(f)$ of far infrared transition radiation due to the extension of the electromagnetic fields traveling with the charge, Eq. (3.15), is plotted versus the frequency of the electric field Fourier component. Four different beam energies are denoted by the Lorentz factor γ.

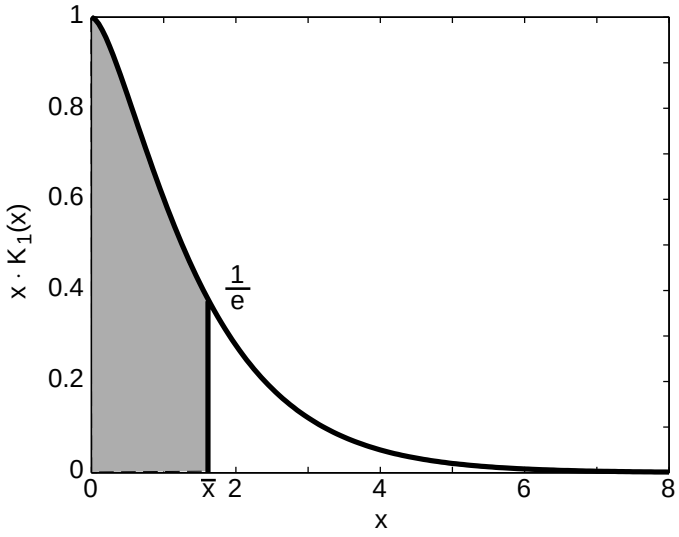


Figure 3.9: The function $x \cdot K_1(x)$. The transverse source dimension is defined as $\bar{x} \cdot K_1(\bar{x}) = 1/e$.

The quantity D is plotted versus the frequency of the Fourier component in Fig. 3.8. $D(f)$ can be interpreted as a spectral acceptance function. It clearly shows the suppression of transition radiation at low frequencies ($f \leq 3\,\mathrm{THz}$). For high frequency and low electron energy one gets $D(f) \approx 1$, since the electric field traveling with the charge is confined within the area of the transition radiator.

For a quantitative description of the source dimension we consider

$$r \cdot \tilde{E}_r(k,r) \sim \frac{kr}{\gamma} K_1\left(\frac{kr}{\gamma}\right) \equiv x \cdot K_1(x) \tag{3.16}$$

with $x = kr/\gamma$. Figure 3.9 shows the function $x \cdot K_1(x)$. The transition radiation source dimension R_s is defined by the argument $\bar{x}$ where the function $x \cdot K_1(x)$ drops to $1/e$. Hence

$$\bar{x}K_1(\bar{x}) = \frac{1}{e} \quad \Rightarrow \quad \frac{kR_s}{\gamma} = 1.66 \quad \Rightarrow \quad R_s = \frac{1.66 \cdot \gamma}{k}\,. \tag{3.17}$$

The transverse dimension of the electromagnetic fields is proportional to the beam energy γ and the wavelength of the Fourier component ($\lambda = 2\pi/k$). With increasing Lorentz factor γ the radial electric field amplitude extends to larger radii, which can be understood in terms of the Lorentz transformation of the field. The increase of the radiation source dimension with respect to the radiation wavelength can be understood in terms of diffraction.

The transverse extension of the electromagnetic field limits the applicability of the optical imaging technique for determining the bunch size. For low emittance bunches and large γ factors the transverse field extension may exceed the whole bunch size and then a meaningful measurement is no longer possible. The transverse beam size $\sigma_r = \sigma_r^*/\sqrt{\gamma}$ is decreasing proportional to the square root of the beam energy, when the strength of the

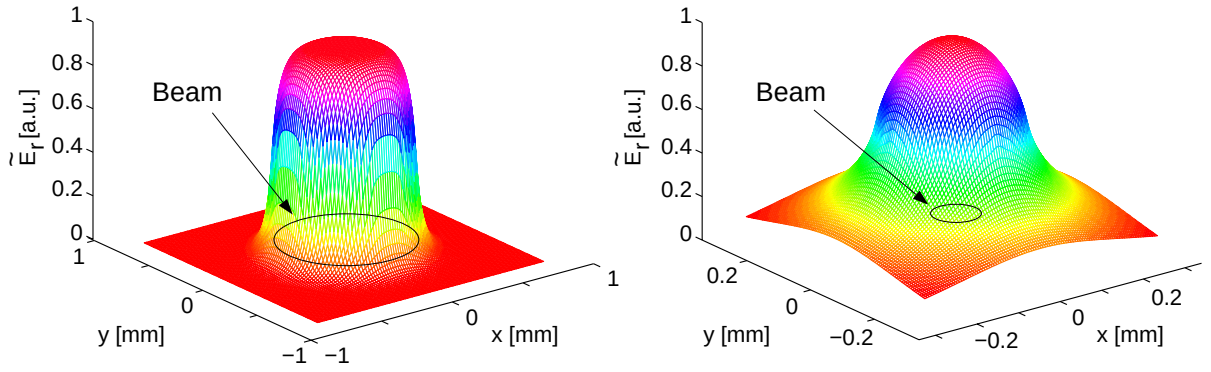


Figure 3.10: Transition radiation field Eq. (3.13) of a uniform charge distribution of radius $a = 230\,\mu$m, $\gamma = 100$ (left) and $a = 83\,\mu$m, $\gamma = 800$ (right). The wavelength is 500 nm. Left: the shape of the uniform charge distribution can be recovered by the electromagnetic fields. Right: the shape of the uniform charge distribution is smeared out.

magnetic lattice is scaled with γ. The source dimension of transition radiation, on the other hand, increases proportional to beam energy. It is evident, that transition radiation of fixed wavelength can be used for the imaging of the transverse charge distribution to a maximum beam energy only [28], the so-called critical electron energy γ_c. Equating the radial beam size σ_r with the source dimensions of the radiation fields $R_s = 1.66\gamma_c/k$ yields

$$\gamma_c = \left(\frac{k^2\sigma_r^{*2}}{2.76}\right)^{1/3} . \tag{3.18}$$

Assuming $\lambda = 500\,$nm (optical transition radiation) and a normalized emittance of $5 \cdot 10^{-6}\,$m, the critical Lorentz factor is $\gamma_c = 924$ corresponding to an electron beam energy of about 470 MeV. It is evident that tight focusing of the electron beam on the transition radiator should be avoided.

The resolution limit of optical transition radiation can be visualized by calculating the radiation source of a uniform transverse charge distribution of radius a

$$\bar{\lambda}(r) = \frac{1}{\pi a^2}\left\{\begin{array}{ll} 1\,, & r < a \\ 0\,, & r > a \end{array}\right\} . \tag{3.19}$$

The field of a ring charge distribution Eq. (3.13) is weighted with Eq. (3.19) and integrated. The evaluation, shown in Fig. 3.10, is performed numerically on a rectangular grid for two different beam energies using a normalized beam emittance of $5 \cdot 10^{-6}$m. The transverse beam widths are $a = 220\,\mu$m at $\gamma = 100$ and $a = 80\,\mu$m at $\gamma = 800$. The left graph shows the transverse electric field distribution ($\lambda = 500\,$nm) for $\gamma = 100 < \gamma_c$, the right graph for $\gamma = 800 > \gamma_c$. Below γ_c the field distribution is almost identical with the transverse charge distribution (3.19), above γ_c the field distribution is much wider and the charge distribution cannot be resolved.

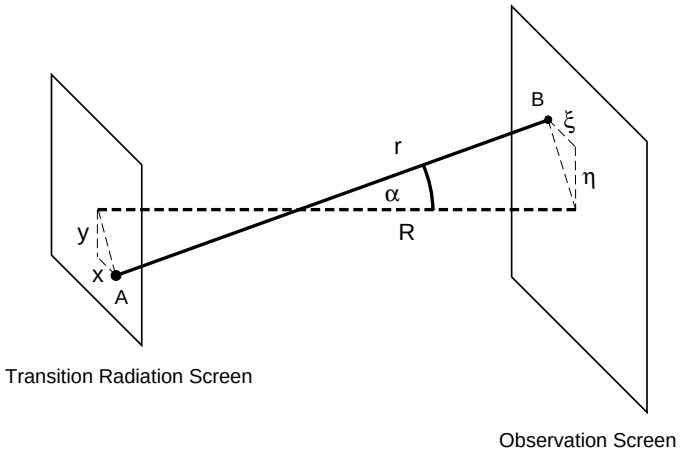


Figure 3.11: Determination of the distance from a point A located on the transition boundary to a point B on an observation screen. This screen may also be the entrance aperture of the detection device.

3.3.2 Huygens-Fresnel Principle

The Ginzburg-Frank formula has been derived by solving the Maxwell equations for the electromagnetic fields traveling with a charge and for the radiation field propagating into the backward hemisphere of the transition boundary. The transition boundary is assumed to be of infinite extent to justify the ansatz of plane waves for the radiation field. The characteristics of the radiation field are derived by the application of boundary conditions, that is the equality of the tangential electric and magnetic field components on both sides of the boundary, at the time the charge undergoes transition. The Ginzburg-Frank formula is therefore applicable only if the transition boundary is large compared to the transverse extension of the electromagnetic fields traveling along with the bunch charge, as is the case for optical transition radiation.

An alternative way to compute the spectral energy density of transition radiation is based on the Fresnel-Kirchhoff scalar diffraction theory. The Huygens-Fresnel principle states that every point on a primary wavefront (which is, here, the field distribution on the transition boundary) can be considered as a continuous emitter of spherical secondary wave amplitudes [29]. To describe the directionality of the secondary emissions, an inclination factor $(1+\cos(\alpha))/2$ is introduced which has its maximum in the forward direction normal to the primary wavefront and vanishes for $\alpha = \pi$. The field amplitude at a given point is determined by the superposition of all secondary wave amplitudes.

The following numerical method is applied to derive the characteristics of transition radiation. The Fourier component of the electric field $\tilde{E}_r$ (Eq. 3.14) is evaluated at a point $A = (x, y)$ on the transition boundary, yielding the value $\tilde{E}_A$. Next, a point $B = (\xi, \eta)$ on an observation screen separated by a distance R from the transition boundary is selected. The distance r between A and B is (see Fig. 3.11)

$$r = \sqrt{(R^2 + (x-\xi)^2 + (y-\eta)^2)}\,. \tag{3.20}$$

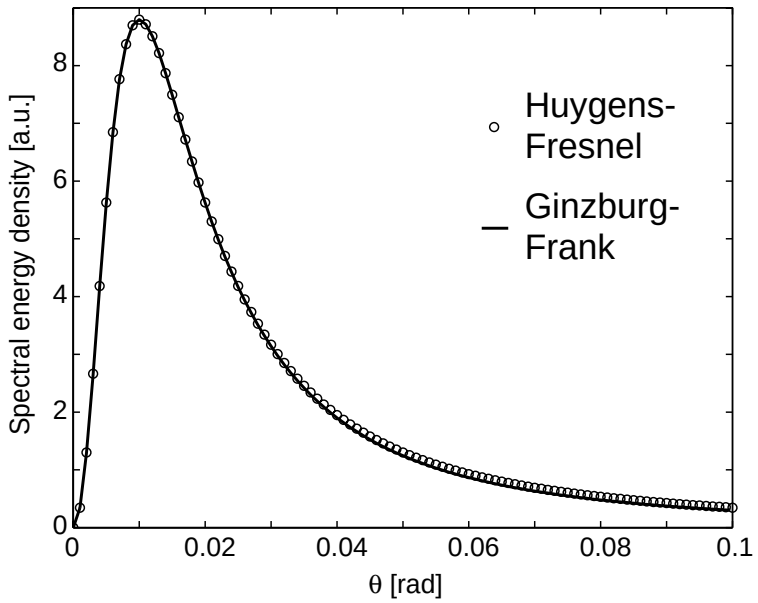


Figure 3.12: Angular distribution of transition radiation as obtained from the Ginzburg-Frank formula and the numerical recipe using the Huygens-Fresnel principle. Parameters: $\gamma = 200$, $\lambda = 2\,\mu$m and $d = 35\,$mm.

and is converted into a phase difference $\Delta\phi_{AB} = r/\lambda$, where λ is the wavelength. The amplitude of the field at B is

$$\tilde{E}_B = \int\int \tilde{E}_A(x,y)\,\frac{1+\cos(\alpha)}{2}\,\frac{\exp(i\Delta\phi_{AB})}{\sqrt{(R^2+(x-\xi)^2+(y-\eta)^2)}}\,dx\,dy\,. \tag{3.21}$$

The integration is performed over the entire transition radiator yielding the sum of the secondary wave amplitudes at the observation screen. The radiation intensity pattern is then derived by calculating the absolute value of the amplitudes squared. The calculation has to be performed for every Fourier component of Eq. (3.14). The Fresnel-Kirchhoff diffraction theory is a scalar theory. In case of transition radiation, however, the polarization of the electric field vector has to be taken into account. The electric field of the secondary wave is polarized in the same direction as the electric field of the bunch charge at the transition boundary. Before being added at point B, the fields of the secondary waves are decomposed into their horizontal and vertical polarization components.

Figure 3.12 compares the angular distribution of transition radiation as obtained with the prediction of the Ginzburg-Frank formula and with the numerical calculation using the Huygens-Fresnel principle. The Lorentz-factor is $\gamma = 200$, the radiation wavelength is $\lambda = 2\,\mu$m and the diameter of the transition radiator is $d = 35\,$mm. There is an excellent agreement between the result of the numerical calculation and the prediction of the Ginzburg-Frank formula. The conditions for the applicability of the Ginzburg-Frank formula are fulfilled, because the transition boundary is much larger than the transverse extension of the electromagnetic fields.

Figure 3.13 shows the angular distribution of transition radiation for different wavelengths.

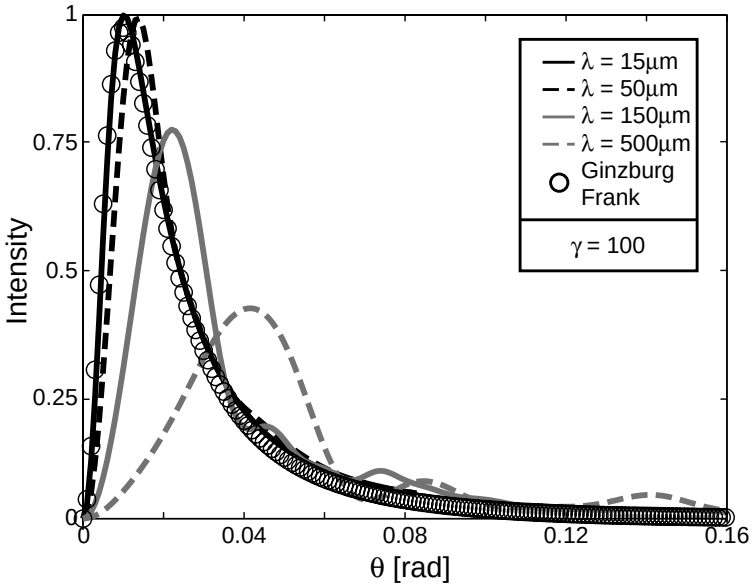


Figure 3.13: Computed angular distribution of transition radiation using the Huygens-Fresnel principle. The prediction of the Ginzburg-Frank formula is indicated by the circles. The diameter of the transition screen is $d = 35\,\mathrm{mm}$.

For wavelengths $\lambda \leq 50\,\mu\mathrm{m}$ the opening angle distribution is in good agreement with the Ginzburg-Frank formula. For larger wavelengths the angular distribution becomes wider and an interference pattern appears. The deviation of the angular distribution from the Ginzburg-Frank formula is explainable by diffraction because the electromagnetic field distribution incident on the transition screen at that wavelength has a greater transverse extension than the screen itself.

Diffraction of the electromagnetic fields at the boundary yields a suppression of the far-infrared transition radiation energy density. A parabolic mirror ($d_M = 100\,\mathrm{mm}$ diameter, $f_M = 200\,\mathrm{mm}$ and $R = 200\,\mathrm{mm}$) is used to collect the far-infrared radiation and to deliver it to a detector. The parabolic mirror defines an acceptance angle of $\theta_{max} = 0.14\,\mathrm{rad}$. The parts of the radiation field which are missing the parabolic mirror due to diffraction do not reach the detector and cannot contribute to the measurement. Figure 3.14 shows an acceptance function indicating the suppression of low frequency field components ($f \leq 3\,\mathrm{THz}$) due to diffraction. The quantity

$$A(f) = \frac{\int_{\mathrm{mirror}} r\,dr\,d\phi\,\tilde{E}^R(k,r)}{\int_0^\infty \int_0^{2\pi} dr\,d\phi\,r\tilde{E}^R(k,r)} \tag{3.22}$$

is evaluated at the given distance R as a function of the radiation frequency $f = kc/2\pi$. Expression (3.22) yields a second spectral acceptance function. It describes the collection efficiency of the detection system. The metallic screen inserted into the vacuum chamber can, in a sense, be considered as a high-pass filter for far-infrared transition radiation. The suppression of low frequencies has to be corrected for when using this radiation for beam diagnostics.

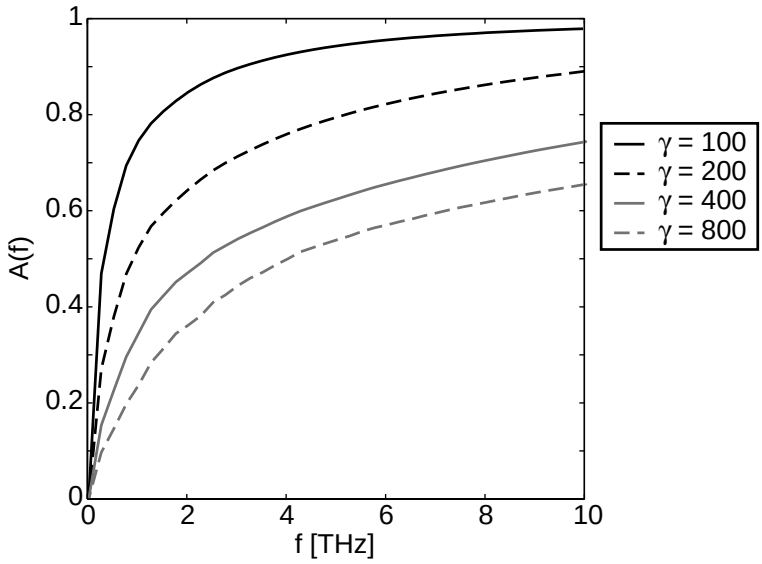


Figure 3.14: Fraction of the electromagnetic fields collected by a parabolic mirror at a distance $R = 200\,\mathrm{mm}$ from the transition boundary. The maximum acceptance angle is $\theta_{max} = 0.14\,\mathrm{rad}$. The diameter of the transition screen is $d = 35\,\mathrm{mm}$.

3.4 Coherent Transition Radiation

The spectral energy density of transition radiation per unit solid angle is described for a sufficiently large transition boundary by the Ginzburg-Frank formula (3.3)

$$U_1 = \frac{e^2}{4\pi^3\epsilon_0 c}\frac{\beta^2\sin^2\theta}{\left(1-\beta^2\cos^2\theta\right)^2}\,.$$

Equation (3.3) yields a proper description of transition radiation in the optical frequency range ($\omega \approx 3\cdot 10^{15}\,\mathrm{s}^{-1}$) where a bunch of N particles radiates N times the power of a single particle. However, at frequencies corresponding to the bunch passage time ($\omega = 2\pi/\sigma_t$, typically $10^{12}\,\mathrm{s}^{-1}$) the phase relations of the single particle emission processes have to be considered leading to coherence effects. The situation is depicted in Fig. 3.15. If the transition radiation wavelength exceeds the bunch length, the individual electrons emit coherently while at shorter wavelength this phase relation is lost and the interference effects average out. The coherence can be described analytically by

$$U_1 = \frac{N^2e^2}{4\pi^3\epsilon_0 c}\left|\rho^T_{q,\omega}\right|^2\left|\rho^L_{q,\omega}\right|^2\frac{\beta^2\sin^2\theta}{\left(1-\beta^2\cos^2\theta\right)^2} \tag{3.23}$$

where $\rho^L_{q,\omega}$ denotes the Fourier transform of the longitudinal part of the charge distribution and $\rho^T_{q,\omega}$ the Fourier transform of the transverse part of the charge distribution. The result can be obtained directly by following the derivation outlined in appendix B for an extended charge distribution. Eq. (3.23) describes coherent transition radiation for a bunch of N particles described by a charge distribution $\rho(x,y,z) = \rho^L(z)\rho^T(x,y)$ crossing a transition boundary perpendicularly in uniform motion. The latter description of coherent transition radiation holds for a transition boundary exceeding the transverse

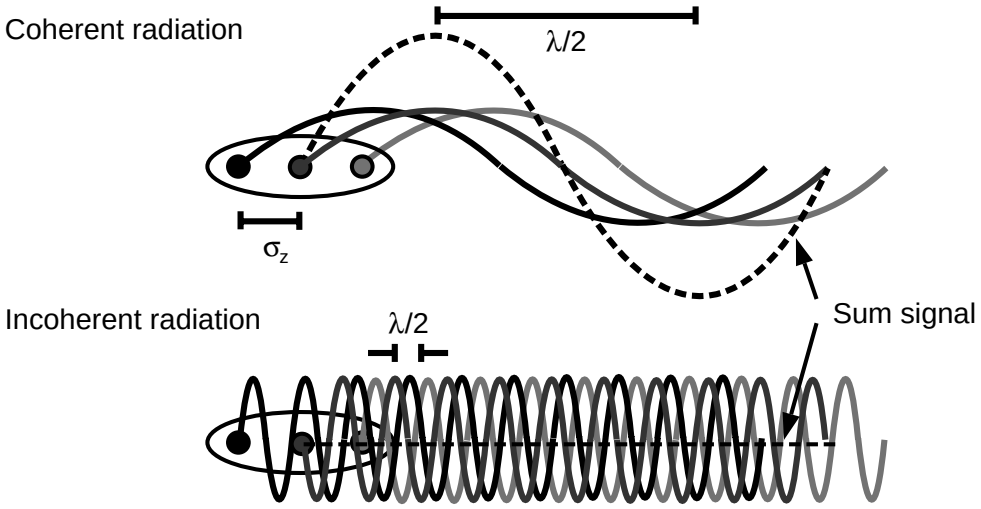


Figure 3.15: Upper graph: phase relation and the resulting field amplitude for the coherent radiation process. The wavelength λ is larger than the bunch length σ_z. Lower graph: at short wavelengths the individual field amplitudes average out.

extension of the electromagnetic fields carried by the charge distribution. In this section we neglect the finite size of the radiator in order to emphasize coherent transition radiation. It should be kept in mind that the formulae derived in this section have to be corrected by the spectral acceptance functions Eq. (3.15) and Eq. (3.22).

The example of a three dimensional Gaussian charge distribution

$$\rho^G(r,\phi,\zeta) = \frac{Ne}{2\pi\sigma_r}\frac{1}{\sqrt{2\pi}\,\sigma_z}\exp\left(-\frac{r^2}{2\sigma_r^2}\right)\exp\left(-\frac{\zeta^2}{2\sigma_z^2}\right) \quad \text{where} \quad \zeta = z - vt \tag{3.24}$$

leads to

$$U_1 = \frac{N^2e^2}{4\pi^3\epsilon_0 c}\frac{\beta^2\sin^2\theta}{\left(1-\beta^2\cos^2\theta\right)^2}\exp\left(-\frac{\omega^2}{v^2}\left(\sigma_z^2+\beta^2\sigma_R^2\sin\theta^2\right)\right) \tag{3.25}$$

3.4.1 Radiation Power

The spectral energy density depends on the number of particles per bunch squared (N^2), so the emitted radiation power is N times larger (typically $N = 10^{10}$) than in the non-coherent optical regime. The coherent peak power can be evaluated for the collider-mode and FEL-mode machine parameters. The machine parameters (in autumn 1999) are

	Collider-mode	FEL-mode
N	$5 \cdot 10^{10}$	$6.25 \cdot 10^9$
E [MeV]	330	330
σ_t [ps]	1.8	0.86
σ_f [GHz]	88.5	185

The single particle spectral energy density at $\gamma = 660$ is $U = 8 \cdot 10^{-17}$ eVs. The radiated coherent energy can be derived using

$$U = N^2 \frac{dU^{\mathrm{sp}}}{d\omega} \frac{\Delta\omega}{\omega} \tag{3.26}$$

where the term $\Delta\omega/\omega$ denotes the frequency band under consideration. Under the assumption of a Gaussian longitudinal bunch charge distribution of variance σ_t the central frequency is $\omega = 1/\sigma_t$ and the frequency interval $\Delta\omega$ can be evaluated using

$$\int_0^\infty d\omega \, \exp\left(-\omega^2\sigma_t^2\right) = \frac{\sqrt{\pi}}{2\sigma_t} \,. \tag{3.27}$$

The energy radiated in the coherent frequency band amounts to $U = 1.6 \cdot 10^{-2}$ J for the collider-mode and $U = 5.1 \cdot 10^{-4}$ J for the FEL-mode. The peak radiation power is

$$\hat{P} = \frac{U}{6\sigma_t} \tag{3.28}$$

where the bunch passing time of a Gaussian bunch is assumed to be 6 times the rms bunch length containing more than 99% of the charges. The peak power radiated by coherent transition radiation is $\hat{P} = 1440$ MW for the collider-mode and $\hat{P} = 99$ MW for the FEL-mode. Coherent transition radiation from short and high charged electron bunches is therefore an extremely intense source of millimeter and sub-millimeter wavelength radiation. Notice that the values quoted for the emitted peak power are reduced by spectral acceptance functions Eq. (3.15) and Eq. (3.22). The expected peak power radiated out of the beam pipe is therefore attenuated by a factor of 20 to 80 depending on the beam energy and radiation wavelength.

3.4.2 Investigation of the Longitudinal and Transverse Form Factor

An application of coherent transition radiation is the determination of the longitudinal charge distribution ρ^L [30, 31, 32, 33, 34]. The investigation of Eq. 3.23 shows that the transverse component of the charge distribution has to be minimized. This can be done by focusing the beam onto the transition radiator, i. e. $\rho^T \to \delta(r)/2\pi$, hence $\rho^T_{q,\omega} \to 1$. The resulting coherent radiation spectrum depends on the Fourier transform of the longitudinal charge distribution only (see Eq. 3.23), hence

$$U_1(\omega,\theta) \approx \frac{N^2 e^2}{4\pi^3\epsilon_0} \left|\rho^L_{q,\omega}\right|^2 \frac{\beta^4 c \sin^2\theta}{\left(1-\beta^2\cos^2\theta\right)^2} \,. \tag{3.29}$$

In accordance with the nomenclature in nuclear physics, the Fourier transformation of the charge distribution is called the bunch form factor. Figure 3.16 shows a set of longitudinal charge distributions ρ^L and their corresponding coherent power spectra $|\rho^L_{q,\omega}|^2$. The upper graph depicts three Gaussian longitudinal charge distributions of different rms width and their corresponding frequency spectra. The shorter the bunch is, the higher frequencies contribute to the coherent radiation spectrum. The lower graph depicts three different longitudinal bunch charge distributions of equal rms width but of different shape. In

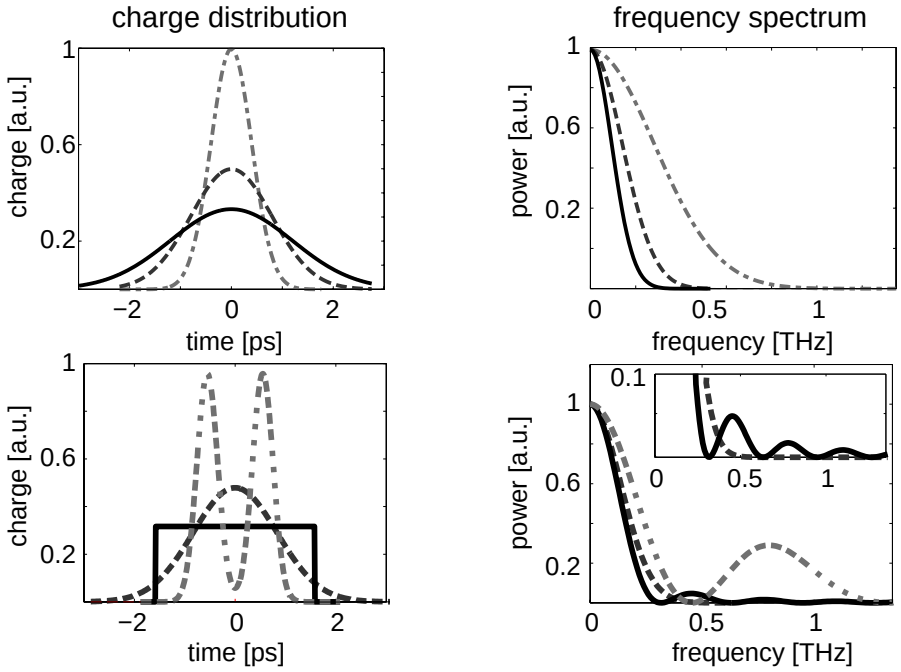


Figure 3.16: Upper graph: Gaussian longitudinal charge distributions of different variance and their corresponding frequency spectra. Lower graph: different longitudinal bunch charge distributions and their frequency spectra.

frequency domain, the three distributions can be distinguished by the visibility of the secondary and higher maxima of the spectra. For frequencies lower than the first minimum it is difficult to distinguish the spectra of the three bunch charge distributions. To a first approximation, the rms bunch length can be determined from the rms width of the longitudinal form factor in the range of the central maximum.

Influence of the Transverse Charge Distribution The finite acceptance angle $\theta_{\max}$ of the optical imaging system permits the detector a limited side-view on the bunch charge distribution. The projected component of the transverse charge distribution has to be taken into account for the energy density of coherent transition radiation. For a Gaussian bunch charge distribution we obtain

$$U_1 \sim N^2 e^2 \exp\left(-\frac{\omega^2}{v^2}\left(\sigma_z^2 + \beta^2\sigma_r^2 \sin^2\theta_{\max}\right)\right). \tag{3.30}$$

The transverse form factor $\rho^T_{q,\omega} \sim \exp\left(-\omega^2\beta^2\sigma_t^2 \sin^2\theta_{\max}/v^2\right)$ limits the determination of the longitudinal form factor $\rho^L_{q,\omega} \sim \exp\left(-\omega^2\sigma_z^2/v^2\right)$. If, however, the condition $\sigma_z \gg \beta\sigma_r \sin\theta_{\max}$ is fulfilled, the influence of the transverse bunch charge distribution is negligible. The parabolic mirror at the TESLA Test Facility has a maximum acceptance angle of $\theta_{max} = 0.14\,\mathrm{rad}$, leading to the condition that $\sigma_r \ll 3.9\,\mathrm{mm}$ (Collider-mode, $\sigma_t = 1.8\,\mathrm{ps}$) and $\sigma_r \ll 1.8\,\mathrm{mm}$ (FEL-mode, $\sigma_t = 0.86\,\mathrm{ps}$). A normalized emittance of $\epsilon_x^N = 5 \cdot 10^{-6}\,\mathrm{m}$ leads to a beam size of $\sigma_x = 91\,\mu\mathrm{m}$ ($\gamma = 660$) which is a lot smaller than the latter boundaries.

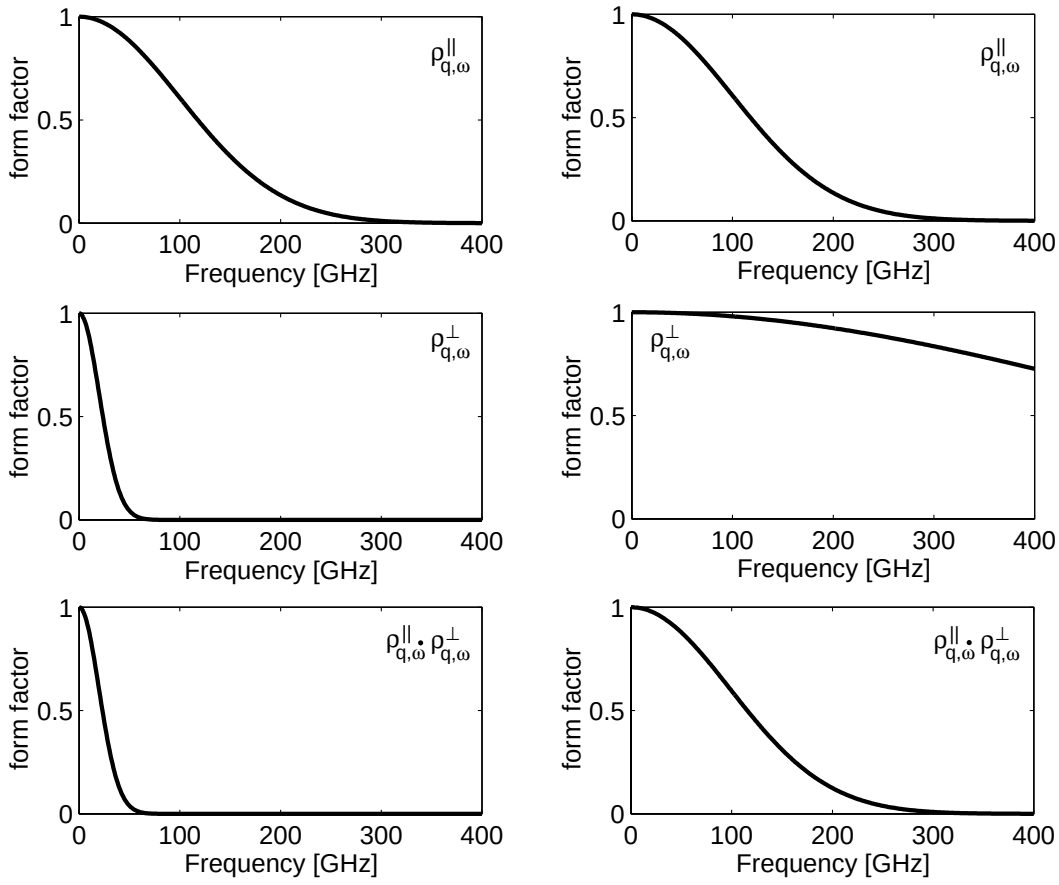


Figure 3.17: Influence of the transverse form factor on the product form factor determined during a measurement using coherent transition radiation. Left column: A large transverse bunch size causes the significant decrease of the transverse form factor towards higher frequencies and dominates the product of the longitudinal and transverse form factors. The product form factor is significantly different from its longitudinal part and will lead to a larger bunch length. Right column: A small transverse beam size (nearly constant transverse form factor) has only little influence on the product of both form factors. The product form factor correctly represents the longitudinal charge distribution.

The influence of the transverse form factor as described by Eq. (3.30) is shown in Fig. 3.17: let us assume a Gaussian bunch of $\sigma_z = 500\,\mu$m and $\sigma_r = 10\,$mm (left column). The longitudinal form factor does not vanish for frequencies below 300 GHz while the transverse form factor vanishes already at 50 GHz. The spectroscopic measurement of the bunch form factor, however, cannot distinguish the two and detects their product (or the entire three-dimensional form factor of the bunch charge distribution). In the present scenario, the transverse part of the form factor is suppressing the longitudinal part and the product pretends a bunch length larger than it actually is. The problem can be solved by focusing the beam as strongly as possible onto the transition radiator to minimize the transverse beam dimension. The right column shows the form factors transverse beam size of $\sigma_r = 600\,\mu$m. The product $\rho^{\parallel}_{q,\omega} \cdot \rho^{\perp}_{q,\omega}$ is now dominated by the longitudinal form factor and a bunch length measurement using coherent radiation is possible.

Chapter 4

Transverse Phase Space Tomography

The transverse phase space distribution of an electron beam can be explored by applying a quadrupole scan in combination with tomographic image reconstruction techniques [35, 36]. For this purpose a set of quadrupoles is used to rotate the phase space distribution in well-defined angular steps between a reconstruction point z_i before the quadrupoles and an observation point z_f behind the quadrupole magnets. The transverse beam density distribution at the observation point is recorded by means of optical transition radiation and a CCD camera. The horizontal and the vertical beam profiles at different phase space rotation angles allow a reconstruction of the initial horizontal and vertical phase space distribution at z_i.

4.1 Theory of Phase Space Tomography

This section introduces the "filtered backprojection algorithm", a standard algorithm for tomographic image reconstruction. The application of the filtered backprojection to transverse beam dynamics and the procedure of the measurement will be presented. The steps of the analysis are illustrated by simulation results.

4.1.1 The Radon Transform

Take a two-dimensional Gaussian distribution $g(x, y)$ which is rotated in space around the z-axis. The rotation by an angle ϕ is described by a 2×2 matrix M_R

$$M_R = \begin{pmatrix} \cos\phi & \sin\phi \\ -\sin\phi & \cos\phi \end{pmatrix} , \tag{4.1}$$

where the coordinates x and y of the distribution g transform according to

$$\begin{pmatrix} u \\ v \end{pmatrix} = M_R \begin{pmatrix} x \\ y \end{pmatrix} . \tag{4.2}$$

The rotation M_R conserves the area of the initial distribution since $det(M_R) = 1$. Hence

$$\int \tilde{g}(u, v)\, du\, dv = \int g(x, y)\, dx\, dy . \tag{4.3}$$

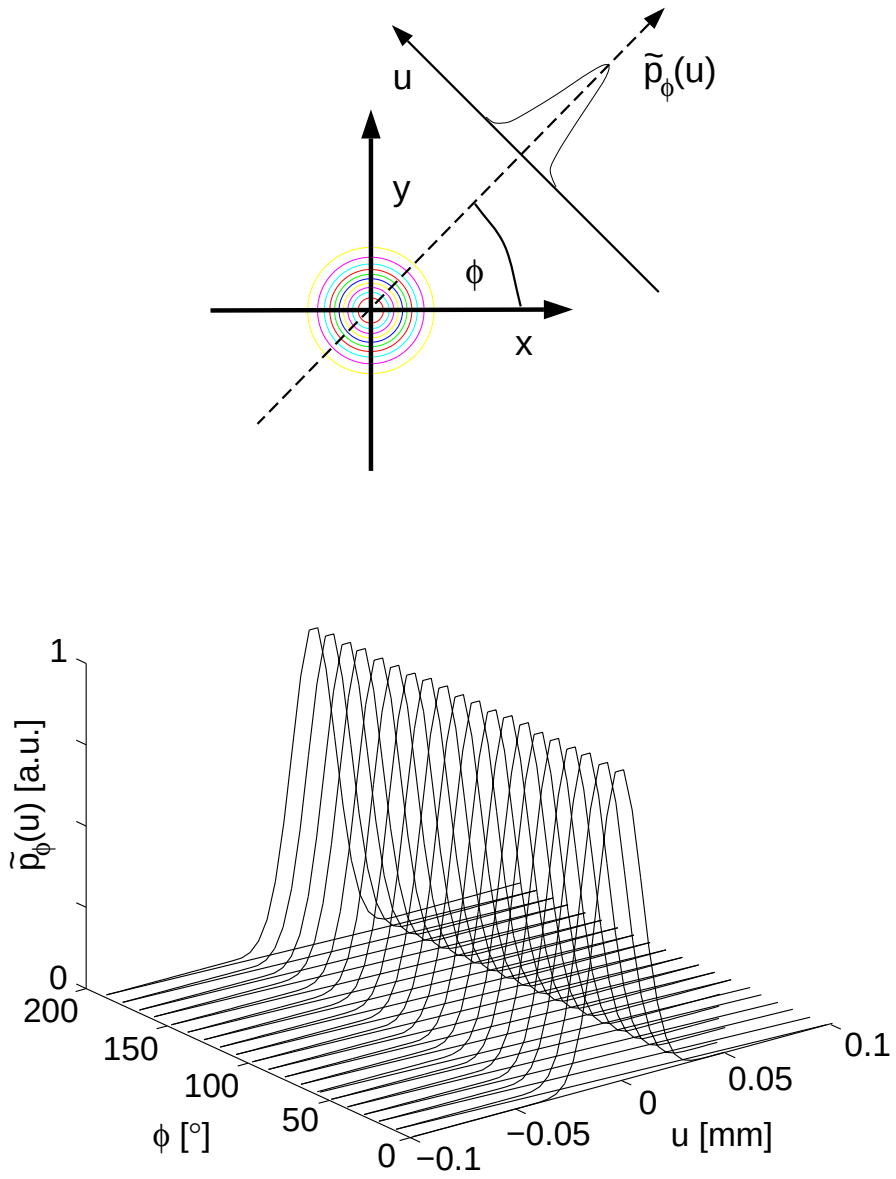


Figure 4.1: The Radon transform of a two-dimensional Gaussian distribution. Upper graph: contour plot of the distribution $g(x, y)$ and the rotated coordinate system (u, v). The distribution is projected onto the u-axis yielding $\tilde{p}_\phi(u)$. Lower graph: The Radon transform of the Gaussian distribution. 18 projections are displayed as a function of the rotation angle ϕ.

The rotated distribution $\tilde{g}$ is then projected onto the u-axis yielding $\tilde{p}(u)$. The projection is not a simple geometric projection, it has to be understood in terms of an integration of the distribution $\tilde{g}$ along a "line of projection". We obtain

$$\tilde{p}(u) = \int \tilde{g}(u, v)\, dv \tag{4.4}$$

or by using an area integral over the entire distribution

$$\tilde{p}(u) = \int \tilde{g}(\tilde{u}, v)\delta(u - \tilde{u})d\tilde{u}\, dv\ . \tag{4.5}$$

The rotation can now be included into the projection by inserting Eq. (4.3) into Eq. (4.5) yielding

$$\tilde{p}_\phi(u) = \int g(x,y)\delta(u - x\cos\phi - y\sin\phi)\,dx\,dy\ , \tag{4.6}$$

where $\tilde{u} = x\cos\phi + y\sin\phi$ has been used. The index denotes the projection angle ϕ. The set of projections $\tilde{p}_\phi(u)$, $0 \le \phi \le \pi$, is called the Radon transform of the distribution $g(x,y)$ [37].

Figure 4.1 shows the initial distribution g, the coordinate systems (x,y) and (u,v) coupled by the rotation matrix M_R and a projection $\tilde{p}_\phi(u)$ at an angle ϕ. The Radon transform is often displayed in a two-dimensional plot where the projections are shown as a function of the rotation angle.

4.1.2 The Filtered Backprojection Algorithm

The reconstruction $g_R(x,y)$ of the initial distribution $g(x,y)$ is obtained formally [38] by

$$g_R(x,y) = \int_0^\pi p_\phi(x\cos\phi + y\sin\phi)\,d\phi \tag{4.7}$$

where $x\cos\phi + y\sin\phi = u$ according to Eq. (4.2). The backprojection described by Eq. (4.7) is illustrated in Fig. 4.2. The profiles of a Gaussian charge distribution, evaluated at four rotation angles ϕ (0°, 45°, 90° and 135°) are shown at the fringe of the lower contour plot (left column). The reconstructed distribution is computed by projecting these profiles back through the reconstruction plane at their specific projection angle each of them yielding a ridge of Gaussian cross-section. The integral sums the contributions from the individual projections and yields the reconstructed distribution g_R. The star-like, wavy structure at the outer rim of the reconstructed image is due to the limited number of projections. Increasing the number of projections averages these artifacts out. Figure 4.3 shows the results of the reconstruction for projections every 20° and 10°. The Radon transform consisting of 18 projections in equi-angular intervals yields a reconstruction without noticeable wavy artifacts.

However, even with arbitrarily fine angular subdivision the backprojection described by Eq. (4.7) is not the exact inverse of the Radon transform. A careful inspection of Fig. 4.2 and Fig. 4.3 shows that the width of the center peak of the reconstructed distribution is larger than the original width. The problem is further illustrated by Fig. 4.4: suppose the initial distribution consists of two Gaussian peaks of the same height but of different width σ. The projections then contain two Gaussian peaks of different heights. Since the backprojection is a linear operation, the reconstructed image will have two peaks of different heights as well. This deficiency can be cured using a filter which enhances structures of large curvature corresponding to high "spatial frequencies" f. The projection $\tilde{p}_\phi(u)$ is convoluted with a spatial filter function $w(u)$ combining a frequency ramp-function $|f|$ which is cut off at a maximum frequency f_{cut} corresponding to half of the sampling frequency. The filter function is

$$w(u) = \frac{1}{8\pi^2}\int |f| L(f)\exp(iuf)\,df\ . \tag{4.8}$$

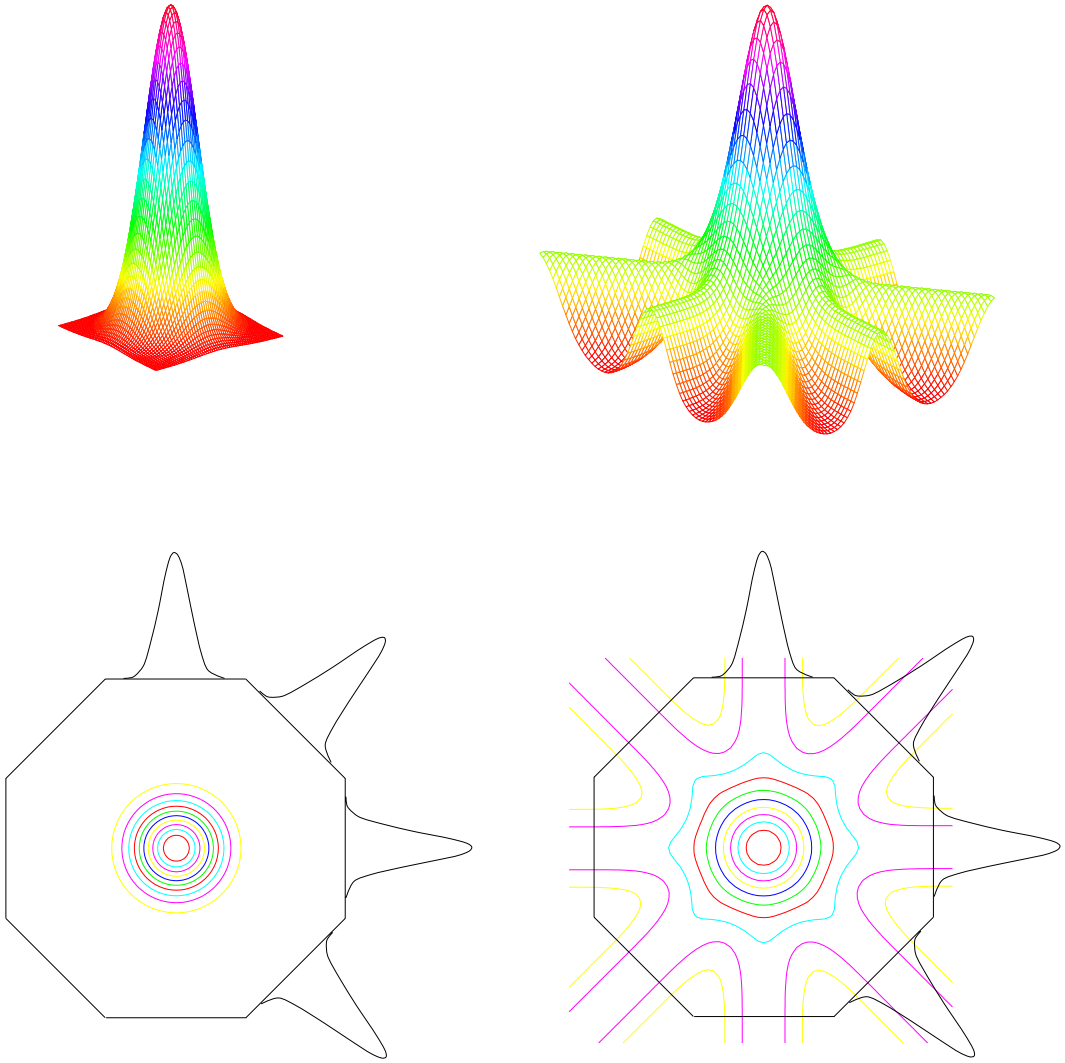


Figure 4.2: The backprojection of a Gaussian distribution. The original distribution is shown on the left side. The lower left graph illustrates the projections of the distribution in angular steps of 45°. The graphs on the right side show the backprojection. The profiles are projected back through the area of reconstruction under their respective projection angle each of them yielding a ridge of Gaussian cross-section. (The ridge might be thought of a sheet of paper placed onto the area of reconstruction which is folded such that the cross-section matches the beam profile.) These backprojections add constructively to produce the reconstructed image.

We obtain the following expression for the filtered projection $\tilde{p}_\phi^F(u)$

$$\tilde{p}_\phi^F(u) = \int \tilde{p}_\phi(u')w(u-u')\,du' \,. \tag{4.9}$$

The ramp function is responsible for the enhancement of large spatial frequencies [38]. In Fig. 4.4 it can be observed that the convolution of the projection with the filter function yields profiles of equal height but of decreased width. A side-effect of the convolution is the appearance of negative components in the projection $\tilde{p}_\phi^F(u)$. These negative components

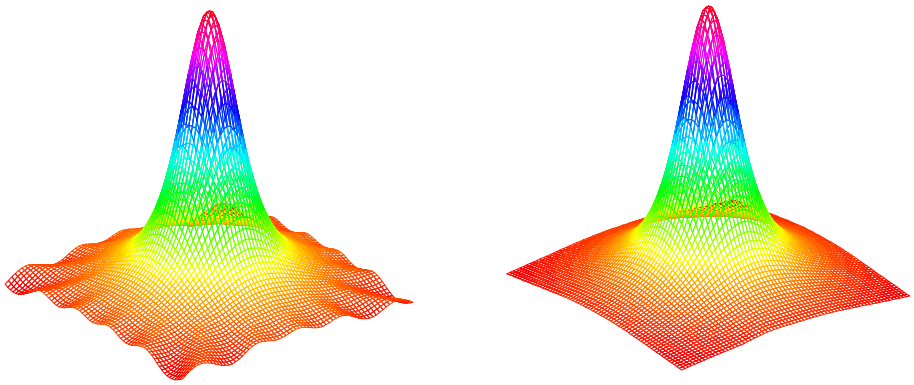


Figure 4.3: The backprojected Radon transform is shown for a different number of projections. Left graph: 9 projections. Right graph: 18 projections. The star-like artifacts at the fringe of the reconstructed image vanish as the number of projections is increased.

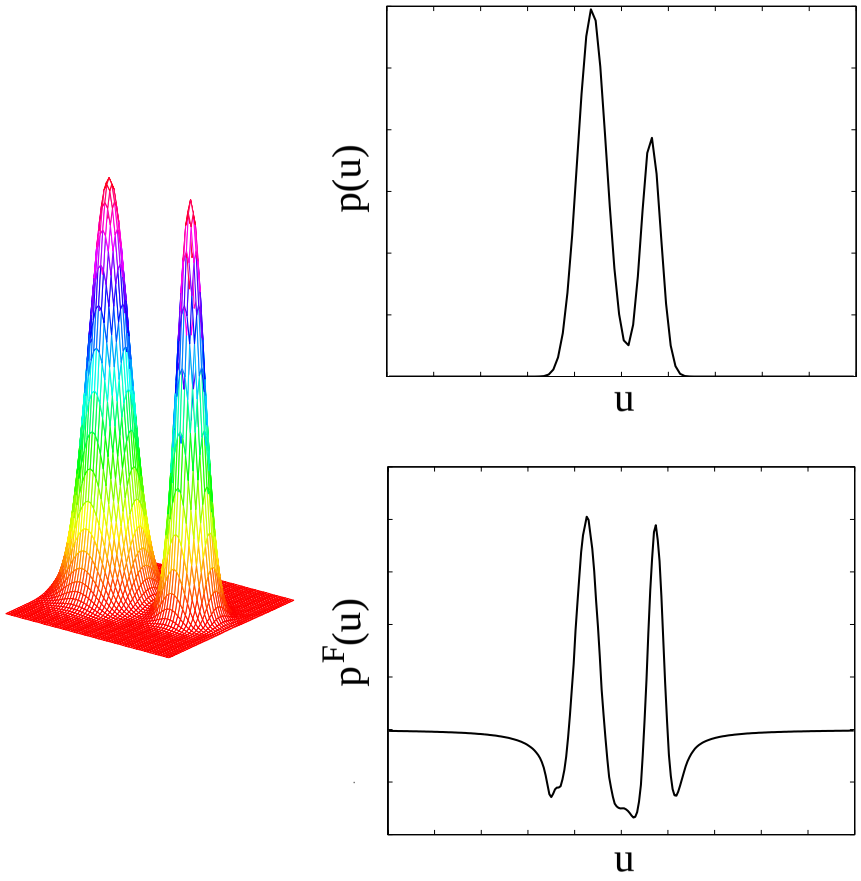


Figure 4.4: The projection of two Gaussian peaks of different width but equal height leads to two Gaussians of different width and different height (Upper right graph). Using a filter function the narrower peak enhances, but does not quite reach the height of the large peak, because high spatial frequencies are suppressed by the low-pass filter $L(f)$.

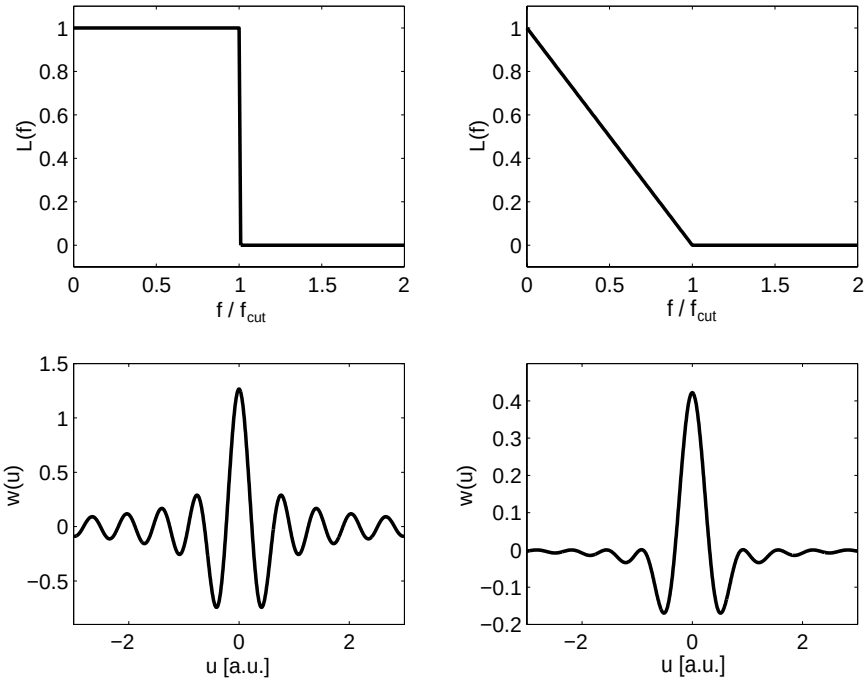


Figure 4.5: The low pass filter $L(f)$ and the filter function $w(u)$ for smoothing parameters $\eta = 0$ (upper and lower left) and $\eta = 1$ (upper and lower right). The right filter curve causes a stronger smoothing, because of the suppression of the secondary maxima.

cancel a positive surplus in the fringe of the area of reconstruction which originates from the backprojected profiles at other angles.

A spatial frequency low-pass filter is introduced because of the discrete sampling of the projections by the detection device. Let Δs be the width of the discrete sampling interval, then the maximum frequency that can be recovered is of the order of $1/2\Delta s$ [38, 39]. A convenient low-pass filter function is [40]

$$L(f) = \begin{cases} 1 - \eta\frac{f}{f_{cut}} & , \quad |f| \leq f_{cut} \\ 0 & , \quad |f| > f_{cut} \end{cases} , \tag{4.10}$$

where the parameter f_{cut} denotes the cut-off frequency and $\eta \, \epsilon \, [0, 1]$ the smoothness parameter. For $\eta = 0$ the low-pass is an edge filter which is, in combination with the ramp function $|f|$, most sensitive to curvy structures because the high frequency components are included. For $\eta > 0$ the higher frequency components are damped, which results in a smoothing of the reconstructed image. The filter function now becomes

$$w(u) = \frac{1}{8\pi^2} \int_{-f_{cut}}^{f_{cut}} |f| \left(1 - \eta\frac{|f|}{f_{cut}}\right) \exp(iuf)\, df \tag{4.11}$$

$$= \frac{1}{4\pi^2} \int_{0}^{f_{cut}} f \left(1 - \eta\frac{f}{f_{cut}}\right) \cos(uf)\, df \tag{4.12}$$

which is evaluated by partial integration to

$$w(u) = \frac{f_{cut}^2}{4\pi^2} \left(\chi(f_{cut}u) - \eta\zeta(f_{cut}u)\right) \tag{4.13}$$

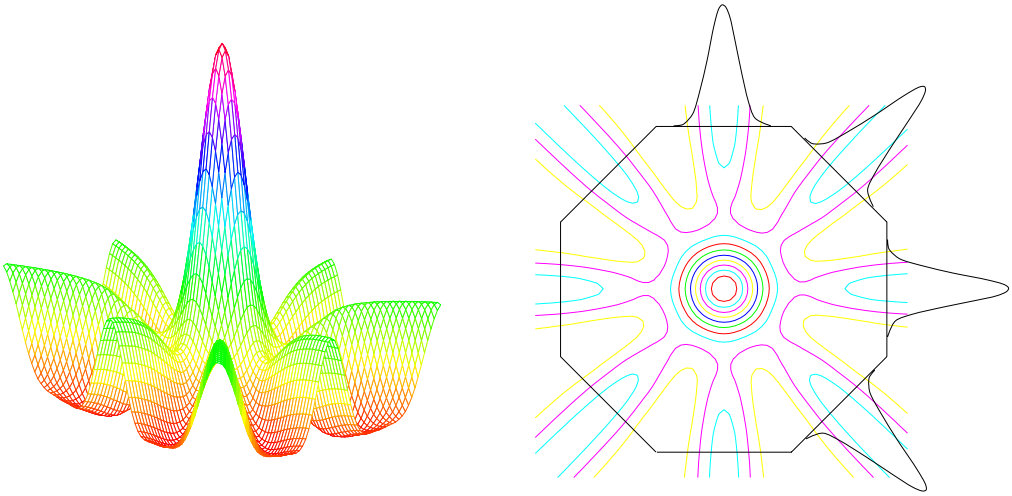


Figure 4.6: The backprojected filtered Radon transform. The reconstructed peak is of the same width and height as the original. The blurred reconstruction in the fringe of figure 4.2 is corrected by the negative components of the filtered projections.

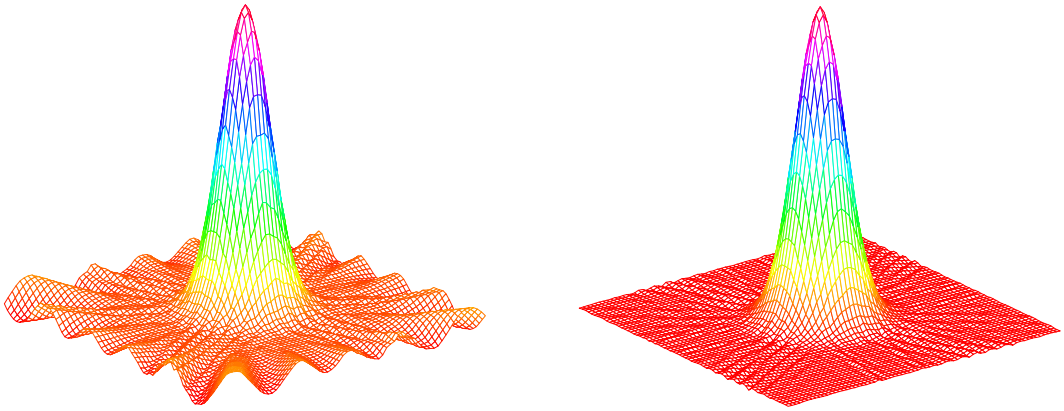


Figure 4.7: The reconstruction of the object is shown for 9 (left) and 18 (right) projections. The star-like, wavy artifacts at the fringe of the reconstructed image vanish for an increasing number of projections. In contrast to Fig. 4.3, the projection have been filtered using Eq. (4.13) prior to the reconstruction. The smoothing parameter $\eta = 0$ has been used.

where

$$\chi(v) = \begin{cases} \frac{\cos v - 1}{v^2} + \frac{\sin v}{v} & , \quad v \neq 0 \\ \frac{1}{2} & , \quad v = 0 \end{cases} \tag{4.14}$$

$$\zeta(v) = \begin{cases} \frac{2\cos v}{v^2} + \left(1 - \frac{2}{v^2}\right)\frac{\sin v}{v} & , \quad v \neq 0 \\ \frac{1}{3} & , \quad v = 0 \end{cases} . \tag{4.15}$$

The function $w(u)$ is shown in Fig. 4.5 for different smoothing parameters $\eta = 0$ and $\eta = 1$. In the following $\eta = 0$ will be used.

The result of the filtered backprojection for the two-dimensional Gaussian distribution is shown in Fig. 4.6 and Fig. 4.7. The backprojected and the original image match at the center of the image. The star-like artifacts disappear for a sufficient number of projections used for the reconstruction as shown for the reconstructions of projections every 45°, 20° and 10°.

4.1.3 Discrete Implementation of the Filtered Backprojection Algorithm

The implementation of the filtered backprojection algorithm is a straight forward discretization of Eq. (4.7), Eq. (4.9) and Eq. (4.13) [38, 41]. The detecting device samples the projections of the transverse charge distribution in discrete steps yielding N sampling points of equal spacing $\bar{u}_k = k\Delta u$, $k = -N/2+1, ..., N/2$. The projections are obtained at m equally spaced angles $\phi_j = \pi j/\bar{M}$, $j = 0, ..., \bar{M}-1$.

The integral (4.9) is approximated by the sum [38]

$$\tilde{p}^F_{\phi_j}(k\Delta u) = \sum_{n=-N/2+1}^{N/2} \tilde{p}_{\phi_j}(n\Delta u) w(|n-k|\Delta u)\cdot\Delta u \tag{4.16}$$

where $k = -N/2+1, ..., N/2$. The filter function $w(u)$ evaluated at the sampling points $\bar{u}_k$ [40] is

$$w(\bar{u}_k) = \begin{cases} \frac{1}{4} - \frac{\epsilon}{6} & , \quad k = 0 \\ -\frac{\epsilon}{\pi^2 k^2} & , \quad k \neq 0 \text{ and even} \\ -\frac{1-\epsilon}{\pi^2 k^2} & , \quad k \neq 0 \text{ and odd} \end{cases} . \tag{4.17}$$

The discretization of the backprojection (A.13) leads to

$$g_R(x,y) = \frac{\pi}{\bar{M}} \sum_{j=0}^{\bar{M}-1} p^F_{\phi_j}\left[x\cos\left(\frac{\pi j}{\bar{M}}\right) + y\sin\left(\frac{\pi j}{\bar{M}}\right)\right] . \tag{4.18}$$

The area of reconstruction is approximated by a rectangular grid $[x_l, y_m]$, where $l, m = 1...N$. At every point (x_{l_0}, y_{m_0}) the value of $u_j = x\cos\left(\pi j/\bar{M}\right) + y\sin\left(\pi j/\bar{M}\right)$ at a given ϕ_j is evaluated. The u_j then have to be compared to the measured $\bar{u}_k$. A linear interpolation routine is used to get the best estimate for the u_j and hence for $\tilde{p}^F_{\phi_j}(u_j)$ such that

$$\tilde{p}^F_{\phi_j}(u_j) = \left((k+1) - \frac{u_j}{\Delta u}\right)\tilde{p}^F_{\phi_j}(k\Delta u) + \left(\frac{u_j}{\Delta u} - k\right)\tilde{p}^F_{\phi_j}((k+1)\Delta u), \tag{4.19}$$

where $k \leq u/\Delta u < k+1$ and $k = -N/2+1, ..., N/2$.

The algorithm described above has been implemented as a Matlab [42] code. The convolution and the backprojection routines are linked in C code for faster processing. Figure 4.8 shows the performance of the tomographic image reconstruction using the example of three asymmetrically arranged Gaussian peaks of different width and height. The presented simulation covers an angular interval of 180° and calculates 180 projections with a resolution of 100 pixels in x and y. The pixel-to-pixel agreement, $\sum_{ij}(g_R(x_i,y_j) - g(x_i,y_j))^2 / \sum_{ij} g(x_i,y_j))^2$, is better than 1%.

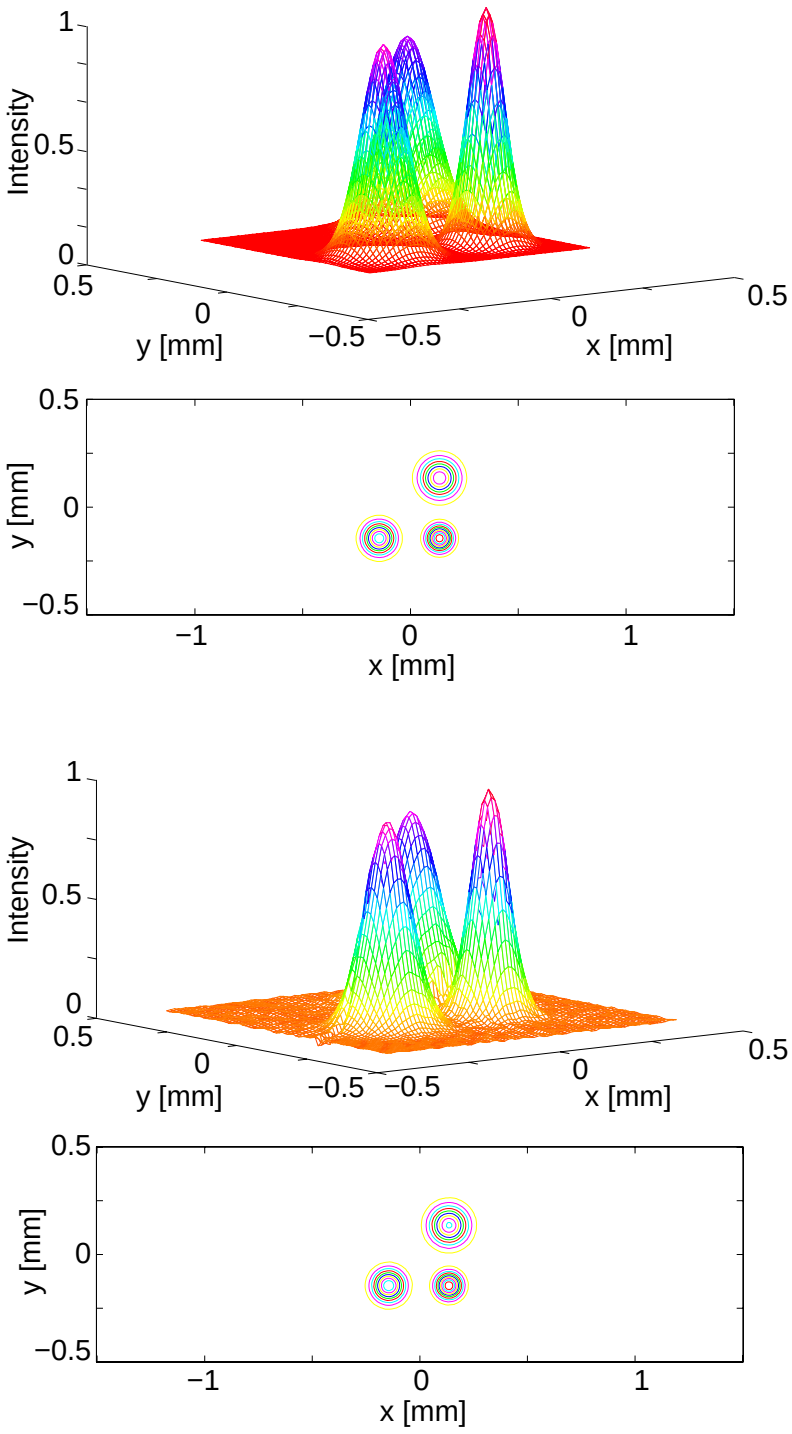


Figure 4.8: Simulation with an asymmetric distribution consisting of three Gaussian peaks of different height and width. The upper graph shows the initial distribution, the lower graph the result of the reconstruction. The pixel-to-pixel agreement of the reconstructed and the original distribution is better than 1%.

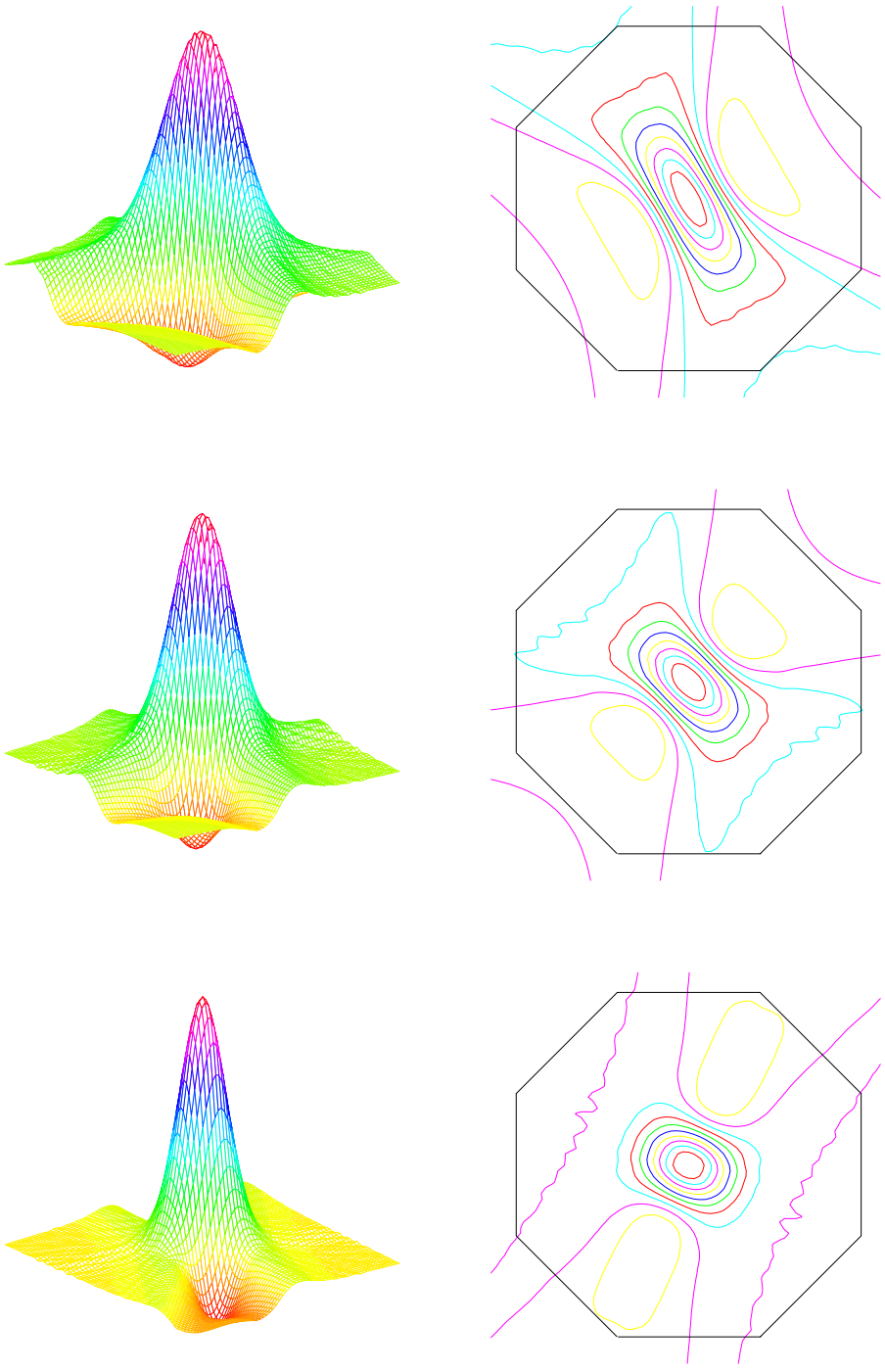


Figure 4.9: Performance of the filtered backprojection algorithm applied to a Radon transformation covering an angular interval of less than 180°. Shown is the reconstruction of a two-dimensional Gaussian with 6 projections from 0 to 60° (top), 9 projections from 0 to 90° (middle) and 12 projections from 0 to 120° (bottom). The reconstructed image is distorted, tilted and contains negative contributions sideways to the maximum.

4.1.4 Reconstruction Artifacts

The Radon transform has to cover an angular interval of 180° to avoid reconstruction artifacts. Problems rise if the Radon transform contains a smaller angular interval. Figure 4.9 illustrates the problem. A Gaussian phase space distribution is chosen for graphical clearness. The distribution is reconstructed according to the algorithm of filtered backprojection. The angular interval spans 60° (top), 90° (middle) and 120° (bottom). The contour plots on the right show that the reconstructed image is tilted and distorted. Furthermore, negative contributions next to the maximum appear. In general the negative contribution of the filtered profiles are needed to cancel the positive surplus of the projections taken at the other rotation angles. If projections at certain angles are missing this cancelation cannot occur and negative contributions remain at the sides of the angular reconstruction interval. The positive surplus at the fringe of the area of reconstruction

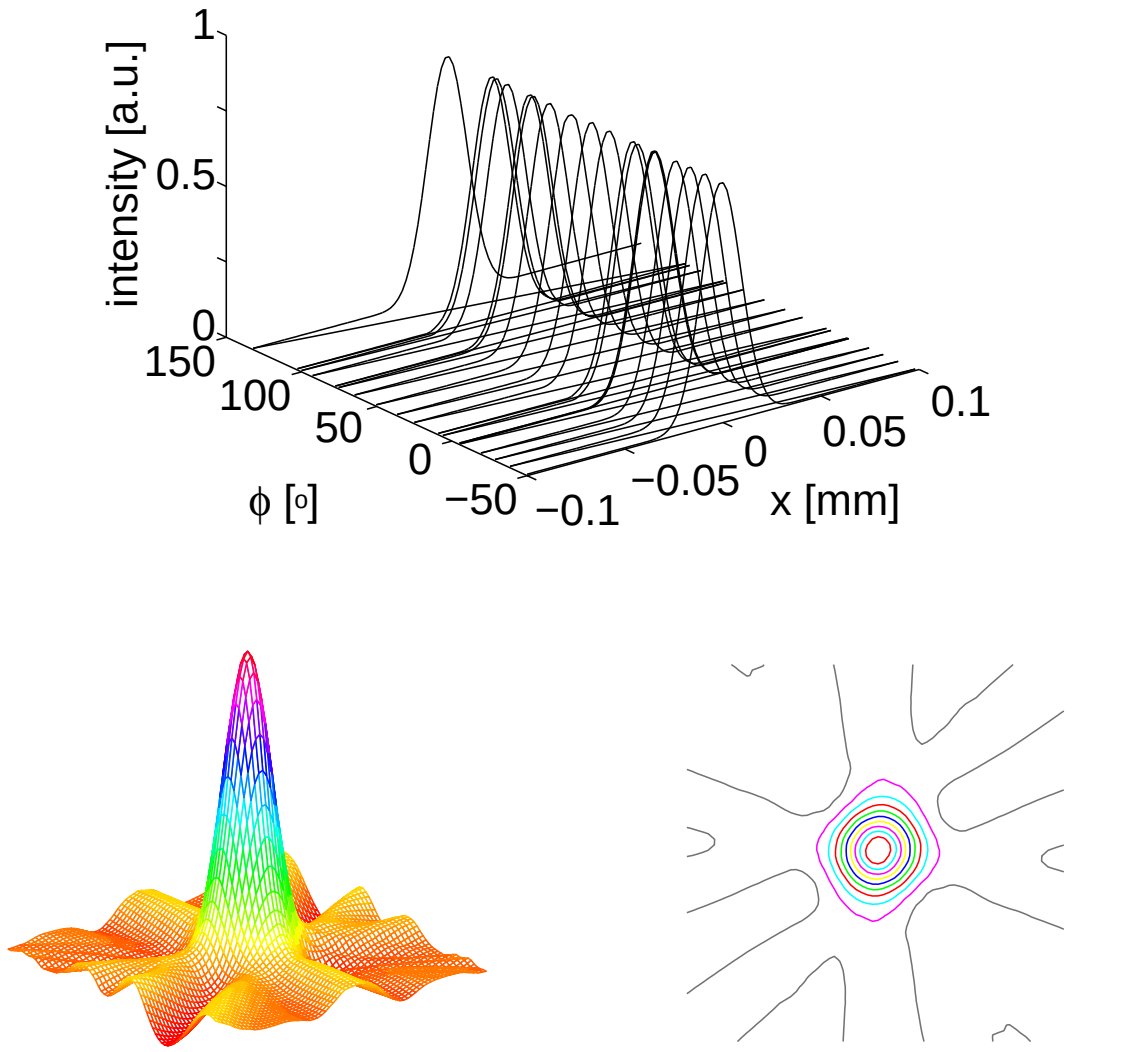


Figure 4.10: Performance of the filtered backprojection algorithm with a Radon transform sampled with varying angular spacing. As a result, the Gaussian peak becomes distorted and the contributions of the backprojected profiles do not cancel in the fringe regions.

within the angular interval is also not compensated due to the missing negative contribution. This effect causes the tilt of the reconstructed distribution.

Figure 4.10 shows artifacts occurring when the projections are not equally spaced. The Gaussian peak is distorted and non-zero contributions occur in the fringe of the area of reconstruction.

Hence, a reconstruction free of artifacts is obtained only if the Radon transform covers an interval of 180° where the individual projections are recorded at a constant angular spacing. If the latter condition cannot be fulfilled, the artifacts can be avoided by an interpolation of adjacent profiles.

4.1.5 Application of the Filtered Backprojection Algorithm to Transverse Beam Dynamics

The task is to determine the transverse phase space distribution $\rho_i(x, x', y, y')$ at a reconstruction point z_i of the beam line. x and y denote the spatial coordinates in the horizontal and vertical plane, x' and y' the horizontal and vertical angular divergence. Two, or more, quadrupoles are used to rotate the phase space distribution. The detection device, an optical transition radiation screen and a CCD camera, are located at a position z_f downstream of z_i. The setup is shown in Fig. 4.11. Under the assumption of linear beam dynamics, the phase space coordinates x, x', y and y' are transformed by a 4×4 transfer matrix M

$$\begin{pmatrix} x \\ x' \\ y \\ y' \end{pmatrix}_f = M \begin{pmatrix} x \\ x' \\ y \\ y' \end{pmatrix}_i \tag{4.20}$$

where the indices i and f denote the position z_i and z_f respectively. The integrated phase space density is conserved yielding

$$\int \rho_f(x_f, x'_f, y_f, y'_f)\, dx_f\, dx'_f\, dy_f\, dy'_f = \int \rho_i(x_i, x'_i, y_i, y'_i)\, dx_i\, dx'_i\, dy_i\, dy'_i\ . \tag{4.21}$$

The OTR screen projects the four-dimensional phase space distribution onto the spatial axes x and y yielding a transverse intensity distribution. This distribution can be projected onto either spatial axis to obtain a transverse beam profile $p(x)$ and $q(y)$. These profiles are identical to a direct projection of the four-dimensional distribution onto the spatial coordinate axes as presented by Fig. 4.12. The projection of the four-dimensional phase space distribution onto the horizontal x-axis at the position z is

$$p_z(x_f) = \int \rho_f(x_f, x'_f, y_f, y'_f)\, dx'_f\, dy_f\, dy'_f = \int \tilde{\rho_f}(x_f, x'_f)\, dx'_f\ . \tag{4.22}$$

or by using an integral over the entire phase space distribution

$$p_z(x_f) = \int \tilde{\rho_f}(x_f, x'_f)\delta(x_f - \tilde{x}_f)\, d\tilde{x}_f\, dx'_f\ . \tag{4.23}$$

A similar relation holds for the vertical projection $q_z(y)$. The beam transfer described

by the matrix M can be included in Eq. (4.23) by

$$p_{z,M}(x_f) = \int \tilde{\rho}_i(x_i, x_i')\delta(x_f - M_{11}x_i - M_{12}x_i')\, dx_i\, dx_i' \,. \tag{4.24}$$

Equation (4.24) denotes the Radon transform of a phase space distribution $\tilde{\rho}_i(x_i, x_i')$ with respect to a generalized rotation described by the matrix M. Notice that M performs not only a rotation, but also a shearing of the initial distribution. The filtered backprojection algorithm is a priori not suited to handle these generalized rotations. A transformation of the Radon transform $p_{z,M}(x_f)$ (Eq. (4.24)) to a Radon transform originated from Cartesian rotations $\tilde{p}_{z,\phi}(u)$ (compare with Eq. (4.6))

$$p_{z,\phi}(x_f) = \int \tilde{\rho}_i(x_i, x_i')\delta(x_f - x_i\cos\phi - x_i'\sin\phi)\, dx_i\, dx_i' \,. \tag{4.25}$$

has to be derived to make use of the tomographic image reconstruction. ϕ denotes the Cartesian rotation angle. The arguments of the δ-function have to be compared to perform the latter transformation. Defining the rotation angle ϕ by

$$\cos\phi = \frac{M_{11}}{\sqrt{M_{11}^2 + M_{12}^2}} \qquad \text{and} \qquad \sin\phi = \frac{M_{12}}{\sqrt{M_{11}^2 + M_{12}^2}} \tag{4.26}$$

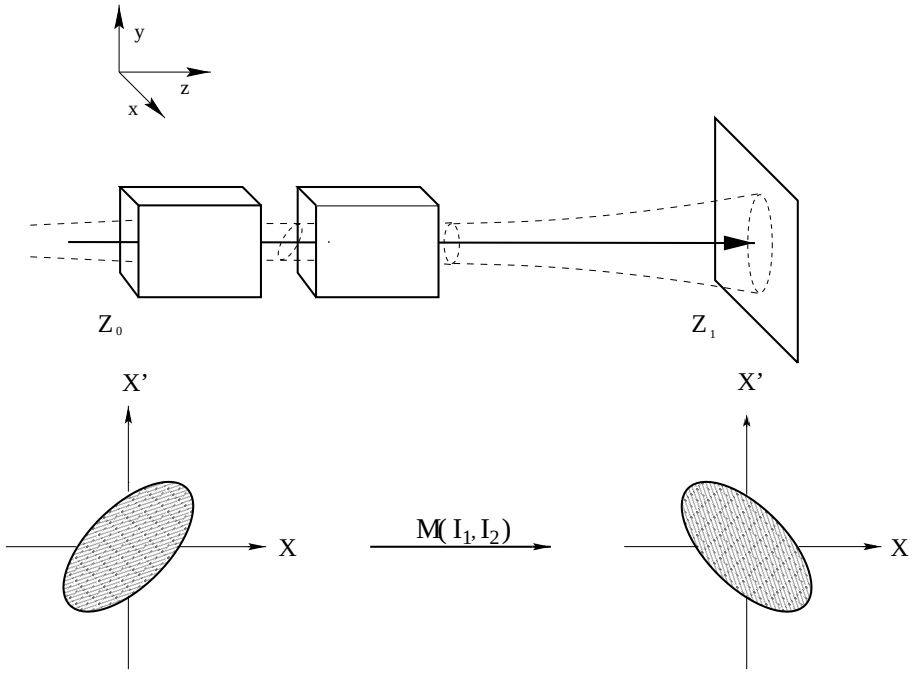


Figure 4.11: The beam line consisting of a quadrupole doublet and an OTR screen for the quadrupole scan is displayed in the upper graph. The associated phase space before the first quadrupole magnet and at the screen is shown below. For graphical clearness Gaussian beams are assumed. The beam transfer matrix M is a function of the quadrupole gradients generated by the currents I_1 and I_2. The detector, usually a CCD camera to record the transition radiation intensity, is not shown.

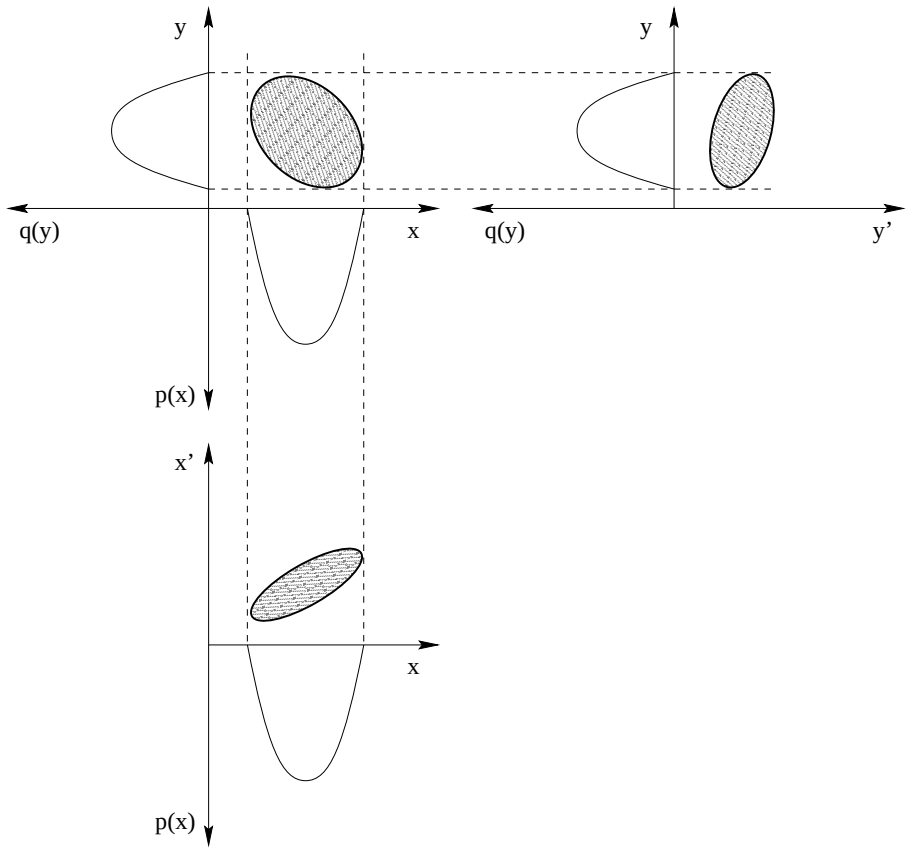


Figure 4.12: The transverse intensity distribution on the OTR screen is a two-dimensional projection of phase space onto the spatial coordinates x and y. The beam profiles obtained from the projection of the OTR intensity distribution on the x and y axes and from the projection of the phase space distribution ($\tilde{\rho}_f(x,x')$ and $\bar{\rho}_f(y,y')$) on the respective spatial axes are equal.

Equation (4.24) can be written as

$$p_{z,M}(x_f) = \int \tilde{\rho}_i(x_i, x_i')\, \delta\left(\sqrt{M_{11}^2 + M_{12}^2}\left(\frac{x_f}{\sqrt{M_{11}^2 + M_{12}^2}} - x_i\cos\phi - x_i'\sin\phi\right)\right) dx_i\, dx_i' \quad (4.27)$$

and after simplifying the argument of the δ-function

$$p_{z,M}(x_f) = \frac{1}{\sqrt{M_{11}^2 + M_{12}^2}} \int \tilde{\rho}_i(x_i, x_i')\, \delta\left(\frac{x_f}{\sqrt{M_{11}^2 + M_{12}^2}} - x_i\cos\phi - x_i'\sin\phi\right) dx_i\, dx_i' \,. \quad (4.28)$$

We arrive at the Cartesian rotation transform by introducing

$$\tilde{p}_{z,\phi}(u) = \left(\sqrt{M_{11}^2 + M_{12}^2}\right) p_{z,M}(x_f) \qquad \text{with} \qquad u = \frac{x_f}{\sqrt{M_{11}^2 + M_{12}^2}} \,. \quad (4.29)$$

In other words, the measured intensity profiles are scaled by $\sqrt{M_{11}^2+M_{12}^2}$, while the axis of projection $\tilde{x}$ is scaled by $1/\sqrt{M_{11}^2+M_{12}^2}$ to compensate for the distortions introduced by the

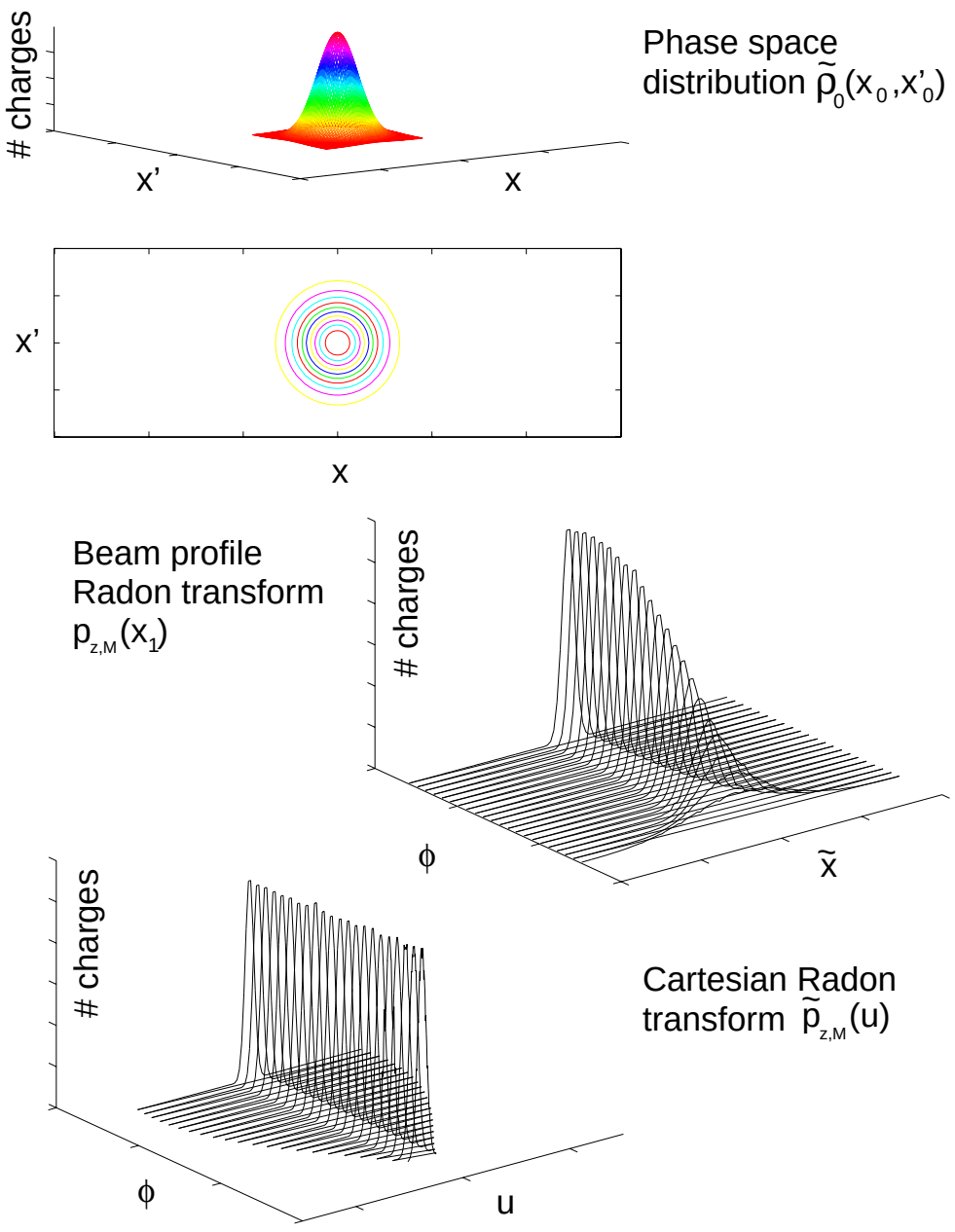


Figure 4.13: A Gaussian phase space distribution is shown as a function of x and x' in a three dimensional view and as a contour plot (upper graph). Middle graph: Radon transform according to relation (4.24). The transport matrix elements are converted to rotation angles. The quadrupole magnet strength has been chosen such that the angular intervals of consecutive projections are equal. Bottom graph: the associated Cartesian Radon transform according to Eq. (4.29).

beam transfer matrix. A similar derivation holds for the vertical plane, where M_{11} and M_{12} are substituted by M_{33} and M_{34} [43, 44].

Equation (4.26) defines the Cartesian rotation angle ϕ in terms of the transport matrix elements. The strength of the quadrupole magnets in the scanning section has to be set such that the Radon transform spans an angular interval of 180° and that the individual profiles are taken at a constant angular spacing.

The previous steps are illustrated in Fig. 4.13. The upper graph shows a Gaussian phase space distribution at the position z_i. The middle graph shows the Radon transform of the Gaussian distribution as obtained from a simulation using the beam line shown by Fig. 4.11. Equation (4.24) has been applied. Notice the defocusing of the beam as a function of the phase space rotation angle. The magnetic fields of the quadrupole magnets have been chosen such that the angular spacing between consecutive projections is equidistant. The lower plot shows the associated Cartesian Radon transform according to Eq. (4.29). Each profile is corrected in height and width as described in Eq. (4.29).

4.1.6 Determination of the Beam Parameters

The transverse beam parameters σ_{ij}, $1 \leq i,j \leq 2$ and $3 \leq i,j \leq 4$, are evaluated statistically as outlined in appendix A. Starting from the reconstructed phase space distribution g_R we obtain

$$\sigma_{ij} = \int \zeta_i \, \zeta_j \, g_R \left(\zeta_i, \zeta_j\right) \, d\zeta_i \, d\zeta_j \tag{4.30}$$

where $\zeta = (x, x', y, y')$. The beam centroid is assumed to be located at the origin of the coordinate system. The beam emittance is evaluated by

$$\epsilon_x = \sigma_{11}\sigma_{22} - \sigma_{12}^2 \quad \text{and} \quad \epsilon_y = \sigma_{33}\sigma_{44} - \sigma_{34}^2 \, . \tag{4.31}$$

4.1.7 Incorporation of Space Charge Effects

The high bunch charges in the TTF linac have a significant influence on the focusing of the beam, in particular in the low energy section. The space charge forces have to be included in the beam transfer matrix M of the accelerator section used for the quadrupole scan. It is sufficient to consider linearized space charge forces by dividing the lattice in intervals of about 1 mm length. At each point, defocusing lenses with a strength

$$k_x = \frac{2Nr_e}{\sqrt{2\pi}} \frac{1}{\sigma_x \left(\sigma_x + \sigma_y\right) \sigma_z \gamma^3} \tag{4.32}$$

$$k_y = \frac{2Nr_e}{\sqrt{2\pi}} \frac{1}{\sigma_y \left(\sigma_x + \sigma_y\right) \sigma_z \gamma^3} \tag{4.33}$$

are added to the magnet lattice. Here, γ denotes the Lorentz factor, r_e is the classical electron radius, σ_x, σ_y and σ_z the rms bunch dimensions. Gaussian shaped bunches are assumed. The transfer matrix M with space charge defocusing is evaluated in several iterations [20]:

1. Assume reasonable transverse beam parameters σ_{11}, σ_{12}, σ_{33} and σ_{34} at the beginning of the accelerator section used for the quadrupole scan.

2. Calculate the beam transfer matrix without space charges and record the beam dimensions σ_x, σ_y and σ_z at every subdivision.

3. Introduce space charge kicks according to formulae (4.32) and (4.33) where the required beam dimensions are obtained from the previous calculation. Record the obtained beam dimensions at every subdivision.

4. Repeat step 2 until the result of the beam transfer matrix converges. The calculation needs approximately 10 iterations.

The beam transfer matrix M is used to calculate the setting of the quadrupole currents to record beam profiles spaced by equal phase space rotation angles. The filtered back-projection algorithm is applied to reconstruct the phase space distribution and a set of reconstructed beam parameters at the beginning of the accelerator section is evaluated. If the initially assumed and the reconstructed beam parameters do not coincide, the initial parameters in 1) have to be varied and the procedure has to be iterated until the reconstructed and the initial beam parameters are self-consistent.

4.2 Parabola Fit Analysis

The transverse emittance and the transverse beam parameters can also be obtained by a parabola fit analysis. The beam size x_{rms} at the measurement point z_f is related to the beam parameters at the reconstruction point z_i by

$$x_{rms}^2 = M_{11}^2\ \sigma_{11}|_{z_i} - 2M_{11}M_{12}\ \sigma_{12}|_{z_i} + M_{12}^2\ \sigma_{22}|_{z_i} \tag{4.34}$$

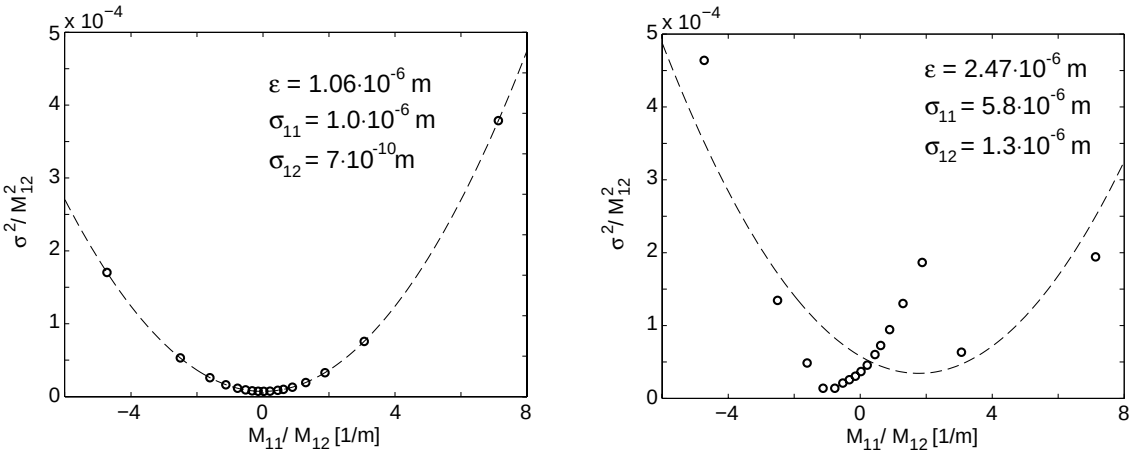


Figure 4.14: Quality of the parabola fit technique for a Gaussian charge distribution (left) and the asymmetric charge distribution (right). The reconstructed beam parameters are shown in the graphs. The input parameters are: $\epsilon = 1.0 \cdot 10^{-6}\,\mathrm{m}$, $\sigma_{11} = 1.0 \cdot 10^{-6}\,\mathrm{m}$, $\sigma_{12} = 0\,\mathrm{m}$ (left graph) and $\epsilon = 1.8 \cdot 10^{-6}\,\mathrm{m}$, $\sigma_{11} = 2.0 \cdot 10^{-6}\,\mathrm{m}$, $\sigma_{12} = 1.0 \cdot 10^{-6}\,\mathrm{m}$ (right graph).

where M_{11} and M_{12} denote the cosine- and sine-like elements of the transfer matrix. Dividing Eq. (4.34) by M_{12}^2 yields

$$\frac{x_{rms}^2}{M_{12}^2} = \frac{M_{11}^2}{M_{12}^2}\,\sigma_{11}|_{z_i} - 2\frac{M_{11}}{M_{12}}\,\sigma_{12}|_{z_i} + \sigma_{22}|_{z_i} \tag{4.35}$$

Hence x_{rms}^2/M_{12}^2 depends parabolically on the ratio of M_{11}/M_{12}. A parabolic fit to the data yields the beam parameters at the reconstruction point z_i. The beam emittance is then derived by Eq. (4.31). Figure 4.14 shows the quality of the parabola fit technique. A Gaussian charge distribution yields a perfect parabolic shape and the second-order polynomial fit recovers the initial beam parameters of $\epsilon = 1 \cdot 10^{-6}$m, $\sigma_{11} = 1 \cdot 10^{-6}\,\mathrm{m}^2$ and $\sigma_{12} = 0\,\mathrm{m}$. The parabola fit for an asymmetric charge distribution consisting of three Gaussians of different height and width does not work well. The initial beam parameters $\epsilon = 1.8 \cdot 10^{-6}$m, $\sigma_{11} = 2 \cdot 10^{-6}\,\mathrm{m}^2$ and $\sigma_{12} = 1 \cdot 10^{-6}\,\mathrm{m}$ cannot be recovered by the fitting procedure.

The conclusion is that the parabola fit technique is suitable only for nearly Gaussian charge distributions but fails for more complicated transverse charge distributions.

Chapter 5

Determination of the Transverse Beam Parameters

Quadrupole scans using the beam produced by the rf photo injector and the thermionic injector will be presented in this chapter. The experimental setup, the processing of the beam intensity profiles, the steps of the tomographic reconstruction and a discussion of the results will be given.

5.1 Experimental Setup

The experimental setup consists of the optical diagnostics system which is used to record the transverse beam intensity distributions and the quadrupole scan accelerator section.

Radiation Screens

Precise beam size measurements are performed with transition radiation which is produced at a screen consisting of a 40 nm thick layer of aluminum evaporated onto a 25 μm thick Kapton foil. The foil (34.5 mm $\times$ 28.5 mm) is stretched in a metallic frame (50 mm $\times$ 40 mm). The screen is mounted at an angle of 45° with respect to the axis of the accelerator yielding a 90° reflection of the radiation. A transition radiation, a scintillating (Al_2O_3) and a calibration screen are mounted on a vertical mover and can be inserted into the beam pipe.

Camera and Readout

The light is collected by an achromatic lens ($f = 100$ mm) and focused directly onto the CCD array of a camera. The light intensity is regulated by gray density filters. The magnification is $V = 0.25$ and the resolution is 60 μm [45]. Standard, interlaced CCD cameras with 512×768 pixels of 20×20 μm size are used. The images are digitized by a Macintosh frame grabber system and made available for data processing.

Calibration Screen

The calibration screen [46] is an aluminum sheet with six markers arranged in a rectangular pattern (2×3). The distance of neighboring markers is 10 mm. The calibration

screen is used to convert the pixels of the CCD image to the transverse dimension of the beam intensity distribution.

Magnetic lattice

The quadrupole scan section consists of two quadrupole magnets which can be powered separately. The 102 mm long magnets are separated by 64 mm. The gradient g is given as a function of the quadrupole current I by

$$g\,[\mathrm{T/m}] = 0.0039281 + 0.71659 \cdot I\,[\mathrm{A}]\ . \tag{5.1}$$

The distance between the second quadrupole and the location of the transition radiation screen is 1873 mm.

5.2 Measurements with the Photo Injector Beam

The rf gun photo injector produced 20 bunches of 1 nC charge at a repetition rate of 1 MHz. The beam energy in the quadrupole scan section was 16 MeV. Space charge effects have to be taken into account for the evaluation of the beam transfer and during the tomographic reconstruction by the application of the self-consistency method outlined in chapter 4. Tomographic measurements using the photo injector beam will be used to present the steps of the analysis.

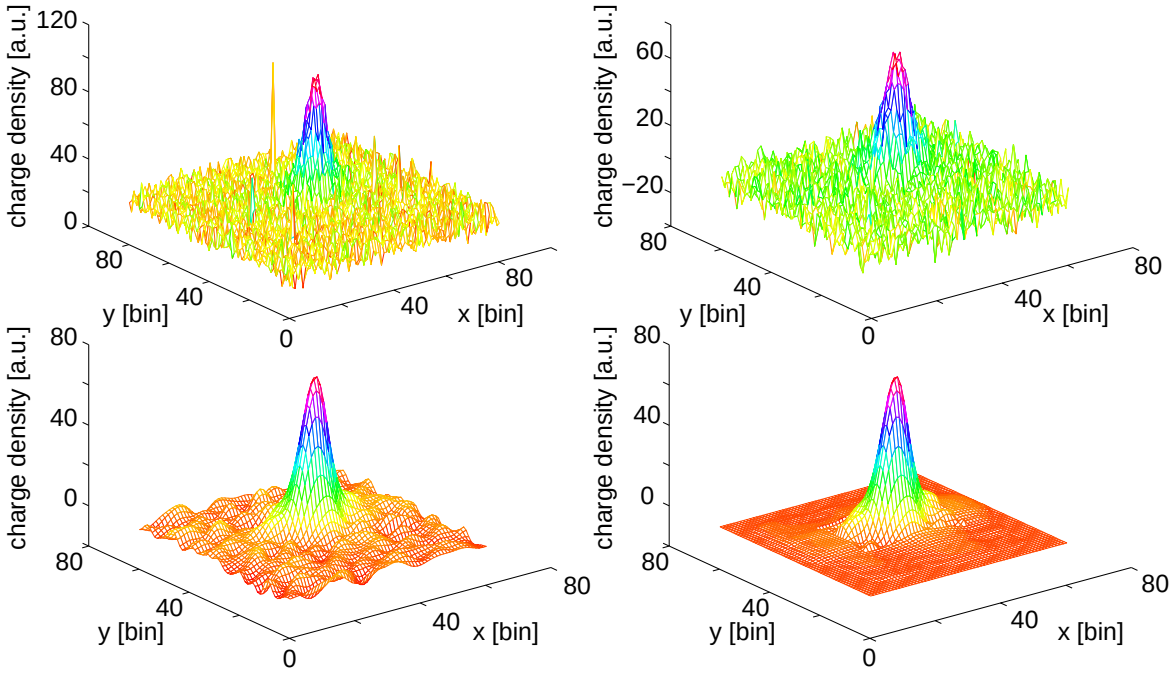


Figure 5.1: Image processing of the acquired beam intensity profiles. Upper left: raw image. Upper right: background subtracted and X-rays removed. Lower left: noise reduction by a two dimensional Fourier transform filter. Lower right: Smoothing of the fringe of the distribution.

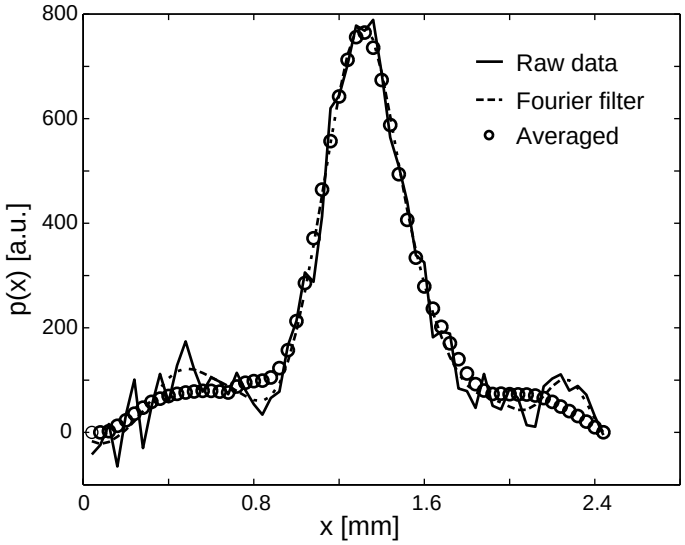


Figure 5.2: Projections belonging to the upper left, lower left and lower right graph of Figure 5.1.

5.2.1 Data Processing

The post-processing of the beam intensity distributions is shown by Fig. 5.1. The raw image taken by the CCD has a non-zero offset and noise is superimposed (upper left graph). The subtraction of a background image, taken without beam at the same quadrupole setting, removes the offset and corrects for damaged pixels on the CCD. The dark current (electrons accelerated by the strong fields of the rf gun which do not originate from the photo effect at the cathode) is subtracted by the background picture as well. X-rays, created by the beam passing the screen, cause excessive signals of single CCD pixels. These spikes are removed and replaced by the average of the signals of the neighboring pixels (upper right graph). A two dimensional Fourier transformation is performed to remove noise from the image. The contour line including 86% ($2\sigma_f$) of the charges is evaluated. The charges included by the contour line are used for the inverse Fourier transformation shown by the lower left graph in Fig. 5.1. The high frequency noise is suppressed yielding a smooth central maximum. The low frequency components, however, become visible in the fringe of the image. Simulation calculations show that these curvy structures are artificial and need to be suppressed. An averaging procedure is applied for the pixel signals with less than 5% of the maximum signal. These signals are replaced with the average of the 20 next neighbors. The resulting image shows a clear peak rising smoothly from the background. Figure 5.2 shows the intensity profiles belonging to the upper left, lower left and lower right graph of Fig. 5.1. The overall shape of the profile does not change, the noise is reduced significantly.

The beam intensity distributions recorded during the quadrupole scans using the photo injector beam are shown by Fig. 5.3. The horizontal and the vertical beam profiles are superimposed on the beam intensity distribution. The second beam spot appearing in the images of the third row originate from an inhomogeneity of the Pockels cell selecting the laser pulses sent to the photo cathode. The resulting inhomogeneity of the laser beam

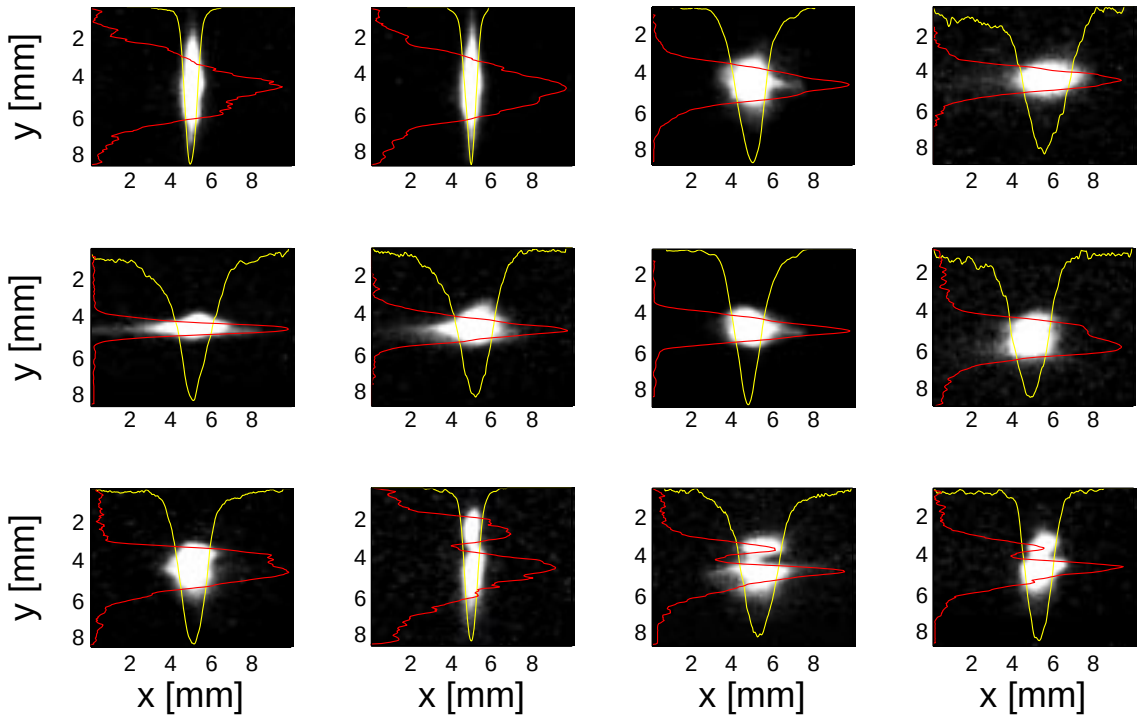


Figure 5.3: Representative set of beam spots and beam profiles during a quadrupole scan performed at the TTF photo injector.

is transferred directly to the electron beam yielding a vertical phase space distribution which differs significantly from a simple Gaussian. The problem of the laser turned out to be a valuable check for the quality of the tomographic reconstruction as will be presented in the following section.

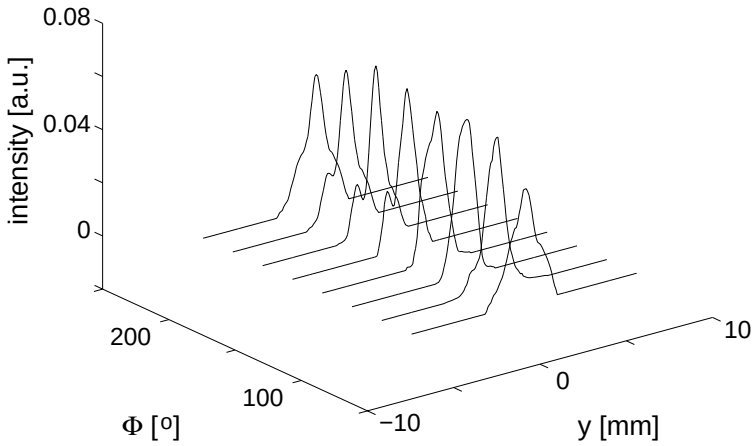


Figure 5.4: Radon transformation of the vertical phase space distribution of the rf gun beam in the injector section. The corrected beam intensity profiles – see Equation (4.29) – are plotted as a function of the phase space rotation angle ϕ.

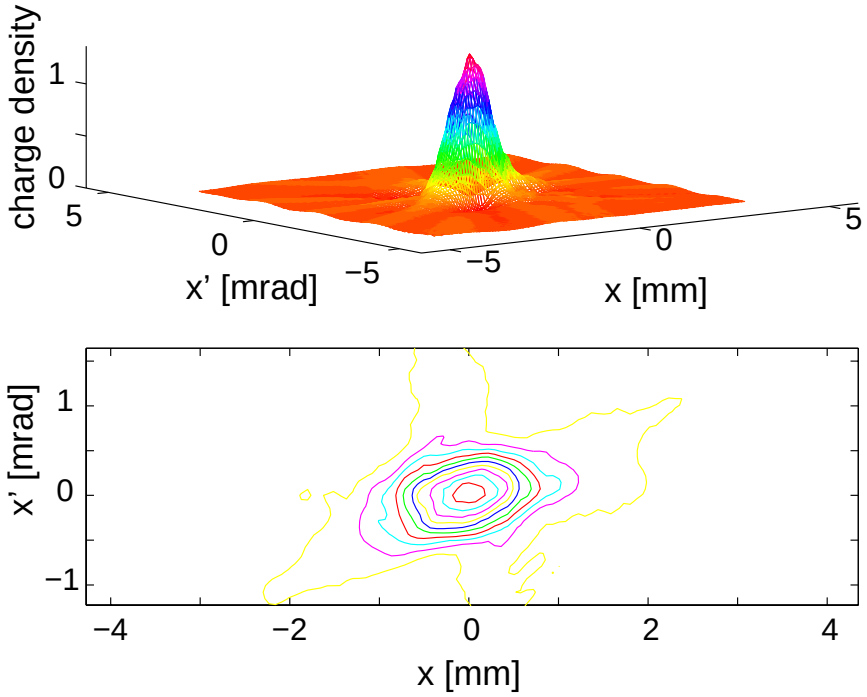


Figure 5.5: Reconstruction of the horizontal phase space distribution from a quadruple scan performed at the TTF photo-injector. Upper graph: three dimensional view. Lower graph: contour plot.

5.2.2 Tomographic Reconstruction

To apply the filtered backprojection algorithm, the beam profiles are corrected in height and width according to Equation 4.29 and then plotted as a function of the phase space rotation angle ϕ in Fig. 5.4. For graphical clearness only eight vertical beam profiles are presented. The double peak is clearly visible in several profiles. For the Radon transform thirteen profiles covering an angular interval of 130° are recorded. It is not possible to cover a larger angular range with the two quadrupole magnets available. The beam is defocused such that the intensity on the transition radiation screen does not suffice for a clear beam image. The data does therefore not cover an angular interval of 180^o and the missing projections are approximated by a linear extrapolation.

Figures 5.5 and 5.6 show a three-dimensional view and a contour plot of the reconstructed horizontal and vertical phase space distributions of the photo-injector beam ($E = 16\,\mathrm{MeV}$, $Q = 1\,\mathrm{nC}$). The reconstruction point, shown at the beginning of the beam line in Fig. 2.8, is located in front of the quadrupole doublet Q1INJ1 behind the capture cavity. A Radon transformation containing 120 (interpolated) profiles has been generated to obtain the reconstructed distributions. The horizontal phase space distribution consists of a single peak and the contour lines are of nearly elliptical shape. A Gaussian charge distribution, yielding ellipses in phase space, is therefore a good approximation. The vertical phase space distribution shows the double peak already seen in the direct image in Fig. 5.3. This result emphasizes the quality of the tomographic reconstruction and shows that the diagnostic technique is capable to reconstruct complex phase space distributions.

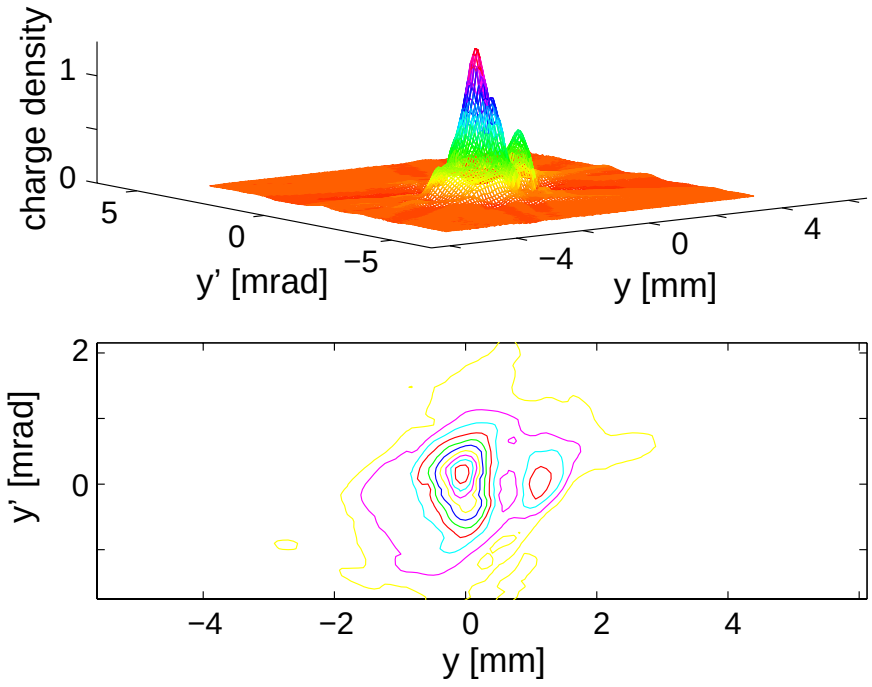


Figure 5.6: Reconstruction of the vertical phase space distribution from a quadruple scan performed at the TTF photo-injector. Upper graph: three dimensional view. Lower graph: contour plot.

5.2.3 Transverse Beam Parameters and Emittance

The transverse beam parameters σ_{11}, σ_{22}, σ_{12}, σ_{33}, σ_{44}, and σ_{34} are evaluated by applying Eq. (4.30)

$$\sigma_{ij} = \int \zeta_i \, \zeta_j \, \rho_k \left(\zeta_i, \zeta_j\right) \, d\zeta_i \, d\zeta_j \quad \text{where} \quad \zeta = (x, x', y, y')$$

to the reconstructed phase space distribution $\rho_1(x, x')$ and $\rho_2(y, y')$. Charge densities lower than a threshold value are not considered to prevent reconstruction artifacts from affecting the evaluation of the beam parameters. The threshold is adjusted dynamically for every measurement, generally about 95% of the integral charge density distribution is used to evaluate the beam parameters. The beam emittance ϵ_x and ϵ_y is then determined using Eq. (4.31)

$$\epsilon_x = \sigma_{11}\sigma_{22} - \sigma_{12}^2 \quad \text{and} \quad \epsilon_y = \sigma_{33}\sigma_{44} - \sigma_{34}^2 \, .$$

Figure 5.7 shows the phase space contour enclosing 39% (1σ emittance) and 86% (2σ emittance) of the charge density. The measured normalized rms emittances are

$$\gamma \cdot \epsilon_x = 5.5 \cdot 10^{-6} \, \mathrm{m} \quad \text{and} \quad \gamma \cdot \epsilon_x = 9.5 \cdot 10^{-6} \, \mathrm{m} \, .$$

The transverse beam parameters are

$$\begin{aligned} \sigma_{11} &= 3.3 \cdot 10^{-7} \, \mathrm{m}^2 \quad \text{and} \quad \sigma_{12} = 5.2 \cdot 10^{-8} \, \mathrm{m} \\ \sigma_{33} &= 3.9 \cdot 10^{-7} \, \mathrm{m}^2 \quad \text{and} \quad \sigma_{34} = 1.3 \cdot 10^{-7} \, \mathrm{m} \, . \end{aligned}$$

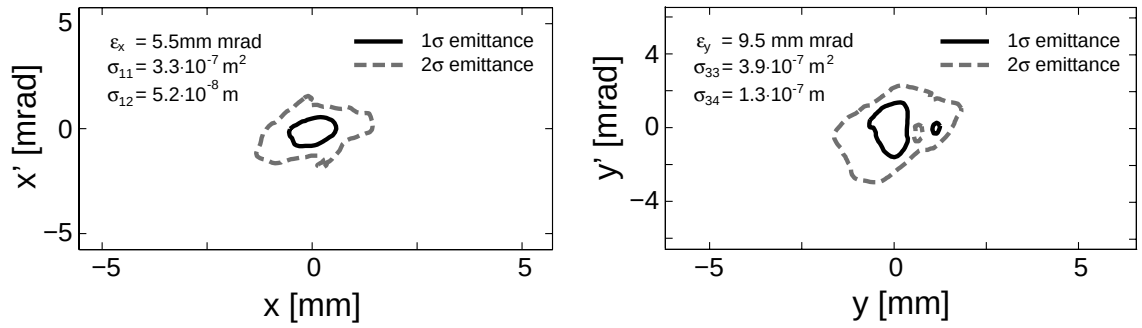


Figure 5.7: Contour plot of the reconstructed horizontal phase space density. The contour lines enclosing the area of the 1σ and 2σ emittance are shown.

5.2.4 Discussion of the Systematic Errors

The accuracy of the emittance measurement is determined by the systematic error of the reconstruction code due to the resolution of the optical imaging system, beam jitter, longitudinal misalignment and field errors of the quadrupole magnets. The interpolation of missing profiles and the uncertainty of the space charge dominated beam transfer add to the systematic uncertainty.

Simulations

The quality of the tomographic reconstruction is estimated by simulations using a symmetric and an asymmetric charge distribution. The symmetric distribution is a Gaussian, the asymmetric distribution consists of three Gaussians of different rms width and height arranged asymmetrically in phase space (see Fig. 4.8). The initial distribution is tracked to the OTR screen for different quadrupole settings and projected onto the x and x' axis. During tracking, a beam jitter and an uncertainty of the transfer matrix M can be introduced by allowing a random variation of the tracked phase space distribution and of the transfer matrix elements. The obtained Radon transform is then used for the tomographic reconstruction. The quality of the reconstruction is judged by the relative difference of the input and output emittances.

Beam Jitter

The beam stability was investigated in the injector by analyzing the beam intensity distributions over a time interval of 40 minutes, which is longer than the time needed for a quadrupole scan. Figure 5.8 shows the horizontal and the vertical beam position and the beam width (determined by the rms of the beam profiles). The horizontal beam centroid is gently drifting towards positive values while the vertical centroid remains stable. The correlated beam movement is corrected for during the reconstruction and should therefore have no influence on the result of the measurement. Notice the appearance of sudden horizontal beam movements towards smaller values. At the time being this effect is not well-understood and needs further investigation. The variation of the beam width over the measurement period of 40 minutes is less than 40 microns (5%).

Distribution	$\Delta\epsilon/\epsilon$	$\Delta\sigma_{11}/\sigma_{11}$ [%]	$\Delta\sigma_{12}/\sigma_{12}$ [%]
Symmetric	4.0 ± 0.1	< 1	< 1
Asymmetric	11.5 ± 1.1	3.8 ± 0.4	5.1 ± 0.3

Table 5.1: Systematic error on the beam parameters determined by simulation of the tomographic reconstruction. 18 projections at a constant angular steps of 10° are computed. The Radon transform is interpolated to 120 profiles. No smoothing is applied in the filtered backprojection. A symmetric and a asymmetric phase space distribution has been used.

Table 5.1 shows the relative systematic error of the reconstructed emittances and beam parameters simulated with the measured beam instability. The symmetric phase space distribution can be recovered with $\Delta\epsilon/\epsilon = (4.0 \pm 0.1)\,\%$, the asymmetric distribution with $\Delta\epsilon/\epsilon = (11.5 \pm 1.1)\,\%$. The beam dimension in the simulation is adapted to the parameters of the measured charge densities (see Fig. 5.7). 18 projections with an angular spacing of 10° have been evaluated and the Radon transform is interpolated to 120 profiles. No smoothing by the filtered backprojection is applied. The computation assumes a longitudinal positioning of the quadrupole magnets and the transition radiation screen of better than 1 mm. The relative error of the quadrupole field strength $\Delta g/g$ should not exceed 1%.

Influence of Space Charge Defocusing

Space charge forces have to be included to calculate the beam transfer in the injector section. The additional space charge defocusing reduces the available range of rotation angles because the intensity on the transition radiation screen does not suffice for a beam image at certain quadrupole settings. It is therefore not possible to obtain a Radon transform covering 180°. The missing beam profiles in the Radon transform have to be extrapolated. Simulations show that the result of the tomographic reconstruction depends on

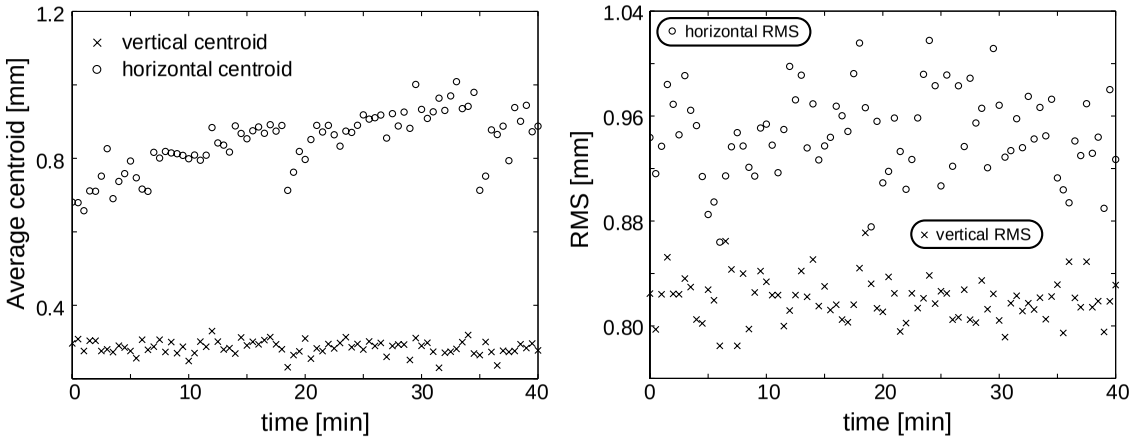


Figure 5.8: Left graph: horizontal and vertical beam position for a period of 40 minutes. Right graph: horizontal and vertical beam size for the same time period.

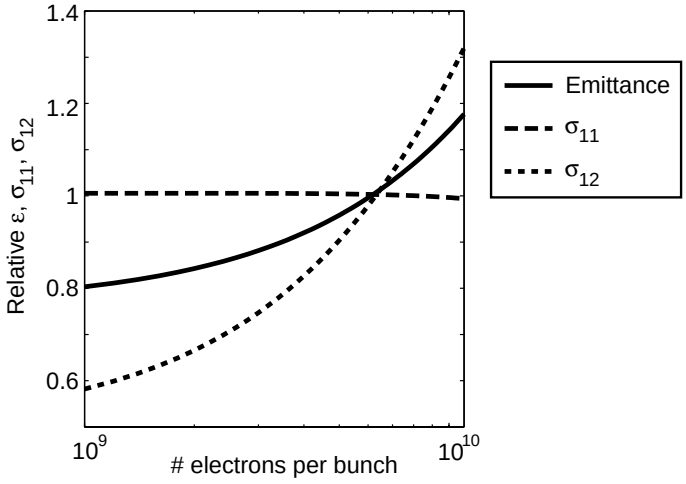


Figure 5.9: Relative emittance and transverse beam parameters as a function of the number of electrons per bunch. The transfer matrix fulfills the self-consistency condition for a simulated bunch charge of $6.25 \cdot 10^9$ electrons. The solid, dashed and dotted curves indicate the systematic error of the reconstructed emittance and beam parameters if the true bunch charge is different than assumed for the self-consistency condition.

which beam profiles are missing. If the waist of the beam is scanned symmetrically, then the systematic error of the reconstructed emittance due to the missing beam profiles will be smaller than $\Delta\epsilon/\epsilon = 10\,\%$.

Figure 5.9 shows the relative systematic change of the emittance and the beam parameters as a function of the bunch charge. The description of the space charge dominated beam transfer depends on the accuracy of the bunch charge measurement. The transfer matrix M has been adjusted to fulfill the condition of self-consistency for $6.25 \cdot 10^{10}$ electrons per bunch. The solid, dashed and dotted curve in Fig. 5.9 show the variation of the emittance and the beam parameters if the true bunch charge differs from this value. Then the beam transfer is not modeled correctly by the program and wrong beam parameters are determined although the self-consistency condition is fulfilled. A bunch charge uncertainty of 10% yields a systematic uncertainty of $\Delta\epsilon/\epsilon = 4\%$, $\Delta\sigma_{11}/\sigma_{11} < 1\%$ and $\Delta\sigma_{12}/\sigma_{12} = 8\%$.

Error Discussion

The transverse emittance of the 16 MeV beam is

$$\gamma\epsilon_x = (5.5\,^{+0.2}_{-0.6} \pm 0.5 \pm 0.3) \cdot 10^{-6}\mathrm{m} \quad (5.2)$$

$$\gamma\epsilon_y = (9.5\,^{+0.4}_{-1.1} \pm 1.3 \pm 0.5) \cdot 10^{-6}\mathrm{m}\,. \quad (5.3)$$

The first error represents the systematic error of the tomographic image reconstruction (beam jitter, longitudinal misalignment, quadrupole field error and interpolation), the second error the uncertainty due to space charge forces and the third error the statistical error of three consecutive measurements. The uncertainty of the space charge term is derived from an estimated uncertainty of the bunch charge measurement of 0.1 nC and from the result of simulations containing only 13 projections in the Radon transform. The

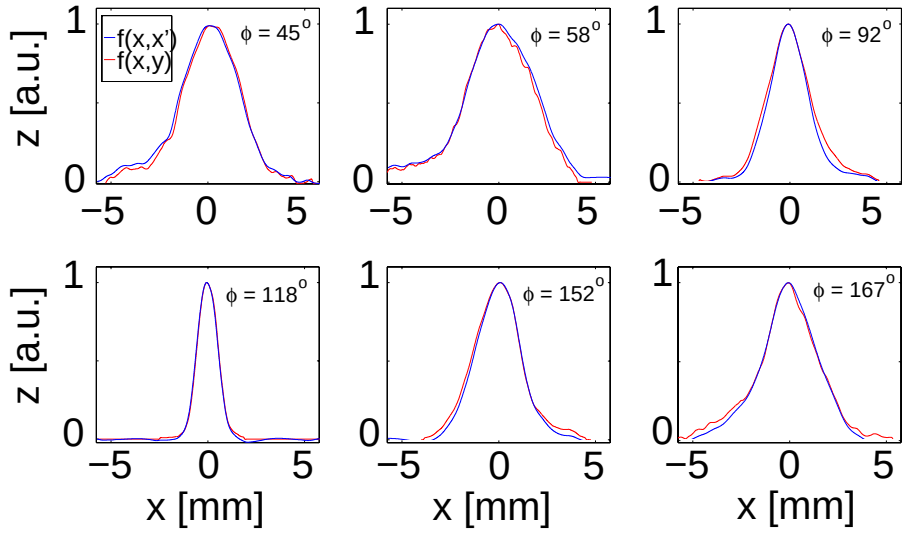


Figure 5.10: Comparison of measured beam profiles and projections of the reconstructed phase space distribution tracked to the OTR screen.

study of systematic effects indicates that there is a tendency to overestimate the emittance. Hence the error bars in Eq. (5.2) and (5.3) are asymmetric. The beam parameters σ_{11}, σ_{12}, σ_{33} and σ_{34} evaluated from the reconstructed horizontal and vertical phase space distribution are

$$\sigma_{11} = (3.3 \pm 0.1 \pm 0.5 \pm 0.2) \cdot 10^{-7}\mathrm{m}^2 \quad (5.4)$$

$$\sigma_{12} = (5.2 \pm 0.1 \pm 1.2 \pm 0.2) \cdot 10^{-8}\mathrm{m} \quad (5.5)$$

$$\sigma_{33} = (3.9 \pm 0.1 \pm 0.5 \pm 0.2) \cdot 10^{-7}\mathrm{m}^2 \quad (5.6)$$

$$\sigma_{34} = (1.3 \pm 0.1 \pm 0.6 \pm 0.1) \cdot 10^{-7}\mathrm{m} \quad (5.7)$$

where the errors represent the systematic errors due to the tomographic image reconstruction, due to space charge forces and the statistical error of the measurement.

The measured horizontal emittance of $5.5 \cdot 10^{-6}$m at the end of the injector represents the best beam quality expectable for the operating parameters used. Smaller emittances can be realized with a higher-gradient rf-accelerating field of about 50MV/m and a smaller laser pulse length of $\sigma_t < 1.5ps$.

Self-consistency Check of the Reconstruction

The reconstructed phase space distribution is tracked forward to the transition radiation screen using the quadrupole settings as in the tomographic scan. Figure 5.10 shows a comparison of the phase space distribution projected onto the spatial coordinate axis and the measured beam intensity distribution. The agreement of the measured and reconstructed beam profiles is excellent. Only slight differences are visible at the tails of the profiles. The reconstruction of the transverse phase space distribution therefore yields reliable numbers for the beam parameters. This result demonstrates the applicability of tomographic image reconstruction techniques for transverse phase space diagnostics.

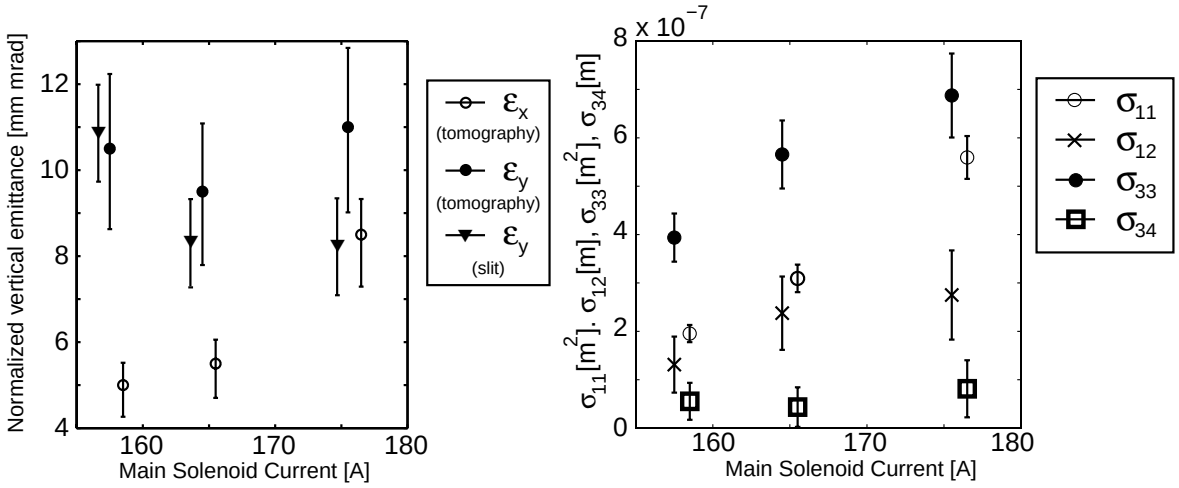


Figure 5.11: Left graph: horizontal and vertical emittance measured at the TTF photo injector by phase space tomography and the slit technique (only vertical emittance determined). Right graph: beam parameters determined by phase space tomography. The emittance and the beam parameters are plotted for different gun solenoid magnetic fields and solenoid currents respectively. Both the primary and secondary solenoid have been varied while keeping a constant ration of $I_p/I_s = 1.8$.

5.2.5 Further Emittance Studies using the Photo Injector Beam

Slit Emittance Measurement

The emittance determination by transverse phase space tomography has been compared to a slit emittance measurement. For this purpose a screen with horizontal slits of 100 μm width and separation is moved into a beam of 1 nC charge and 16 MeV energy. The image of the beam has been recorded using optical transition radiation and a CCD camera. The idea of the method resembles the hole-camera principle of geometrical optics. The observed distribution and the width of the images of the individual slits can be used to determine the beam width and angular divergence [47]. Figure 5.11 (left) shows a comparison of the vertical beam emittances measured by the tomographic and the slit technique using the photo injector beam. The emittances agree within errors.

Optimization of Solenoid Currents

The fields of the gun solenoids are varied to minimize the emittance of the rf gun beam. Two solenoid current scans with different laser spot diameters on the photo cathode have been performed to determine the optimum solenoid setting. Figure 5.11 shows the beam emittance and the beam parameters measured for three different settings of the solenoid coils, i. e. 158 A & 86 A, 165 A & 90 A, 176 A & 96 A for the primary and secondary solenoids respectively. The normalized horizontal and vertical emittance (left) and the beam parameters (right) are plotted versus the primary solenoid current. The laser spot diameter on the photo cathode is $d = 3$ mm. The horizontal emittance is increasing with increasing solenoid current. The variations of the vertical emittance are not significant. Currents of 165 A and 90 A yield a normalized horizontal and vertical emittance

of $\gamma\epsilon_x = 5.5 \cdot 10^{-6}$m and $\gamma\epsilon_y = 9.5 \cdot 10^{-6}$ m respectively and have been used as standard solenoid settings.

Figure 5.12 shows the normalized horizontal and vertical emittance as a function of the the variation of the primary and secondary solenoid currents for a laser spot diameter of $d = 10$ mm. A fixed ratio between the solenoid currents $I_p/I_s = 1.8$ is maintained. The minimum emittance is obtained at $I_p = 166$ A as shown in the left column. In a second step, the primary solenoid is fixed at $I_p = 166$ A and the current of the secondary solenoid is varied. The optimum emittance of $\gamma\epsilon_x = 9 \cdot 10^{-6}$ m and $\gamma\epsilon_y = 17 \cdot 10^{-6}$ m is found at $I_p = 166$ A and $I_s = 82$ A. The larger emittances are mainly caused by the larger laser spot on the photo cathode.

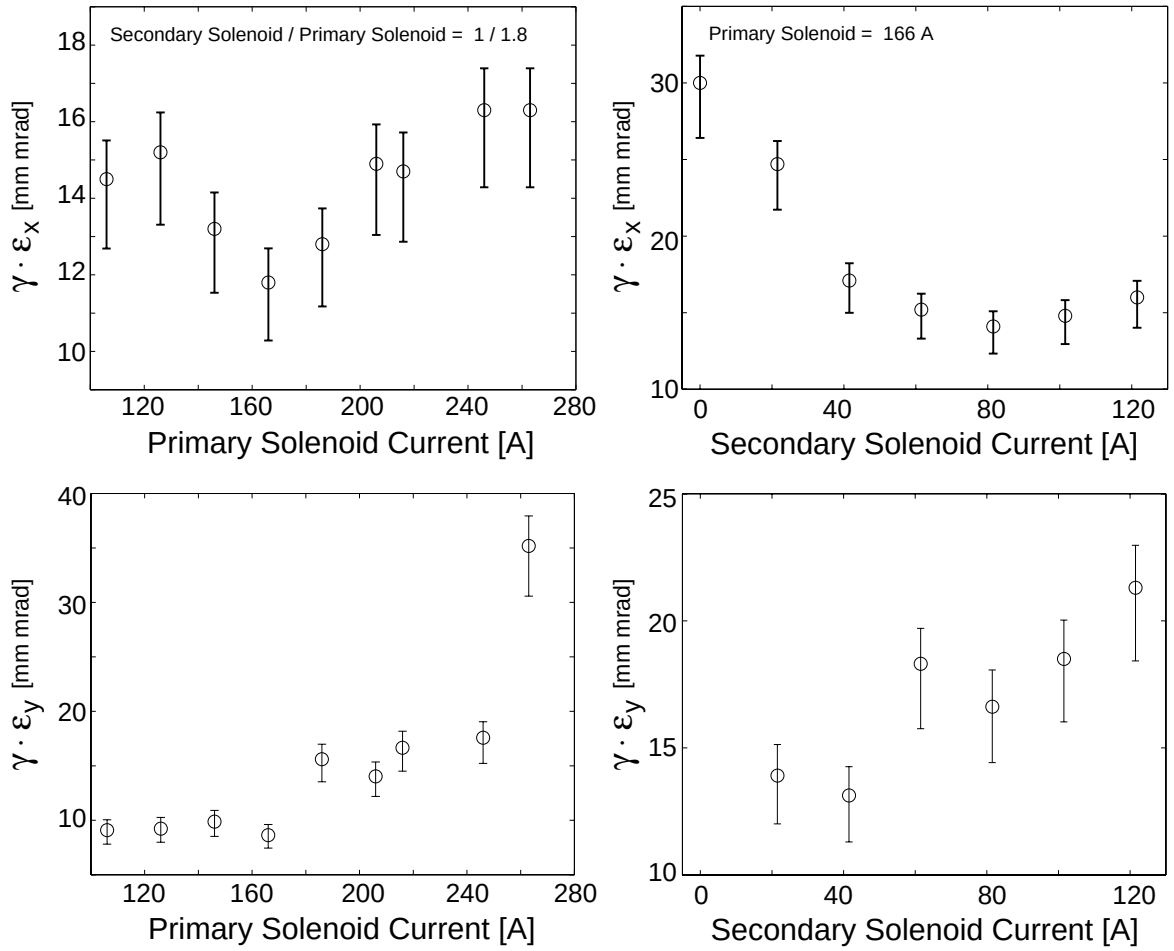


Figure 5.12: Normalized horizontal and vertical emittance measured at the TTF photo injector using a quadrupole scan with tomographic image reconstruction techniques. Left column: variation of the primary and secondary gun solenoid current at constant ratio of $I_p/I_s = 1.8$. Right column: variation of the secondary solenoid with the primary fixed at $I_p = 166$ A. Top row: horizontal emittance. Bottom row: vertical emittance. The laser spot diameter on the photo cathode is $d = 10$ mm

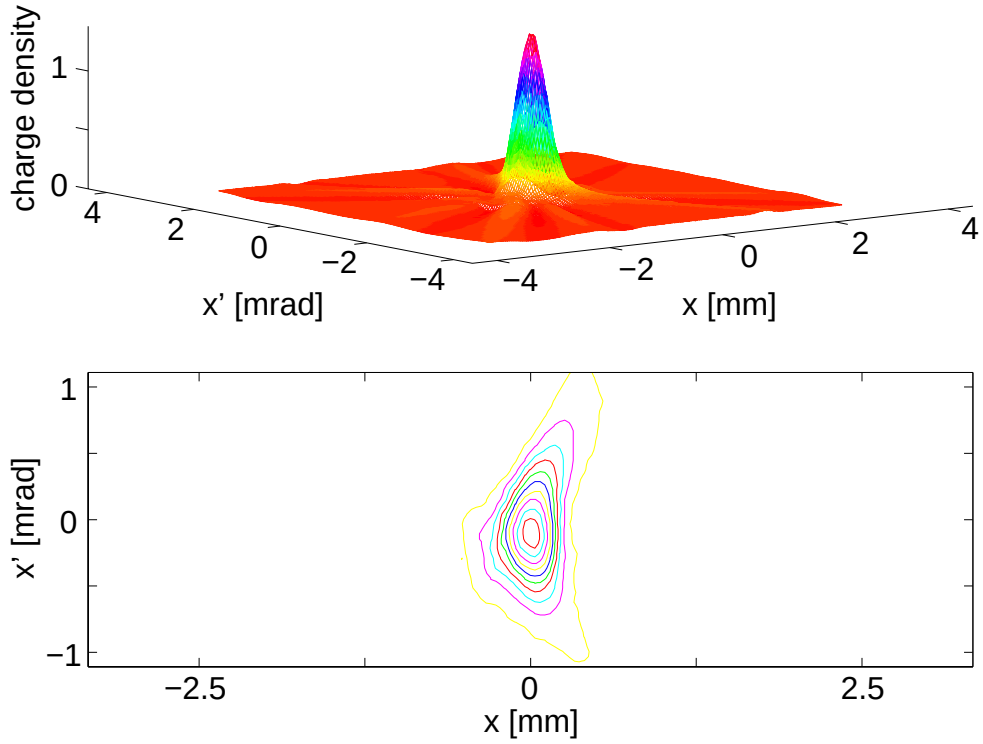


Figure 5.13: Horizontal phase space distribution measured at the TTF thermionic injector. Upper graph: three-dimensional view. Lower graph: contour plot of the phase space area.

5.3 Measurements with Thermionic Injector Beam

The TTF thermionic injector was operated with beam currents between 1 and 5 mA, with 2 Hz macro-pulses of 30 μs length and with a bunch repetition rate of 216 MHz. The total number of electrons per bunch is $2.3{\cdot}10^8$. The beam energy at the quadrupole scan section was 9 MeV. Space charge effects in the scanning section can be neglected because of the lower bunch charge.

Figure 5.13 shows the reconstructed horizontal phase space distribution from a scan covering an angular interval of 160°. The charge distribution shows a single peak whose contour lines are almost elliptic close to the center. The elliptic contour lines hint at a Gaussian charge distribution. A close inspection of the upper graph reveals still some star-like blurring which is a remainder of the missing angular interval of 20^o. Figure 5.14 shows the contour lines corresponding to the σ and the 2σ emittances. The transverse phase space distribution in the vertical plane is of similar shape.

The normalized beam emittance and the beam parameters obtained for an average beam current of $\bar{I} = 3$mA are

$$\begin{aligned} \gamma\epsilon_x &= (3.8 - 0.5 + 0.2 \pm 0.4) \cdot 10^{-6}\text{m} \\ \gamma\epsilon_y &= (3.3 - 0.4 + 0.2 \pm 0.4) \cdot 10^{-6}\text{m} \\ \sigma_{11} &= (1.1 \pm 0.1 \pm 0.1) \cdot 10^{-7}\text{m}^2 \end{aligned}$$

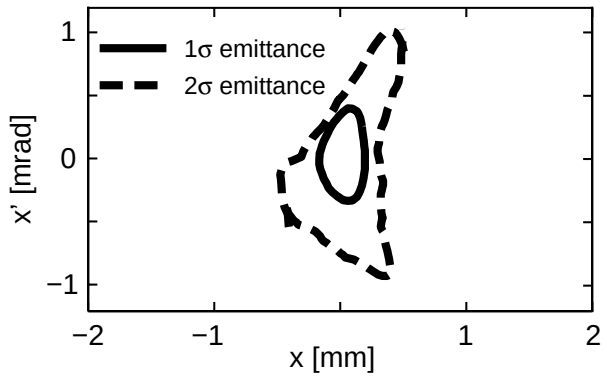


Figure 5.14: Horizontal phase space distribution measured at the TTF thermionic injector. The contour lines represent the σ and the 2σ emittances.

$$\begin{aligned}
\sigma_{12} &= (4.6 \pm 0.3 \pm 0.2) \cdot 10^{-8}\mathrm{m} \\
\sigma_{33} &= (1.3 \pm 0.1 \pm 0.1) \cdot 10^{-7}\mathrm{m}^2 \\
\sigma_{34} &= (9.8 \pm 0.5 \pm 0.3) \cdot 10^{-8}\mathrm{m}\,.
\end{aligned}$$

The horizontal emittance and the beam parameters σ_{11} and σ_{12} have been measured as a function of the beam current shown in Fig. 5.15. The transverse emittance is increasing with beam current while the beam parameters remain constant. The increase of the transverse emittance can be explained by stronger space charge forces in the thermionic gun. The design emittance for an average beam current of 8mA is $\gamma \cdot \epsilon = 5 \cdot 10^{-6}$m. The design current could not be achieved because of efficiency problems of the cathode. However, it can be seen that an extrapolation of the normalized emittance will is larger than the design value of the thermionic injector.

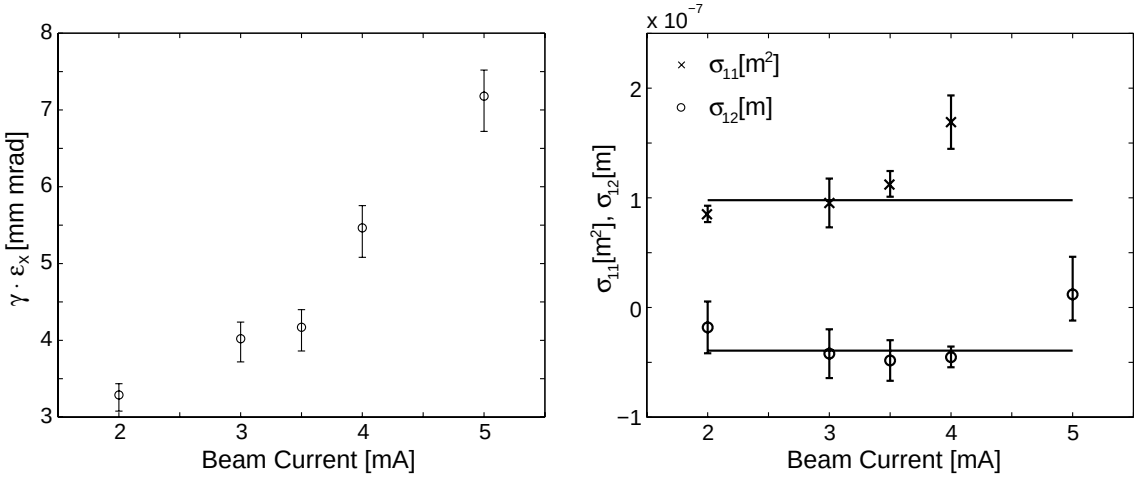


Figure 5.15: Normalized horizontal emittance (left) and the horizontal beam parameters σ_{11} and σ_{12} measured at the TTF thermionic injector versus the average beam current.

5.3.1 Parabola Fit Analysis

The beam profiles recorded during a quadrupole scan measurement are analyzed using the parabola fit analysis. The beam size x_{rms}^2 divided by the beam transfer matrix element M_{12}^2 is plotted versus the quotient of M_{11}/M_{12}. The data obtained from a quadrupole

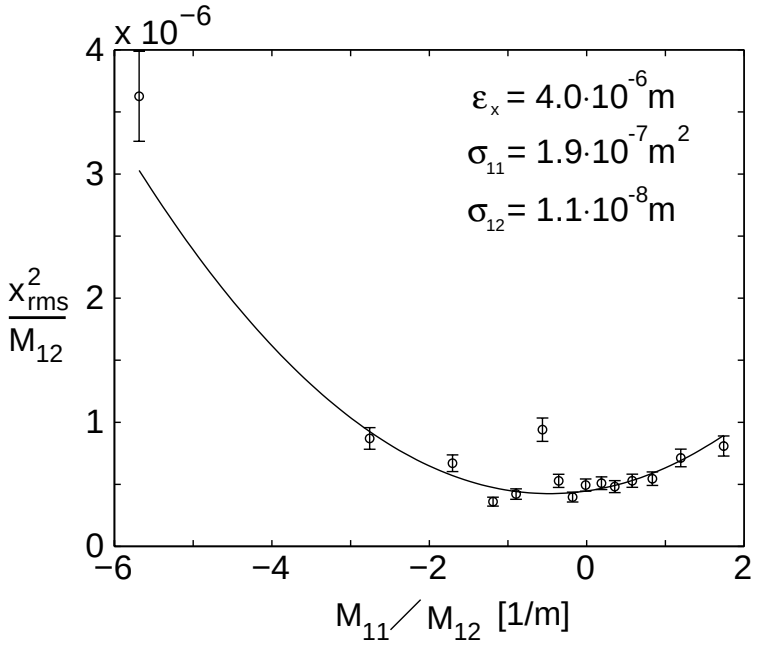


Figure 5.16: Parabola fit analysis of the beam profiles taken during a quadrupole scan. The error bars indicate the statistical error of the measurement.

scan performed with the thermionic injector beam are shown in Figure 5.16. The beam current is 3 mA. The parabolic fit to the data yields the normalized emittance and the beam parameters

$$\gamma\epsilon_x = (4.0 \pm 0.5) \cdot 10^{-6}\mathrm{m} \quad (5.8)$$

$$\sigma_{11} = (1.9 \pm 0.2) \cdot 10^{-7}\mathrm{m}^2 \quad (5.9)$$

$$\sigma_{12} = (1.1 \pm 0.2) \cdot 10^{-8}\mathrm{m}\,. \quad (5.10)$$

The error bars indicate the quadratic sum of the systematic (image processing, beam stability fluctuations, beam transfer) and the statistical error of three consecutive measurements. The emittance and the beam parameters, as indicated in Figure 5.16, yield similar results as obtained by phase space tomography. The error of the emittance and the beam parameters can be obtained directly from the fit procedure. The quality of the parabola fit could be improved by recording additional data points at larger M_{11}/M_{12}.

Chapter 6

Time Domain Techniques for Bunch Length Measurements

6.1 Streak Camera

6.1.1 Experimental Setup

The streak camera is a device for the detection and the time-resolved investigation of light pulses in the picosecond regime. Figure 6.1 shows the working principle. The light

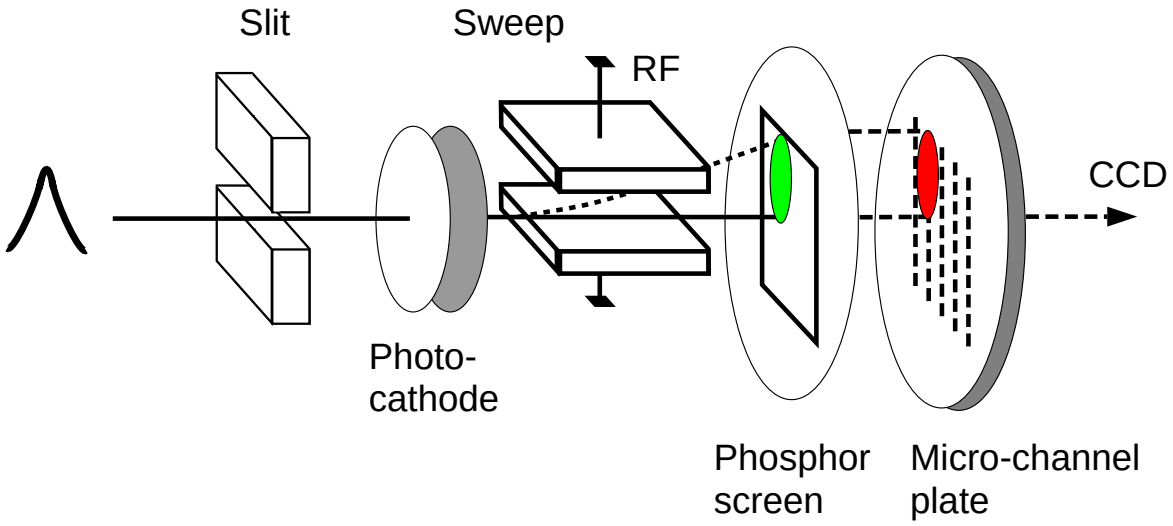


Figure 6.1: Principle of the streak camera.

pulse travels through a dispersion-free optical system and a slit before hitting the photo cathode of the streak camera. The slit reduces the transverse dimension of the image on the photo cathode. The light pulse is converted to an electron pulse, which is accelerated and swept transversely by a fast rf electric field. The resulting transverse distribution is projected onto a phosphor screen. The image is amplified by a multi-channel plate and then detected by a CCD camera.

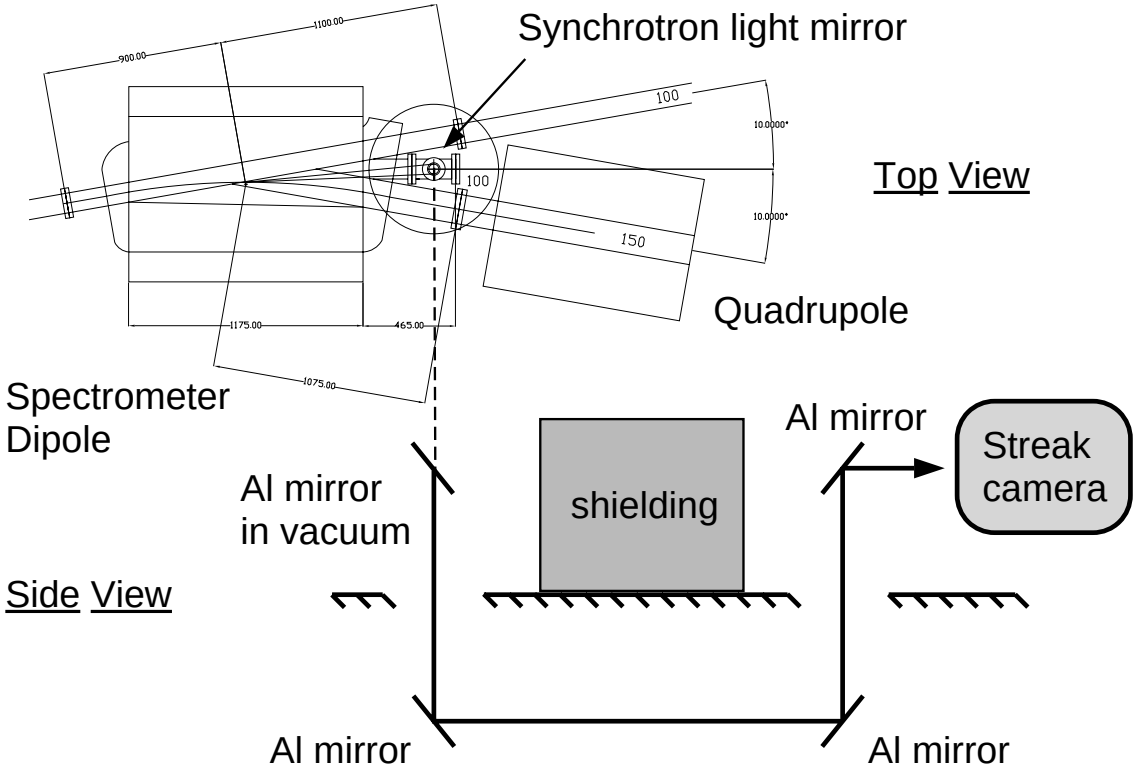


Figure 6.2: The TTF spectrometer dipole magnet with the synchrotron light mirror. The light is reflected by a polished aluminum block through a quartz glass window vertically out of the vacuum chamber. The light pulses are guided through a 11 m long light beam line out of the tunnel. Three aluminum mirrors reflect the synchrotron light to an experimental area where the streak camera is installed.

The streak camera[1] manufactured by the ARP company has an intrinsic time resolution of $\sigma_{\rm res} = 2\,{\rm ps}$. A degradation of the temporal resolution may be due to the transverse dimension of the photo-electron pulse, which is convoluted with the longitudinal electron distribution during the sweep. To fully exploit the time resolution of the streak camera tube a slit width of $\sigma_{\rm slit} < \sigma_{\rm res}$ has to be used. In the present experiment, the bunch length was expected to be in the order of 10 picoseconds, so a slit of 1.9 mm width ($\sigma_t = (6.2 \pm 0.1)\,{\rm ps}$) was inserted in front of the photo cathode. The slit is oriented such that the narrow dimension is parallel to the orientation of the sweep. During the bunch length measurement, the residual transverse dimension of the electron pulse $\sigma_{\rm slit}$ has to be deconvoluted from the measured length of the phosphor screen σ_l by

$$\sigma_z = \sqrt{\sigma_l^2 - \sigma_{\rm slit}^2} \tag{6.1}$$

yielding the bunch length σ_z. The timing of the streak camera was adjusted by slowly increasing the sweeping speed of the tube. The delay of the phase stabilized timing signal, a 216 MHz sub-harmonic of the master oscillator, is re-adjusted at each step. The

[1] I thank Dr. Terry Garvey, Michel Bernard and Bernard Leblond from LAL, Orsay, France for making the LAL streak camera available.

camera is operable when stable light pulses are detected by the CCD camera at maximum sweeping speed.

Synchrotron Light Delivery Synchrotron light generated in the spectrometer dipole at $E = 170\text{MeV}$ is extracted by a synchrotron light mirror as shown in Fig. 6.2. The mirror is a $50 \times 50\,\text{mm}$ polished aluminum block. The light is reflected through a quartz window vertically out of the beam pipe and is guided through an underground beam line of 11 m length to the optical diagnostics experimental area. The light beam line consists of three aluminum mirrors of 76 mm diameter. No focusing lenses are used. The streak camera and the synchrotron light beam are aligned by adjusting the last two mirrors.

6.1.2 Bunch Length Measurements

The electron bunches produced by the TTF photo injector ($Q = 3\,\text{nC}$, UV laser pulse length $\sigma_t = 15\,\text{ps}$) have been transfered to the spectrometer magnet with the magnetic compressor being switched off. During the acceleration from 16 to 160 MeV, the longitudinal charge distribution can be considered as invariant. Synchrotron radiation light pulses, produced in the spectrometer dipole, are detected with the streak camera. Figure 6.3 shows the measurements yielding an rms bunch length of $\sigma_z = (1.95 \pm 0.08)\,\text{mm}$ and $\sigma_z = (3.27 \pm 0.06)\,\text{mm}$. The left graph has been obtained for an rf phase in the gun cavity of 20° yielding an optimum bunch compression without a significant reduction of the bunch charge. The right graph is obtained at a rf phase of 45° yielding a reduced bunch compression.

The streak camera measurements of the injector bunch length are summarized in Fig. 6.4. The left graph shows the rms bunch length as a function of the rf gun phase at a fixed bunch charge of $Q = 3\,\text{nC}$. The bunch length decreases with decreasing rf phase. The effect is explainable by longitudinal bunching due to the head-tail velocity modulation imposed on the bunch by the rf field. The phase $\phi = 0$ indicates the phase of the rf field where the

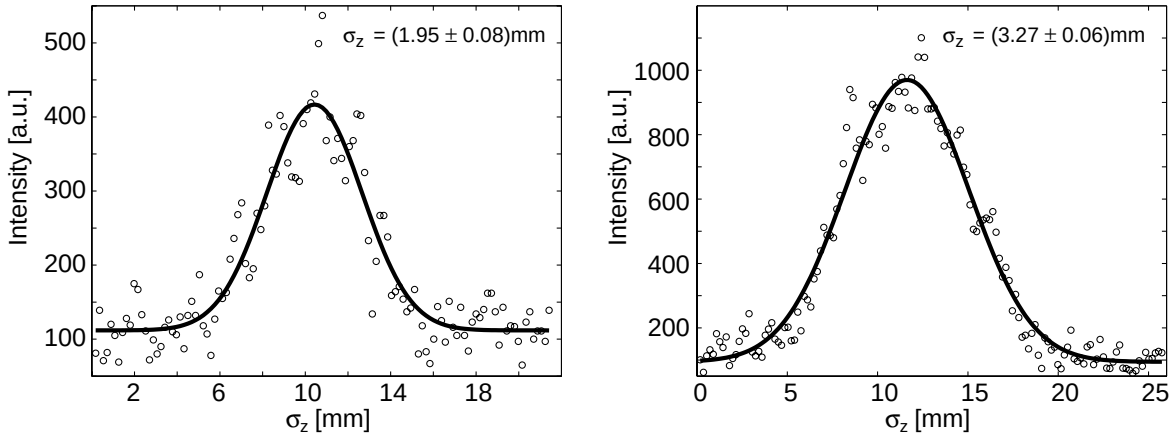


Figure 6.3: Longitudinal bunch charge profiles produced by the TTF photo injector at rf gun phase settings of 20° (left) and 45° (right). Data is presented as circles, the solid curve indicates a Gaussian fit.

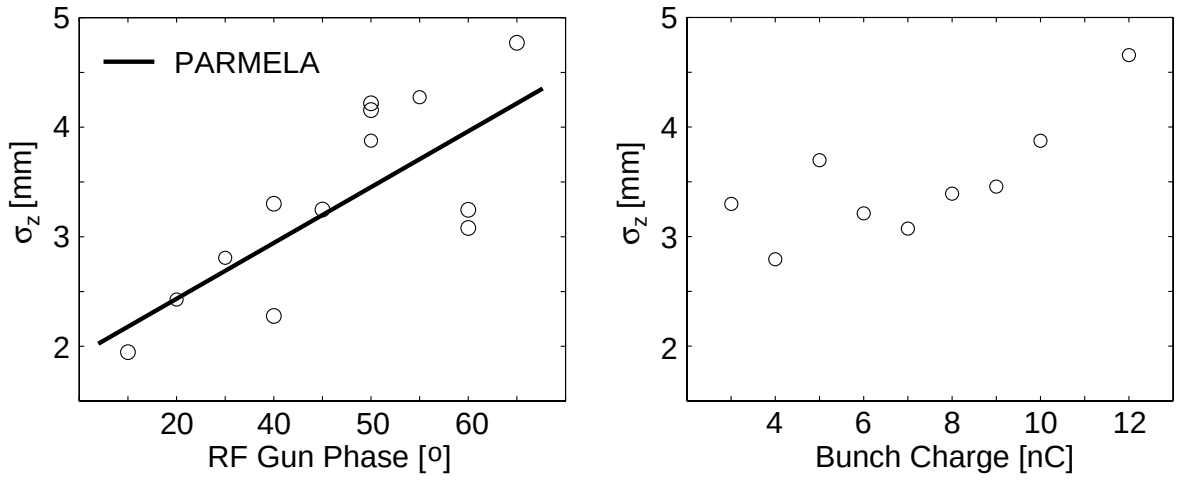


Figure 6.4: Streak camera bunch length measurements. Left: rms bunch length versus rf gun phase (Q = 3nC). Right: rms bunch length versus bunch charge (rf gun phase set to 30°). The solid line indicates the prediction by PARMELA. The error of the bunch length measurement is within the marker size.

electric field changes sign and thus from acceleration to deceleration. The solid line is the prediction by PARMELA [48]. The right graph shows the rms bunch length as a function of the bunch charge at a fixed gun rf phase of 30°. The bunch length does not change significantly for bunch charges smaller than 8 nC. Larger bunch charges cause a gradual lengthening of the longitudinal charge distribution. This lengthening can be explained by longitudinal space charge forces whose strength is rising proportional to the bunch charge.

The laser pulse length has been reduced by a factor of 2 during the run in spring 1999. The reduction of the laser pulse length reduces the electron bunch length by the same factor since the longitudinal space charge forces are of equal magnitude (Q = 3 nC, 16 ps laser pulse length compared to Q = 1 nC, 8 ps laser pulse length). Unfortunately, the streak camera was no longer available to investigate the electron bunches produced with the short laser pulses.

6.2 Longitudinal Phase Space Rotations

6.2.1 Theory and Simulation

The longitudinal dispersion of a magnetic chicane followed by an off-crest acceleration in an rf cavity can be used to translate the longitudinal charge profile into an energy profile of the bunch. Time slices are transfered to slices of constant energy behind the rf cavity. An energy profile measurement in the spectrometer behind the rf cavity yields then an image of the longitudinal bunch charge distribution in front of the chicane.

Figure 6.5 shows a sketch of the TTF linac including the rf module #1, the magnetic chicane, rf module #2 and the dispersive section at the experimental area. To demonstrate the method, an asymmetric charge distribution is used in the simulation. The evolution of

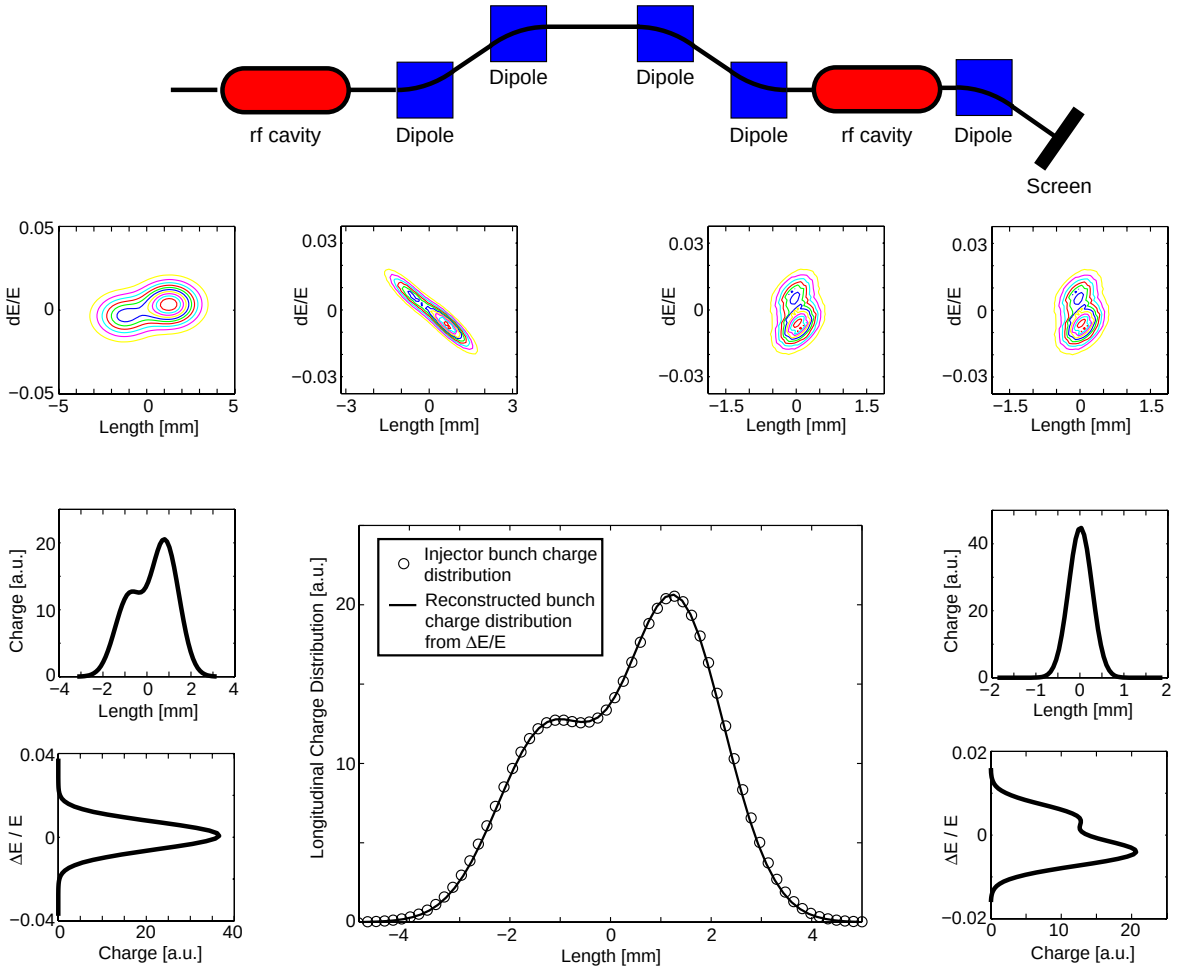


Figure 6.5: The longitudinal charge distribution of an electron bunch can be measured using the longitudinal dispersion of the magnetic chicane compressor followed by an off-crest acceleration in an rf cavity. The longitudinal phase space distribution produced by the injector, behind rf module #1, behind the magnetic chicane and behind rf module #2 is shown. The parameters of the rf module #1 and the magnetic chicane are adjusted for optimum bunch compression. The parameters of the rf module #2 are adjusted to rotate the longitudinal phase space distribution between the beginning of the chicane and the experimental area by $\pi/2$. The center graph shows a comparison of the original longitudinal charge distribution with the reconstructed distribution using the energy profile in the spectrometer section. The agreement is perfect.

this distribution along the linac is shown in Fig. 6.5. The parameters of the rf module #1 and the chicane are adjusted to obtain optimum bunch compression. The gradient and the phase of rf module #2 are adjusted to rotate the longitudinal phase space distribution between the beginning of the chicane and the dispersive section by $\pi/2$. The simulation parameters are listed in Tab. 6.1.

Equation (2.23) describes the bunch energy spread ($\bar{\sigma}_{66}$) as a function of the injector bunch length (σ_{55}), the injector energy spread (σ_{66}), the parameters of rf module #1 (M_{65}, M_{66}

$U_{\rm acc1}$	10 MV	$U_{\rm acc2}$	10 MV	ϕ_1	-14.4°	ϕ_2	-15.9°
R_{65}	$-3.24\,{\rm m}^{-1}$	R_{66}	0.58	U_A	$275.0\,{\rm m}^{-2}$	M_{56}	0.18 m
M_{65}	$-5.76\,{\rm m}^{-1}$	M_{66}	0.18	S_A	$543.3\,{\rm m}^{-2}$		
σ_z^i	1.8 mm	σ_z^f	0.27 mm	σ_E^i	$8.7 \cdot 10^{-3}$	σ_E^f	$5.7 \cdot 10^{-3}$

Table 6.1: Parameters of the simulation.

and U_A) and #2 (R_{65}, R_{66} and S_A) and the longitudinal dispersion M_{56} of the bunch compressor. Time slices in front of the chicane are transformed into energy slices behind rf module #2 if one chooses the transfer matrix elements such that $M_{56}R_{65} + R_{66} \to 0$. Equation (2.23) then reduces to

$$\begin{aligned} \bar{\sigma}_{66} &= \sigma_{55}R_{65}^2 + U_A^2\Big\{\sigma_{55}(1 + M_{56}M_{65})^2 + \sigma_{66}M_{56}^2M_{66}^2 + S_A^2M_{56}^2\sigma_{55}^2\Big\}^2 \\ &\approx \sigma_{55}R_{65}^2\,. \end{aligned}$$

The non-linear term of the second rf acceleration stage can be neglected because of the short bunch length behind the chicane.

The longitudinal charge distribution in front of rf module #1 and the energy distribution behind rf module #2 are shown in Fig. 6.5. From the projections one can see that the energy distribution behind module #2 is a direct image of the longitudinal charge distribution in front of module #1. The center graph in Fig. 6.5 shows in a quantitative way that the reconstructed and the original charge profile agree perfectly.

The phase space rotation method can also be used to observe the longitudinal compression within the chicane by varying the parameters of the second rf module. The position z_i where the longitudinal charge profile is to be determined is again given by the condition of the form $M_{56}R_{65} + R_{66} \to 0$. Here, M_{56} denotes the longitudinal dispersion between z_i and the end of the chicane.

Resolution The resolution of the method is limited by the resolution of the spectrometer and the validity of linear beam transfer including the applied quadratic corrections. The energy resolution of the TTF spectrometer is $\Delta E/E = 2 \cdot 10^{-4}$. Hence, the spatial resolution is given, in linear approximation, by

$$\Delta z = \frac{\Delta E/E}{R_{65}}\,. \tag{6.2}$$

Δz can be minimized by choosing R_{65} (at a given field gradient) as large as possible,

$$R_{65}^M = \lim_{\Phi\to\pi/2} \frac{dE\sin\Phi}{E_i + dE\cos\Phi}\frac{2\pi}{\lambda} = \frac{dE}{E}\frac{2\pi}{\lambda} \approx \frac{2\pi}{\lambda} = 27.2\left[\frac{1}{\rm m}\right] \tag{6.3}$$

since both rf modules operate at the same field gradient. For maximum resolution the second module has to be operated with a phase $\Phi = \pi/2$. The TTF spectrometer then yields a spatial resolution of

$$\Delta z|_{\rm res} = 7.5\,\mu{\rm m} \tag{6.4}$$

reconstructed at $M_{56}(z_0 \rightarrow z_1) = 3.7\,\mathrm{cm}$ corresponding to a chicane position at the end of the third dipole magnet.

The spatial resolution at the beginning of the chicane ($M_{56} = 0.18\,\mathrm{m}$) is

$$\Delta z|_{\mathrm{res}} = \frac{M_{56}\Delta E/E}{R_{66}} = 36\,\mu\mathrm{m} \tag{6.5}$$

where R_{66} is chosen unity (rf phase $\Phi_0 = \pi/2$). In the present configuration, the resolution is sufficient to determine electron pulse length produced by the chicane compressor. Non-linear effects like cavity wake-fields and longitudinal space charge forces are small and can be neglected.

The bunch length determination by phase space rotations is, in a sense, a single bunch time-domain measurement with a resolution of about $40\,\mu$m. Intensified CCD cameras with a gating of faster than 100 ns are commercially available and capable to resolve the bunch spacing at the TTF linac. An excellent application of this method is the direct observation of electron beam micro-bunching at the Stanford FEL center [49].

6.2.2 Bunch Length and Energy Distribution Measurements

For the measurements the TTF linac was operated with macropulses consisting of 20 bunches of 1 nC charge with a repetition rate of 1 MHz. The gun cavity rf phase was 20° to produce the shortest bunches possible. The laser pulse length was $\sigma_t = 8\,\mathrm{ps}$.

Energy Spread at the Injector

The energy spread at a beam energy of 16 MeV was measured in the dispersive section of the injector by means of optical transition radiation. The minimum energy spread was $\sigma_E/E = 1.9 \cdot 10^{-3}$.

Energy Distribution at the Experimental Area

RF module #1 is operated at a gradient 10 MV/m and a de-phasing angle of 14° to optimize the bunch compression in the magnetic chicane ($E = 90\,\mathrm{MeV}$). The beam is accelerated in the second rf module to the final beam energy of 170 MeV. The beam energy distribution is recorded in the spectrometer located in the experimental area using optical transition radiation.

Figure 6.6 shows the measured energy profiles at the experimental area. The measurements were taken at different machine settings as shown by Tab. 6.2. The energy profile on the left corresponds to a relative energy deviation of $9.2 \cdot 10^{-3}$ (FWHM), the profile on the right to $3.3 \cdot 10^{-3}$ (FWHM). The lower plots show the compression of the longitudinal charge distribution through the chicane with the vertical dashed line indicating the chicane position where the condition $M_{56}R_{65} + R_{66} \rightarrow 0$ is fulfilled. The energy profile on the left corresponds to a FWHM bunch length of 2.6 mm at the first dipole magnet ($\sigma_z = 1.1\,\mathrm{mm}$, $\sigma_t = 3.8\,\mathrm{ps}$), the profile on the right to 280 μm in the third dipole magnet

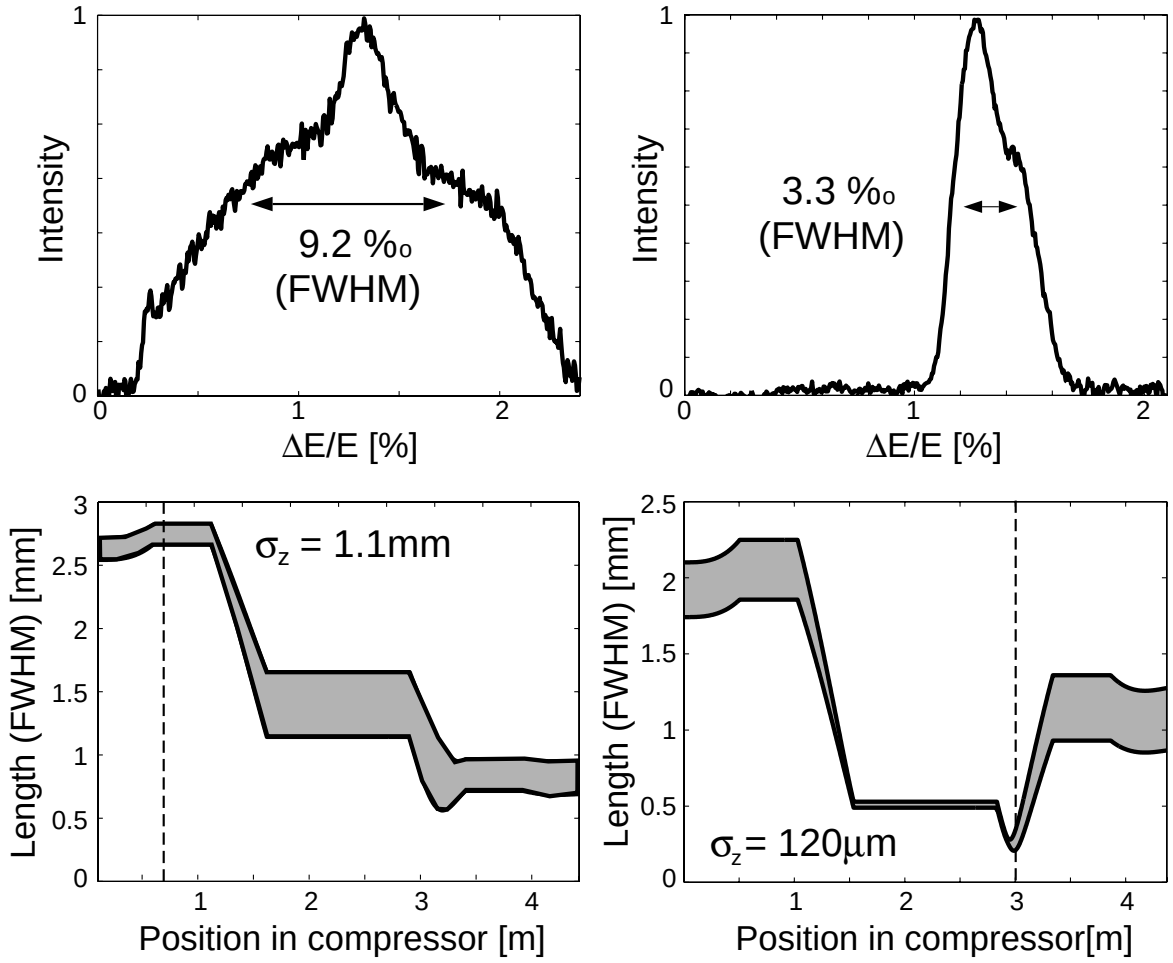


Figure 6.6: Energy profile measurements performed behind the TTF spectrometer dipole magnet at different rf parameter settings. The energy deviation yields $6 \cdot 10^{-3}$ (left) and $3.3 \cdot 10^{-3}$ (right) FWHM. The lower plots show the evaluated rms confidence intervals of the bunch length throughout the chicane. The dashed line indicates the longitudinal position where the measured energy profile matches the longitudinal charge distribution. Left: optimum compression. Right: over-compression.

($\sigma_z = 120\,\mu$m, $\sigma_t = 400$ fs).

The step-wise reduction of the rms bunch length in the magnetic chicane is shown in Fig. 6.6. The confidence interval is obtained from a comparison of the measurements and simulation. The rms energy spread at the spectrometer dipole magnet is computed for a set of the following parameters: bunch length and energy spread in front of module #1, gradient and phase of both rf modules and longitudinal dispersion of the chicane compressor. Gradient and phase of the rf modules and the final rms energy spread are measured within their error intervals. A comparison of the measured data and the results of the simulation yields a set of possible solutions describing the compression of the longitudinal charge distribution for the accelerator setting used. The set of possible bunch lengths is indicated as the confidence interval (shaded area) in Fig. 6.6.

	$\Delta E/E\,[10^{-3}]$	$\sqrt{\sigma_{55}}$ [mm]	ΔE_1 [MV/m]	ΔE_2 [MV/m]	Φ_1 [^{o}]	Φ_2 [^{o}]
Left	9.2 ± 0.2	1.1 ± 0.1	76.5 ± 0.3	65.2 ± 0.3	13.5 ± 5	14 ± 5
Right	3.3 ± 0.2	0.14 ± 0.03	76.5 ± 0.3	65.2 ± 0.3	20.5 ± 5	34 ± 5

Table 6.2: TTF machine settings yielding the energy profiles shown in Fig. 6.6. The columns indicate from left to right: relative energy spread measured in the dispersive section, reconstructed rms bunch length, field gradient of cavity module #1 and #2, rf phase of module #1 and #2. The injection energy is 16.5 MeV. The errors are statistical errors of the measurements.

The average rms bunch length at $E = 16\,\mathrm{MeV}$ is $\sigma_z = (990 \pm 180)\,\mu\mathrm{m}$. The result is in accord with the streak camera measurement ($\sigma_z = (1.95 \pm 0.08)\,\mathrm{mm}$) if a correction is made for the different laser pulse lengths.

The lower left graph of Figure 6.6 shows the optimum bunch compression of the longitudinal charge distribution. Here, the parameters of the first acceleration module are set to obtain a final bunch length of $\sigma_z = (350 \pm 130)\,\mu\mathrm{m}$, $\sigma_t = (1.1 \pm 0.4)\,\mathrm{fs}$, and energy spread of $(1.5 \pm 0.1)\,\mathrm{MeV}$ behind the magnetic chicane. The lower right graph shows an example for a longitudinal over-compression, where the minimum bunch length is obtained at the third dipole magnet. The final bunch length at the end of the chicane is $\sigma_z = (500 \pm 120)\,\mu\mathrm{m}$, $\sigma_t = (1.7 \pm 0.4)\,\mathrm{ps}$. The final energy spread of $(550 \pm 30)\,\mathrm{keV}$ is smaller than for optimum compression. The correlation of the longitudinal phase space is opposite with higher energy leading lower energy electrons. This opposite correlation is decreased, eventually removed and inverted, by the off-crest acceleration in the second rf module increasing the energies of the trailing with respect to the leading electrons. The result is an energy profile of reduced width.

Chapter 7

Fourier Transform Spectroscopy

A Martin-Puplett interferometer is used to determine the longitudinal pulse shape by autocorrelation of the incoming radiation pulse. The coherent power spectrum and the bunch form factor is derived using a Fourier transformation. This section outlines the working principle and the spectral acceptance function of the Martin-Puplett interferometer. Several data analysis techniques will be presented. Simulation results showing the errors and limitations of the method and measurements will be presented.

7.1 Description of the Martin-Puplett interferometer

A Martin-Puplett interferometer is a Michelson-type interferometer used in the millimeter and sub-millimeter wavelength range. A schematic view is shown in Fig. 7.1. The interferometer used at TTF consists of two parabolic mirrors, three wire grids, two roof mirrors and two pyroelectric detectors. These components are mounted on a stable aluminum plate which is supported by an adjustable table. The interferometer components are designed to have high precision and optical quality [50].

Wire Grids

The wire grids with an aperture of 90 mm are wound from 20 μm diameter gold-plated tungsten wire with a spacing of 100 μm. The grids have been built on a winding machine in the workshops of the University of Aachen. The wire grids are mounted in a metallic frame which is placed into the interferometer. The use of a microscope is essential during the assembly of the grid to straighten out the wires and ensure a regular spacing.

Parabolic Mirrors

Aluminum parabolic mirrors with optical quality have been built in the workshops of the Fraunhofer Institute für Produktionstechnik (IPT) in Aachen and of the University of Aachen. The mirrors have a focal length of 200 mm and an aperture of 100 $\times$ 100 mm. The parabolic mirrors are mounted on a three-point suspension and are equipped with micrometer screws to vary the position of the reflective plane and the reflection angle.

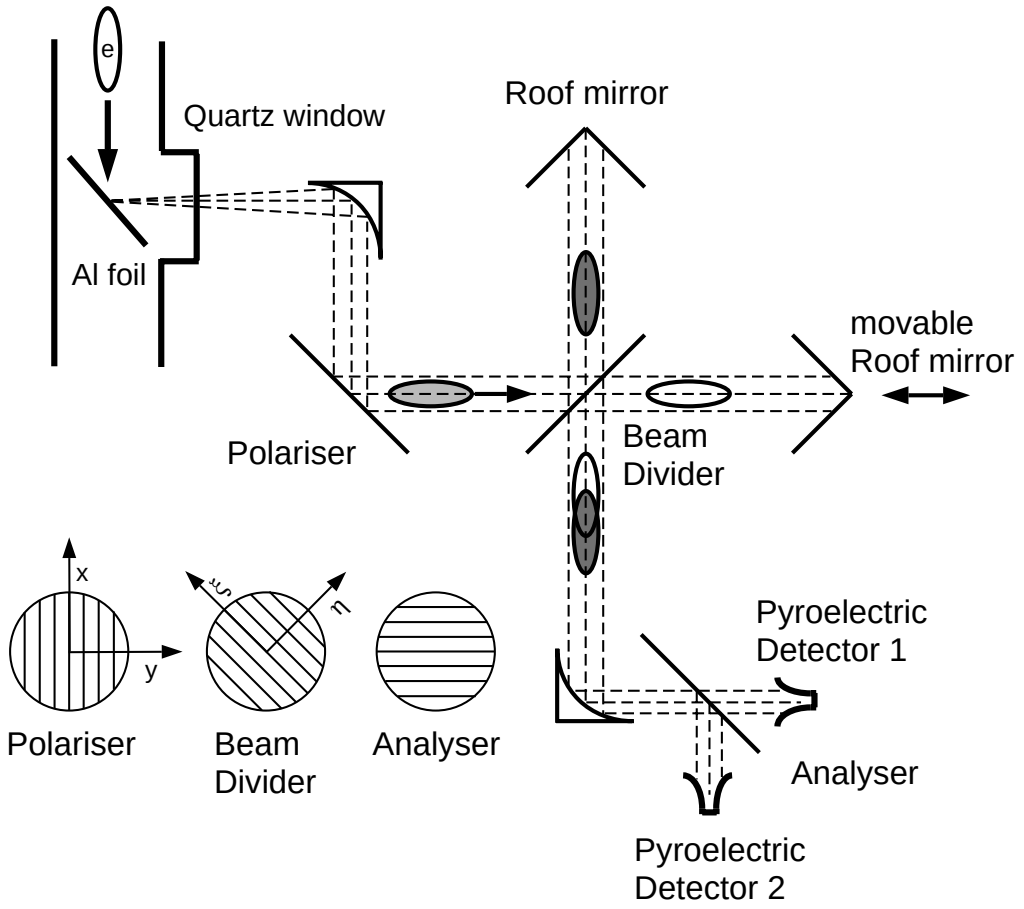


Figure 7.1: Schematic view of the Martin Puplett interferometer consisting of parabolic mirrors, wire grids, roof mirrors and two detectors.

Roof Mirrors

The roof mirrors consist of two polished aluminum mirrors which are glued under an angle of 90° into an aluminum girder. The aperture of the roof mirrors matches the clear aperture of the wire grids. The movable roof mirror is mounted on top of an optical mover driven by a stepping motor. The roof mirrors are equipped with a single micrometer screw to vary the vertical reflection angle of the mirror.

Pyroelectric Detectors

Two pyroelectric detectors Molectron PI-45 with integrated FET operational amplifier are used in the interferometer. The specification of the PI-45 detector can be taken from Table 7.1. A resistor of 100 MΩ is connected to the FET to achieve an signal of 30 V/W at a bandwidth of 4 kHz. A second variable amplifier is available. The detector and the electronic circuit is housed in an aluminum box which is mounted in the interferometer. A polished aluminum horn antenna of 83 mm length and 35.8° full opening angle is mounted in front of the pyroelectric detector to increase its active diameter. The analogue signal produced by the pyroelectric detector is transfered out of the TTF tunnel using an additional current driving amplifier. A 12 bit, 1 MHz bandwidth ADC digitizes the signal

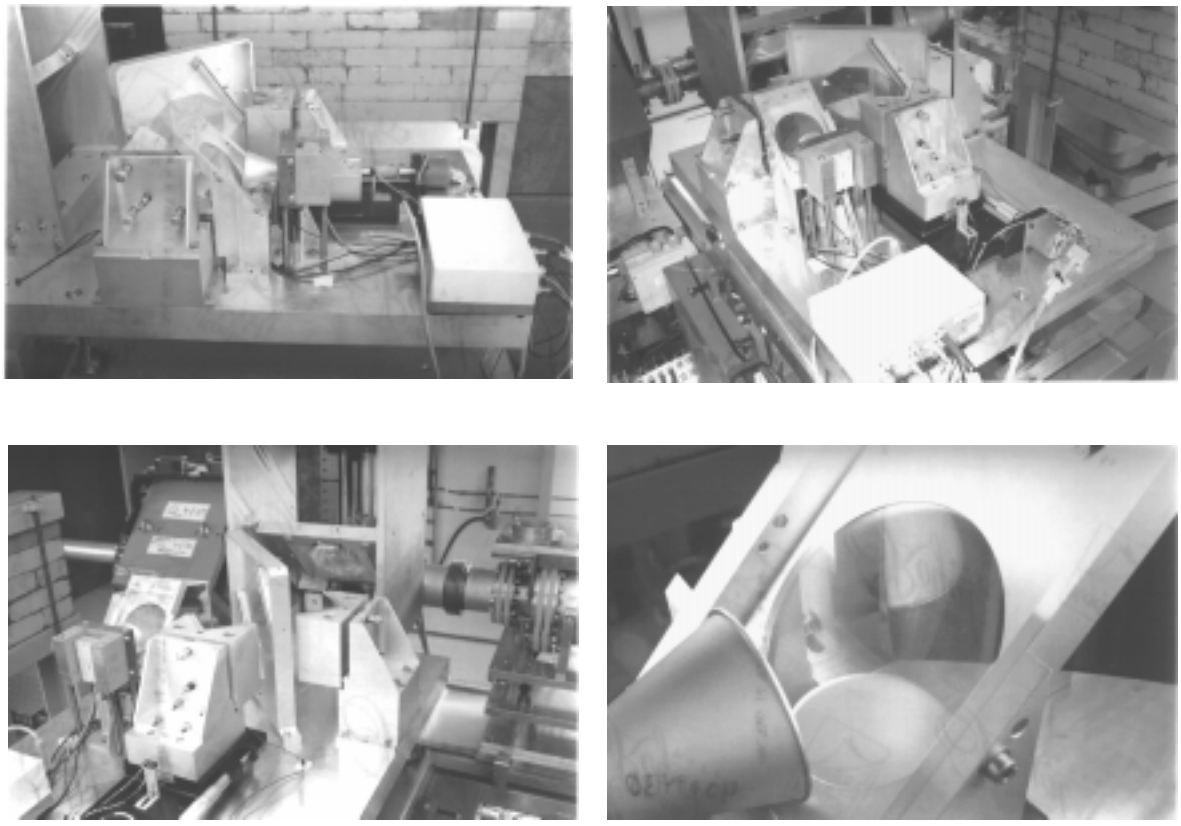


Figure 7.2: Different views on the TTF Martin-Puplett interferometer. The radiation is collected by a parabolic mirror located in front of the vacuum window, and reflected into the interferometer by the polarizing wire grid. The beam splitter transmits / reflects radiation into both interferometer arms and sends the recombined beam towards the second parabolic mirror. The radiation pulse is passing the smaller aperture analyzing grid and is focused onto two pyroelectric detectors equipped with horn antennas.

produced during the 800 μs long macropulse.

Assembly of the Interferometer

The first parabolic mirror of the interferometer is placed in front of the vacuum window. The height of the paraboloid is fixed by the height of the transition radiation screen and the vacuum window. The transverse position of the mirror is fixed by the condition that the transition radiation target has to be in the focal plane of the paraboloid. The mirror produces a parallel wavefront radiation beam which is reflected vertically up towards the polarizing wire grid. The grid reflects the radiation horizontally into the interferometer. The radiation is horizontally polarized because of the wire orientation. The beam divider grid is reflecting and transmitting polarization components parallel and orthogonal to the wire orientation towards the roof mirrors. The beam divider grid is oriented at an angle of 54.73° with respect to the vertical to obtain an "apparent" angle of 45° of the dividing grid (see Figure 7.6)[1]. The position of one roof mirror is fixed while the other

[1]Notice that: $\tan(\angle \mathrm{BAC}) = \tan\beta / \cos\alpha$.

Material	$LiTaO_3$
Critical temperature	610°C
Temperature stability	0.2%/°C
Crystal thickness	100 μm
Crystal diameter	5 mm
Capacity	75 pF
Voltage Supply	±15 V
max. DC current	6 mA
max. output power	50 mW

Table 7.1: Specification of the pyroelectric detector PI-45 [51]

is mounted on an optical mover equipped with a remotely controllable stepping motor. The recombined radiation from both arms is focused onto the pyroelectric detectors by a second parabolic mirror. The analyzing grid which is located between the mirror and the detectors, transmits the radiation polarized orthogonal to the wires to detector #1 and reflects the radiation polarized parallel to the wires to detector #2. The pyroelectric crystals are located in the focal plane of the parabolic mirror.

Compared to a Michelson, the Martin-Puplett interferometer is a polarizing interferometer and has the advantage of two radiation output ports. The ratio of the difference and the sum of the two detector signals yields an interference pattern which is less sensitive to beam intensity fluctuations than the individual detector signals [52].

7.2 Working Principle of the Interferometer

The incoming radiation pulse is polarized horizontally by the first wire grid (polarizer) and split by the beam divider to both interferometer arms. The beam divider grid is oriented at an apparent angle of 45° with respect to the polarizer to deliver equal field amplitudes to both arms. The orientation of the polarization is flipped by two roof mirrors so that the radiation pulse transmitted first, is now reflected by the beam divider and vice versa. Generally, the linear polarization in front of the beam divider is transformed into elliptical polarization after the recombination, depending on the position of the movable roof mirror. The analyzing grid transmits one principal axis of the elliptical polarization into the pyroelectric detector #1 while the other is reflected into the pyroelectric detector #2. Hence the two detectors measure anti-correlated signals when the roof mirror is moved. The sum signal measures the total radiation power passing the interferometer.

The amplitude and the state of polarization of the millimeter wavelength radiation beam can be described by a complex two-dimensional vector, each of the components representing the field amplitude along the axis perpendicular to the direction of propagation. An optical device can therefore be represented by a 2×2 transfer matrix S relating the input and output of the field amplitude and polarization state [29]. We choose a coordinate

system where the x and y axis are oriented parallel and orthogonal to the wires of the polarizing grid respectively. The optical elements of the Martin-Puplett interferometer can be represented by the following transfer matrices.

Polarizing grid The polarizing grid polarizes the millimeter wavelength radiation. With p_1 and p_2 denoting the spectral reflectivity of the horizontal and vertical polarization state, we obtain the transfer matrix

$$P = \begin{pmatrix} p_1 & 0 \\ 0 & p_2 \end{pmatrix} \tag{7.1}$$

The coordinate system is chosen to be aligned with the principal axes of the polarizing grid.

Analyzing grid The analyzing grid is oriented at an angle of $\chi = -90°$ with respect to the polarizing grid, hence

$$A = \begin{pmatrix} 0 & 1 \\ -1 & 0 \end{pmatrix} \cdot \begin{pmatrix} a_1 & 0 \\ 0 & a_2 \end{pmatrix} \cdot \begin{pmatrix} 0 & -1 \\ 1 & 0 \end{pmatrix} = \begin{pmatrix} a_2 & 0 \\ 0 & a_1 \end{pmatrix} \tag{7.2}$$

where

$$\begin{pmatrix} \cos\chi & \sin\chi \\ -\sin\chi & \cos\chi \end{pmatrix} = \begin{pmatrix} 0 & -1 \\ 1 & 0 \end{pmatrix} \tag{7.3}$$

has been used. The coefficients a_1 and a_2 denote either the reflectivity or the transmission of the analyzing grid, depending on which detector is used.

Beam Splitter and Roof Mirrors: The transfer matrix of the beam splitter and roof mirrors is evaluated in a coordinate system where the ξ axis is oriented parallel to the wires of the beam splitter and the η axis orthogonal to the wires. In a second step, the transfer matrices are rotated by 45° to transform $\vec{e}_\xi$ and $\vec{e}_\eta$ to $\vec{e}_x$ and $\vec{e}_y$.

The radiation incident on the beam splitter is transfered to either arm of the interferometer according to the grid's spectral reflectivity ρ_ξ and ρ_η and spectral transmission τ_ξ and τ_η for the horizontal (ξ) and vertical (η) field component. An incident polarization state of $1/\sqrt{2}(\vec{e}_\xi + \vec{e}_\eta)$ yields the reflected field component $1/\sqrt{2}\,(\rho_\xi\vec{e}_\xi + \rho_\eta\vec{e}_\eta)$ or the transmitted field component $1/\sqrt{2}\,(\tau_\xi\vec{e}_\xi + \tau_\eta\vec{e}_\eta)$.

The transfer matrix of the roof mirror (horizontal deflection) is

$$R = \begin{pmatrix} -1 & 0 \\ 0 & 1 \end{pmatrix} \tag{7.4}$$

as can be seen from Fig. 7.3. The matrix R has to be rotated by 45° because of the orientation of the roof mirror in the (ξ,η) coordinate system. We obtain

$$\tilde{R} = \begin{pmatrix} \frac{\sqrt{2}}{2} & \frac{\sqrt{2}}{2} \\ -\frac{\sqrt{2}}{2} & \frac{\sqrt{2}}{2} \end{pmatrix} \cdot \begin{pmatrix} -1 & 0 \\ 0 & 1 \end{pmatrix} \cdot \begin{pmatrix} \frac{\sqrt{2}}{2} & -\frac{\sqrt{2}}{2} \\ \frac{\sqrt{2}}{2} & \frac{\sqrt{2}}{2} \end{pmatrix} = \begin{pmatrix} 0 & 1 \\ 1 & 0 \end{pmatrix} \tag{7.5}$$

After the reflection by the roof mirrors, the radiation pulses have the polarization states $1/\sqrt{2}\,(\rho_\xi \exp i\delta\vec{e}_\eta + \rho_\eta \exp i\delta\vec{e}_\xi)$ (reflected by the beam splitter) and $1/\sqrt{2}\,(\tau_\xi\vec{e}_\eta + \tau_\eta\vec{e}_\xi)$

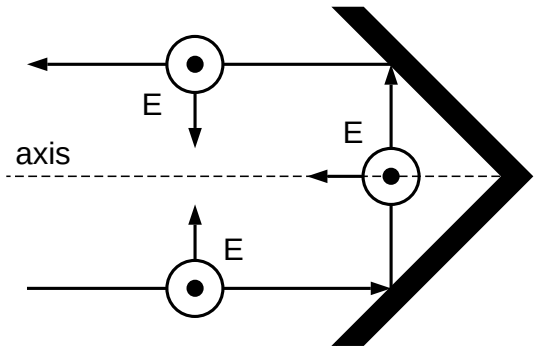


Figure 7.3: Polarization components during reflection at a vertical roof mirror. The incident light is polarized under 45° with respect to the roof mirror axis. The electric field component parallel to the orientation of the roof mirror ($E_{\parallel}$) is invariant, the orthogonal component ($E_{\perp}$) is inverted.

(transmitted by the beam splitter) respectively. δ denotes the path difference of both interferometer arms.

The beamlets are recombined after passing the beam splitter a second time yielding the state vector $1/\sqrt{2}\,((\tau_\xi\rho_\eta \exp i\delta + \tau_\eta\rho_\xi)\vec{e}_\eta + (\tau_\eta\rho_\xi \exp i\delta + \tau_\xi\rho_\eta)\vec{e}_\xi)$. The transfer matrix of the entire beam splitter and roof mirror complex therefore yields

$$\tilde{B} = \begin{pmatrix} 0 & \tau_\xi\rho_\eta \exp i\delta + \tau_\eta\rho_\xi \\ \tau_\eta\rho_\xi \exp i\delta + \tau_\xi\rho_\eta & 0 \end{pmatrix} = \begin{pmatrix} 0 & E \\ D & 0 \end{pmatrix} \tag{7.6}$$

The matrix $\tilde{B}$ has to be rotated by 45° to transform $\vec{e}_\xi$ and $\vec{e}_\eta$ to $\vec{e}_x$ and $\vec{e}_y$. Hence

$$B = \frac{1}{2}\begin{pmatrix} 1 & -1 \\ 1 & 1 \end{pmatrix} \cdot \begin{pmatrix} 0 & D \\ E & 0 \end{pmatrix} \cdot \begin{pmatrix} 1 & 1 \\ -1 & 1 \end{pmatrix} = \frac{1}{2}\begin{pmatrix} -(D+E) & D-E \\ -(D-E) & D+E \end{pmatrix} \tag{7.7}$$

Notice that a perfect beam splitter yields $\rho_\xi = 1$, $\rho_\eta = 0$, $\tau_\xi = 0$, $\tau_\eta = 1$, $\delta = 0$, hence

$$B = \begin{pmatrix} -1 & 0 \\ 0 & 1 \end{pmatrix} \tag{7.8}$$

Incident horizontally polarized radiation will therefore remain horizontally polarized (since $\delta = 0$), but acquires a phase shift of π. As stated above, elliptical polarization will be obtained for $\delta \neq 0$. The optical transfer matrix of the entire interferometer is given by $S = A \cdot B \cdot P$.

Intensity at the Detector The detector is not sensitive to the polarization state of the incident radiation. Initially horizontally and vertically polarized radiation yield the radiation intensity $|S_{11}|^2 + |S_{21}|^2$ and $|S_{12}|^2 + |S_{22}|^2$ respectively. The normalized response function can therefore be expressed as

$$\mathcal{R} = \frac{1}{2}\sum_{i,j} |S_{ij}|^2 = \frac{1}{2}\mathrm{Tr}\left(S^+ S\right) . \tag{7.9}$$

where the S_{ij} denote the elements of the optical transfer matrix. For $S = A \cdot B \cdot P$ we obtain

$$\mathcal{R} = \frac{1}{2}\mathrm{Tr}\left((ABP)^{+}(ABP)\right) = \frac{1}{2}\mathrm{Tr}\left(P^{+}B^{+}A^{+}ABP\right) = \frac{1}{2}\mathrm{Tr}\left(PP^{+}B^{+}A^{+}AB\right) \quad (7.10)$$

yielding

$$\mathcal{R} = \frac{1}{8}\left\{(D^{*}+E^{*})(D+E)\left(p_1^2a_1^2+p_2^2a_2^2\right)+(E^{*}-D^{*})(E-D)\left(p_1^2a_2^2-p_2^2a_1^2\right)\right\} \quad (7.11)$$

where D and E are defined by Eq. (7.6). The expansion of $\mathcal{R}$ into $\mathcal{R} = R_0 + Q\exp(i\delta) + Q^{*}\exp(-i\delta)$ yields a term $Q\exp(i\delta)$ varying with the phase difference δ imposed by the movement of the roof mirror and a dc offset R_0. The signal enhancement factor of the interferometer is defined by Q/R_0. The expansion yields

$$R_0 = \frac{1}{4}\left\{\left(p_1^2a_2^2+p_2^2a_1^2\right)(\rho_\xi\tau_\eta+\rho_\eta\tau_\xi)^2+\left(p_1^2a_1^2+p_2^2a_2^2\right)(\rho_\xi\tau_\eta-\rho_\eta\tau_\xi)^2\right\} \quad (7.12)$$

$$Q = \frac{1}{8}\left\{\left(p_1^2a_2^2+p_2^2a_1^2\right)(\rho_\xi\tau_\eta+\rho_\eta\tau_\xi)^2-\left(p_1^2a_1^2+p_2^2a_2^2\right)(\rho_\xi\tau_\eta-\rho_\eta\tau_\xi)^2\right\} \quad (7.13)$$

and $Q^{*} = Q$ [53]. The optimum performance of the interferometer is obtained by using ideal wire grids, hence setting $p_1 = a_1 = 1$, $p_2 = a_2 = 0$, $\rho_\xi = \tau_\eta = 1$ and $\rho_\eta = \tau_\xi = 0$, yielding $Q = Q^{*} = -1/8$ and $R_0 = 1/4$, hence

$$\mathcal{R} = \frac{1}{8}\left(2-\exp(i\delta)-\exp(-i\delta)\right) = \frac{1}{4}\left(1-\cos\delta\right) . \quad (7.14)$$

a_1 and a_2 can either denote the reflectivity or the transmission of the analyzing grid. Let a_1 and a_2 in Eq. (7.14) denote the reflectivity, then $\mathcal{R}$ describes the detector response of the reflected radiation (pyro #2). The detector response caused by the transmitted radiation (pyro #1) can be described by choosing $a_1 = 0$ and $a_2 = 1$ yielding

$$\mathcal{R} = \frac{1}{8}\left(2+\exp(i\delta)+\exp(-i\delta)\right) = \frac{1}{4}\left(1+\cos\delta\right) . \quad (7.15)$$

The recorded reflected and transmitted radiation intensity $\mathcal{R}$ will be anti-correlated. For example, for $\delta = 0$, the entire radiation power is transmitted and only one detector records a signal. As the mirror moves, the reflected radiation intensity increases, while the transmitted intensity decreases and so forth. This feature has been utilized in the present interferometer design by the installation of two detectors recording the reflected and the transmitted electric field component of the analyzing grid (installed at an angle of 45°). The total radiation power reaching the analyzing grid is recorded by the sum of the two signals. The ratio of the difference and the sum of the two detector signals yields an interference pattern which is insensitive to beam instabilities.

7.3 Frequency-dependent Acceptance Function

7.3.1 Spectral Transmission and Reflectivity of Wire Grids

A theoretical description of the scattering of electromagnetic waves by a regular grid of parallel cylindrical wires with circular cross-section and an experimental confirmation of

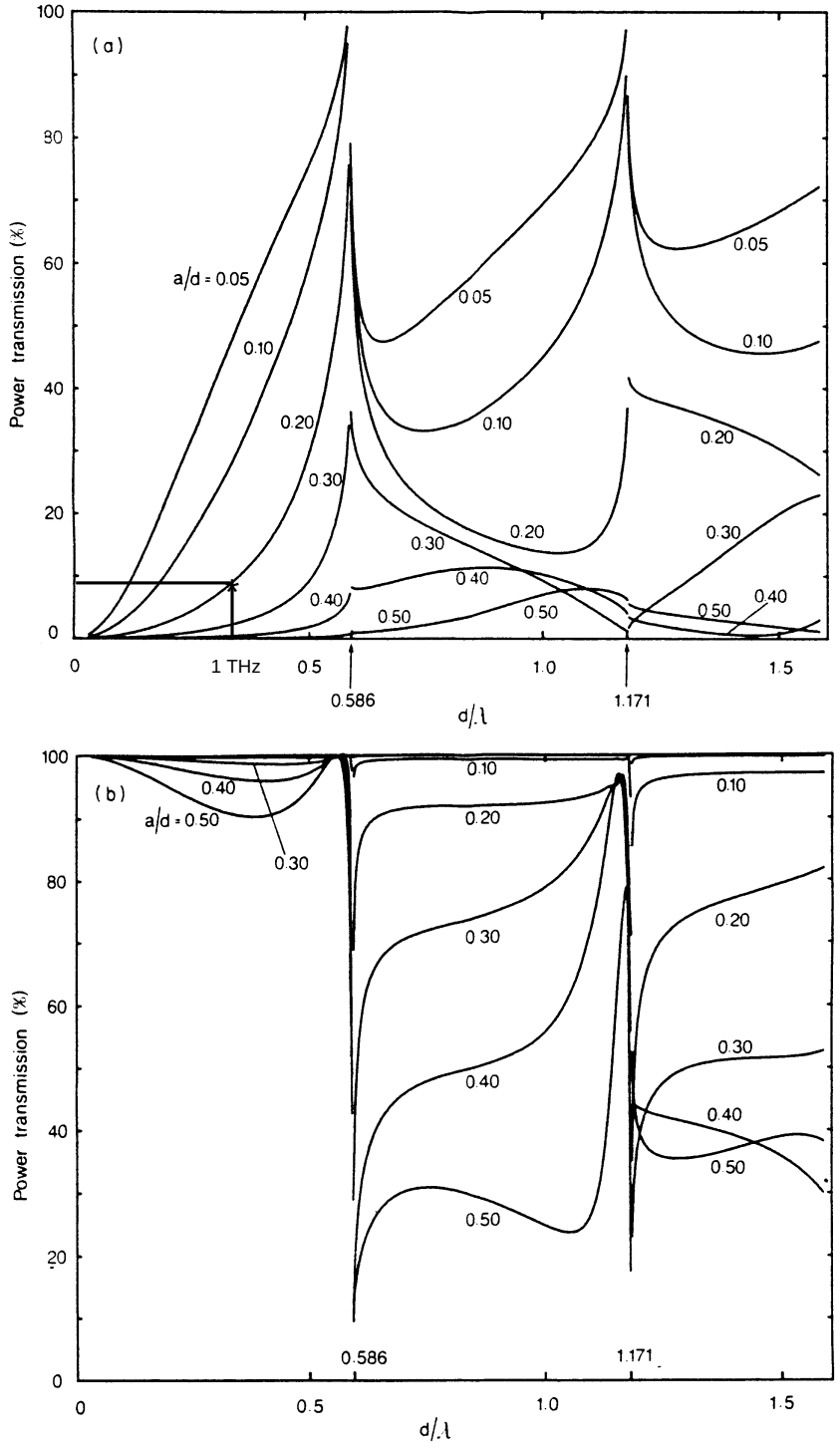


Figure 7.4: Computed power transmission of a wire grid as a function of d/λ (ratio of wire spacing and the radiation wavelength). The curves denote different ratios of wire diameter and wire spacing. Upper graph: polarization of the electric field vector parallel to the wire grid. Lower graph: polarization of the electric field vector perpendicular to the wire grid [54]. The star marks the curve predicted for the interferometer grids.

the theory is well-established in literature [55, 56, 57]. Figure 7.4 shows the power transmission of a wire grid versus the quotient of the wire spacing and the radiation wavelength d/λ. The resistance of the gold plated tungsten wire is $\rho = 5.5 \cdot 10^{-9}\,\Omega$m. The radiation is approaching the grid under at incidence angle of 45°. The upper and the lower graph show the power transmission of the polarization components parallel and perpendicular to the orientation of the wires.

The wire grid acts as an ideal polarizer ($\tau_{\parallel} = 0$ and $\tau_{\perp} = 1$) only in the limiting case of $\lambda \to \infty$. At shorter wavelength the transmission of the "forbidden" polarization component is increasing while the transmission of the "permitted" component is slightly decreasing. At a critical wavelength $\lambda_c = 0.59d$ the grid becomes transparent to incident radiation of both polarization states. The same applies for $\lambda = \lambda_c/n$, where $n = 1, 2, 3, \ldots$. The factor 0.59 is caused by the orientation of the wires and is derived in the next section. Wire grid serve as a proper polarizers, beam dividers and analyzers only for wavelengths significantly longer than λ_c. Unwanted diffraction patterns will occur at shorter wavelengths. The critical wavelength for 100 μm wire spacing is $\lambda_c = 170\,\mu$m (corresponding to $f_c = 1.76$ THz), which is beyond the range covered in the experiments.

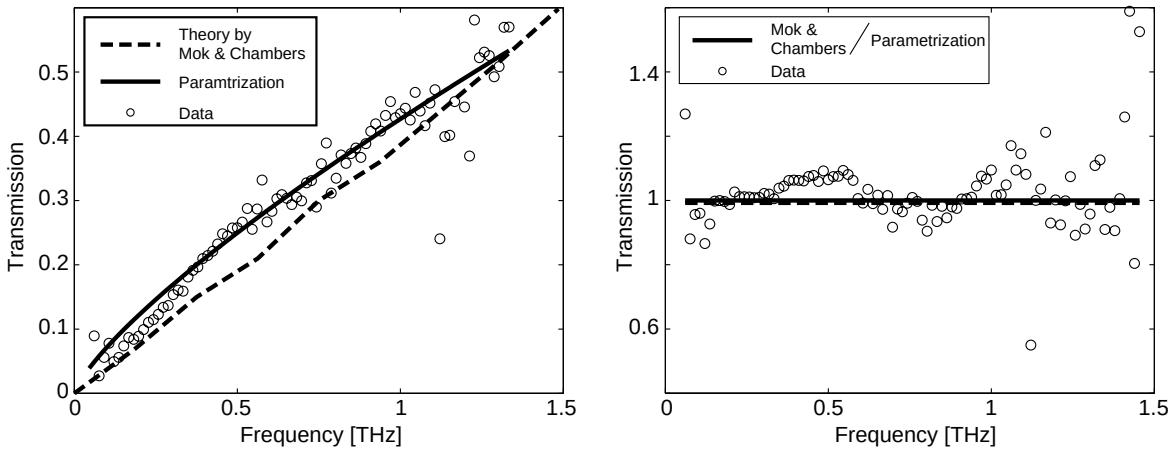


Figure 7.5: Transmission of the wire grids used for the Martin-Puplett interferometer as a function of radiation frequency. Left: transmission of the polarization component parallel to the wires. Right: transmission of the polarization component orthogonal to the wires. Data obtained by THz spectroscopy are indicated as circles. The dashed curve denotes the prediction of [55]. The solid curve is the parameterization used to describe the spectral transmission of the wire grids.

Transmission Measurement of the Wire Grids The spectral transmission of the wire grids has been measured [58] by I. Wilke and M. Khazan using time-domain THz spectroscopy[2]. Figure 7.5 shows the measured amplitude transmission of the wire grids used in the Martin-Puplett interferometer. The left graph shows the spectral transmission of the polarization component parallel to the wires, the right graph shows the transmission

[2]I thank Dr. Ingrid Wilke and Mr. Maxim Khazan for performing spectral transmission measurements using time-domain Fourier-transform spectroscopy.

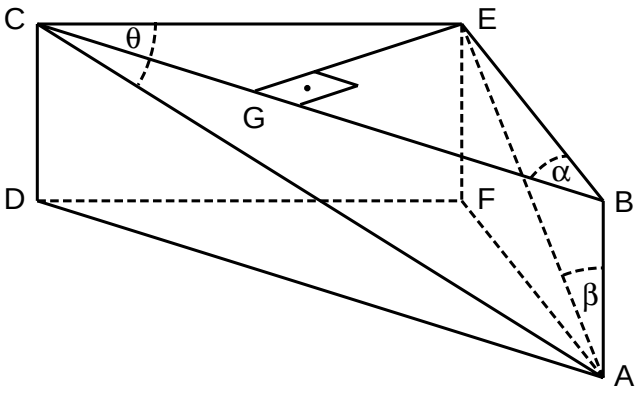


Figure 7.6: Beam divider geometry.

of the orthogonal polarization component. There is good agreement between the measurement and the theoretical prediction by [55] (dashed line). The solid line indicates an exponential parameterization of the data and is used to describe the spectral transmission of the wire grids.

7.3.2 Spectral Acceptance of the Wire Grid Beam Divider

The spectral acceptance of a wire grid depends not only on the wire parameters (diameter, wire spacing, wire material), but also on the orientation of the wire grid relative to the incident radiation. Figure 7.6 shows the geometry of the beam divider grid. The wire grid is located in the ABCD plane with the wires oriented along AC. The radiation is incident along CE. The plane ABEF represents the projected plane of the wire grid perpendicular to the propagation of the electromagnetic radiation. The projected wire orientation is along AE.

The following coordinate system is introduced: the z-axis points along the direction of the wires along AC, the x-axis is oriented perpendicular to the wires in the plane of the grid ABCD. The y-axis is oriented perpendicular to the plane of the grid, along GE. In polar coordinates, the unit vector $\vec{e}$ is defined as

$$\vec{e} = (\sin\theta\cos\phi, \sin\theta\sin\phi, \cos\theta) \tag{7.16}$$

where θ is the angle $\angle$ ACE in Fig. 7.6. ϕ is oriented in the x, y plane.

An incident electromagnetic wave with momentum $\vec{k}$ and magnitude $|k| = \omega/c$ has a momentum component perpendicular to the orientation of the wire grid (in the x,y plane), which is $\kappa = |\vec{e}\cdot\vec{k}| = |k|\sin\theta$. κ is called the effective wave number of the radiation interacting with the grid. The wire grid is operated in zeroth diffraction order, for wave numbers smaller than $|k|_0 = 2\pi/d$ (normal incidence). For arbitrary incidence, the Bragg diffraction condition is $(k_x + 2\pi n/d)^2 = \kappa^2$, where n denotes an integer. Using $k_x = \kappa\cos\phi$, the lowest critical wave number is given by

$$|k|_c = \frac{|k|_0}{\sin\theta\,(1+\cos\phi)}\,. \tag{7.17}$$

Equation (7.17) can be more conveniently expressed by the angle $\alpha = \angle$ CBE, denoting half of the reflection angle of the wire grid, and $\beta = \angle$ BAE, denoting the apparent angle of the wire grid in the projection plane with respect to the vertical. The colatitude θ can be expressed in terms of α and β by

$$\sin\theta = \frac{\mathrm{AE}}{\mathrm{AC}} = \frac{\mathrm{AE}}{\sqrt{\mathrm{CD}^2 + \mathrm{AD}^2}} = \frac{\mathrm{AE}}{\sqrt{\mathrm{AB}^2 + \mathrm{BC}^2}} = \frac{1}{\sqrt{\cos^2\beta + \frac{\sin^2\beta}{\cos^2\alpha}}} \tag{7.18}$$

where $\mathrm{BC}^2/\mathrm{AE}^2 = (\mathrm{BC}^2\mathrm{BE}^2)/(\mathrm{BE}^2\mathrm{AE}^2) = \sin^2\beta/\cos^2\alpha$ has been used. We obtain finally

$$\sin\theta = \frac{\cos\alpha}{\sqrt{1 - \sin^2\alpha\cos^2\beta}}\,. \tag{7.19}$$

The azimuthal angle ϕ can be found by equating the y component of the unit vector Eq. (7.16, $\sin\theta\sin\phi$, with

$$\sin(\pi - \alpha) = \frac{\mathrm{EG}}{\mathrm{CE}} = \cos\alpha \tag{7.20}$$

(see Fig. 7.6), hence

$$\cos\phi = \sin\alpha\cos\beta\,. \tag{7.21}$$

Equation (7.19) and (7.21) introduced into Eq. (7.17) yields for the lowest critical wave number

$$\frac{|k|_c}{|k|_0} = \frac{1}{\cos\alpha}\sqrt{\frac{1 - \sin\alpha\cos\beta}{1 + \sin\alpha\cos\beta}}\,. \tag{7.22}$$

The quotient $\frac{|k|_c}{|k|_0}$ yields for $\alpha = 45°$ (90° deflection at the wire grid): $\frac{|k|_c}{|k|_0} = 0.59$ for $\beta = 0°$, $\frac{|k|_c}{|k|_0} = 0.82$ for $\beta = 45°$ and $\frac{|k|_c}{|k|_0} = 1.41$ for $\beta = 90°$.

Equation (7.22) describes the variation of the critical wavenumber for non-perpendicular incidence on a wire grid. Fig. 7.4 shows the transmitted radiation power at a wire grid where $\alpha = 45°$ and $\beta = 0°$. Notice that the critical wave number, hence the performance of the grid, can be improved by a factor of 2.4, if β is changed to 90°. The abscissa of Fig. 7.4 will be scaled by 2.4 while the characteristic of the data is invariant. The optimum spectral acceptance of the beam divider can be achieved for $\beta = 90°$. More generally stated, the orientation of the beam divider wires should be as parallel as possible to the reflection direction. To optimize the present interferometer assembly, the beam divider should be oriented horizontally. As a direct consequence, the roof mirrors, the polarizing and the analyzing grid then have to rotated by 45°.

Figure 7.7 shows the quantity Q (Eq. (7.13)) of the beam divider–roof mirror configuration of the Martin-Puplett interferometer as a function of the radiation frequency. The spectral transmission and reflectivity functions ρ_ξ, ρ_η, τ_ξ and τ_η (see Fig. 7.4) are inserted into Eq. (7.13). The polarizing and analyzing grids are assumed to be ideal. The beam divider angles are $\alpha = 45°$ and $\beta = 45°$.

The spectral acceptance of the beam divider–roof mirror configuration decreases gradually from $Q = 1.0$ to $Q = 0.8$ for frequencies up to 1 THz ($a/d = 0.2$) which is the frequency range covered by the experiments. The acceptance is decreasing linearly at larger frequencies. Ideally, a ratio $a/d = 0.3$ yields a flat response up to 1.2 THz.

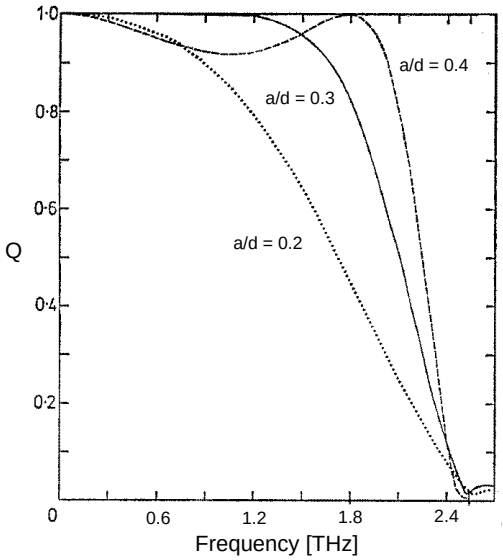


Figure 7.7: The factor Q (Eq. (7.13)) of the beam divider - roof mirror configuration [55]. The curves correspond to different quotients of wire diameter a and wire spacing d.

7.3.3 Diffraction in the Interferometer

Diffraction phenomena of freely propagating electromagnetic fields can be described in the slowly varying envelope (SVE) approximation [59]. The time dependent wave equation

$$-\frac{1}{c^2}\frac{\partial^2 \vec{E}}{\partial t^2} + \nabla^2 \vec{E} = 0\,. \tag{7.23}$$

can be solved by the general ansatz for an electromagnetic wave traveling in z direction

$$E(r,z,t) = E_0(r,z)\exp(-i\,(kz - \omega t))\,. \tag{7.24}$$

We obtain in cylindrical coordinates

$$\frac{\partial^2 E_0(r,z)}{\partial r^2} + \frac{1}{r}\frac{\partial E_0(r,z)}{\partial r} + \frac{\partial}{\partial z}\left\{\frac{\partial E_0(r,z)}{\partial z} - ikE_0(r,z)\right\} - ik\frac{\partial E_0(r,z)}{\partial z} = 0\,. \tag{7.25}$$

The SVE approximation implies that the variation of the field amplitude E_0 within a wavelength is small compared to the field amplitude, hence $\partial E_0/\partial z \ll kE_0$. The equation then yields

$$\frac{\partial E_0(r,z)}{\partial r^2} + \frac{1}{r}\frac{\partial E_0(r,z)}{\partial r} - 2ik\frac{\partial E_0(r,z)}{\partial z} = 0\,. \tag{7.26}$$

Equation (7.26) is suitable to describe diffraction phenomena as the decrease of the field amplitude along the direction of propagation z is coupled to an increase of the radial boundary of the field distribution.

Equation (7.26 is solved by

$$\frac{E_p(r,\phi,z)}{E_0} = L_p^0\left(\frac{2r^2}{w^2}\right)\frac{w_0}{w}\exp\left(-\left(\frac{r}{w}\right)^2\right)\exp(i(\omega t - \Phi_L - \Phi_T)) \tag{7.27}$$

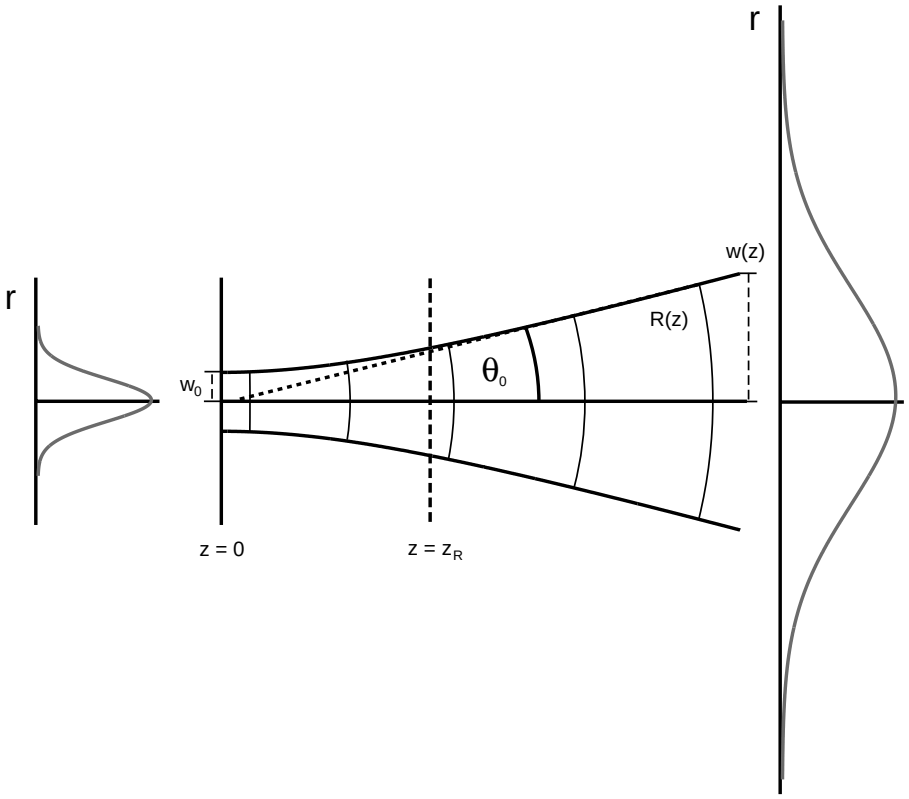


Figure 7.8: Field intensity distribution of the $I_0(r,z)$-mode of waist w_0 and Rayleigh length z_0. $R(z)$ denotes the radius of the surfaces of constant phase, θ_0 denotes the far-field divergence angle.

where

$$\Phi_T = \frac{kr^2}{2R}\,, \quad \Phi_L = kz - (2p+1)\arctan\left(\frac{z}{z_0}\right). \tag{7.28}$$

$L_p^0(r)$ denotes the Laguerre polynomials of order p. The azimuthal order is set to zero to describe the radial symmetry of transition radiation. p indicates the number of zeros in the radial field distribution. A Gaussian field distribution ("Gaussian beam") is the solution for $p = 0$.

The angular distribution of transition radiation can in principle be expressed by a superposition of the $E_p(r,\phi,z)$, $p = 0,1,2,\ldots$. For the discussion of diffraction effects in the Martin-Puplett interferometer it is sufficient to consider a Gaussian field distribution ($p = 0$) of appropriate dimension because diffraction affects the field amplitudes at large radii only. The intensity distribution of a Gaussian field distribution $I_0(r,z) = E_0^* E_0$ is shown in Fig. 7.8. The shape of the radial field amplitude distribution is invariant while the field propagates along the z-axis. Starting from $z = 0$, the beam size increases as

$$w = w_0\sqrt{1 + \left(\frac{z}{z_0}\right)^2} \tag{7.29}$$

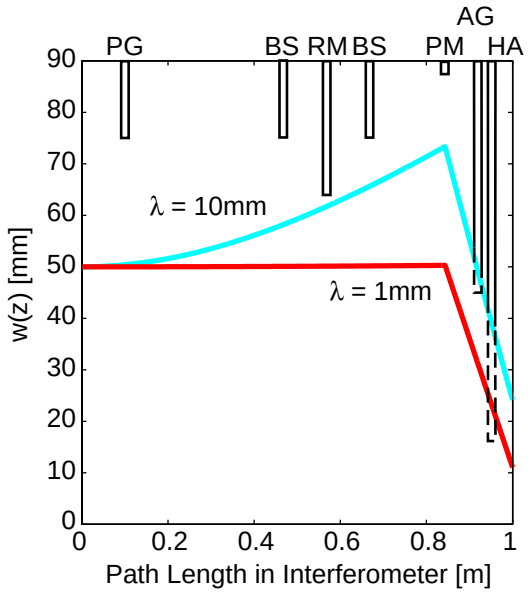


Figure 7.9: The diffracted electromagnetic field envelope in the Martin-Puplett interferometer. The aperture radius of the following optical elements is shown. PG: Polarizing Grid, BS: Beam Splitter, RM: Roof Mirror, PM: Parabolic Mirror, AG: Analyzing Grid, HA: Horn Antenna. The field envelope is drawn for $\lambda = 1\,\mathrm{cm}$ and $\lambda = 1\,\mathrm{mm}$.

where $w_0 = 2\sigma$ denotes the waist dimension of the light beam and

$$z_0 = \frac{\pi w_0^2}{\lambda} \tag{7.30}$$

is called the Rayleigh-length. The divergence angle θ_0 is

$$\theta = \frac{\lambda}{\pi w_0}\,. \tag{7.31}$$

The beam size $w(z)$ at a given axial position z is, by convention, defined as $E_{0,0}(w) := E_0/e$ or $I_{0,0}(w) := I_0/e^2$ respectively. The transverse phase factor Φ_T describes the wave front of the propagating light wave. The bending radius of these surfaces of constant phase is

$$R(z) = z\left(1 + \left(\frac{z_0}{z}\right)^2\right) \tag{7.32}$$

yielding $R \to \infty$ for $z \to 0$ (plane waves at the waist), $R = 2z_0$ for $z = z_0$ (maximum bending) and $R \to z$ for $z \to \infty$ (spherical waves with origin at $z = 0$). The longitudinal phase term Φ_L indicates the phase of the field distribution along the direction of propagation.

Propagation through an optical system A complex beam parameter

$$q = z + iz_0 \quad \text{or} \quad \frac{1}{q} = \frac{1}{R} - i\frac{\lambda}{\pi w^2} \tag{7.33}$$

is introduced to transform the field amplitude along the optical beam line. Transfer matrices

$$L_d = \begin{pmatrix} 1 & d \\ 0 & 1 \end{pmatrix} \text{ (drift d)} \quad \text{or} \quad L_f = \begin{pmatrix} 1 & 0 \\ -\frac{1}{f} & 1 \end{pmatrix} \text{ (thin lens, focal length } f) \tag{7.34}$$

describe the beam transfer [29] and can be used to transform the complex beam parameter q [59] according to

$$q_f = \frac{L_{11} q_i + L_{12}}{L_{21} q_i + L_{22}} \,. \tag{7.35}$$

Diffraction Figure 7.9 shows the envelope of the electromagnetic fields traveling through the Martin-Puplett interferometer. The envelope covers the first parabolic mirror ($z = 0$) entirely (see chapter 3), so that w_0 is equal to the effective mirror radius. The optical transfer matrix L of the Martin-Puplett interferometer consists of a drift, a parabolic mirror with 200 mm focal length, a drift of 1200 mm including the passage through the polarizer, beam splitter, roof mirrors, a second parabolic mirror with 200 mm focal length and the final drift of 110 mm through the analyzing grid to the detector. The transition radiator is in the focal plane of the first parabolic mirror, hence the initial complex beam parameter is $q_0 = \pi w_0/(-i\lambda)$ (the slope of the light envelope after the first parabolic mirror vanishes). The aperture of the optical elements is sufficiently large that the evaluated light beam envelope passes the elements without losses. However, a limiting effect occurs at the horn antenna of the detector. The detector dimension (see appendix F) therefore limits the spectral acceptance of the interferometer. The acceptance becomes wavelength dependent only for $\lambda > 2\,\text{mm}$ as is indicated for the $\lambda = 10\,\text{mm}$ envelope.

7.3.4 Detector Acceptance

The detection of far-infrared radiation is based on energy absorption by the pyroelectric crystal leading to a heating which is accompanied by the creation of surface charges. The spectral dependence of the detection process is influenced by the dimension (5 mm diameter and 100 μm thickness) and the permittivity of the pyroelectric crystal. The crystal diameter causes a long-wavelength cut-off because diffraction effects reduce the coupling of electromagnetic fields whose wavelength exceeds the detector diameter. The thickness and the permittivity of the crystal lead to an interference effect at the front and the back surface of the crystal. The interference effect was discovered in the course of the measurements and not known before. The effect was investigated also by other groups [34, 60] and improved the understanding of the measured coherent power spectra. In the following we let t be the amplitude transmission of electromagnetic fields entering the crystal and r be the amplitude reflection at the back and the front surface. E_0 denotes the incident electric field amplitude, then the final electric field amplitude inside the detector is

$$E_{in} = \{E_0 t \exp(i\omega t) + E_0 t r \exp(-i\omega t)\exp(-i\delta)\} \sum_{n=0}^{\infty} \left(r^2 \exp(-2i\delta)\right)^2 \tag{7.36}$$

$$= E_0 t \left\{\exp(i\omega t) + r \exp(-i\omega t)\exp(-i\delta)\right\} \frac{1}{1 - r^2 \exp(-2i\delta)} \tag{7.37}$$

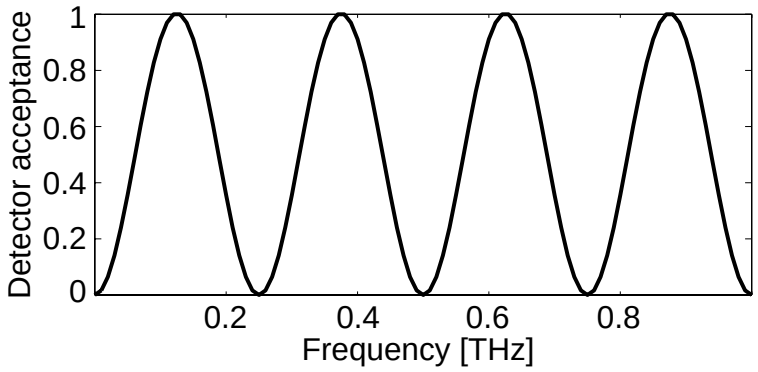


Figure 7.10: The acceptance function of the pyroelectric detector is dominated by an interference effect at the front and the back face of the crystal. Minima of the acceptance function repeat every 250 GHz.

where $\delta = 2\pi nd/\lambda$ is the phase of a reflected beamlet with respect to the incident wave E_0. n denotes the refractive index of the crystal. The detected intensity $I_{in} = E_{in}(E_{in})^*$ is

$$I_{in} = \frac{E_0^2 t^2 \left(1 + r^2\right)}{1 + r^4 - 2r^2 \cos 2\delta} \tag{7.38}$$

Figure 7.10 shows the expected detector response I_{in}/I_0 as a function of radiation frequency. The interference effect yields an oscillatory acceptance function. Minima and maxima of the acceptance function repeat every 250 GHz which is determined by the optical path length of $nd = 600\ \mu$m.

Calibration Measurement of the Detector Acceptance The pyroelectric detector acceptance is shown in Fig. 7.11. The data originate from a calibration measurement[3] [61] performed with output power calibrated GaAs Read-type IMPATT diodes. The detector acceptance has been measured at 10 dedicated frequencies (see appendix F). The result is a slight increase of the acceptance between 72 and 128 GHz, a maximum at 156 GHz and a decrease toward larger frequencies. The increase below 156 GHz is explainable by the reduced radiation coupling due to the detector diameter, the decrease towards larger frequencies by the interference effect. The oscillatory characteristic of the latter effect is shown as solid curve, representing the optimum fit of Eq. (7.38) to the data. Only four data points ($f > 150$ GHz) of the calibration measurement are available to perform the adjustment. Besides, the coherent power spectra measured with the shortest bunches at the TTF linac have been investigated to determine the frequency interval between the maxima and the minima of the acceptance function. The rapid decrease of the detector acceptance at low radiation frequencies is described by a vertical line at $f = 135$ GHz in Fig. 7.11 followed by smooth interpolation of the data towards smaller frequencies. The gray curve is finally used to model the acceptance of the pyroelectric detectors. The quality of the calibration data is not yet satisfactory and it is advisable to repeat the calibration for an increased frequency range. For the time being, the uncertainty of

[3] thanks to Dr. Jürgen Freyer, Lehrstuhl für Allgemeine und Angewandte Elektronik, TU München, for the use of the millimeter-wave radiation sources to perform the calibration measurement of the pyroelectric detectors.

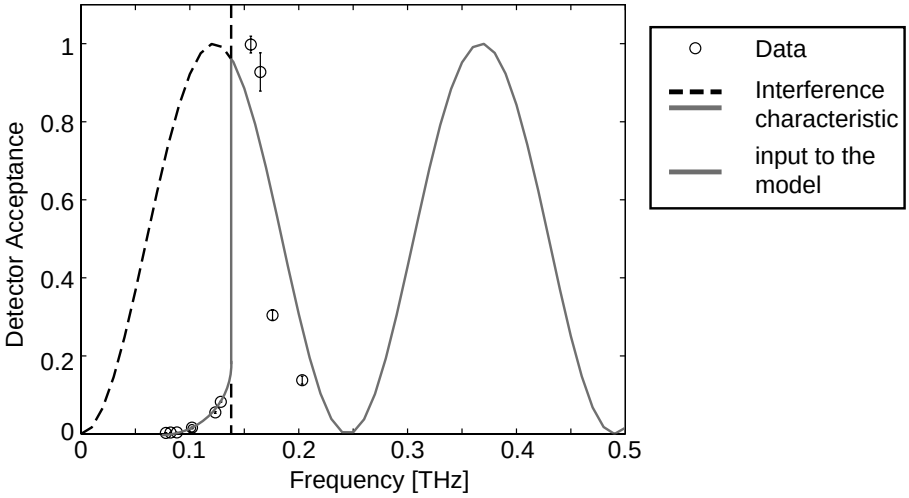


Figure 7.11: Spectral acceptance of the pyroelectric detector. The data of the calibration measurement are shown as circles. The solid line indicates the interference characteristic of the detector crystal matched best to the result of the calibration measurement. The detector acceptance is reduced below 130 GHz due to diffraction effects. The gray curve is included into the interferometer acceptance to account for the destructive interference in the crystal and the small frequency cut-off of the pyroelectric detectors.

the detector acceptance function limits the precision of the Martin-Puplett interferometer.

A second result of the calibration measurements is the effective diameter of the horn antenna mounted on the pyroelectric detector (see appendix F). The effective diameter of the horn antenna is $d = 32.1\,\mathrm{mm}$, while the true diameter is 55.9 mm.

7.3.5 Transmission of the Quartz Window

The spectral transmission of the quartz Suprasil II vacuum window has been measured [58] using time-domain THz spectroscopy. Figure 7.12 shows the amplitude transmission which is decreasing continuously from $T = 0.8$ at $f = 200\,\mathrm{GHz}$ to $T = 0.2$ at $f = 1.5\,\mathrm{THz}$. A linear fit to the data yields $T = 0.86 - 0.52 \cdot f\,[\mathrm{THz}]$ and is used to model the interferometer acceptance function.

7.3.6 Aluminum Foils of Finite Thickness

The electric characteristics of the aluminum transition radiation films can be described by macroscopic quantities because the thickness of 40 nm corresponds to about 80–100 atomic layers. This thickness is sufficient for high reflectivity in the optical regime but the question is whether the incident sub-millimeter radiation may penetrate the metallic layer since the wavelength is much larger than the thickness of the aluminum film. If penetration occurs, it will be frequency selective and will lead to an additional acceptance function.

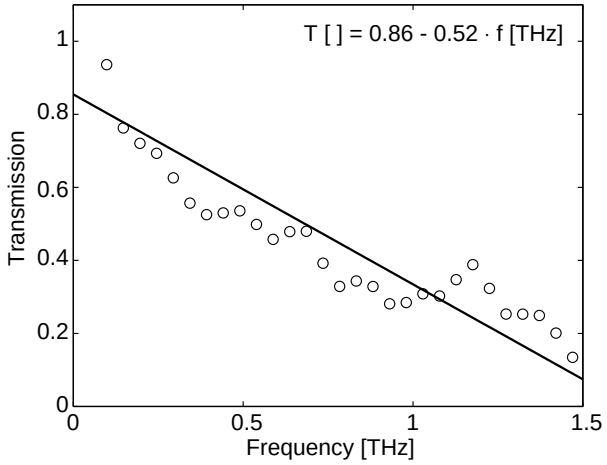


Figure 7.12: Transmission of the Suprasil II quartz glass window as a function of radiation frequency.

For simplicity the bunch fields are replaced by a free-propagating sub-millimeter electromagnetic wave incident perpendicularly onto the metallic boundary. The electric and magnetic fields inside the conductor can be described by

$$\vec{E} = \vec{E}_0 \exp\left(-\sqrt{\frac{\mu\mu_0\sigma\omega}{2}}\, z\right) \exp\left(i\sqrt{\frac{\mu\mu_0\sigma\omega}{2}}\, z - i\omega t\right) \tag{7.39}$$

$$\vec{H} = (1+i)\sqrt{\frac{\sigma}{2\mu\mu_0\omega}}\, \vec{n} \times \vec{E} \tag{7.40}$$

where $\vec{n}$ points along the direction of propagation of the electromagnetic wave. σ denotes the conductivity and μ the permeability of the metal. The conductivity of aluminum at a temperature of 20°C is $\sigma = 3.54 \cdot 10^7\, 1/\Omega\,\mathrm{m}$. Both field amplitudes drop exponentially in the metal. The penetration depth δ, where the fields have dropped to $1/e$ of their surface

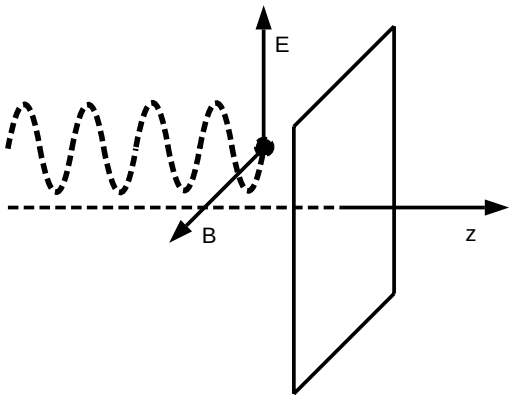


Figure 7.13: A free-propagating electromagnetic wave incident perpendicularly onto a metallic boundary.

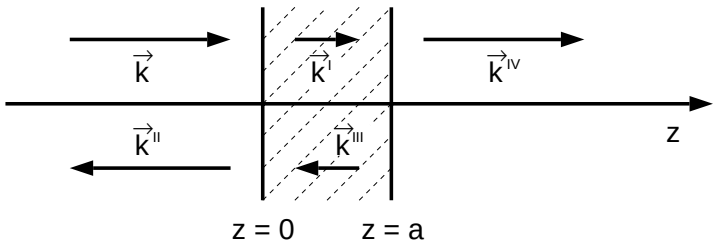


Figure 7.14: A free-propagating electromagnetic wave with momentum k is incident perpendicularly onto an aluminum sheet of thickness a. The wave is partially reflected (k^{II}) and transmitted (k^I) at the first boundary. At the second boundary the transmitted part is again partially reflected (k^{III}) and transmitted (k^{IV}).

values, is called the skin depth

$$\delta = \sqrt{\frac{2}{\mu\mu_0\sigma\omega}}\,. \tag{7.41}$$

For aluminum, $\mu = 1$, we obtain a skin depth of 280 nm at a frequency of $f = 100\,\mathrm{GHz}$, which is clearly larger than the thickness of the aluminum layer. Obviously the second boundary of the aluminum layer has to be taken into account to calculate a reflection and transmission coefficient for the incident wave. Assume a metallic layer of thickness a and a coordinate system arranged as in Fig. 7.14. The electromagnetic wave with momentum (k) is incident from the left and is split into a reflected (k^{II}) and transmitted wave (k^I) at the first boundary at $z = 0$. At the second boundary ($z = a$) the wave with momentum (k^I) is split again into a reflected and transmitted component with momentum (k^{III}) and (k^{IV}) respectively. In steady state, the electric fields in vacuum are given by

$$\vec{E}^m = \vec{E}_0^m \exp(ik^m z - i\omega t) \tag{7.42}$$

$$\vec{H}^m = \frac{\vec{k}^m \times \vec{E}^m}{\mu_0\omega} \tag{7.43}$$

and in the metal by

$$\vec{E}^n = \vec{E}_0^n \exp(-Az)\exp(iAz - i\omega t) \tag{7.44}$$

$$\vec{H}^n = \frac{(1+i)}{\sqrt{2}}\sqrt{\frac{\sigma}{\mu\mu_0\omega}}\vec{n} \times \vec{E}^n \tag{7.45}$$

where $A = \sqrt{\mu\sigma\omega/2}$ and $\vec{k} = k\vec{e}_z$ has been used. The superscripts m and n denote the different field components either in vacuum or in the material, so Eq. (7.42) describes E, E^{II} and E^{IV} and Eq. (7.44) E^I and E^{III} respectively.

The tangential component of the electric field ($\vec{n} \times \vec{E}$) and of the magnetic field ($\vec{n} \times \vec{H}$) have to be continuous at $z = 0$. Using $\vec{n} \times \left(\vec{k} \times \vec{E}\right) = -\vec{E}\left(\vec{n} \cdot \vec{k}\right)$, we obtain a set of four equations

$$E_0 + E_0^{II} = E_0^I + E_0^{III} \tag{7.46}$$

$$\frac{E_0 k}{\mu_0\omega} - \frac{E_0^{II} k^{II}}{\mu_0\omega} = \frac{(1+i)}{\sqrt{2}}\sqrt{\frac{\sigma}{\mu\mu_0\omega}}\left(E_0^I - E_0^{III}\right) \tag{7.47}$$

$$E_0^{IV}\exp\left(ik^{IV}a\right) = E_0^I\exp(-Aa+iAa) + E_0^{III}\exp(Aa-iAa) \tag{7.48}$$

$$\frac{k}{\mu_0\omega}E_0^{IV}\exp ik^{IV}a = \frac{(1+i)}{\sqrt{2}}\sqrt{\frac{\sigma}{\mu\mu_0\omega}}\left(-E_0^{III}\exp(Aa-iAa) + E_0^I\exp(-Aa+iAa)\right) . \tag{7.49}$$

Equations (7.46) – (7.50) can be solved for E_0^I, E_0^{II}, E_0^{III} and E_0^{IV} as a function of the amplitude of the incoming wave E_0. We obtain for the reflected amplitude E_0^{II}

$$E_0^{II} = E_0\left(\frac{\left(\frac{1}{\mu_0^2c^2}-i\frac{\sigma}{\mu_0\omega}\right)\sinh(Aa-iAa)}{\left(\frac{1}{\mu_0^2c^2}+i\frac{\sigma}{\mu_0\omega}\right)\sinh(Aa-iaA)+\frac{2(1+i)}{\mu_0 c}\sqrt{\frac{\sigma}{2\mu\mu_0\omega}}\cosh(Aa-iAa)}\right). \tag{7.50}$$

Figure 7.15 shows the amplitude reflectivity E_0^{II}/E_0 as a function of the thickness of the aluminum layer. The frequency of the electromagnetic wave is $f = 100\,\mathrm{GHz}$ ($\lambda = 3.1\,\mathrm{mm}$). We get the important result that a 40 nm aluminum film is not at all penetrated by the electromagnetic wave.

An experimental test was made to verify this surprising result. The transmission of the transition radiation screen was measured using time-domain THz-spectroscopy [58]. No signal was observable. From the signal to noise ration of better than 6000 we can conclude that the transmission in the frequency band between 200 GHz and 1.5 THz is smaller than $1.5\cdot10^{-3}$. The important conclusion is that the reflection of far-infrared transition radiation by thin 40 nm aluminum foil amounts to 100% without noticeable frequency dependence.

7.3.7 Spectral Acceptance of the Martin-Puplett Interferometer

The suppression of high-frequency and low-frequency components of the far-infrared transition radiation field distribution inside the Martin-Puplett interferometer has been discussed in this section. To summarize:

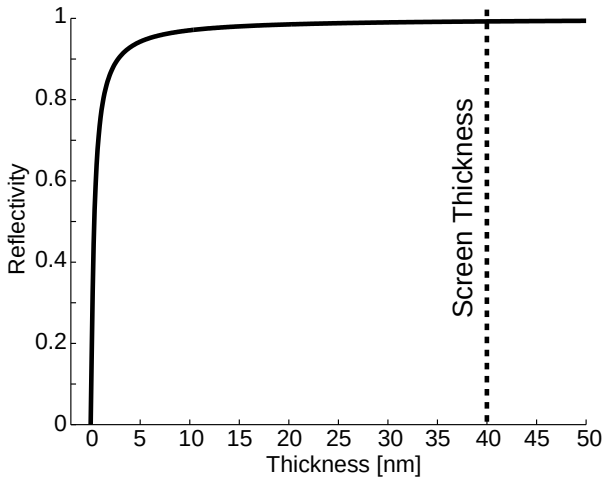


Figure 7.15: Amplitude reflectivity E_0^{II}/E_0 as a function of the thickness of the aluminum film. The radiation frequency is $f = 100\,\mathrm{GHz}$.

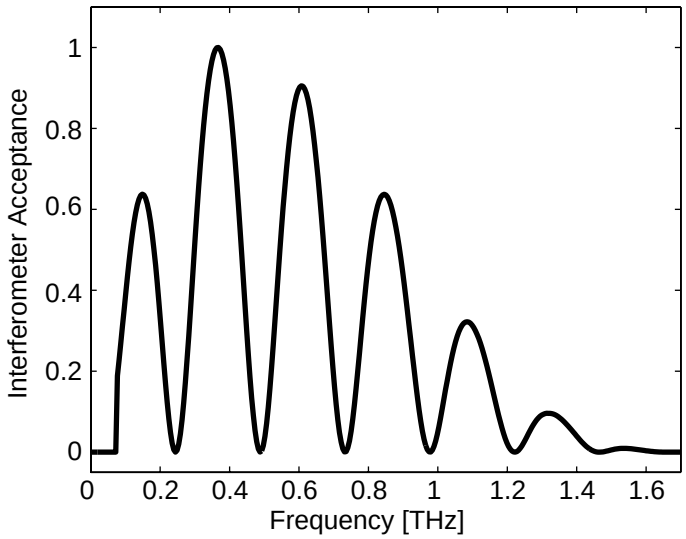


Figure 7.16: The spectral acceptance function of the TTF Martin-Puplett interferometer.

1. Suppression of low frequencies:
   (a) At low frequencies the source dimension of transition radiation exceeds the diameter of the aluminum foil. (chapter 3).
   (b) The enlarged opening angle due to Fresnel diffraction (chapter 3).
   (c) Diffraction in the interferometer.
   (d) Efficiency reduction of the pyroelectric detector at frequencies lower than 130 GHz.
2. Attenuation of high frequencies:
   (a) The transmission of the quartz window (chapter 3).
   (b) The reflectivity of the polarizing grid.
   (c) The spectral acceptance of the beam splitter and the roof mirrors.
   (d) The transmission and reflectivity of the analyzing grid.
3. Attenuation of intermediate frequencies:
   (a) The interference effect in the pyroelectric detector.

(1a), (1b) and the influence of the transverse beam size on the form factor (3) depend on beam energy and the transverse beam emittance. Figure 7.16 shows the overall interferometer acceptance for $E = 170\,\mathrm{MeV}$, $\gamma\epsilon = 5 \cdot 10^{-6}\,\mathrm{m}$.

7.3.8 Systematic Error of the Acceptance Function

The systematic error of the spectral acceptance function has been evaluated using the errors of the transmission measurements performed with the optical elements of the interferometer and by varying the parameters of the diffraction calculation.

Quartz Window and Wire Grids: A linear fit of the quartz window transmission (Fig. 7.12) has been included in the interferometer model. The transmission data of the wire grid have been fitted by an exponential curve (Fig. 7.5). The rms scatter of the window and grid transmission data around the fit yield $(\sigma_T^w)_{\mathrm{rms}} = 0.022$ and $(\sigma_T^g)_{\mathrm{rms}} = 0.01$ respectively. The errors of the window, polarizer, beam splitter and analyzer transmission and reflectivity coefficients are uncorrelated and add quadratically.

Diffraction: The influence of diffraction on the spectral transfer function can be estimated by varying the dimension of the transition radiation screen, the size of first parabolic mirror of the interferometer, the active detector dimension and the beam energy. The transition radiation screen and the parabolic mirror have rectangular shape but are approximated by circles of equal area in the model. To obtain an error estimate of the approximation, the diameter is varied to either enclose or inscribe the rectangular screen and mirror. The active detector diameter is varied by 10% and the beam energy by 5%. A small size of the transition radiation screen, parabolic mirror and active detector diameter in combination with a higher beam energy causes the strongest suppression of long radiation wavelengths. On the other hand, a large transition radiation screen, mirror and detector diameter and a lower beam energy reduces the suppression. The difference of both computations yields an error band for the diffractive terms in the interferometer acceptance function. The diffractive error is added quadratically to the errors obtained previously.

Transverse Beam Size: The assumed transverse beam size is varied by a factor between 0.5 and 2. The difference of the frequency domain expressions is added quadratically to the previously obtained errors. The error caused by the transverse beam size is small compared to the other errors because of the small transverse emittance.

Detector: The thickness and the permittivity of the pyroelectric crystal, which determine the separation of the maxima and minima of the acceptance function, is adapted to the calibration measurements and the data taken with the shortest bunch length measured at TTF. A variation of the optical path length within 30 μm was possible to describe the measurements. The amplitude reflectivity in Eq. (7.38) is a free parameter to fit the interference characteristic to the calibration measurement. Unfortunately only four points of the calibration measurement, $f > 130\,\mathrm{GHz}$, are suitable to determine r yielding a large uncertainty of this parameter.

The error interval of the interferometer acceptance function is shown in Fig. 7.17.

7.4 The Autocorrelation Function

Autocorrelation and Power Spectrum

The radiation intensity at the pyroelectric detectors (Eq. (7.14) and Eq. (7.15)) can be rewritten in terms of radiation intensities I

$$I_{\pm} = \frac{1}{4} I_0 \left(1 \pm \cos(\omega\tau)\right) . \tag{7.51}$$

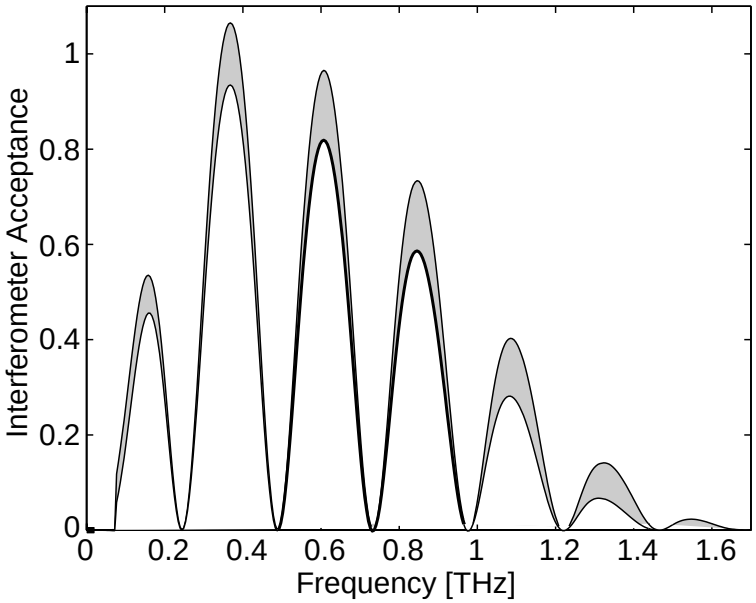


Figure 7.17: The spectral acceptance of the Martin-Puplett interferometer. Superimposed is the error interval of the acceptance function.

The phase difference δ has been substituted by the angular frequency ω and the time difference τ corresponding to the path difference in the two arms of the interferometer. In case of a continuous spectrum

$$I_{\pm}(\tau) = \frac{1}{4}\int_0^{\infty} \tilde{I}(\omega)\,(1 \pm \cos(\omega\tau))\; d\omega\,. \tag{7.52}$$

The difference of both detector signals is evaluated to subtract correlated signal fluctuations originating from beam instabilities, hence

$$I_{+}(\tau) - I_{-}(\tau) = \frac{1}{4}\int_0^{\infty} \tilde{I}(\omega)\cos(\omega\tau)\, d\omega\,. \tag{7.53}$$

The radiation spectrum can now be evaluated by inverting the cosine Fourier transformation of Eq. (7.53)

$$\tilde{I}(\omega) = \frac{8}{\pi}\int_0^{\infty} (I_{+}(\tau) - I_{-}(\tau))\cos(\omega\tau)\, d\tau\,. \tag{7.54}$$

The Fourier transformation of the difference interferogram $I_{+}(\tau) - I_{-}(\tau)$ yields the frequency spectrum of the incident radiation pulse. The difference interferogram is normalized by the sum of the two signals to correct for radiation intensity fluctuations during the measurement.

Simulation

Three longitudinal charge distributions are considered: a Gaussian and two asymmetric distribution composed of two Gaussians. The beam energy is 170 MeV and the normalized emittance is $\epsilon = 5 \cdot 10^{-6}$ m. The transverse charge distribution is assumed to be Gaussian. The coherent transition radiation spectrum and the autocorrelation response of the Martin-Puplett interferometer are simulated as follows:

1. Determination of the longitudinal bunch form factor $\tilde{\rho}_{q,\omega}$ by Fourier transformation of the longitudinal charge distribution.

2. Convolution of the form factor with the spectral acceptance function of the interferometer.

3. Computation of the coherent power spectrum $|\tilde{\rho}_{q,\omega}|^2$ and application of an inverse Fourier transformation to obtain the autocorrelation function (Eq. 7.54).

Figure 7.18 shows the longitudinal charge distribution of the Gaussian (left) and the asymmetric (middle, right) bunches. The second row shows the coherent power spectrum $|\tilde{\rho}_{q,\omega}|^2$. The power spectrum is obtained by Fourier transformation of the longitudinal charge distribution, by a multiplication with the acceptance function and by squaring the result. The autocorrelation function (third row, solid line) is obtained by an inverse

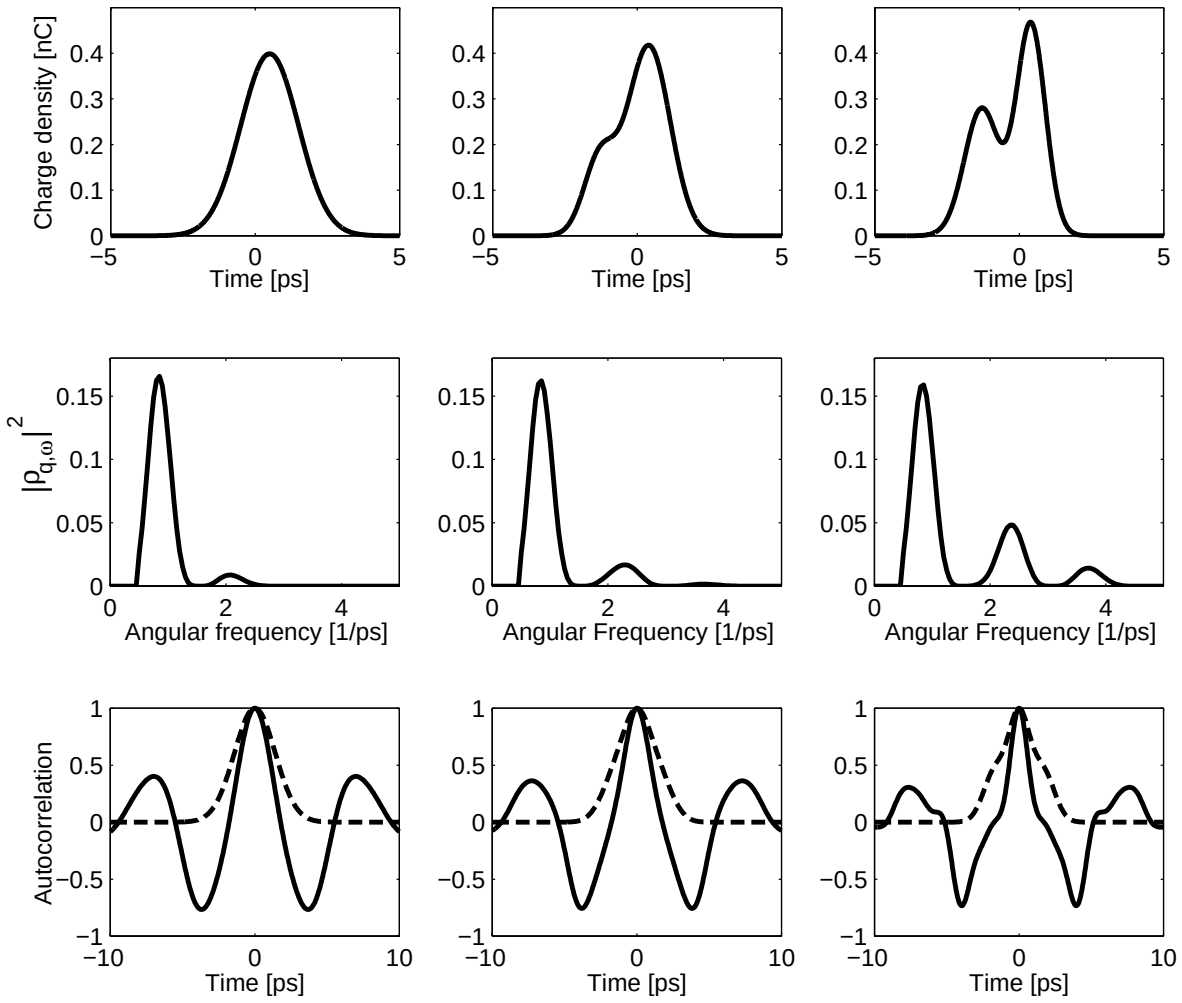


Figure 7.18: Top: Three longitudinal charge distributions versus time. Middle: The expected longitudinal from factor versus angular frequency ω. Bottom: The expected autocorrelation in the Martin-Puplett interferometer (solid curve). Superimposed is the autocorrelation of the longitudinal charge distribution disregarding the spectral acceptance (dashed curve).

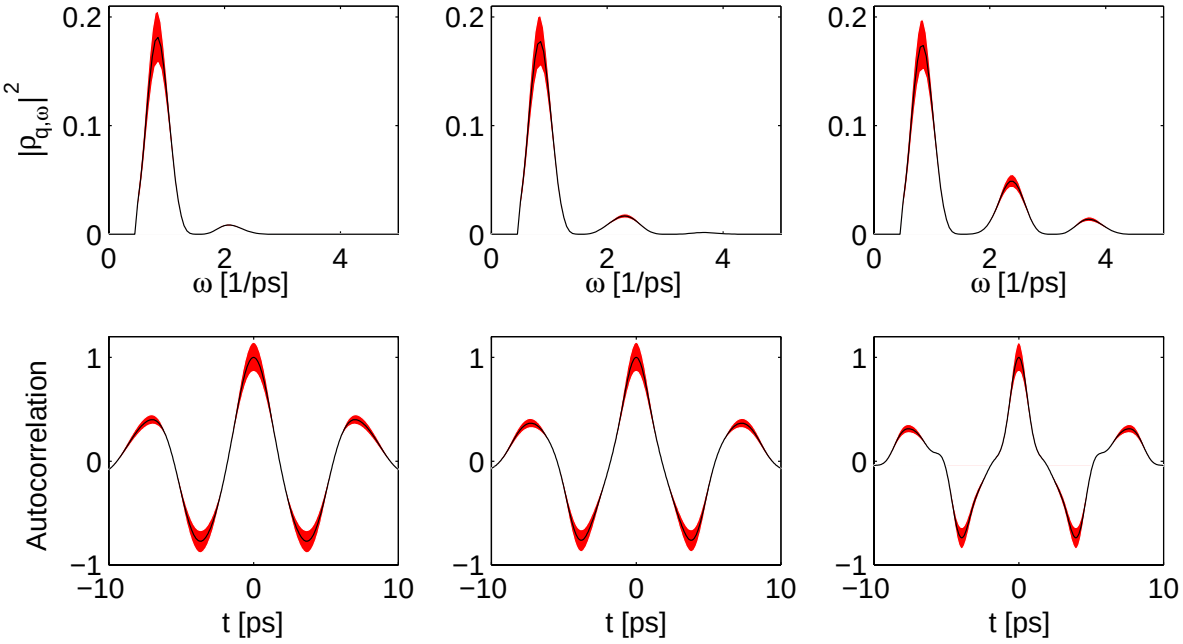


Figure 7.19: Top: the longitudinal from factor versus angular frequency. Bottom: the autocorrelation function. The shaded area denotes the uncertainty interval of the conversion from the charge distribution to the form factor and autocorrelation function.

Fourier transformation. Superimposed is the autocorrelation function without any spectral corrections (dashed line).

The spectral corrections cause significant oscillations of the autocorrelation function due to missing frequency components. The main maximum is narrower with spectral corrections than without. The FWHM of the autocorrelation function is therefore not a reliable measure of the bunch length. To learn about the shape of the longitudinal distribution, more sophisticated analysis techniques have to be applied to the entire autocorrelation and the coherent power spectrum.

Error Investigation The uncertainty of the bunch form factor and the autocorrelation function are dominated by the imprecise knowledge of the spectral acceptance of the interferometer. Figure 7.19 shows the error intervals of the form factors and the autocorrelation functions for the three charge distributions.

7.5 Reconstruction of the Longitudinal Charge Distribution

The variety of effects influencing the spectral acceptance of the interferometer make a direct determination of the longitudinal bunch charge distribution difficult. The analysis presented in this section therefore follows the opposite way: a "reasonable" longitudinal bunch charge distribution is assumed and Fourier transformed. After the application of the interferometer acceptance function, a prediction of the coherent power spectrum and the

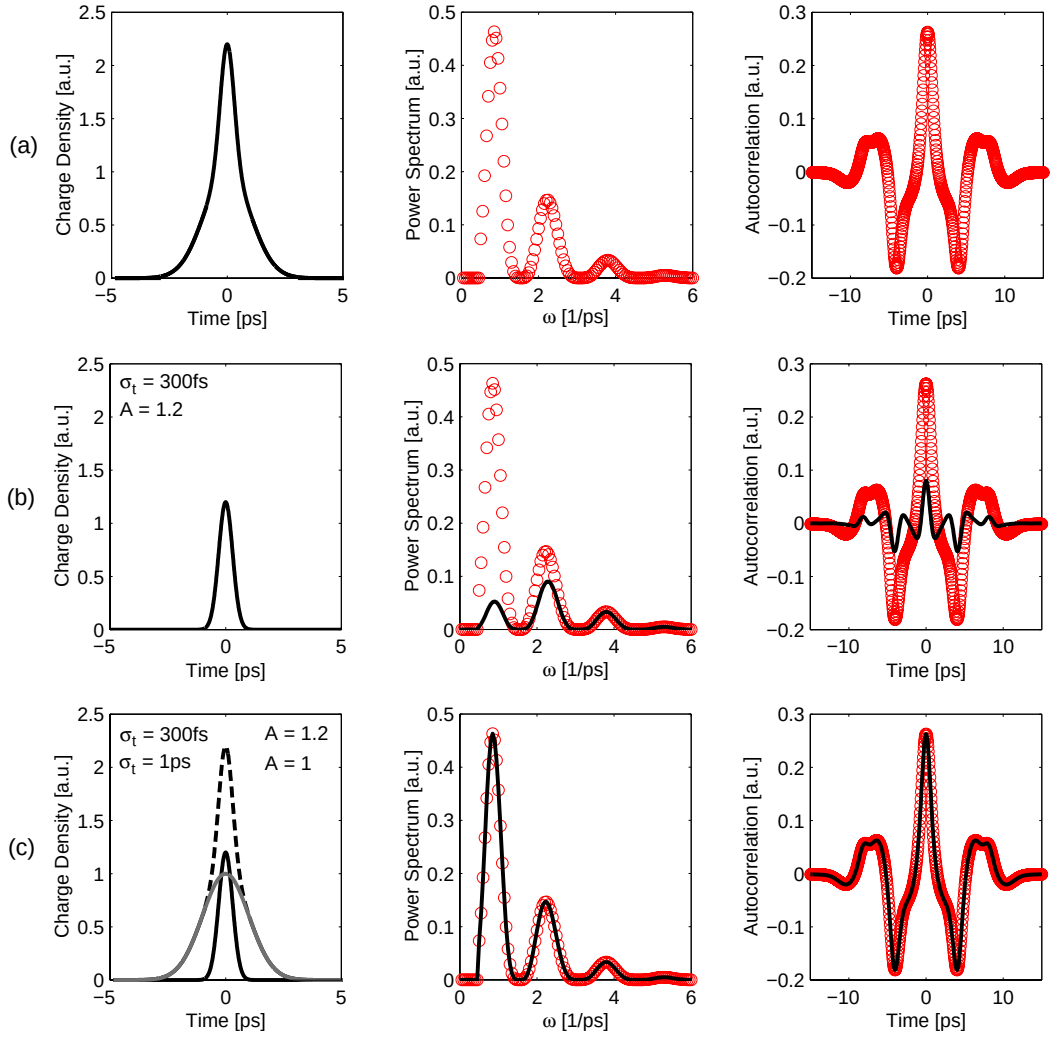


Figure 7.20: Reconstruction of a symmetric longitudinal bunch charge distribution. Left column: bunch charge distribution. Middle column: coherent power spectrum. Right column: autocorrelation. Row (a): simulated bunch charge distribution, coherent power spectrum and autocorrelation. Row (b) shows a Gaussian distribution of amplitude $A_1 = 1.2$ and rms width of $\sigma_z = 300\,\mathrm{fs}$ fitting best to the highest order maximum of the simulated power spectrum. The power spectrum and the autocorrelation are shown as solid curves. Row (c) shows a second Gaussian distribution superimposed contributing the missing lower frequency contributions ($A_2 = 1$ and $\sigma_2 = 1\,\mathrm{ps}$). The corresponding power spectrum and the autocorrelation are presented as solid curves.

autocorrelation function is made. The parameters of the initial bunch charge distribution are varied until the predictions are in good agreement with the measured autocorrelation and power spectrum. This procedure does of course not yield a unique description but appears to be the most useful compromise in view of the many limiting effects. In general, the measured data cannot be described by a single Gaussian distribution. A sum of several Gaussian distributions of different amplitudes A_i and widths σ_i, which can even be displaced, have to be considered. The reconstruction of a symmetric and an asymmetric bunch charge distribution will be discussed in the following.

Symmetric Charge Distribution

Consider a charge distribution composed of two Gaussians of amplitudes $A_1 = 1.2$, $A_2 = 1$ and variance $\sigma_1 = 300\,\text{fs}$ and $\sigma_2 = 1\,\text{ps}$ respectively. Row (a) of Fig. 7.20 shows the bunch charge distribution, the coherent power spectrum and the autocorrelation of the charge distribution as circles. To reconstruct the initial charge distribution, a single Gaussian is assumed first. The amplitude and the width of the Gaussian is varied until its Fourier transformation fits the highest order maximum of the coherent power spectrum (b). A second Gaussian distribution is superimposed to match the lower frequency components. In the present case, the rms width of the second distribution may not be shorter than 1 ps to prevent contributions at frequencies larger than 500 GHz in the power spectrum. The amplitude and the rms width is varied until an agreement is reached.

Asymmetric Charge Distribution

The question arises whether asymmetric charge distributions are analyzable with the presented method. See Fig. 7.21, row (a), as an example and consider the asymmetric charge distribution introduced in Fig. 7.18. The simulated coherent power spectrum and the autocorrelation are shown as circles. Row (b) shows a Gaussian charge distribution whose frequency contribution fits to the highest order maximum of the coherent power spectrum. In contrast to Fig. 7.20, we obtain too large low frequency components which cannot be compensated by just adding a Gaussian curve of smaller rms width. Hence a more complicated bunch charge distribution must be considered.

The Gaussian charge distribution of amplitude A_1 is separated into two Gaussians of amplitude $A_1/2$ and equal rms width. In a second step the two Gaussians are separated in time. The adaption of the highest order maximum will degrade but while continuing the separation, the adaption will eventually improve. The optimum separation of the two peaks is found for the best re-adaption of the highest order maximum of the coherent power spectrum (c). The lower frequency components are also reduced. Thirdly, we superimpose a Gaussian distribution of larger rms width. The amplitude and the width of the charge distributions are varied until the coherent power spectrum and the autocorrelation function agree with the simulation (d).

It can be very time-consuming to work out arbitrary longitudinal charge distributions using the presented method. The use of a superposition of Gaussian charge distributions is sufficient for the present data quality which is heavily impeded by the interferometer acceptance.

Error Investigation The three longitudinal charge distributions of Fig. 7.19 have been used to investigate the systematic error which is due to the interferometer acceptance. The autocorrelation and the coherent power spectrum are evaluated for the upper and lower boundary curves of the interferometer acceptance function. The charge distribution is then reconstructed using the method outlined above. The error range of the longitudinal charge distributions is shown as the shaded area in Fig. 7.22. The error is largest at the maxima and local minima of the distributions. Allowing for a variation of the line shape within the full range of the error band, it is still possible to distinguish between a

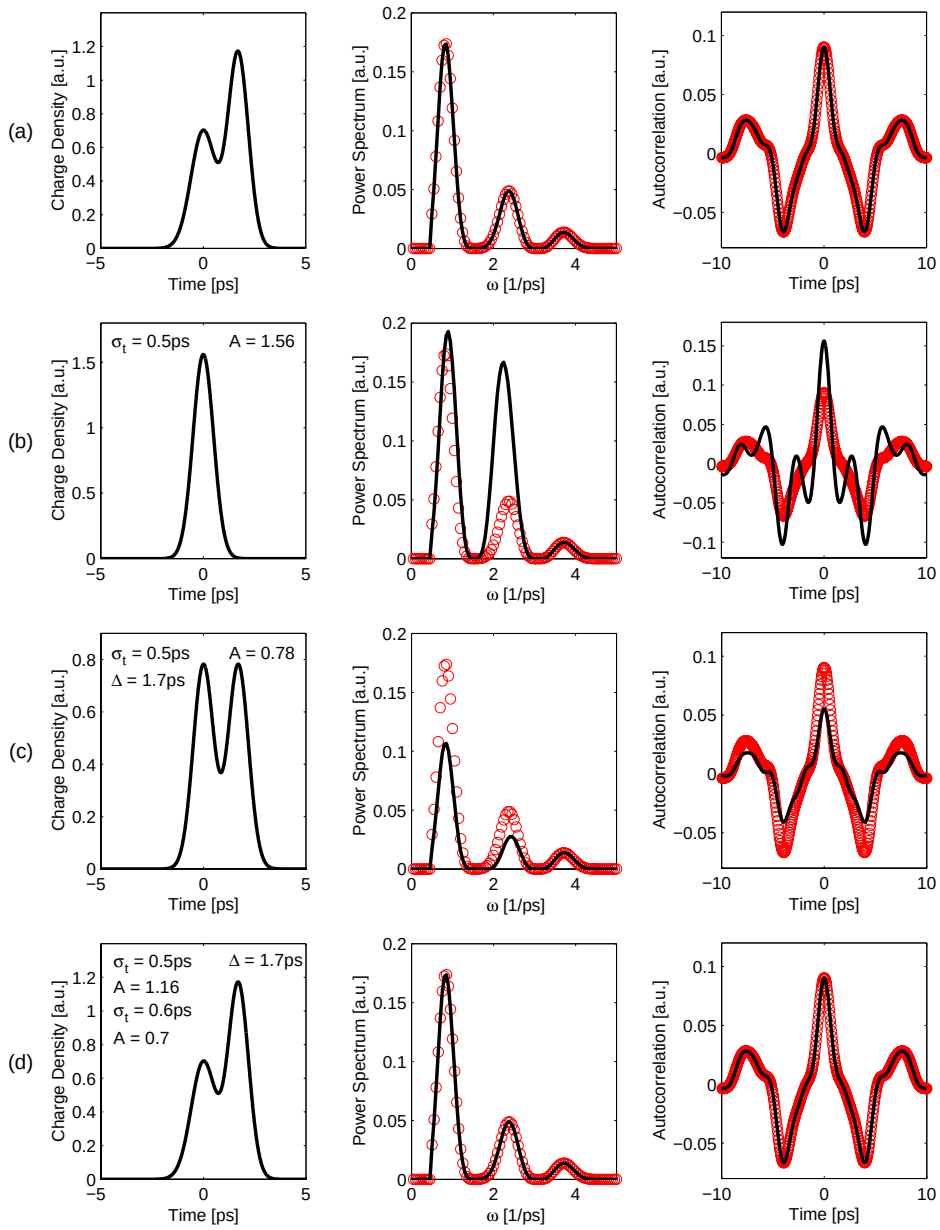


Figure 7.21: Reconstruction of an asymmetric longitudinal bunch charge distribution. Left column: bunch charge distribution. Middle column: coherent power spectrum. Right column: autocorrelation. Row (a): simulated bunch charge distribution, coherent power spectrum and autocorrelation. Row (b) shows a Gaussian distribution of amplitude $A_1 = 1.56$ and rms width of $\sigma_1 = 500\,\mathrm{fs}$ fitting best to the highest order maximum of the simulated power spectrum. The corresponding power spectrum and the autocorrelation are shown as the solid curves. The lower frequency contributions exceeding the simulated power spectrum indicate a more complicated charge distribution. Row (c) shows two Gaussian distributions of amplitude $A_1/2$ and rms width σ_1 separated by $\Delta = 1.7\,\mathrm{ps}$. At a separation of Δ, the highest order maximum of the simulated (circles) and predicted power spectrum (solid curve) are, again, in agreement. The lower frequency components are reduced. The amplitude and the rms width of both Gaussians has been optimized, as shown in (d), to obtain the simulated charge distribution.

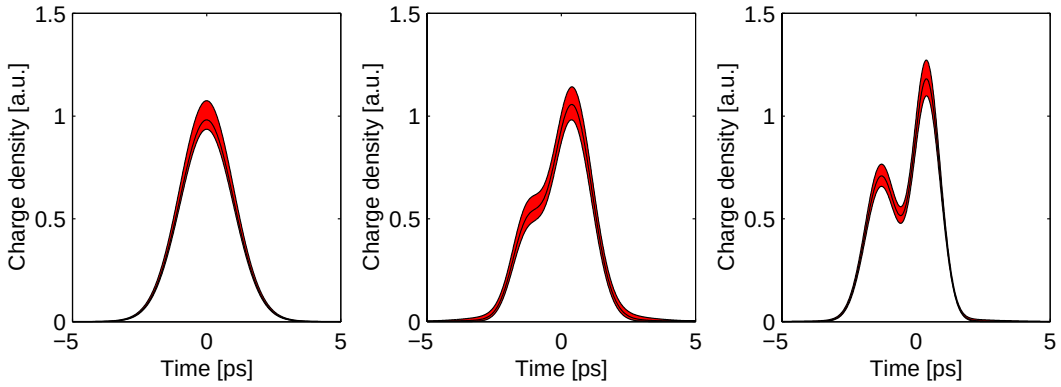


Figure 7.22: Estimation of the systematic error of the time- and frequency-domain fitting technique to determine the longitudinal bunch charge distribution. The charge distributions introduced in Fig. 7.19 are reconstructed. The shaded area denotes the uncertainty of the reconstructed bunch shape. The error is mostly due to the uncertainty of the spectral acceptance function of the interferometer.

single peak, shoulder and double peak distribution. The method is, on the other hand, not able to predict the forward-backward symmetry of the longitudinal charge distribution, because this information is contained neither in the power spectrum nor in the autocorrelation.

More sophisticated data analysis techniques, as the application of a Kramers Kronig analysis on the bunch form factor, make sense only if the form factor is known precisely over a large spectral interval. A Kramers Kronig analysis [62], which has been successfully applied at the linac of the Cornell synchrotron [63], can be used to reconstruct the phase information of the longitudinal form factor. Once the phase is known, a direct inverse Fourier transformation can be used to derive the bunch charge distribution. In the present case, a deconvolution of the longitudinal form factor with the interferometer acceptance would lead to large uncertainties in frequency intervals where the acceptance function is small. The technique would become applicable when a different detection device with a flat spectral acceptance, for example a photo acoustic detector, is used.

7.6 Determination of the Bunch Length

7.6.1 Analysis of the Autocorrelation

Under the assumption of a Gaussian charge distribution, the bunch length and the width of the autocorrelation function are closely related. A Gaussian of variance σ_z yields an autocorrelation with a variance of $2\sigma_z$. The idea is to predict the length of the longitudinal charge distribution directly from the width of the autocorrelation function. The influence of the interferometer acceptance function on this simple method will be investigated in this section.

A simulation is used to investigate the error of the bunch length determination using the

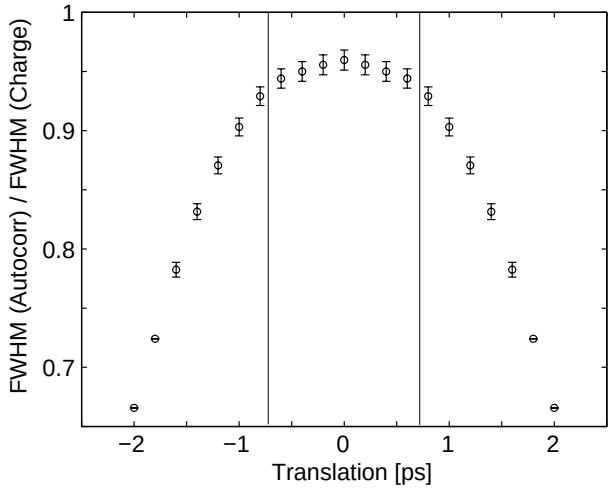


Figure 7.23: FWHM of the autocorrelation used for the determination of the bunch length. The simulated charge distribution consists of two Gaussians of equal rms width σ but different height A_i ($\sigma = 1\,\mathrm{ps}$, $A_1 = 1$, $A_2 = 0.6$). The ratio of the width of the autocorrelation and the width of the charge distribution is plotted versus the separation of the two Gaussians. The error bars are due to the uncertainty of the spectral acceptance of the Martin-Puplett interferometer.

FWHM of the autocorrelation function. The longitudinal charge distribution is described by two Gaussians of equal rms width ($\sigma = 1\,\mathrm{ps}$) but of different height A_i ($A_1 = 1$, $A_2 = 0.6$). To vary the FWHM of the initial charge distribution, the two Gaussians are separated in small steps relative to each other. Figure 7.23 shows the ratio of the FWHM evaluated from the autocorrelation function and the FWHM of the initial charge distribution as a function of the translation of the two Gaussians. The error bars are due to the uncertainty of the spectral acceptance of the interferometer.

For a negligible separation of the two Gaussians, the ratio of the two is close to unity. The ratio is decreasing for a larger separation of the charge contributions. The initial charge distribution becomes longer, at large variations a shoulder or a double peak is formed. The width of the autocorrelation, on the other hand, does not change, which is explainable by the suppression of the low frequencies by the acceptance function. The bunch length is therefore under-estimated.

To conclude, the FWHM of the interferogram measured by the TTF Martin-Puplett interferometer is a good measure of the FWHM bunch length only under the assumption of Gaussian longitudinal bunch shapes. More complicated bunch shapes lead to results which deviate from the correct FWHM value easily by a factor of two.

7.6.2 On-line Monitoring of the Bunch Length

It is possible to monitor the bunch length on-line by observing the detector signal amplitude. Figure 7.24 shows the coherent power spectrum of Gaussian charge distributions of $\sigma_t = 1\,\mathrm{ps}$ (left) and $\sigma_t = 2.5\,\mathrm{ps}$ (right). The spectral acceptance function of the Martin-

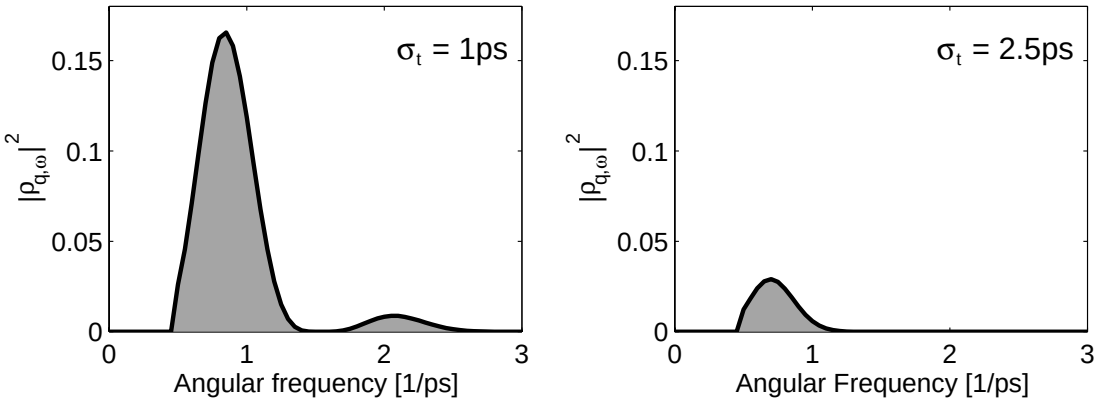


Figure 7.24: Coherent power spectrum of a Gaussian charge distribution. Left: $\sigma_t = 1\,\mathrm{ps}$. Right: $\sigma_t = 2.5\,\mathrm{ps}$. The detector response is proportional to the integral coherent power spectrum marked by the shaded area. Shorter bunches yield larger signals.

Puplett interferometer is included in the computation. The detector signal is proportional to the integral of the power spectrum shown in Fig. 7.24 (shaded area). For a constant bunch charge and average beam current, shorter bunches will cause larger detector signals. Figure 7.25 shows the expected relative detector signal versus bunch length under the assumption of the charge distributions in Fig. 7.19. This method has been extensively used in optimizing the bunch compression.

7.7 Bunch Length Measurements

Bunch length measurements performed with the Martin-Puplett interferometer are presented in this section. The instrument has been used to determine the longitudinal charge distribution of the beam produced by the photo injector and the thermionic gun.

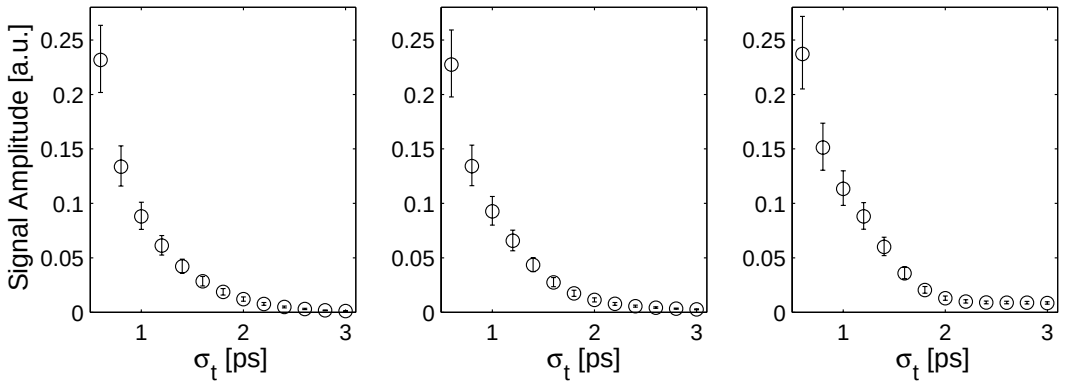


Figure 7.25: Pyroelectric detector signal as a function of the bunch length. Bunch charge and average beam current are invariant. The error bars are due to the uncertainty of the acceptance function. The left, middle and right graph corresponds to the respective longitudinal charge distribution introduced in Fig. 7.19.

7.7.1 Measurements with the Photo Injector Beam

The rf gun photo injector produced 20 bunches of 1 nC charge with a repetition rate of 1 MHz. To measure the bunch length, the beam was transfered to the high energy experimental area ($E = 170$ MeV) with and without the use of the magnetic chicane. Bunch compression using the magnetic chicane was investigated.

Alignment of the Interferometer

The interferometer is aligned using the light of a diode laser which is guided into the beam pipe about 3 m upstream of the interferometer and reflected by the transition radiation screen. The laser beam is aligned on the accelerator axis by centering the spot on the first mirror and on the transition radiation screen.

The polarizing grid of the interferometer is covered with a stretched aluminum foil to reflect the laser beam. The beam divider is replaced by a stretched transparent foil acting as an optical beam divider. The plane of the foil is identical to the wire grid. The pyroelectric detectors and the analyzing grid are replaced by two small apertures of 2 mm diameter distant by 130 mm to define the position and the angle of the laser beam in the interferometer.

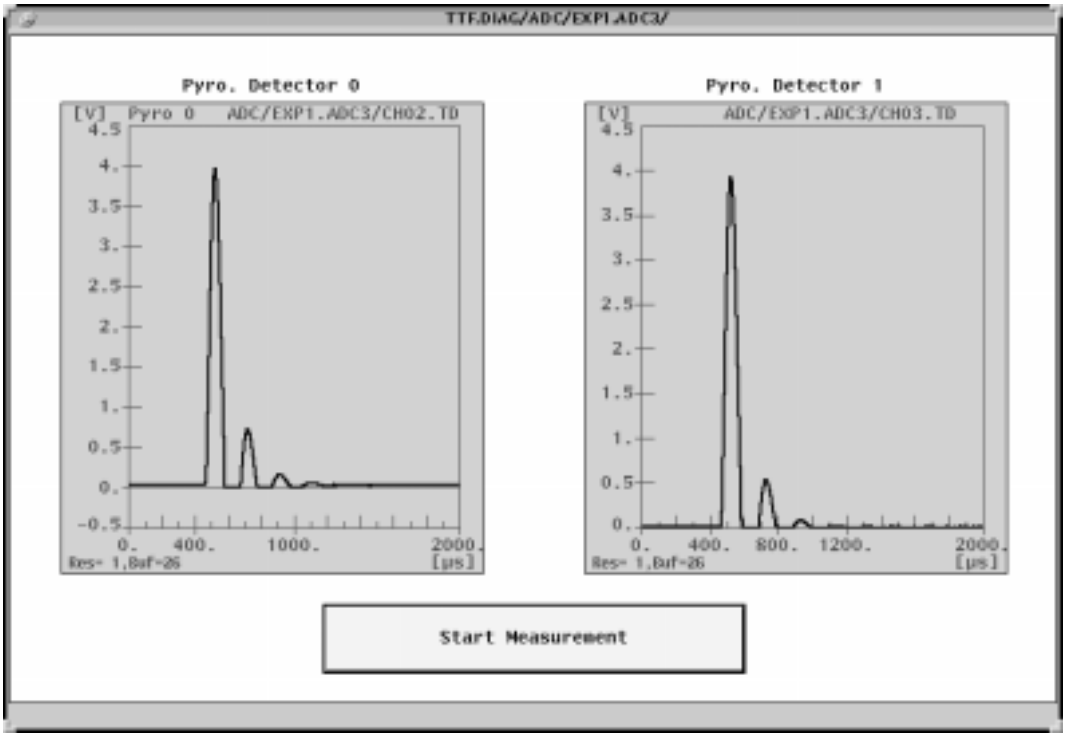


Figure 7.26: The signal of the pyroelectric detectors sampled by an ADC. The signal is the integrated response over a macropulse. The duration of the detector signal is explained by the 4 kHz bandwidth of the amplifier. The difference between the main maximum and the offset prior to the maximum is proportional to the incident radiation intensity.

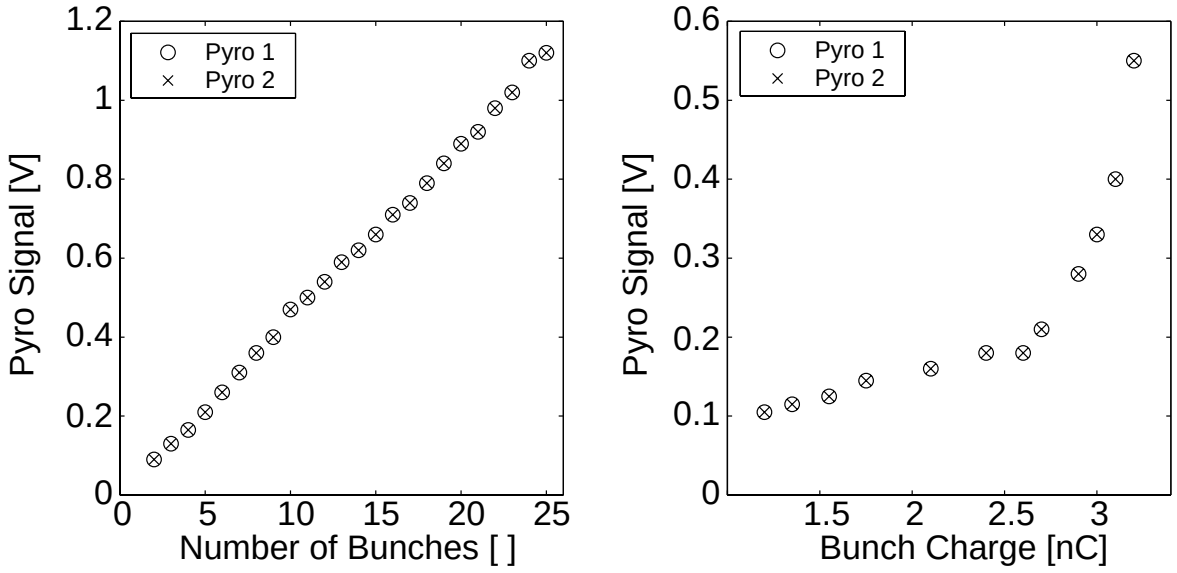


Figure 7.27: Left graph: pyroelectric detector signal as a function of the number of bunches ($Q = 1.2\,\mathrm{nC}$). Right graph: pyroelectric detector signal as a function of bunch charge for three bunches.

The interferometer table is arranged such that the table is leveled out and that the laser beam hits the center of the first parabolic mirror. The parabolic mirror is adjusted that the reflected laser beam hits the beam splitter at the correct height and that it hits the center of the two roof mirrors. The tilt of the roof mirrors is adjusted to produce a single light spot on the transparent beam splitter foil. The second parabolic mirror is then adjusted to transfer the laser beam through the two apertures.

Data Acquisition

Figure 7.26 shows the signal shape of the pyroelectric detectors. The incident radiation intensity is proportional to the signal peak. The peak is determined by evaluating the maximum of a parabolic fit applied to a data sample surrounding the peak. The detector signals are sampled every macropulse by the ADC. The detector signals, typically five signals per position of the roof mirror, are stored for off-line data processing.

Coherence of Transition Radiation

The size of the pyroelectric detector signal depends on the number of bunches and the bunch charge. A linear increase of the detector signal is expected when the number of bunches is increased and the bunch charge is kept constant. This linear increase is indeed observed as shown in the left graph of Fig. 7.27. In the contrary, according to Eq. (3.23), a quadratic increase of the detector signal is expected for a variation of the bunch charge. The non-linear dependence of the detector signal versus bunch charge is presented in the right graph of Fig. 7.27. The conclusion is that the transition radiation generated by the electron bunches is in fact coherent.

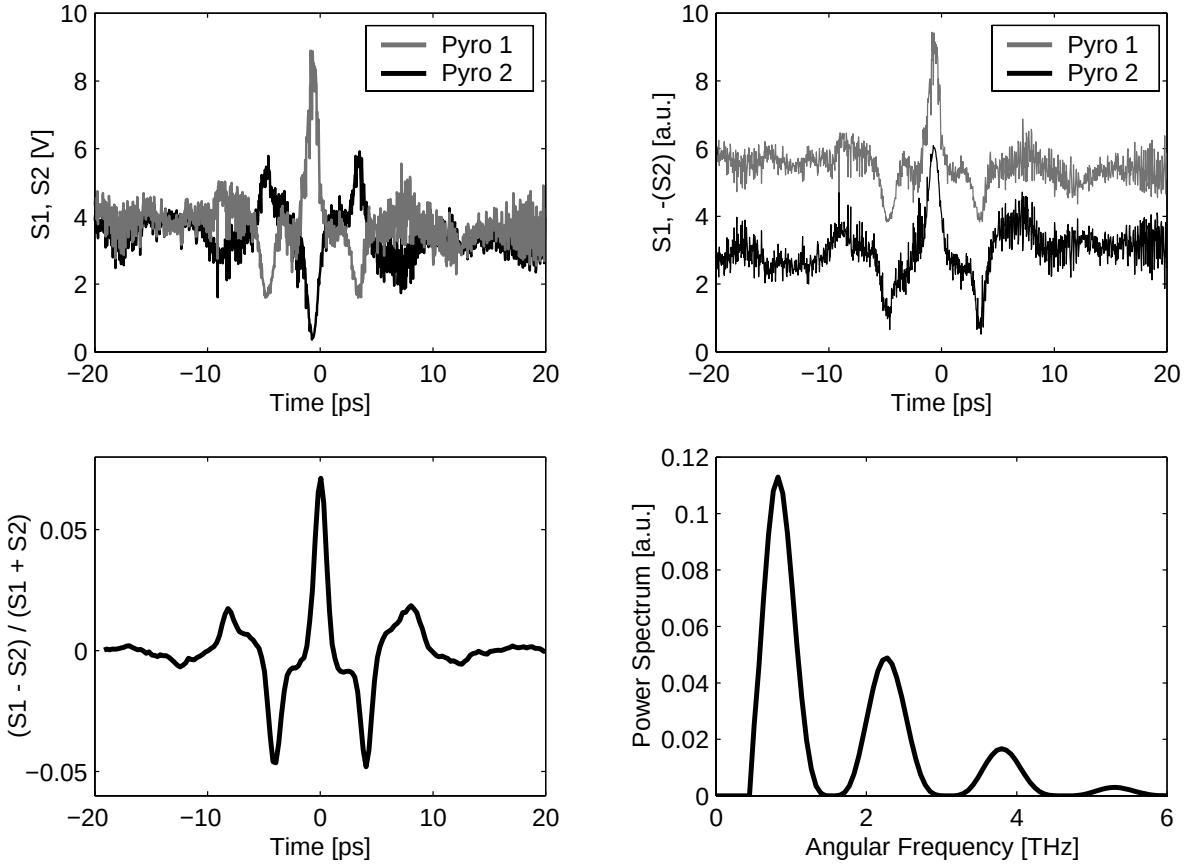


Figure 7.28: Upper left: raw signals detected by the pyroelectric detectors during an interferometer scan. Upper right: the two signals are scaled, and plotted with an arbitrary offset of 3 and 6 V. Signal #2 is inverted. Lower left: normalized difference interferogram. Lower right: coherent power spectrum obtained by Fourier transformation.

Autocorrelation and Coherent Power Spectrum

Figure 7.28 shows the raw signals of the pyroelectric detectors during an interferometer scan. The anti-correlated response of the two detectors is caused by observing either the transmitted or the reflected radiation component behind the analyzing grid. The sum of both signals is proportional to the radiation power. A scaling correction is needed for the slightly different amplification of the two detectors. The scaling factor is obtained by comparing the main maxima (obtained by a parabolic fit of the data around the peak) of both signals and the signal average. The scaled signals are depicted in the upper right graph of Fig. 7.28 with an offset of 3 and 6 V. The detector signals are subtracted from each other and normalized to their sum yielding an improved signal-to-noise ratio. Correlated intensity fluctuations which are caused by bunch charge variations and orbit instabilities cancel in he normalized difference interferogram shown in the lower left graph of Fig. 7.28. The coherent power spectrum (lower right graph) is evaluated by Fourier transformation.

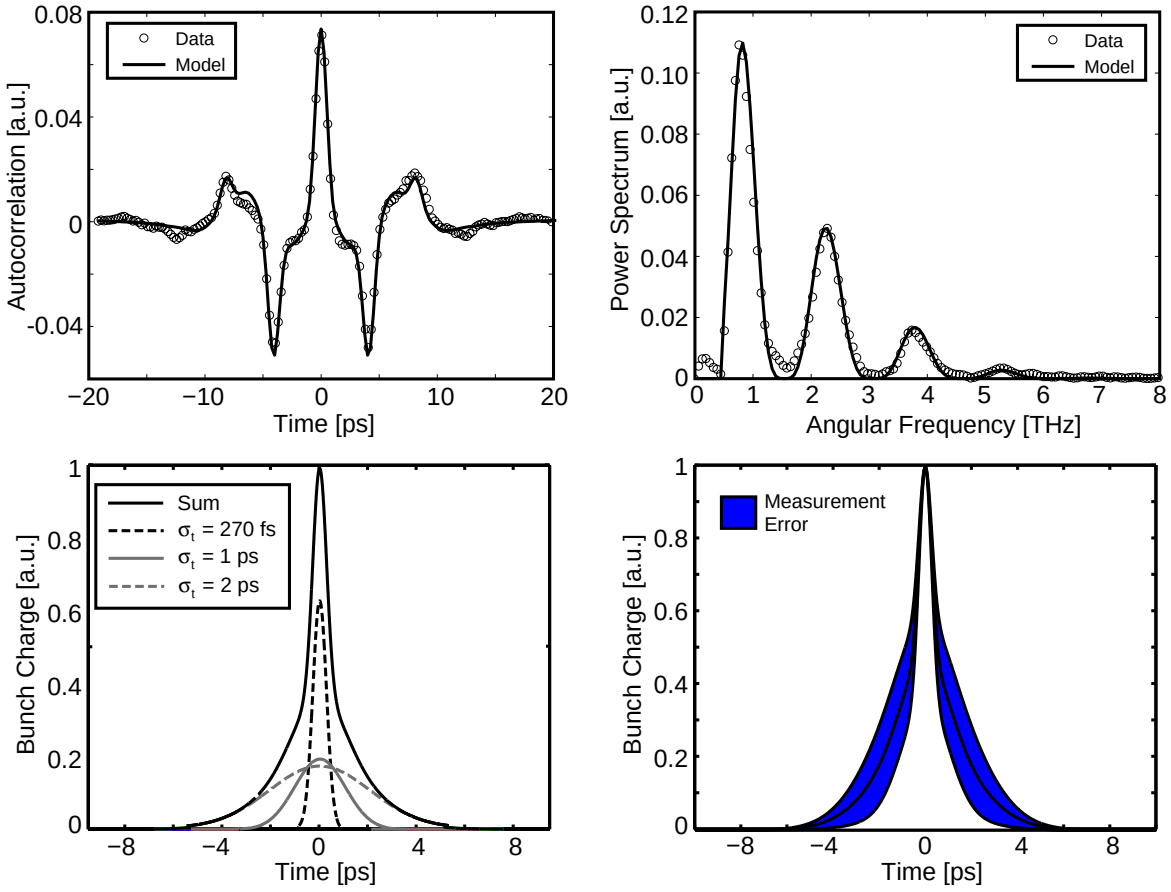


Figure 7.29: Shortest bunch measured at the TTF linac. Upper left: autocorrelation. Upper right: coherent power spectrum. Data is represented by circles. Lower left: longitudinal charge distribution matching the measured autocorrelation and the coherent power spectrum. The solid curve shown in the upper graphs depicts the predicted autocorrelation and coherent power spectrum of the longitudinal pulse shape. Lower right: error estimate of the longitudinal charge distribution.

Bunch Length and Bunch Shape Determination

The time- and frequency-domain fitting analysis can be applied to the data shown in Fig. 7.28. A superposition of three Gaussian distributions of different amplitude and variance is required to reproduce the measured autocorrelation and coherent power spectrum. Figure 7.29 (lower left) shows the longitudinal bunch charge distribution

$$\rho^L(t) = A_1 \exp\left(-\frac{t^2}{2\sigma_1^2}\right) + A_2 \exp\left(-\frac{t^2}{2\sigma_2^2}\right) + A_3 \exp\left(-\frac{t^2}{2\sigma_3^2}\right) \tag{7.55}$$

with

$$A_1 = 0.62\,, \quad \sigma_1 = 270\,\mathrm{fs}\,, \quad A_2 = 0.20\,, \quad \sigma_2 = 1\,\mathrm{ps}\,, \quad A_3 = 0.18\,, \quad \sigma_2 = 2\,\mathrm{ps} \tag{7.56}$$

matching the measured autocorrelation and coherent power spectrum. The autocorrelation and the coherent power spectrum computed from the longitudinal charge distribution

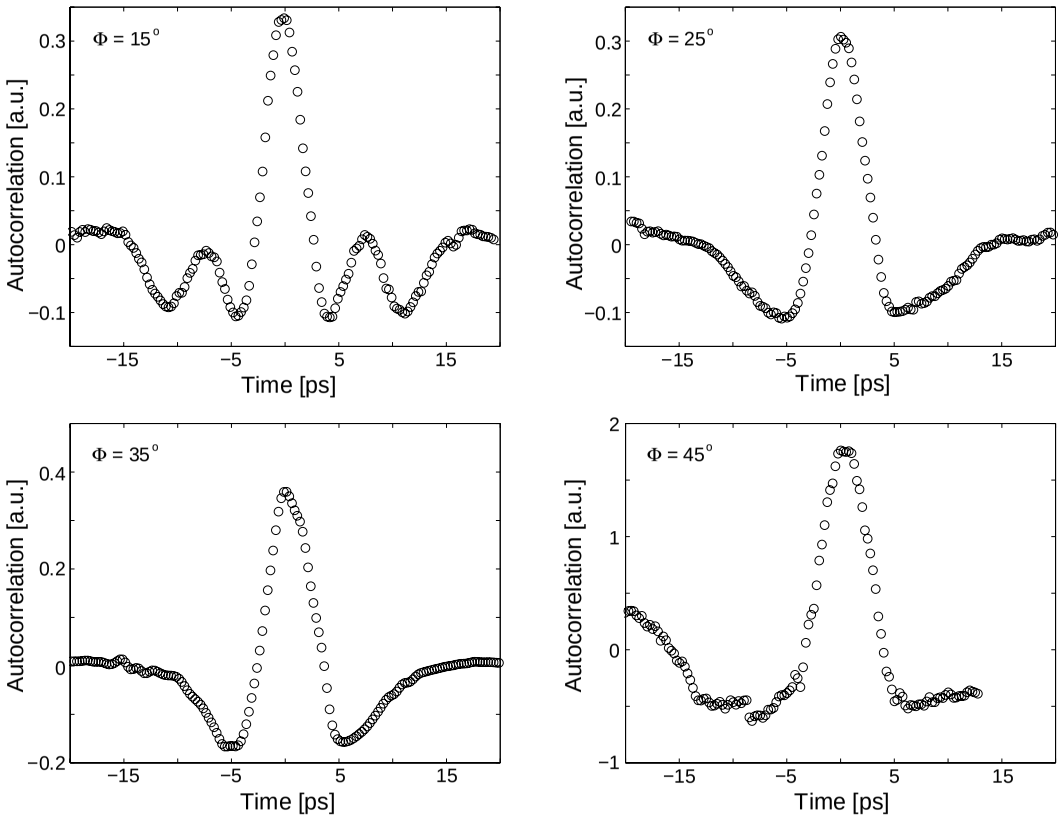


Figure 7.30: Autocorrelation measured by the Martin-Puplett interferometer for different rf gun phases. It is not possible to reproduce the interferograms using the time- and frequency-domain fitting technique.

of Eq. (7.55) are presented in Fig. 7.29 (top row). The measurements are described very well. The error of the longitudinal charge distribution is determined by convoluting the charge distribution Eq. (7.55) with the upper and lower bound of the interferometer acceptance curve. The lower right graph of Fig. 7.29 shows the resulting confidence interval as shaded area. The solid line depicts the mean bunch charge distribution. The narrow peak of the bunch charge distribution is determined more precisely than the tails of the distribution which is caused by the uncertainties of the acceptance curve at low frequencies.

The FWHM bunch length of the charge distribution of Eq. (7.55) is (1.33 ± 0.45) ps, corresponding to $\sigma_z = (200 \pm 70)\,\mu$m or $\sigma_t = (660 \pm 25)$ fs respectively. The measurement presented by Fig. 7.29 depicts the shortest bunch studied with the Martin-Puplett interferometer at the TTF linac. The result is in agreement with the shortest bunch length determined by longitudinal phase space rotations. Also the pulse shape, a narrow peak superimposed onto a wider basis, is consistent.

Measurements without Compression

The longitudinal bunch charge distribution has been measured without the use of the chicane compressor to investigate the applicability of the method in the limit of long bunch

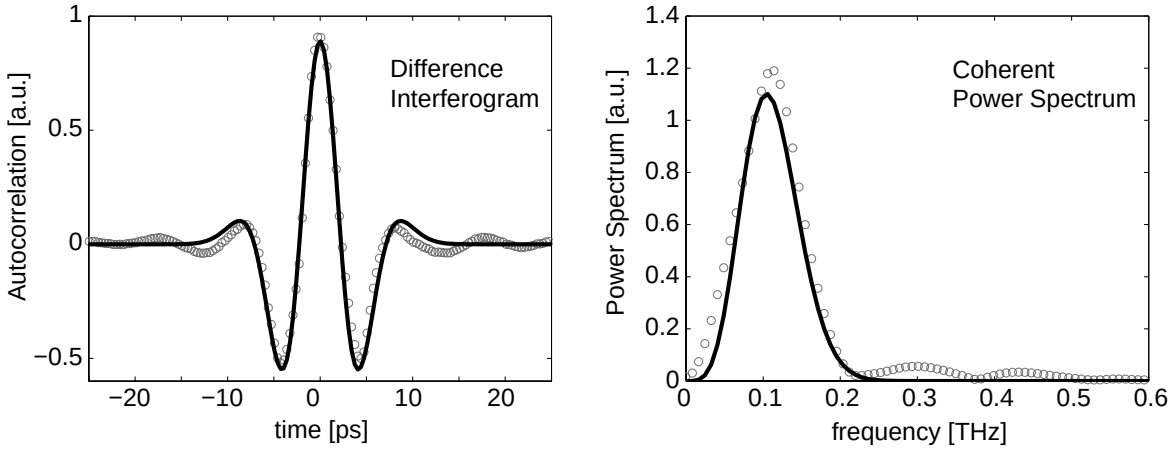


Figure 7.31: Interferogram and coherent power spectrum measured with the beam of the thermionic injector. Data are represented by circles. The solid line represents the prediction of the longitudinal bunch charge distribution of Eq. (7.55) using the interferometer model.

lengths. The injector parameters used for the streak camera measurements in chapter 6 have been applied. Figure 7.30 shows four interferograms measured by the Martin-Puplett interferometer for different phases of the gun rf field Φ. It is conspicuous that the shape of the interferogram is different from previous measurements. The shape can, in fact, not be predicted by the interferometer model. The model predicts, independent of the shape of the charge distribution, larger oscillations at the tail of the interferogram. The problem consists in the Fourier transformation of the measurement. The coherent power spectrum reaches merely a frequency of 200 GHz which is below the first minimum of the interferometer acceptance curve. The coherent power spectrum is suppressed in the entire frequency interval so that the analysis is very much impeded. The investigation of the FWHM of the autocorrelation function yields bunch lengths which are under-estimating the result obtained with the streak camera measurement by a factor of 2–4.

The present analysis is not applicable for coherent power spectra which do not exceed the frequency of the first minimum of the interferometer acceptance function. Only with the first appearance of frequency contributions larger than 250 GHz bunches shorter than $\sigma_t = 2\,\mathrm{ps}$ can be confidently predicted.

7.7.2 Measurements at the TTF Thermionic Injector

The TTF thermionic injector was operated at an average beam current of 5 mA and produced 30 μs long macropulses with a bunch to bunch repetition rate of 216 MHz. The bunch charge is 37 pC. The beam was accelerated to an energy of 80 MeV and transfered to the experimental area.

Figure 7.31 shows an interferogram and the coherent power spectrum. The small secondary maxima in the coherent power spectrum indicate a bunch length shorter than 2 ps. A Gaussian bunch charge distribution fitted to the data yields an rms bunch length

of $\sigma_z = 0.6$mm ($\sigma_t = 1.9$ ps). Further investigations of the thermionic injector bunch length using the Martin-Puplett interferometer have been performed by [50] yielding a minimum length of $\sigma_z = 0.5$ mm ($\sigma_t = 1.6$ ps).

7.8 Possible Improvements of the Interferometer

The Martin-Puplett interferometer is limited by the acceptance of the pyroelectric detectors suppressing frequencies due to an interference effect on the front and back side of the crystal. It is advisable to replace the detector by a Golay cell (photo-acoustic detector) having a flat acceptance in the in the frequency range between 30 GHz and 3 THz [64]. Golay-cells have a larger sensitive detector dimension which improves the low frequency acceptance.

The overall acceptance of the interferometer can be improved by wire grids wound with wires of 10 μm diameter and 30 μm spacing. The ratio of wire diameter and wire spacing of $a/d = 0.3$ is favorable for a flat acceptance of the beam splitter. The wire grid acceptance can further be improved by a rotation of the grids: a vertical orientation of the polarizer in the present setup improves the acceptance limit of the interferometer already by a factor of 1.4.

The transmission out of the beam pipe can be improved by the use of a crystalline quartz window. These windows are transparent for radiation up to 3 THz. A further improvement can be achieved only by the use of a diamond window, which is transparent in the entire spectrum of infrared radiation.

The acceptance of the pyroelectric detector can be improved by increasing the distance to the second parabolic mirror. Diffraction losses inside the beam pipe cannot be significantly reduced, because of the limited size of the pipe and the vacuum window. An interesting option is the use of a diffraction radiation screen, which is an aluminum foil with a circular hole at the center. The electron bunch is traveling through the hole whereas the coherent radiation is reflected from the foil yielding an almost "non-destructive" bunch length measurement [65].

Chapter 8

Hilbert Transform Spectroscopy

High-T_C Josephson junctions offer a new spectroscopic method to determine the longitudinal bunch form factor. The principle is to investigate the modification of the current-voltage characteristic of a Josephson junction due to incident radiation. Applying a Hilbert transformation to this modification the frequency spectrum of the radiation can be derived. Since the principle of Hilbert transform spectroscopy is based on a purely electric measurement, it offers the possibility of high-speed spectroscopy in the millimeter- and sub-millimeter wavelength regime.

8.1 Electric Properties of a Josephson Junction

8.1.1 The Josephson Effect

A Josephson junction consists of two superconductors separated by a thin insulating layer. The electrons in a superconductor form Cooper-pairs which can be described by a single macroscopic quantum mechanical wave function. If the insulating layer is sufficiently thin, Cooper-pairs will penetrate from one superconductor to the other by the quantum mechanical tunnel effect. The Josephson equations are

$$I_J = I_c \sin \phi(t) \tag{8.1}$$

$$\frac{d\phi}{dt} = \frac{2e}{\hbar} U(t) \tag{8.2}$$

where I_c is the critical current of the junction, $\phi(t)$ is the phase difference of the Cooper pair wave functions on both sides of the insulating layer and $U(t)$ is the voltage across the junction. For currents $|I| < I_c$ the dc Josephson effect occurs. According to (8.2) U vanishes in this case. The detection of microwave radiation is based on the ac Josephson effect, hence the junction is operated with a dc current $I = I_0 > I_c$, leading to a non-vanishing voltage U. Incident radiation modifies the current-voltage characteristic of the junction, and this change is used to determine the spectral distribution of the radiation.

Josephson junctions used for a spectral analysis in the range 100-1000 GHz have to be designed to have a negligible capacitance. Their electrical performance is then well described by the so-called Resistively Shunted Junction (RSJ) model. An equivalent circuit

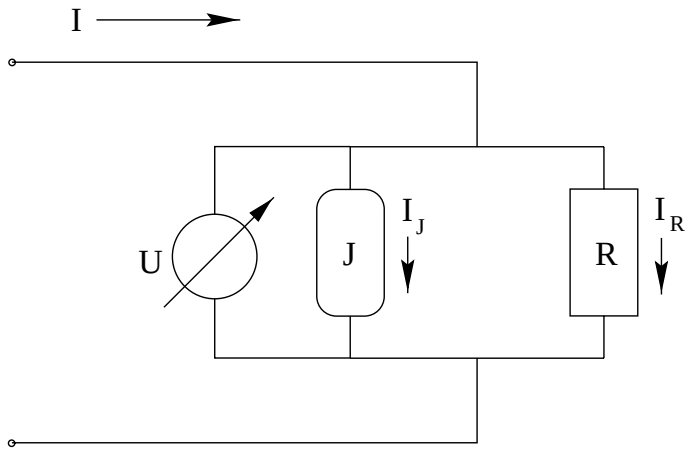


Figure 8.1: Equivalent circuit of a resistively shunted Josephson junction (RSJ model).

is shown in Fig. 8.1. Both Cooper pairs and unpaired electrons are able to tunnel through the insulating layer of the Josephson junction. An applied current I splits up into a Cooper-pair (or Josephson) current (I_J) and a single-electron "resistive" current (I_R). The Cooper pair current obeys the Josephson equations.

8.1.2 DC Characteristic of the Josephson Junction

The equivalent circuit for an "autonomous" Josephson junction (without incident microwave radiation) is shown in Fig. 8.1. The bias current of the junction is a pure dc current $I_0 > I_c$. According to Kirchhoff's law, the current I_0 splits into both branches of the circuit and the following equation holds:

$$I_0 = I_J + I_R = I_c \sin\phi + \frac{\hbar}{2eR}\frac{d\phi}{dt} \; . \tag{8.3}$$

Solving the differential equation for $\phi(t)$ and using Eq. (8.2), an expression for the time-dependent voltage $U(t)$ across the junction is derived. As shown in appendix E.1 the result is [66, 67]

$$U(t) = RI_c \cdot \frac{(I_0/I_c)^2 - 1}{I_0/I_c - \cos(\omega_0\, t)} \quad \text{for} \quad I_0 > I_c \tag{8.4}$$

where $\omega_0 = \frac{2e}{\hbar} RI_c \sqrt{(I_0/I_c)^2 - 1}$ is the Josephson frequency. An arbitrary constant phase has been omitted. This equation shows that for $I_0 > I_c$ an oscillating voltage $U(t)$ arises which derives from an alternating Cooper-pair current as well as a resistive single-electron current. The voltage $U(t)$ has a dc component and is not purely sinusoidal as can be seen from Fig. 8.2. For a bias current just above the critical current a strongly distorted sine wave is observed while with increasing bias current the oscillation becomes more and more sinusoidal. Taking the time-average of Eq. (8.4) one obtains (see appendix A)

$$\overline{U} = \left\{ \begin{array}{ll} 0 & \text{for} \quad I_0 \le I_c \\ R\sqrt{I_0^2 - I_c^2} & \text{for} \quad I_0 > I_c \end{array} \right\} \; . \tag{8.5}$$

The current-voltage characteristic of the junction, obtained by plotting I_0 as a function of $\overline{U}$, is shown as the dashed-dotted curve in Fig. 8.3.

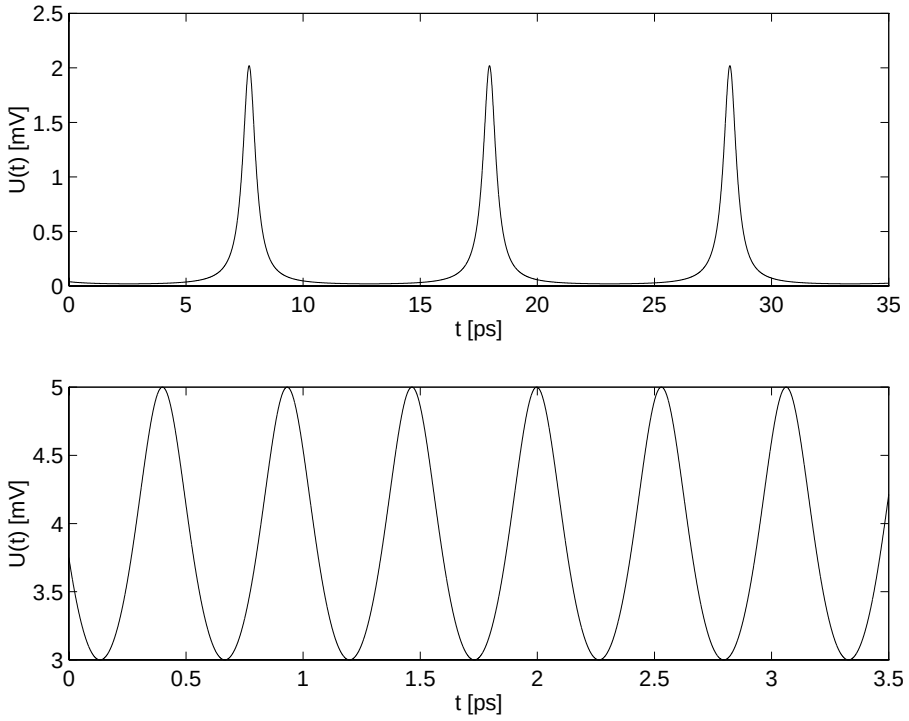


Figure 8.2: Time dependence of voltage U(t) across the Josephson junction for the autonomous case (no incident radiation). Top graph: $I_0/I_c = 1.02$, bottom graph: $I_0/I_c = 4$. The resistance R is assumed to be 1 Ω, the critical current is 1 mA.

8.1.3 Josephson Junction with Incident Radiation

The incident microwave radiation is modeled by a small sinusoidal ac current which is superimposed with the dc bias current. We consider first the case of monochromatic radiation, the generalization to a continuous spectrum is straight forward. The total bias current is now the sum of a dc component I and an ac component with amplitude I_s and frequency $\omega_s/2\pi$

$$I(t) = I + I_s \sin \omega_s t \; . \tag{8.6}$$

The generalization of Eq. (8.3) reads

$$I + I_s \sin \omega_s t = I_c \sin \phi + \frac{\hbar}{2eR} \frac{d\phi}{dt} \; . \tag{8.7}$$

The differential equation (8.7) has no analytic solution. It can be solved approximately if the amplitude I_s of the ac current, representing the incident radiation, is small compared to the dc bias current. A second-order perturbation approach [66, 67, 68], outlined in appendix E, yields a correction to the dc current

$$\Delta I = -\frac{1}{4I} \left(\frac{2eRI_c}{\hbar} \right)^2 \cdot \frac{I_s^2}{\omega_s^2 - \omega_0^2} \quad \text{for} \quad (\omega_s \neq \omega_0) \tag{8.8}$$

where

$$\omega_0 = \frac{2e\overline{U}}{\hbar} \tag{8.9}$$

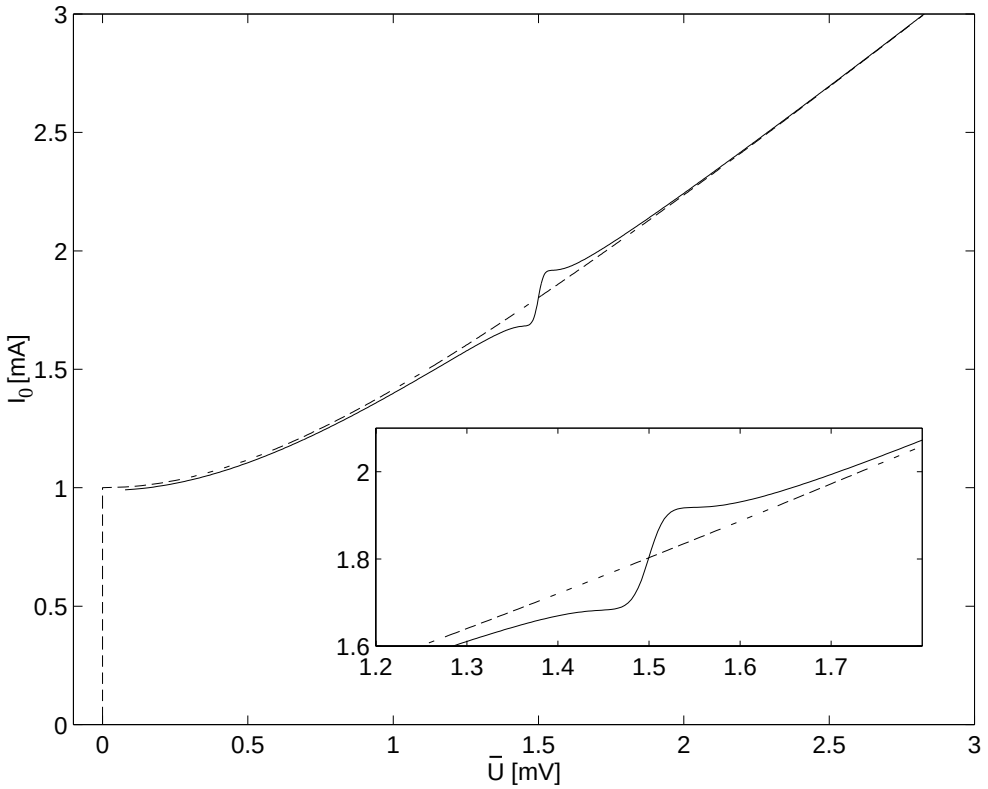


Figure 8.3: Dashed-dotted curve: time-averaged voltage across the junction as a function of the dc bias current. Solid curve: modification of dc characteristic curve due to monochromatic incident radiation. The dc current-voltage characteristic acquires a step at the voltage $\overline{U} = \hbar/2e\omega_s$. The height of the step is proportional to the incident radiation power. The RSJ model is assumed.

denotes the frequency of the unperturbed Josephson oscillation at the given dc bias. The frequency ω_0 is often called the working point of the junction, since it gives the frequency of the unperturbed Josephson oscillation. The working point is changed by varying the dc bias current.

Equation (8.8) diverges for $\omega_0 = \omega_s$, but this divergence disappears if the internal noise in the junction is taken into account. With noise included the equation can be written as

$$\Delta I = -\frac{1}{8I\omega_0}\left(\frac{2eRI_c}{\hbar}\right)^2 \cdot \left(\frac{\omega_s - \omega_0}{(\omega_s - \omega_0)^2 + \gamma^2} - \frac{\omega_s + \omega_0}{(\omega_s + \omega_0)^2 + \gamma^2}\right) \tag{8.10}$$

where γ is a damping term introduced by the noise. Hence the junction responds to the incident monochromatic radiation in such a way that the dc current-voltage characteristic acquires a step ΔI in current at the voltage $\overline{U} = \hbar/2e\omega_s$. The height of the step is proportional to the incident radiation power. This is shown schematically in Fig. 8.3.

8.1.4 Hilbert Transform Spectrometry

Incident radiation consisting of a number of discrete spectral lines will lead to corresponding discrete current steps in the I-U curve. Now we want to demonstrate that the

Josephson junction, as described by the RSJ model, may equally well serve as a detector for electromagnetic radiation with a continuous spectral distribution $S_i(\omega_s)$ [69]. The basic point is the observation that the voltage response of the junction depends quadratically on the amplitude I_s of the ac current (see Eq. (8.10)), hence intensities can be added. For this reason the voltage response to a continuous radiation spectrum is simply obtained by integrating Eq. (8.8) over the frequency range of the radiation, taking the spectral intensity $S_i(\omega_s)$ as a weight factor.

$$\Delta I = -\left(\frac{2e}{\hbar}\right)^2 \frac{R^2 I_c^2}{4I} \int_0^\infty \frac{S(\omega_s)\, d\omega_s}{\omega_s^2 - \omega_0^2} \,. \tag{8.11}$$

The pole in the integrand requires a careful mathematical treatment. The equation can be written in the following way

$$\Delta I = -\frac{1}{8I\omega_0} \left(\frac{2eRI_c}{\hbar}\right)^2 \mathcal{P} \int_{-\infty}^\infty \frac{S(\omega_s)\, d\omega_s}{\omega_s - \omega_0} = -\frac{\pi}{8I\omega_0} \left(\frac{2eRI_c}{\hbar}\right)^2 H[S(\omega_s)] \tag{8.12}$$

where $\mathcal{P}$ denotes the principal value of the integral and

$$H[S(\omega_s)] = \frac{1}{\pi}\, \mathcal{P} \int_{-\infty}^\infty \frac{S(\omega_s)\, d\omega_s}{\omega_s - \omega_0} \tag{8.13}$$

is the so-called Hilbert transform (see appendix E) of the radiation spectrum $S(\omega_s)$. Note that by evaluating the principal value of the integral one can use the noise-free Eq. (8.8) instead of (8.10). The spectral intensity of the incident radiation, computed by the inverse Hilbert transform of (8.12), is

$$S(\omega_s) = H^{-1}(g(\omega_0)) \tag{8.14}$$

with the function

$$g(\omega_0) = \frac{8}{\pi} \left(\frac{\hbar}{2e}\right)^2 \frac{\Delta I(\omega_0) I(\omega_0) \omega_0}{R^2 I_c^2} \,. \tag{8.15}$$

Equation (8.15) shows the quantities that have to be measured to determine the radiation spectrum. The current-voltage characteristic of the Josephson junction has to be scanned both with and without incident radiation. During the scan the bias current is increased in small steps. At each step the Josephson frequency $\omega_0 = 2eU/\hbar$ and the modification $\Delta U(\omega_0)$ due to the radiation are measured. The current modification ΔI is derived from ΔU via the differential resistance $R_d = d\overline{U}/dI$ of the unperturbed I-U curve. These quantities are used to compute the function $g(\omega_0)$ which is Hilbert-transformed to obtain the spectral intensity $S(\omega_s)$ of the incident radiation. The square root of $S(\omega_s)$ then yields the longitudinal bunch form factor.

8.2 The Josephson Junction

High-T_C Josephson junctions have been fabricated by epitaxial growth of $YBa_2Cu_3O_{7-x}$ on $NdGaO_3$ bicrystal substrates [70]. A schematic view of the detector which incorporates the antennas for millimeter and sub-millimeter wave detection is shown in Fig. 8.4. The size of the antenna varies from 1.8 mm at the outer bound to several micrometers

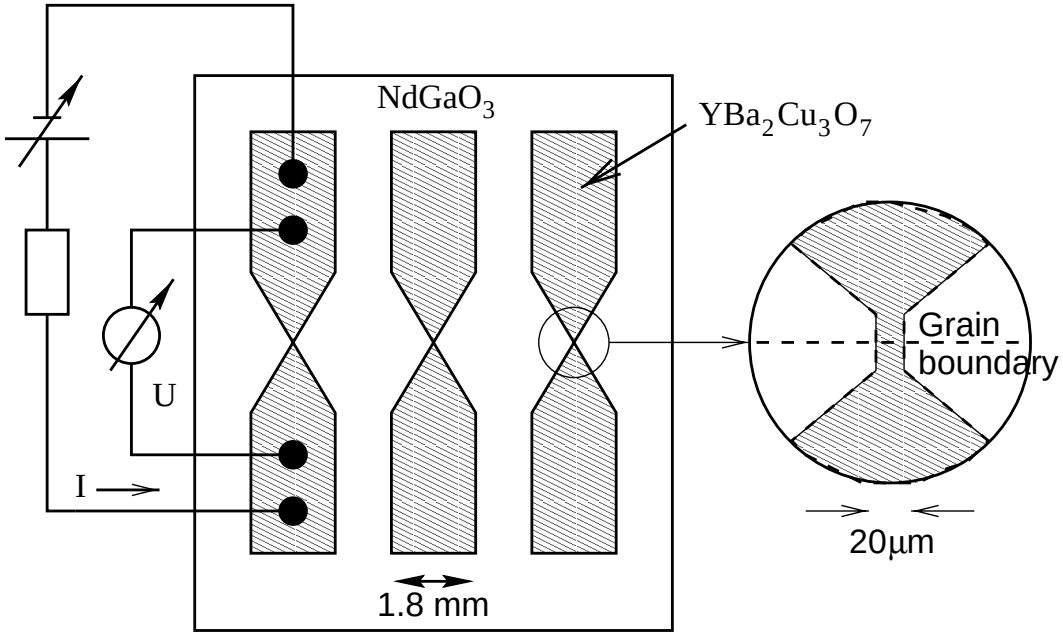


Figure 8.4: A schematic view of the Josephson junction used as a detector for millimeter and sub-millimeter wave radiation.

at the center. Here, a grain boundary in the substrate cuts the thin film of the high-T_c superconductor, which then works as a Josephson junction. The electrical properties of grain boundary high-T_c junctions are very close to those predicted by the RSJ model [71]. An electrical circuit to bias the junction with a dc current and to measure the potential difference across the contact is connected to the antennas. The junction features a large dynamic range of approximately 10^5 and a high sensitivity of $\approx 10^{-14}$ W/Hz$^{1/2}$ Noise Equivalent Power (NEP) to millimeter- and sub-millimeter radiation [72]. The resolution is around 1 GHz in the temperature range from 4 to 78 K [70].

The Josephson spectrometer was mounted at the same diagnostic station of the linac which had been used to determine the bunch length with the Martin-Puplett interferometer. Coherent transition radiation generated at the front face of an aluminum foil was guided through a quartz window to the antenna of the Josephson junction, using an arrangement of mirrors and wire grid polarizers. A grid served as a low pass filter for millimeter radiation. The junction was installed inside a pumped aluminum pipe placed in a liquid nitrogen bath ($T = 78\,\mathrm{K}$). The millimeter wavelength radiation was transfered to the junction through an over-sized cylindrical wave-guide equipped with a copper horn antenna for better radiation coupling[1]. The Josephson junction was current-biased. The voltage response signal of the junction was amplified by a factor of 10^4, time-averaged by a digital oscilloscope and recorded as a function of the unperturbed Josephson frequency ω_0, derived from the time-averaged junction voltage $\overline{U}$. The operation of the spectrometer was controlled by a personal computer through an IEEE-488 interface.

[1] see also [73] for a more complete description of the experimental setup.

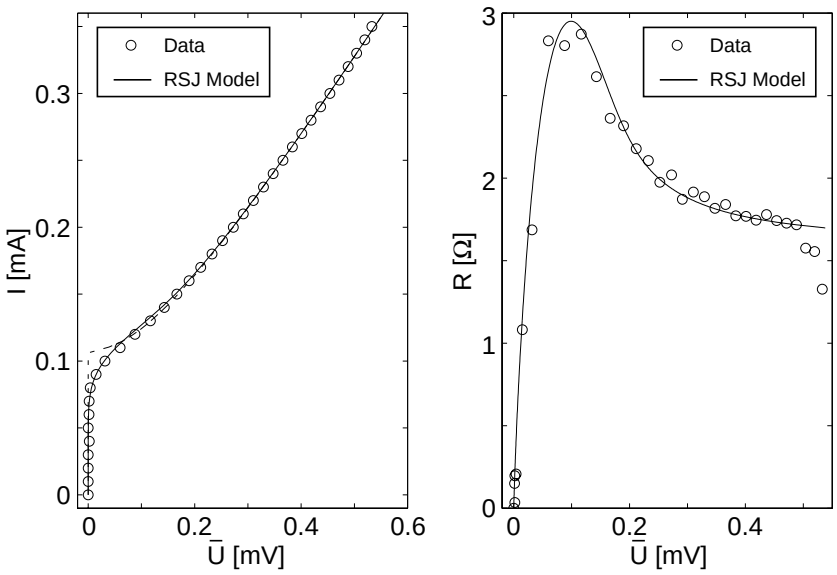


Figure 8.5: Left: the current-voltage characteristic of the Josephson junction without incident radiation. Measured data points are marked by circles. Dashed-dotted line: the theoretical I-U curve (8.5) with fitted values for I_c and R. Solid curve: convolution of the theoretical I-U curve with Gaussian-distributed noise. Right: the differential resistance R_d as determined from differentiation of the I-U characteristic (solid curve), compared with point-to-point difference quotients (circles).

8.3 Bunch Length Measurements

The TTF thermionic gun was operated with the same parameters as for the interferometer measurements. The gun produced bunches of $2.3 \cdot 10^8$ electrons at a repetition rate of 216 MHz. Te macropulse length was 30 μs at a repetition rate of 2 Hz. The buncher cavity rf phase was adjusted for optimum bunching.

8.3.1 The Intrinsic Parameters of the Junction

Figure 8.5 shows the characteristic I-U curve of the Josephson junction used. The measured data points are presented as circles. A non-linear characteristic caused by the ac Josephson effect is observed at low bias currents while an Ohmic characteristic (linear relation between potential difference and bias current) is observed for large bias currents. The intrinsic parameters I_c and R of the junction are measured by fitting the theoretical I-U curve (8.5) to the data. The result is

$$I_c = 0.11 \text{ mA} \qquad R = 1.62\,\Omega\ . \tag{8.16}$$

The fit is shown as the dashed-dotted line in the left graph of Fig. 8.5. The agreement with the data is quite satisfactory except in the vicinity of I_c where a gradual increase of the voltage is measured instead of the steep rise predicted by theory. The difference is due to noise in the junction. A better representation of the experimental I-U curve is

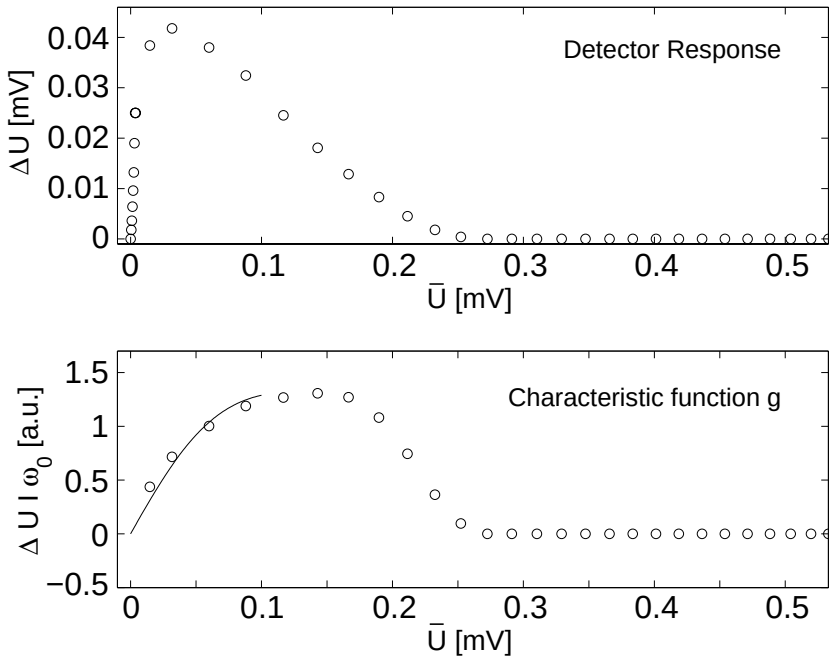


Figure 8.6: The analysis of the spectroscopic measurement to obtain the coherent transition radiation spectrum. Upper graph: The detector response ΔU as a function of $\bar{U}$. Lower graph: The characteristic function $g(\omega_0)$, as defined by Eq. (8.15), plotted versus $\bar{U} = \hbar/2e\omega_0$. The solid curve shows the extrapolation of $g(\omega_0)$ for small $\bar{U}$. The measured characteristic I-U curve of the Josephson junction without radiation is shown in Fig. 8.5.

obtained if the theoretical curve is convoluted with a Gaussian noise distribution.

$$\bar{U}(I) = \frac{1}{\sqrt{(2\pi\sigma^2)}} \int R\sqrt{I'^2 - I_c^2}\, \exp\left(-\frac{(I'-I)^2}{2\sigma^2}\right) dI' \; . \tag{8.17}$$

The variance σ is a fit parameter. The resulting solid curve in Fig. 8.5a, corresponding to $\sigma = 0.02$ mA, provides a perfect description of the data.

The differential resistance of the junction $R_d = d\bar{U}/dI$ is computed by differentiation of the I-U curve with noise (8.17) or by taking the slopes between adjacent data points. The right graph of Fig. 8.5 shows that both methods are in good agreement. In the further analysis, the differential resistance obtained from the I-U fit curve is used to avoid the point-to-point fluctuations in the data.

8.3.2 The Spectroscopic Measurement

The spectroscopic information is contained in the difference $\Delta\bar{U}$ between the characteristic curves with and without radiation, which is shown in the upper graph in Fig. 8.6. $\Delta\bar{U}$ is transformed to ΔI by $\Delta I = \Delta\bar{U}/R_d$, where R_d is the differential resistance shown in the right graph of Fig. 8.5. The detector current response ΔI, the dc bias current I and the time-averaged voltage across the junction $\bar{U}$ are multiplied to compute the characteristic function $g(\omega_0)$ as defined by Eq. (8.15). $g(\omega_0)$ is shown in the lower plot in Fig. 8.6. The

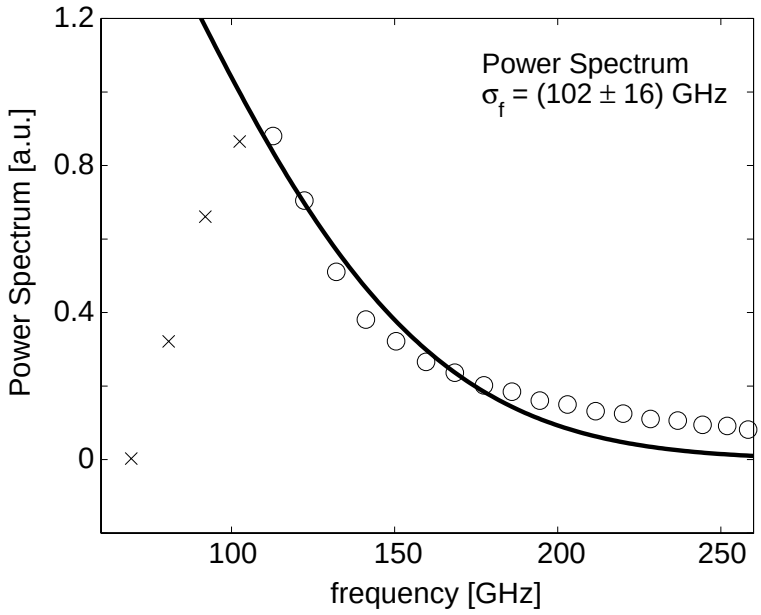


Figure 8.7: The coherent radiation spectrum as obtained from a discrete Hilbert transform of the characteristic function g. Corrections must be applied for data points marked with crosses. The decrease below $f = 100$ GHz is due to the WR-10 waveguide cut-off. These data points are not used in the analysis. The solid curve indicates a Gaussian fit to the power spectrum.

determination of ΔI is problematic for small frequencies (i. e. dc bias currents close to I_c). The differential resistance R_d drops to zero when I approaches I_c. The data at small values of $\bar{U}$ are quite sensitive to measurement errors and noise in the junction, which has a significant influence on the differential resistance in the vicinity of I_c. Therefore the frequency range $0 < f_0 < 50$ GHz has been omitted from the present analysis. Since, however, $g(\omega_0)$ is needed at all frequencies to perform the Hilbert transform, a smooth extrapolation function of the form

$$g(\omega_0) \propto \frac{\omega_0}{\omega_0^2 + const} \quad \text{for} \quad f_0 = \omega_0/(2\pi) < 50 \text{ GHz} \; . \tag{8.18}$$

is used in the range $0 < f_0 < 50$ GHz, shown as a solid curve in Fig. 8.6. The extrapolation function has to vanish at $\bar{U} = 0$ to generate an antisymmetric characteristic function $g(\omega_0)$. The Hilbert transformation of $g(\omega_0)$ then leads to a symmetric power spectrum.

The intensity spectrum was calculated using an algorithm of discrete Hilbert-transform [42]. Figure 8.7 shows the evaluated coherent radiation spectrum. The spectrum is plotted in the frequency range between 60 and 260 GHz. The power spectrum has a maximum at a frequency close to 100 GHz. The decrease towards smaller frequencies is explained by transmission losses of the radiation for frequencies close to cut-off frequency (60 GHz) of the WR-10 waveguide, diffraction of the radiation delivery line, transmission losses in the quartz window and diffraction of the bunch electromagnetic fields at the finite size transition radiator. These effects have been discussed in detail in chapter 7.

8.3.3 Data Analysis

The main uncertainty of the experiment originates from the wavelength-dependent acceptance of the detector system. Read-out errors of the voltage response ΔU, which was determined from a digital oscilloscope after averaging over 15 seconds, cause additional uncertainties. The precision of the read-out of the Josephson voltage is estimated to be better than 1 μV, the bias current power supply stability to 1 μA. The analysis of this proof-of-principle experiment has been carried out without a detailed consideration of the spectral acceptance function. The main interest was to show the applicability of a Josephson junction as detector for coherent transition radiation.
A Gaussian-shaped frequency spectrum of the radiation is assumed for the determination of the rms bunch length. A Gaussian fit applied to the data, shown as a solid curve in Fig. 8.7, results in

$$\sigma_f = (102 \pm 16)\ \mathrm{GHz}\ . \tag{8.19}$$

σ_f refers to the intensity spectrum which is proportional to the square of the form factor. The rms bunch length is therefore given by

$$\sigma_t = \frac{1}{2\pi\sqrt{2}\sigma_f} = 1.2\,\mathrm{ps}\ . \tag{8.20}$$

The resulting rms bunch length is smaller than the bunch lengths determined by the Martin-Puplett interferometer. The experiment, however, shows that a Josephson junction can be applied to record the form factor of picosecond electron bunches and that a pulse length of correct magnitude is derived. Improvements can be expected from a quasi-optical coupling of the radiation to the junction and an improved electronic read-out. A special cryostat equipped with a quartz window is in preparation. The bandwidth of the read-out electronics will be adapted to a bandwidth sufficient to measure selected bunches within TTF macropulses [74]. The experience collected during the proof-of-principle experiment and the improvements proposed show great promise that Hilbert transform spectroscopy will become a quick and reliable technique to determine sub-picosecond electron bunch lengths.

Chapter 9

Conclusion and Outlook

Transverse phase space tomography has been successfully applied to determine the beam emittance and beam parameters at the TESLA Test Facility linac. The beam emittance produced by the photo injector was optimized by adjusting the gun solenoids to provide a compensation of the correlated emittance growth. The solenoid currents leading to a normalized beam emittance of $\gamma\epsilon_x = (5.5 \pm {}^{0.7}_{0.9}) \cdot 10^{-6}\,\mathrm{m}$ and $\gamma\epsilon_y = (9.5 \pm {}^{1.7}_{1.8}) \cdot 10^{-6}\,\mathrm{m}$ are $I_{\mathrm{primary}} = 165\,\mathrm{A}$ and $I_{\mathrm{secondary}} = 90\,\mathrm{A}$. The vertical emittance agrees with an emittance measurement performed with a screen of narrow horizontal slits. In the tomographic method it turned out to be essential to include linearized space charge forces in the beam transfer computations and to demand self-consistency between the reconstructed beam parameters and the parameters assumed for the beam transfer computation. The resulting beam parameters have been successfully used as input values for beam transfer computations, yielding a magnetic lattice with 100% beam transmission to the end of the linac.

Phase space tomography has also been used to determine the transverse phase space distribution of the beam produced by the thermionic injector. At a beam current of $I_{\mathrm{beam}} = 3\,\mathrm{mA}$, a normalized emittance of $\gamma\epsilon_x = (3.8 \pm {}^{0.4}_{0.7}) \cdot 10^{-6}\,\mathrm{m}$ and $\gamma\epsilon_y = (3.3 \pm {}^{0.4}_{0.7}) \cdot 10^{-6}\,\mathrm{m}$ has been measured. Due to limited optical resolution it was not possible to obtain reliable numbers for the transverse emittance and the beam parameters behind the first rf module. Measurements with an improved optical system are needed.

The longitudinal charge distribution has been investigated using a streak camera and rotations of the longitudinal phase space density. The measurements of the streak camera ($\sigma_t = 2\,\mathrm{ps}$ resolution) reliably determined the rms bunch length and the shape of the longitudinal charge distribution of the photo injector beam. The bunch length varied between $\sigma_z = (1.95 \pm 0.08)\,\mathrm{mm}$ and $\sigma_z = (4.72 \pm 0.09)\,\mathrm{mm}$ depending on the rf phase of the gun cavity. The longitudinal bunch shape agrees well with a Gaussian distribution. Longitudinal phase space rotations yield an rms injector bunch length of $\sigma_z = (990 \pm 90)\,\mu\mathrm{m}$. The injector bunch length determined by the two methods is compatible, because the laser pulse length was reduced by a factor of 2 between the two measurements.

The proper operation of the magnetic chicane compressor has been demonstrated by longitudinal phase space rotations and the Martin-Puplett interferometer yielding a minimum rms bunch length of $\sigma_z = (350 \pm 130)\,\mu\mathrm{m}$ and $\sigma_z = (200 \pm 70)\,\mu\mathrm{m}$ respectively. The pulse

shape reconstructed by both techniques is similar: a narrow peak superimposed onto a wider basis. The shape of the charge distribution can be explained by an uncorrelated bunch energy distribution in front of the chicane compressor.

A Martin-Puplett interferometer and a Josephson junction have been applied as far-infrared coherent transition radiation spectrometers. Considerable effort has been made to evaluate the spectral acceptance of the Martin-Puplett interferometer. The measurement of the coherent transition radiation power spectrum is affected by diffraction effects at the finite size transition radiator, the transmission of the quartz window, the transmission and the reflectivity of the wire grids, the radiation diffraction in the interferometer and the acceptance of the pyroelectric detectors. In spite of the fairly large corrections, it was possible to model the autocorrelation and the coherent power spectrum of the compressed pulses and to successfully determine the rms bunch length and the bunch shape. However, a comparison of bunch length measurements of the uncompressed beam of the photo injector showed a discrepancy between the interferometer and streak camera results. The Martin-Puplett interferometer is not suited for bunch lengths exceeding $\sigma_t = 2\,\mathrm{ps}$ because of severe acceptance limitations at frequencies below 100 GHz.

A Josephson junction has been applied as a frequency-selective far-infrared spectrometer for the first time to determine the longitudinal bunch form factor. The Josephson junction offers a possibility for high-speed spectroscopy in the millimeter- and sub-millimeter wavelength range. A proof-of-principle measurement has been performed at the TTF linac using the thermionic injector beam. It is planned to improve the Josephson junction detector by using a cryostat with direct optical coupling of the radiation. The read-out electronics will be adjusted to a bandwidth sufficient to measure selected bunches within TTF macropulses. The Josephson spectrometer will be set up in parallel with a Martin-Puplett interferometer to have a direct comparison of both methods. The measurement of a particular electron bunch within a macropulse will be possible by triggering the apparatus on the same bunch at every beam crossing. The other option is a measurement of an average bunch length within a macropulse by sampling the current-voltage characteristic of the junction within a single macropulse.

Appendix A

Beam Dynamics and Parameters

The beam transfer, the phase space description of charged particle beams and the first order beam-matrix formalism for the definition of the beam parameters will be outlined in this section. A beam line is a set of magnetic elements and accelerating structures placed along a reference path. The reference particle follows the reference trajectory, the path through the center of the magnetic elements, and has the design momentum. The transverse coordinates used in this chapter are labeled x for the horizontal plane and y for the vertical plane. The longitudinal coordinate is labeled l.

A.1 The Transfer Matrix Formalism

A charged particle in a beam line can be represented by a six-dimensional vector $\vec{X}$

$$\vec{X} = (x, x', y, y', l, \delta) \tag{A.1}$$

where x and y denote the horizontal and vertical displacement of the particle, x' and y' the horizontal and vertical angle of the particle's trajectory with respect to the reference trajectory. l and δ denote the longitudinal displacement and the fractional momentum deviation ($\delta = \Delta p/p$) with respect to the reference particle. The knowledge of $\vec{X}$ at an initial position i of the beam line determines the particle coordinates at a final position f. If the magnetic fields depend linearly on the deviation of the particle from the reference path, beam transfer can be reduced to the process of matrix multiplication

$$(X_f)_k = \sum_{k=1}^{6} M_{kl} \, (X_i)_l \tag{A.2}$$

where M is a 6×6 square matrix, called the beam transfer matrix.

The entire beam line can be modeled by multiplying transfer matrices sequentially from the end to the beginning of the line, hence

$$M_{tot} = M_n \cdot M_{n-1} \cdot ... \cdot M_2 \cdot M_1 \tag{A.3}$$

and by replacing M in Equation (A.2) by the product matrix M_{tot}.

A.2 Beam Transfer Matrices

Drift Space A drift space is a region free of electromagnetic fields. The length of the drift space is denoted by L. The transfer matrix is

$$M_D(L) = \begin{pmatrix} 1 & L & 0 & 0 & 0 & 0 \\ 0 & 1 & 0 & 0 & 0 & 0 \\ 0 & 0 & 1 & L & 0 & 0 \\ 0 & 0 & 0 & 1 & 0 & 0 \\ 0 & 0 & 0 & 0 & 1 & 0 \\ 0 & 0 & 0 & 0 & 0 & 1 \end{pmatrix} \tag{A.4}$$

Quadrupole Magnet A quadrupole magnet focuses the beam in one plane, defocuses it in the other. The transfer matrix for a horizontally focusing quadrupole magnet of strength k and length L is

$$M_Q(k,L) = \begin{pmatrix} \cos(\Omega) & \frac{1}{\sqrt{k}}\sin(\Omega) & 0 & 0 & 0 & 0 \\ -\sqrt{k}\sin(\Omega) & \cos(\Omega) & 0 & 0 & 0 & 0 \\ 0 & 0 & \cosh(\Omega) & \frac{1}{\sqrt{k}}\sinh(\Omega) & 0 & 0 \\ 0 & 0 & \sqrt{k}\sinh(\Omega) & \cosh(\Omega) & 0 & 0 \\ 0 & 0 & 0 & 0 & 1 & 0 \\ 0 & 0 & 0 & 0 & 0 & 1 \end{pmatrix} \tag{A.5}$$

where $\Omega = \sqrt{k} \cdot L$. For a vertically focusing quadrupole magnet, the upper left block matrix $M_{q,ij}$, $1 \leq i,j \leq 2$, and the middle block matrix $M_{q,ij}$, $3 \leq i,j \leq 4$, have to be interchanged.

Dipole Sector Magnet In a dipole sector magnet the central trajectory has a radius of curvature R and exits perpendicular to the pole-face boundaries. The deflection angle of the beam is α. The transfer matrix is

$$M_B(R,\alpha) = \begin{pmatrix} \cos(\alpha) & R\sin(\alpha) & 0 & 0 & 0 & R(1-\cos(\alpha)) \\ -\frac{1}{R}\sin(\alpha) & \cos(\alpha) & 0 & 0 & 0 & \sin(\alpha) \\ 0 & 0 & 1 & L & 0 & 0 \\ 0 & 0 & 0 & 1 & 0 & 0 \\ -\sin(\alpha) & -R(1-\cos(\alpha)) & 0 & 0 & 1 & -R(\alpha-\sin(\alpha)) \\ 0 & 0 & 0 & 0 & 0 & 1 \end{pmatrix} \tag{A.6}$$

Rectangular Dipole Magnet The rectangular dipole magnet consists of straight pole-face boundaries which are not perpendicular to the central beam trajectory. The magnet can be described by a combination of a dipole sector magnet and a "magnetic wedge" of angle ψ_i at the entrance ($i = 1$) and the exit ($i = 2$) of the magnet [75]. ψ denotes the rotation of the pole-face with respect to the orientation of a sector magnet pole face. The transfer matrix yields

$$M_R(R,\alpha,\psi) \quad = \quad M_F(\psi) \cdot M_B(R,\alpha) \cdot M_F(\psi) \qquad \text{with} \tag{A.7}$$

$$M_F(\psi_i) = \begin{pmatrix} 1 & 0 & 0 & 0 & 0 & 0 \\ \tan(\psi_i)/R & 1 & 0 & 0 & 0 & 0 \\ 0 & 0 & 1 & 0 & 0 & 0 \\ 0 & 0 & -\tan(\psi_i)/R & 1 & 0 & 0 \\ 0 & 0 & 0 & 0 & 1 & 0 \\ 0 & 0 & 0 & 0 & 0 & 1 \end{pmatrix}$$

The sign convention is such that $\psi_i > 0$ denotes horizontal defocusing and vertical focusing.

Standing Wave Cavity The beam gains energy (ΔE) and experiences focusing while traveling through a standing wave cavity of length l. The transfer matrix is

$$M_S(\Delta E, \phi, l) = \begin{pmatrix} \cos(a) - \sqrt{2}\sin(a) & \frac{\sqrt{8}\, lE\, \sin(a)}{\Delta E} & 0 & 0 & 0 & 0 \\ \frac{-3\,\Delta E\, \sin(a)}{\sqrt{8}\, l\,(E+\Delta E)} & \frac{EK}{(E+\Delta E)} & 0 & 0 & 0 & 0 \\ 0 & 0 & \cos(a) - \sqrt{2}\sin(a) & \frac{\sqrt{8}\, lE\, \sin(a)}{\Delta E} & 0 & 0 \\ 0 & 0 & \frac{-3\,\Delta E\, \sin(a)}{\sqrt{8}\, l\,(E+\Delta E)} & \frac{EK}{(E+\Delta E)} & 0 & 0 \\ 0 & 0 & 0 & 0 & 1 & 0 \\ 0 & 0 & 0 & 0 & 0 & \frac{E}{(E+\Delta E)} \end{pmatrix} \quad \text{(A.8)}$$

where $a = \log\left(1 + \Delta E/(\sqrt{8}\, E)\right)$, $K = \cos(a) + \sqrt{(2)}\sin(a)$ [76]. E denotes the injection beam energy. Equation (A.8) holds for on-crest acceleration of relativistic beams.

Coordinate Rotation A coordinate rotation of the transverse coordinates is described by a rotation matrix

$$M_R(\beta) = \begin{pmatrix} \cos(\beta) & 0 & \sin(\beta) & 0 & 0 & 0 \\ 0 & \cos(\beta) & 0 & \sin(\beta) & 0 & 0 \\ -\sin(\beta) & 0 & \cos(\beta) & 0 & 0 & 0 \\ 0 & -\sin(\beta) & 0 & \cos(\beta) & 0 & 0 \\ 0 & 0 & 0 & 0 & 1 & 0 \\ 0 & 0 & 0 & 0 & 0 & 1 \end{pmatrix} \quad \text{(A.9)}$$

The angle β denotes the angle of rotation. It is possible to describe the beam transfer through a vertical bend or a skew quadrupole by multiplying matrix (A.9) in front and behind of matrices (A.6) and (A.5) with the respective coordinate rotation angle of $\pm\pi/2$ and $\pm\pi/4$.

A.3 First Order Beam Matrix Formalism

In an accelerator it is often of more concern to study the dynamics of a bunch of particles rather than the single particle motion. Every particle in a bunch, in case of the TESLA Test Facility there are up to 10^{10} electrons, appears as a point in a six-dimensional phase space whose coordinates are x, x', y, y', l, and δ. Assume an arbitrary charge distribution $\rho(\zeta)$, where $\zeta = (\zeta_1, \zeta_2, \zeta_3, \zeta_4, \zeta_5, \zeta_6)$ denotes the phase space variables $(x, x', y, y', l, \delta)$. The characteristics of the charge distribution (transverse beam width, transverse angular divergence, bunch length and momentum deviation) can be described by a statistical approach using the first moments α_j and the second moments σ_{ij}, $1 \leq i, j \leq 6$, of the

charge distribution

$$\alpha_j = \int \zeta_j \, \rho(\zeta) \, d\zeta \tag{A.10}$$

$$\sigma_{ij} = \int (\zeta_i - \alpha_i)(\zeta_j - \alpha_j) \, \rho(\zeta) \, d\zeta \, . \tag{A.11}$$

The α_j define the beam centroid coordinates in phase space. The second moments form the covariance matrix σ of the bunch charge distribution ρ. The diagonal elements σ_{jj} represent the variances of the phase space coordinates, the off-diagonal elements σ_{ij}, $i \neq j$, the covariances of the respective coordinates. The matrix σ is called the beam matrix.

The diagonal elements of the beam matrix describe the transverse beam width (σ_{11} in the horizontal and σ_{33} in the vertical plane), the transverse angular divergence (σ_{22} in the horizontal and σ_{44} in the vertical plane), the bunch length (σ_{55}) and the fractional momentum deviation (σ_{66}). The off-diagonal elements describe covariances of the transverse planes (σ_{12}, σ_{34}), coupling between the transverse planes (σ_{13}, σ_{14}, σ_{23} and σ_{24}) and the coupling between the transverse and longitudinal coordinates (σ_{15}, σ_{16}, σ_{25}, σ_{26}, σ_{35}, σ_{36}, σ_{45} and σ_{46}). Since the beam matrix elements describe the characteristics of the bunch charge distribution in six-dimensional phase space, they are called the beam parameters.

As an example, consider a two-dimensional Gaussian charge distribution

$$\rho_2(x, x') = \exp\left(-\frac{x^2}{2\sigma_{11}} + \frac{\sigma_{12}}{\sigma_{11}\sigma_{22}} x x' - \frac{x'^2}{2\sigma_{22}} \right) \tag{A.12}$$

which can be represented by an ellipse in the (x, x') phase space. A contour line of ρ_2 is defined by $\rho_2(x, x') = \exp(C)$ with

$$\sigma_{22} x^2 - 2\sigma_{12} x x' + \sigma_{11} x'^2 = C = \text{constant} \tag{A.13}$$

C defines the phase space area enclosed by the contour line. The ellipse given by Equation (A.13) can be rewritten in terms of a two-dimensional beam matrix σ_2 yielding

$$\vec{X}^T \sigma_2^{-1} \vec{X} = C \tag{A.14}$$

where $\vec{X}^T$ is the transpose of the coordinate vector $\vec{X}$. σ_2 denotes the real, positive definite and symmetric beam matrix. In particular, it is

$$\sigma_2 = \begin{pmatrix} \sigma_{11} & \sigma_{12} \\ \sigma_{12} & \sigma_{22} \end{pmatrix}, \quad \sigma_2^{-1} = \frac{1}{\det \sigma} \begin{pmatrix} \sigma_{22} & -\sigma_{12} \\ -\sigma_{12} & \sigma_{11} \end{pmatrix}, \quad \vec{X} = \begin{pmatrix} x \\ x' \end{pmatrix} \tag{A.15}$$

so that Equation (A.13) becomes

$$\sigma_{22} x^2 - 2\sigma_{12} x x' + \sigma_{11} x'^2 = \det \sigma_2 \, . \tag{A.16}$$

The constant C of Equation (A.13) is evaluated to be the determinant of the σ_2 matrix. The ellipse described by Equation (A.16) is shown in Figure A.1 along with the physical interpretation of the beam matrix elements. $\sqrt{\sigma_{11}}$ defines the horizontal spatial extent, $\sqrt{\sigma_{22}}$ the angular extent of phase space occupied by the bunch. The off-axis element σ_{12} is a measure of the covariance of the angular and spatial coordinate, i. e. of the orientation

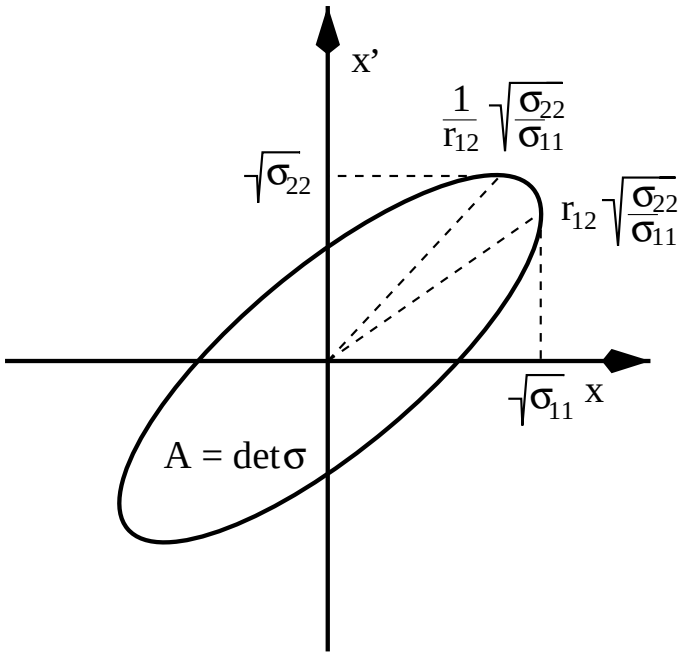


Figure A.1: The horizontal phase space ellipse and the physical interpretation of the beam matrix elements.

(tilt) of the ellipse. The area enclosed by the ellipse is $A = \pi \cdot \det\sigma$.

A six-dimensional ellipsoid can be expressed in terms of Equation (A.14) as well. The physical interpretation of the elements of the six-dimensional beam matrix is straight forward: the square roots of the diagonal elements describe the extent of the phase space ellipsoid on the respective coordinate axis. This is in particular

- $\sqrt{\sigma_{11}}$: the width of the beam ellipsoid in the horizontal plane.
- $\sqrt{\sigma_{22}}$: the horizontal angular divergence of the beam ellipsoid.
- $\sqrt{\sigma_{33}}$: the width of the beam ellipsoid in the vertical plane.
- $\sqrt{\sigma_{44}}$: the vertical angular divergence of the beam ellipsoid.
- $\sqrt{\sigma_{55}}$: the longitudinal extent of the beam ellipsoid
- $\sqrt{\sigma_{66}}$: the fractional momentum deviation of the beam ellipsoid.

The off-diagonal elements describe the covariance of the phase space ellipsoid with respect to a pair of its coordinate axis. A convenient quantity to measure the covariance of the phase space ellipsoid is the correlation defined as

$$r_{ij} = \frac{\sigma_{ij}}{\sqrt{\sigma_{ii}\sigma_{jj}}}, \quad \text{for} \quad 1 \leq i, j \leq 6\,. \tag{A.17}$$

The correlation ranges between -1 and 1. $r_{ij} = 0$ denotes a circular phase space distribution, $r_{ij} = 1$ a linear distribution with slope 1. A correlation between 0 and 1 denotes a tilted phase space distribution as shown in Figure A.1.

A.3.1 Beam Transfer

The beam matrix will undergo a transformation when the bunch of particles passes a beam line. Inserting the identity $I = MM^{-1} = M^{-1}M$ into Equation (A.14) we obtain

$$\vec{X}_i^T \left(M^T M^{T^{-1}}\right) \sigma_i^{-1} \left(M^{-1} M\right) \vec{X}_i = 1 \tag{A.18}$$

$$\left(M\vec{X}_i\right)^T \left(M\sigma_i M^T\right)^{-1} \left(M\vec{X}_i\right) = 1 \tag{A.19}$$

$$\vec{X}_f^T \sigma_f^{-1} \vec{X}_f = 1 \tag{A.20}$$

where M denotes the transfer matrix of the beam line, the indices i and f denote the initial and final position of the beam respectively. The beam matrix can be transformed through a beam line using the single particle transfer matrix M. The beam parameters can therefore be obtained at any position of the beam line if they are measured once. The transformation law is

$$\sigma_f = M\sigma_i M^T \ . \tag{A.21}$$

It should be noted that for magnetostatic beam lines the determinant of the transfer matrix is unity, hence the determinants of σ_f and σ_i are identical since

$$\det \sigma_f = \det\left(M\sigma_i M^T\right) = \det M \cdot \det \sigma_i \cdot \det M^T = \det \sigma_i \tag{A.22}$$

A direct consequence of Equation (A.22) is the conservation of the volume enclosed by the phase space ellipsoid, known as Liouville's theorem.

The transformation laws of the beam matrix elements in a beam line have been derived for the special case of Gaussian charge distributions. In contrast to the Gaussian case, an arbitrary charge distribution is not completely described by the covariance matrix. Nevertheless, the transfer of the variances and covariances of an arbitrary distribution through a beam line can still be described by the beam matrix formalism.

A.3.2 Beam Emittance

The beam emittance is defined as the phase space volume occupied by a certain fraction, typically 1σ, of the beam. The emittance is a measure of the beam quality. A low emittance beam has a small angular divergence after it is tightly focused or when it is transfered with large cross-section over large distances without external focusing. In the beam matrix formalism, the emittance is equal to the determinant of the beam matrix (see Figure A.1), hence

$$\det \sigma = \sigma_{11}\sigma_{22} - \sigma_{12}^2 = < x^2 >< x'^2 > - < xx' >^2 = \epsilon_x^2 \, . \tag{A.23}$$

Here the two-dimensional horizontal projection of the charge distribution is used. An identical relation holds for the vertical transverse (y, y') and the longitudinal phase space distribution (l, δ).

Appendix B

Derivation of the Ginzburg-Frank formula

This chapter presents the derivation of the Ginzburg-Frank formula describing the spectral and angular distribution of transition radiation. The radiation originates from the transition of charged particles in uniform linear motion of velocity $\vec{v}$ through a plane boundary of two media of different permittivities ϵ_1 and ϵ_2. The particles are assumed to travel along the z-axis directed perpendicular to the boundary. The configuration is shown in Fig. B.1.

(1) Electromagnetic fields carried by a particle bunch

Maxwell's equations can be used to derive the wave equation for the scalar and vector potential $\Phi(\vec{r},t)$ and $\vec{A}(\vec{r},t)$ [77]

$$\frac{\epsilon}{c^2}\frac{\partial^2\Phi(\vec{r},t)}{\partial t^2} - \nabla^2\Phi(\vec{r},t) = \frac{\rho(\vec{r},t)}{\epsilon\epsilon_0} \tag{B.1}$$

$$\frac{\epsilon}{c^2}\frac{\partial^2\vec{A}(\vec{r},t)}{\partial t^2} - \nabla^2\vec{A}(\vec{r},t) = \mu_0\vec{j}(\vec{r},t) \tag{B.2}$$

where Φ and $\vec{A}$ are related to the electric and magnetic fields $\vec{E}$ and $\vec{B}$ by

$$\vec{E} = -\vec{\nabla}\Phi - \frac{\partial\vec{A}}{\partial t}, \quad \vec{B} = \vec{\nabla}\times\vec{A}\,. \tag{B.3}$$

$\rho(\vec{r},t)$ denotes the charge density of the bunch and $\vec{j}(\vec{r},t)$ the current density. For particles traveling along a straight line, ρ and $\vec{j}$ are related by $\vec{j} = \rho\vec{v}$, hence either of Eq. (B.1) and (B.2) gives a complete description of the problem.

The differential equations (B.1) and (B.2) can be solved in frequency domain, where they transform into algebraic equations. The Fourier transformation takes the transverse coordinate $\vec{r}_\perp$ into a transverse momentum $\vec{q}$ and time t into frequency ω. The longitudinal coordinate is not transformed because of the boundary conditions which have to be fulfilled at $z = 0$. For the scalar potential Φ we obtain

$$\Phi(\vec{r}_\perp,z,t) = \frac{1}{(2\pi)^3}\int d^2q\,d\omega\,\Phi_{q,\omega}(z)\exp\left(i\vec{q}\cdot\vec{r}_\perp - i\omega t\right) \tag{B.4}$$

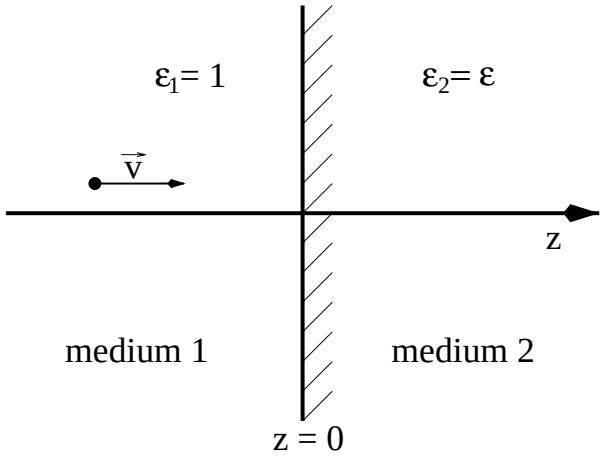


Figure B.1: Configuration used for the derivation of the Ginzburg-Frank Equations.

$$\vec{A}(\vec{r}_\perp, z, t) \;=\; \frac{1}{(2\pi)^3}\int d^2q\, d\omega\, \vec{A}_{q,\omega}(z)\exp\left(i\vec{q}\cdot\vec{r}_\perp - i\omega t\right). \tag{B.5}$$

The algebraic equation for $\Phi_{q,\omega}$ can be derived by inserting Eq. (B.4) into Eq. (B.1) yielding

$$\Phi_{q,\omega}(z) = \frac{\rho_{q,\omega}(z)}{\epsilon\epsilon_0}\left[q^2 + \frac{\omega^2}{v^2} - \frac{\epsilon\omega^2}{c^2}\right]^{-1}. \tag{B.6}$$

Differential Eq. (B.2) is solved by a similar expression given by

$$\vec{A}_{q,\omega} = \frac{\epsilon}{c^2}\vec{v}\,\Phi_{q,\omega}\,. \tag{B.7}$$

Using Eq. (B.3), the electric field yields

$$\vec{E}^{Q}_{q,\omega} = i\left[\omega\vec{v}\left(\frac{\epsilon}{c^2} - \frac{1}{v^2}\right) - q^2\right]\Phi_{q,\omega}\,. \tag{B.8}$$

The superscript Q in Eq. (B.8) indicates that the field is produced by a charged particle bunch. The Fourier transform of a charge distribution $\rho_{q,\omega}$ has to be derived and inserted into Eq. (B.8). The Fourier transform of a single particle and, as an example of a particle bunch, a Gaussian charge distribution of transverse variance σ_r^2 and longitudinal variance σ_z^2 will be considered.

Single particle The charge distribution of a single particle in uniform motion with velocity v is

$$\rho^e(\vec{r}, t) = e\delta(\vec{r}_\perp)\delta(z - vt) \tag{B.9}$$

yielding the Fourier transformation

$$\rho^e_{q,\omega}(z) = e\int d^2r_\perp\, dt\, \delta(r_\perp)\delta(z - vt)\exp\left(-i\vec{q}\,\vec{r}_\perp + i\omega t\right) = \frac{e}{v}\exp\left(i\frac{\omega z}{v}\right) \tag{B.10}$$

Radiation Fields

The electric radiation field has to satisfy the homogeneous wave equation

$$\frac{\epsilon}{c^2}\frac{\partial^2 \vec{E}(\vec{r},t)}{\partial t^2} - \vec{\nabla}^2 \vec{E}(\vec{r},t) = 0\,. \tag{B.11}$$

which can be transformed into frequency domain using

$$\vec{E}(\vec{r},t) = \frac{1}{(2\pi)^3}\int d^2q\, dt\, \vec{E}_{q,\omega}(z) \exp\left(i\vec{q}\cdot\vec{r}_\perp - i\omega t\right). \tag{B.12}$$

The boundary at $z = 0$ is assumed to be of infinite extent, hence the radiation field can be characterized by a plane wave propagating in z direction. The ansatz for the z component is

$$\vec{n}\cdot\vec{E}^R_{q,\omega}(z) = i\begin{pmatrix} a_+ \\ a_- \end{pmatrix}\exp\left(\pm i k_z z\right) \tag{B.13}$$

where a_+ and a_- are yet undetermined coefficients and $\vec{n}$ is a unity vector pointing along the z axis. Two coefficients and two signs are introduced in Eq. (B.13) because the radiation wave can propagate either forward into medium 2 ($z > 0$, a_+, and upper sign) or can be reflected backward into medium 1 ($z < 0$, a_-, and lower sign). Equations (B.11) and (B.13) lead to a relation among radiation frequency ω, transverse $\vec{q}$ and longitudinal k_z momentum

$$\left(\frac{\epsilon\omega^2}{c^2} - q^2 - k_z^2\right)\vec{E}_{q,\omega}(z) = 0 \quad \Rightarrow \quad k_z = \sqrt{\frac{\epsilon\omega^2}{c^2} - q^2}\,. \tag{B.14}$$

The transverse electric field components can be derived using $\vec{\nabla}\cdot\vec{D} = 0$ yielding

$$\epsilon\frac{\vec{q}}{q}\cdot\vec{E}^R_{q,\omega} = \mp\frac{\epsilon k_z}{q}\vec{n}\cdot\vec{E}^R_{q,\omega}\,. \tag{B.15}$$

The complete expression for the electric radiation field is

$$\vec{E}^R_{q,\omega} = i\begin{pmatrix} a_+ \\ a_- \end{pmatrix}\left[\vec{n} \mp \frac{\vec{q}}{q^2}\sqrt{\frac{\epsilon\omega^2}{c^2} - q^2}\right]\exp\left(\pm i\sqrt{\frac{\epsilon\omega^2}{c^2} - q^2}\; z\right). \tag{B.16}$$

Boundary Conditions

The coefficients a_+ for $z > 0$ (medium 2) and a_- for $z < 0$ (medium 1) have to be determined from the boundary conditions the sum of the charge and the radiation field has to fulfill at the interface. The normal component of the $\vec{D}$-field and the tangential component of the $\vec{E}$-field have to be continuous at $z = 0$.

Normal component:

$$\epsilon_1\vec{n}\cdot\left(\vec{E}^Q_{q,\omega} + \vec{E}^R_{q,\omega}\right)\Big|^{\text{medium 1}}_{z=0} = \epsilon_2\vec{n}\cdot\left(\vec{E}^Q_{q,\omega} + \vec{E}^R_{q,\omega}\right)\Big|^{\text{medium 2}}_{z=0} \tag{B.17}$$

leads to

$$\epsilon_1 a_- + \epsilon_1 \omega v \left(\frac{\epsilon_1}{c^2} - \frac{1}{v^2}\right) \frac{\rho_{q,\omega}}{\epsilon_1 \epsilon_0} \left[q^2 + \frac{\omega^2}{v^2} - \frac{\epsilon_1 \omega^2}{c^2}\right]^{-1} = \epsilon_2 a_+ + \epsilon_2 \omega v \left(\frac{\epsilon_2}{c^2} - \frac{1}{v^2}\right) \frac{\rho_{q,\omega}}{\epsilon_2 \epsilon_0} \left[q^2 + \frac{\omega^2}{v^2} - \frac{\epsilon_2 \omega^2}{c^2}\right]^{-1} . \quad \text{(B.18)}$$

Tangential component:

$$\vec{q} \cdot \left(\vec{E}^Q_{q,\omega} + \vec{E}^R_{q,\omega}\right)\Big|_{z=0}^{\text{medium 1}} = \vec{q} \cdot \left(\vec{E}^Q_{q,\omega} + \vec{E}^R_{q,\omega}\right)\Big|_{z=0}^{\text{medium 2}} \quad \text{(B.19)}$$

leads to

$$\sqrt{\frac{\epsilon_1 \omega^2}{c^2} - q^2} a_- - \frac{\rho_{q,\omega}}{\epsilon_1 \epsilon_0} \frac{q^2}{\left(q^2 + \frac{\omega^2}{v^2} - \frac{\epsilon_1 \omega^2}{c^2}\right)} = -\sqrt{\frac{\epsilon_2 \omega^2}{c^2} - q^2} a_+ - \frac{\rho_{q,\omega}}{\epsilon_2 \epsilon_0} \frac{q^2}{\left(q^2 + \frac{\omega^2}{v^2} - \frac{\epsilon_2 \omega^2}{c^2}\right)} . \quad \text{(B.20)}$$

Equation (B.18) and (B.20) can be solved for a_+ and a_-. For the special case of $\epsilon_1 = 1$ (vacuum) and $\epsilon_2 = \epsilon$ (medium), we obtain

$$a_- = \frac{e}{\epsilon_0 \omega} \frac{\beta \kappa^2 (\epsilon - 1) \left(1 - \beta^2 + \beta\sqrt{\epsilon - \kappa^2}\right)}{(1 - \beta^2 + \beta^2 \kappa^2) \left(1 + \beta\sqrt{\epsilon - \kappa^2}\right) \left(\sqrt{\epsilon - \kappa^2} + \epsilon\sqrt{1 - \kappa^2}\right)} \quad \text{(B.21)}$$

$$a_+ = \frac{e}{\epsilon \epsilon_0 \omega} \frac{\beta \kappa^2 (\epsilon - 1) \left(1 - \beta^2 \epsilon - \beta\sqrt{1 - \kappa^2}\right)}{(1 - \beta^2 \epsilon + \beta^2 \kappa^2) \left(1 - \beta\sqrt{1 - \kappa^2}\right) \left(\sqrt{\epsilon - \kappa^2} + \epsilon\sqrt{1 - \kappa^2}\right)} \quad \text{(B.22)}$$

where $\kappa = qc/\omega$ has been used [23]. The combination of Eq. (B.21) and (B.22) with Eq. (B.16) describes the electric transition radiation field between vacuum and a medium of permittivity ϵ with the restriction of infinite boundaries.

(4) Radiated energy into the backward hemisphere

The energy U contained in a propagating electromagnetic wave is described by

$$U = \epsilon_0 \int dx\, dy \int_{-\infty}^{\infty} dz \left|\vec{E}^R(\vec{r}, t)\right|^2 . \quad \text{(B.23)}$$

The knowledge of the electric field is sufficient for the evaluation of the radiated energy, since the electric and magnetic fields, in time average, store the same energy. In the following, the radiation into the backward hemisphere, which is used for beam diagnostics at the TESLA Test Facility, is evaluated.

Let $t = 0$ be the time of transition from medium 1 to medium 2. To use the plane wave radiation field, we have to choose the time t large enough that the radiation field and the charge field are well separated. The center of the coordinate system, i. e. $z = 0$, is shifted to the center of the radiation pulse. This coordinate transformation causes an unknown phase factor in the coefficient a_-, but justifies the use of symmetric boundaries on the integrals (B.23) [78].

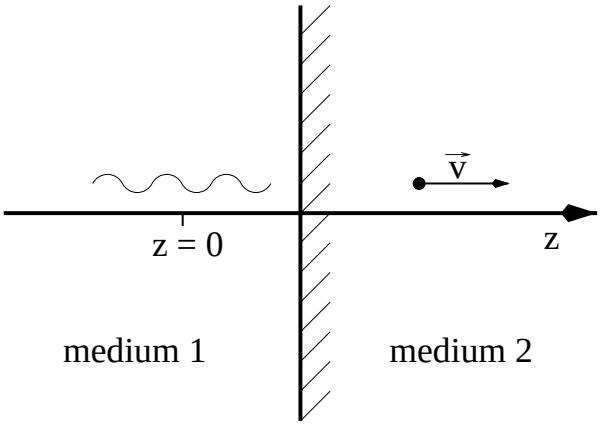


Figure B.2: Translation of the origin of the coordinate system into the middle of the radiation pulse.

The Fourier decomposition of $\vec{E}^R(\vec{r},t)$, see Eq. (B.12), is introduced into Eq. (B.23) leading to a frequency domain description of the radiated energy

$$U = \epsilon_0 \int dx\, dy \int_{-\infty}^{\infty} dz \int \frac{d^2q\, d^2q'\, d\omega\, d\omega'}{(2\pi)^6} \cdot \\ \cdot \vec{E}^R_{q,\omega}(z) \vec{E}^{R^*}_{q',\omega'}(z) \exp\left(i\left(\vec{r}_\perp \cdot \left(\vec{q} - \vec{q}^{\,'}\right) - t\left(\omega - \omega'\right)\right)\right). \tag{B.24}$$

1. The integration over $dx\, dy$ yields

$$\int dx\, dy \exp\left(i\left(\vec{r}_\perp \cdot \left(\vec{q} - \vec{q}^{\,'}\right)\right)\right) = (2\pi)^2 \delta^2\left(\vec{q} - \vec{q}^{\,'}\right) \tag{B.25}$$

   hence

$$U = \epsilon_0 \int_{-\infty}^{\infty} dz \int \frac{d^2q\, d\omega\, d\omega'}{(2\pi)^4} \vec{E}^R_{q,\omega}(z) \vec{E}^{R^*}_{q,\omega'}(z) \exp\left(-i\left(\omega - \omega'\right)t\right). \tag{B.26}$$

2. The radiation field Eq. (B.16) is introduced into Eq. (B.26) and then integrated over z using

$$\int dz\, e^{-iz\left(\sqrt{\frac{\omega^2}{c^2}-q^2} - \sqrt{\frac{\omega'^2}{c^2}-q^2}\right)} = 2\pi\delta\left(\sqrt{\frac{\omega^2}{c^2}-q^2} - \sqrt{\frac{\omega'^2}{c^2}-q^2}\right) \tag{B.27}$$

   We obtain

$$U = 2\pi\epsilon_0 \int \frac{d^2q\, d\omega\, d\omega'}{(2\pi)^4} (a_-)\left(a_-^*\right) \delta\left(\sqrt{\frac{\omega^2}{c^2}-q^2} - \sqrt{\frac{\omega'^2}{c^2}-q^2}\right) \cdot \\ \cdot \left[\vec{n} \mp \frac{\vec{q}}{q^2}\sqrt{\frac{\omega^2}{c^2}-q^2}\right] \cdot \left[\vec{n} \mp \frac{\vec{q}}{q^2}\sqrt{\frac{\omega'^2}{c^2}-q^2}\right]. \tag{B.28}$$

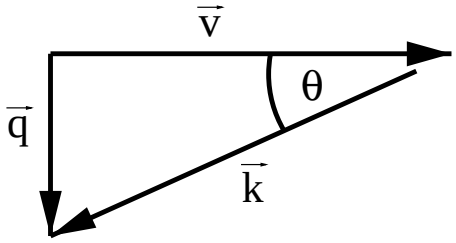


Figure B.3: Transverse momentum $\vec{q}$, the total momentum $\vec{k}$ and the polar angle of emission of the transition radiation.

Note that a_- and a_-^* depend on (q,ω) and (q,ω') respectively. The δ-expression in Eq. (B.28) implies $\omega = \omega'$, hence $a_- \cdot a_-^* = |a_-|^2$. The additional phase factor introduced by the coordinate translation cancels out. Equation (B.28) can be simplified using the equality of ω and ω' yielding

$$U = \epsilon_0 \int \frac{d^2\,d\omega\,d\omega'}{(2\pi)^4} |a_-|^2 \frac{\omega^2}{c^2 q^2} \delta\left(\sqrt{\frac{\omega^2}{c^2} - q^2} - \sqrt{\frac{\omega'^2}{c^2} - q^2}\right) . \tag{B.29}$$

3. The integration over ω' can now be carried out using

$$\delta\left(\sqrt{\frac{\omega^2}{c^2} - q^2} - \sqrt{\frac{\omega'^2}{c^2} - q^2}\right) = \frac{c^2}{\omega}\sqrt{\frac{\omega^2}{c^2} - q^2}\,[\delta(\omega - \omega') + \delta(\omega + \omega')] \tag{B.30}$$

hence

$$U = 2\epsilon_0 \int \frac{d^2q\,d\omega}{(2\pi)^3} |a_-|^2 \frac{\omega^2}{q^2 c} \sqrt{1 - \frac{q^2c^2}{\omega^2}} . \tag{B.31}$$

4. The angular distribution of transition radiation can be evaluated by expressing the transverse momentum $\vec{q}$ by the total momentum $\vec{k}$ of the radiation and its emission angle $\pi - \theta$, hence $q = k\cos\theta$. The vectors are shown in Fig. B.3. There is no need to introduce an azimuthal emission angle because of symmetry. The differential d^2q becomes $2\pi q dq = 2\pi\omega^2/c^2 \sin\theta\cos\theta d\theta$ and we obtain

$$U = 2\pi \int_0^\infty d\omega \int_0^\pi d\theta\, \sin\theta\, U_1(\omega,\theta) \tag{B.32}$$

with

$$U_1(\omega,\theta) = \frac{2\epsilon_0}{(2\pi)^3} |a_-|^2 \frac{\omega^2}{c} \frac{\cos^2\theta}{\sin^2\theta} \tag{B.33}$$

being the differentiated spectral energy density.

Introducing a_- from Eq. (B.21), we obtain the Ginzburg-Frank [23] formula describing the opening angle and the spectral power density distribution of transition radiation:

$$U_1 = \frac{e^2}{4\pi^3\epsilon_0 c} \frac{\beta^2 \sin^2\theta\cos^2\theta}{(1-\beta^2\cos^2\theta)^2} \frac{(\epsilon-1)^2\left(1-\beta^2+\beta\sqrt{\epsilon-\sin^2\theta}\right)^2}{\left(1+\beta\sqrt{\epsilon-\sin^2\theta}\right)^2\left(\epsilon\cos\theta-\sqrt{\epsilon-\sin^2\theta}\right)^2} \tag{B.34}$$

For the special case of $\epsilon \to \infty$, that is in case of a metallic boundary for frequencies well below the plasma frequency of the metal, we obtain the simplified expression

$$U_1 = \frac{e^2}{4\pi^3 \epsilon_0 c} \frac{\beta^2 \sin^2 \theta}{(1 - \beta^2 \cos^2 \theta)^2} \,. \tag{B.35}$$

Expression (B.35) denotes the Ginzburg-Frank formula as commonly applied for the computation of transition radiation in accelerators.

Appendix C

Electromagnetic Fields of Relativistic Electron Bunches

The transverse source size of transition radiation is defined by the projection of the electromagnetic fields, carried by a charge distribution traveling in uniform motion through a beam pipe, onto the transition boundary. The charge distribution is assumed to travel along the axis of a cylindrical vacuum chamber of either perfect or high conductivity. Maxwell's Equations are solved with proper boundary conditions to obtain the electromagnetic fields inside the pipe.

(1) Fields of the Charge Distribution

The electric and magnetic fields of a charge distribution traveling on the axis of a cylindrical beam pipe are described by the vacuum solution of the Maxwell Equations. The charge distribution is assumed to travel in the center of the beam pipe and to be azimuthally symmetric. The Maxwell Equations in vacuum are

$$\nabla \cdot \vec{E} = \frac{\rho}{\epsilon_0} \quad , \quad \nabla \cdot \vec{B} = 0 \tag{C.1}$$

$$\nabla \times \vec{E} = -\frac{d\vec{B}}{dt} \quad , \quad \nabla \times \vec{B} = \mu_0 \vec{j} + \frac{1}{c^2}\frac{d\vec{E}}{dt}. \tag{C.2}$$

From symmetry only the radial and longitudinal components of the electric field (E_r and E_z) and the azimuthal component of magnetic field (B_θ) have to be considered. ρ denotes the charge density. The current j has only an axial component, which originates from the moving charge distribution. The Maxwell Equations for the above field components read in cylindrical coordinates

$$\nabla \cdot \vec{E} = \frac{1}{r}\partial_r (rE_r) + \partial_z E_z = \frac{\rho}{\epsilon_0} \tag{C.3}$$

$$\nabla \cdot \vec{B} = \frac{1}{r}\partial_\theta B_\theta = 0 \tag{C.4}$$

$$\nabla \times \vec{E} = -\partial_t \vec{B} \quad \left\{ \begin{array}{rcl} \frac{1}{r}\partial_\theta E_z &=& 0 \\ \partial_z E_r - \partial_r E_z &=& -\partial_t B_\theta \\ \frac{1}{r}\partial_\theta E_r &=& 0 \end{array} \right. \tag{C.5}$$

$$\nabla \times \vec{B} = \mu_0 \vec{j} + \frac{1}{c^2}\partial_t \vec{E} \quad \left\{ \begin{array}{rcl} -\partial_z B_\theta &=& \frac{1}{c^2}\partial_t E_r \\ \frac{1}{r}\partial_r (rB_\theta) &=& \mu_0 j_z + \frac{1}{c^2}\partial_t E_z \end{array} \right. \tag{C.6}$$

Here ∂_r, ∂_θ and ∂_z denote $\partial/\partial r$, $\partial/\partial\theta$ and $\partial/\partial z$ respectively. Equations (C.4), (C.5) and (C.6) show that B_θ, E_r and E_z are independent of the azimuthal coordinate θ (azimuthal symmetry). The fields depend on the radial coordinate r and the longitudinal coordinate $\zeta = z - \beta ct$ taking into account that the fields travel together with the charge at a velocity of βc. Maxwell's equations are solved in frequency domain where the longitudinal coordinate ζ is transformed into the wave number k by a Fourier transformation. The transverse coordinates are not transformed to retain the transverse component of the electromagnetic fields at different wave numbers k. The field components are

$$E_{r,z}(\zeta, r) = \int_{-\infty}^{\infty} \tilde{E}_{r,z}(k, r) \exp(ik\zeta) dk \tag{C.7}$$

$$B_\theta(\zeta, r) = \int_{-\infty}^{\infty} \tilde{B}_\theta(k, r) \exp(ik\zeta) dk \tag{C.8}$$

$$\rho(\zeta, r) = \int_{-\infty}^{\infty} \tilde{\rho}(k, r) \exp(ik\zeta) dk \tag{C.9}$$

The Fourier components obey the equations

$$\frac{1}{r}\frac{\partial(r\tilde{E}_r)}{\partial r} + ik\tilde{E}_z = \frac{\tilde{\rho}}{\epsilon_0} \tag{C.10}$$

$$\frac{1}{r}\frac{\partial \tilde{B}_\theta}{\partial \theta} = 0 \tag{C.11}$$

$$ik\tilde{E}_r - \frac{\partial \tilde{E}_z}{\partial r} = ik\beta c\tilde{B}_\theta \tag{C.12}$$

$$-ik\tilde{B}_\theta = -ik\frac{\beta}{c}\tilde{E}_r \tag{C.13}$$

$$\frac{1}{r}\frac{\partial\left(r\tilde{B}_\theta\right)}{\partial r} = -\frac{ik\beta}{c}\tilde{E}_z + \mu_0\tilde{j}_z \ . \tag{C.14}$$

Inserting Eq. (C.13) into Eq. (C.12) yields a relation between $\tilde{E}_z$ and $\tilde{E}_r$

$$\frac{\partial \tilde{E}_z}{\partial r} = \frac{ik}{\gamma^2}\tilde{E}_r \ . \tag{C.15}$$

Equation (C.15) inserted into (C.10) yields a well known second order differential equation for $\tilde{E}_z$

$$\frac{\partial^2 \tilde{E}_z}{\partial r^2} + \frac{1}{r}\frac{\partial \tilde{E}_z}{\partial r} - \frac{k^2}{\gamma^2}\tilde{E}_z = \frac{ik}{\gamma^2}\frac{\tilde{\rho}}{\epsilon_0} \ . \tag{C.16}$$

The two independent solutions of the homogeneous equation are the modified Bessel functions $I_0(kr/\gamma)$ and $K_0(kr/\gamma)$. The inhomogeneous differential equation will be solved for a ring charge distribution of radius a with azimuthal symmetry

$$\tilde{\rho}(k, r, a) = \frac{\delta(r-a)}{2\pi a} q\tilde{\lambda}(k) \tag{C.17}$$

where $\tilde{\lambda}(k)$ denotes the Fourier transform of the longitudinal charge distribution and q the total charge. $\tilde{E}_z$ is written as a superposition of I_0 and K_0 in the following form

$$\tilde{E}_z(k, r) = \left\{ \begin{array}{ccc} c_1(k) I_0\left(\frac{kr}{\gamma}\right) & , & r < a \\ c_2(k) K_0\left(\frac{kr}{\gamma}\right) & , & r > a \end{array} \right\} + c_3(k) I_0\left(\frac{kr}{\gamma}\right) \ . \tag{C.18}$$

The terms $c_1(k)I_0\left(kr/\gamma\right)$ and $c_2(k)K_0\left(kr/\gamma\right)$ describe the field $\tilde{E}_z$ originating from the ring charge distribution $\tilde{\rho}(k,r)$. Fields inside the ring ($r < a$) can only be given by $I_0\left(kr/\gamma\right)$, since $K_0\left(kr/\gamma\right)$ diverges for $r \to 0$. Fields outside ($r > a$) are given by $K_0\left(kr/\gamma\right)$, since K_0 is decreasing with radius. The term $c_3(k)I_0\left(kr/\gamma\right)$ describes the effect of the cylindrical boundary. I_0 has been chosen because it is not divergent at $r \to 0$. The coefficients $c_1(k)$, $c_2(k)$ and $c_3(k)$ have to be determined by boundary conditions at $r = a, b$.

(2) Vacuum Chamber of Infinite Conductivity

The longitudinal component $\tilde{E}_z(k,r)$ has to fulfill the following boundary conditions

- The continuity of $\tilde{E}_z$ at $r = a$.
- A vanishing longitudinal field component at the beam pipe, i. e. $\tilde{E}_z(k,b) = 0$.
- Eq. (C.16) has to hold. This introduces the charge term into the ansatz (C.18).

These boundary conditions at $r = a, b$ yield the following equations

$$c_1(k)I_0\left(\frac{ka}{\gamma}\right) = c_2(k)K_0\left(\frac{ka}{\gamma}\right) \tag{C.19}$$

$$c_2(k)K_0\left(\frac{kb}{\gamma}\right) = -c_3(k)I_0\left(\frac{kb}{\gamma}\right) \tag{C.20}$$

Equation (C.16) is integrated over an infinitesimal radial interval from $a - \epsilon \leq r \leq a + \epsilon$ to take the charge term into account. The left hand side yields

$$\int_{a-\epsilon}^{a+\epsilon} dr\, r \left\{\frac{1}{r}\partial_r r \partial_r \tilde{E}_z - \frac{k^2}{\gamma^2}\tilde{E}_z\right\} = r\partial_r \tilde{E}_z \Big|_{a-\epsilon}^{a+\epsilon} + 2\epsilon\frac{k^2}{\gamma^2} a\tilde{E}_z(k,a) \tag{C.21}$$

$$= a\frac{k}{\gamma}\left\{-c_2(k)K_1\left(\frac{ka}{\gamma}\right) - c_1(k)I_1\left(\frac{ka}{\gamma}\right)\right\} \tag{C.22}$$

where $\epsilon \to 0$ has been used [27]. The first term of integral (C.21) describes the discontinuity of the derivative of the field at $r = a$. The second term is of the order of ϵ, because of the continuity of $\tilde{E}_z$ at $r = a$. The right hand side of Eq. (C.16) integrated over the same radial interval yields

$$\frac{ik}{\gamma^2\epsilon_0}\int_{a-\epsilon}^{a+\epsilon} dr\, r\, \frac{\delta(r-a)}{2\pi a}\, q\tilde{\lambda}(k) = \frac{ik}{\gamma^2}\frac{q}{2\pi\epsilon_0}\tilde{\lambda}(k)\ . \tag{C.23}$$

where the ring charge distribution Eq. (C.17) has been used. Eq. (C.22) and (C.23) yield the third boundary condition

$$-c_2(k)K_1\left(\frac{ka}{\gamma}\right) - c_1(k)I_1\left(\frac{ka}{\gamma}\right) = \frac{iq}{2\pi\epsilon_0\gamma a}\tilde{\lambda}(k)\ . \tag{C.24}$$

For the coefficients $c_1(k)$, $c_2(k)$ and $c_3(k)$ we obtain

$$c_1(k) = -\frac{ik}{2\pi\epsilon_0\gamma^2} q\tilde{\lambda}(k) K_0\left(\frac{ka}{\gamma}\right) \tag{C.25}$$

$$c_2(k) = -\frac{ik}{2\pi\epsilon_0\gamma^2} q\tilde{\lambda}(k) I_0\left(\frac{ka}{\gamma}\right) \tag{C.26}$$

$$c_3(k) = \frac{ik}{2\pi\epsilon_0\gamma^2} q\tilde{\lambda}(k) I_0\left(\frac{ka}{\gamma}\right) \frac{K_0\left(\frac{kb}{\gamma}\right)}{I_0\left(\frac{kb}{\gamma}\right)} \tag{C.27}$$

where the Wronskian $I_0(ka/\gamma)K_1(ka/\gamma) + I_1(ka/\gamma)K_0(ka/\gamma) = \gamma/ka$ has been used [79]. These coefficients are introduced into ansatz (C.18) yielding an expression for the longitudinal component of the electric field $\tilde{E}_z(k,r)$

$$\tilde{E}_z(k,r) = \frac{ik}{2\pi\epsilon_0\gamma^2} q\tilde{\lambda}(k) \left[\begin{cases} -K_0\left(\frac{ka}{\gamma}\right) I_0\left(\frac{kr}{\gamma}\right), r < a \\ -I_0\left(\frac{ka}{\gamma}\right) K_0\left(\frac{kr}{\gamma}\right), r > a \end{cases} + I_0\left(\frac{ka}{\gamma}\right) \frac{K_0\left(\frac{kb}{\gamma}\right)}{I_0\left(\frac{kb}{\gamma}\right)} I_0\left(\frac{kr}{\gamma}\right) \right] . \tag{C.28}$$

The field components $\tilde{E}_r(k,r)$ and $\tilde{B}_\theta(k,r)$ can be derived from Eq. (C.15) and (C.13), respectively. The result obtained is

$$\tilde{E}_r(k,r) = \frac{k}{2\pi\epsilon_0\gamma} q\tilde{\lambda}(k) \left[\begin{cases} -K_0\left(\frac{ka}{\gamma}\right) I_1\left(\frac{kr}{\gamma}\right), r < a \\ I_0\left(\frac{ka}{\gamma}\right) K_1\left(\frac{kr}{\gamma}\right), r > a \end{cases} + I_0\left(\frac{ka}{\gamma}\right) \frac{K_0\left(\frac{kb}{\gamma}\right)}{I_0\left(\frac{kb}{\gamma}\right)} I_1\left(\frac{kr}{\gamma}\right) \right] \tag{C.29}$$

and $\tilde{B}_\theta = \beta/c\,\tilde{E}_r$.

(3) Vacuum Chamber of Finite Conductivity

For the vacuum solution of Eq. (C.16) we make the ansatz (C.18)

$$\tilde{E}_z(k,r) = \left\{ \begin{array}{c} c_1(k) I_0\left(\frac{kr}{\gamma}\right), \ r < a \\ c_2(k) K_0\left(\frac{kr}{\gamma}\right), \ r > a \end{array} \right\} + c_3(k) I_0\left(\frac{kr}{\gamma}\right) \tag{C.30}$$

$$\tilde{E}_r(k,r) = -i\gamma \left[\left\{ \begin{array}{c} c_1(k) I_1\left(\frac{kr}{\gamma}\right), \ r < a \\ -c_2(k) K_1\left(\frac{kr}{\gamma}\right), \ r > a \end{array} \right\} + c_3(k) I_1\left(\frac{kr}{\gamma}\right) \right] \tag{C.31}$$

$$\tilde{B}_\theta(k,r) = -i\gamma\frac{\beta}{c} \left[\left\{ \begin{array}{c} c_1(k) I_1\left(\frac{kr}{\gamma}\right), \ r < a \\ -c_2(k) K_1\left(\frac{kr}{\gamma}\right), \ r > a \end{array} \right\} + c_3(k) I_1\left(\frac{kr}{\gamma}\right) \right] \tag{C.32}$$

where $\tilde{E}_r$ and $\tilde{B}_\theta$ are derived from Eq. (C.15) and (C.13) respectively.

The Maxwell Equations have to be solved inside the metal of the beam pipe. The average charge density ρ in the metal vanishes in the frequency range considered (frequencies smaller than the electron plasma frequency in the metal). The time varying magnetic field induces a radial current in the beam pipe obeying Ohm's law $\tilde{j}_r = \sigma\tilde{E}_r$, where σ denotes the conductivity of the metal. The wall currents are described by an additional term in Eq. (C.6)

$$\left(\nabla \times \vec{B}\right)_r = -\partial_z B_\theta = \mu_0 j_r + \frac{1}{c^2}\partial_t E_r \, . \tag{C.33}$$

Hence the Fourier-transformed Maxwell Equations become

$$\frac{1}{r}\frac{\partial(r\tilde{E}_r)}{\partial r} + ik\tilde{E}_z = 0 \tag{C.34}$$

$$\frac{1}{r}\frac{\partial\tilde{B}_\theta}{\partial\theta} = 0 \tag{C.35}$$

$$-\frac{\partial\tilde{E}_z}{\partial r} + ik\tilde{E}_r = ik\beta c\tilde{B}_\theta \tag{C.36}$$

$$\frac{1}{r}\frac{\partial(r\tilde{B}_\theta)}{\partial r} = -\frac{ik\beta}{c}\tilde{E}_z \qquad \text{and} \tag{C.37}$$

$$\tilde{B}_\theta = \tilde{E}_r\left(\frac{\beta}{c} - \frac{\mu_0\sigma}{ik}\right) . \tag{C.38}$$

Inserting Eq. (C.38) into Eq. (C.36) we obtain

$$\frac{\partial\tilde{E}_z}{\partial r} = \left(\frac{ik}{\gamma^2} + \mu_0\sigma\beta c\right)\tilde{E}_r . \tag{C.39}$$

A second order differential equation is obtained for $\tilde{E}_z$ if Eq. (C.39) is substituted into Eq. (C.34).

$$\frac{1}{r}\frac{\partial}{\partial r}\left(r\frac{\partial\tilde{E}_z}{\partial r}\right) = \left(\frac{ik}{\gamma^2} + \mu_0\sigma\beta c\right)\frac{1}{r}\frac{\partial\left(r\tilde{E}_r\right)}{\partial r} \tag{C.40}$$

$$= \left(\frac{k^2}{\gamma^2} - ik\mu_0\sigma\beta c\right)\tilde{E}_z \tag{C.41}$$

The penetration depth of the high frequency field inside the metal is small compared to the thickness of the beam pipe. The radius r is therefore $r \approx b =$ constant. Hence Eq. (C.41) reduces to an Helmholtz wave equation

$$\left(\partial_r^2 + \lambda^2\right)\cdot\tilde{E}_z = 0 \tag{C.42}$$

where $\lambda^2 = (ik\mu_0\sigma\beta c - k^2/\gamma^2)$. Eq. (C.42) is solved by

$$\tilde{E}_z(k,r) = d\exp\left(\pm i\lambda(r-b)\right) \quad \text{for} \quad r \geq b . \tag{C.43}$$

where the coefficient d depends on the wave number k and the radius of the charge distribution a. In the following the positive sign in the exponential is used to describe an exponential drop of the field for $r > b$.

Expression (C.43) can be used to evaluate the azimuthal magnetic field component inside the metal. The differentiation of Eq. (C.38) leads to

$$\frac{1}{r}\frac{\partial\left(r\tilde{B}_\theta\right)}{\partial r} = \frac{1}{r}\frac{\partial\left(r\tilde{E}_r\right)}{\partial r}\left(\frac{\beta}{c} - \frac{\mu_0\sigma}{ik}\right) . \tag{C.44}$$

and after the substitution of Eq. (C.34) we obtain (while keeping $r \approx b =$ constant inside the metal)

$$\frac{\partial\tilde{B}_\theta}{\partial r} = \left(\mu_0\sigma - \frac{ik\beta}{c}\right)d\exp\left(i\lambda(r-b)\right) . \tag{C.45}$$

The integration leads to

$$\tilde{B}_\theta(k,r) = -d\frac{k}{\lambda\beta c}\left(1+\frac{\lambda^2}{k^2}\right)\exp\left(i\lambda(r-b)\right) \quad \text{for} \quad r \geq b\ . \tag{C.46}$$

The radial electric field $\tilde{E}_r$ is related to the azimuthal magnetic field by Eq. (C.38). This yields

$$\tilde{E}_r(k,r) = -d\,\frac{k}{\lambda}\exp\left(i\lambda(r-b)\right) \quad \text{for} \quad r \geq b\ . \tag{C.47}$$

The longitudinal electric fields $\tilde{E}_z$ has to be continuous at $r=a$, $\tilde{E}_z$ and $\tilde{B}_\theta$ have to be continuous at $r=b$ and Eq. (C.16) has to hold to fulfill the boundary conditions. The following equations are obtained

$$c_1(k)I_0\left(\frac{ka}{\gamma}\right) = c_2(k)K_0\left(\frac{ka}{\gamma}\right) \tag{C.48}$$

$$-c_2(k)K_1\left(\frac{ka}{\gamma}\right) - c_1(k)I_1\left(\frac{ka}{\gamma}\right) = \frac{i}{\gamma}\frac{q}{2\pi\epsilon_0 a}\tilde{\lambda}(k) \tag{C.49}$$

$$c_2(k)K_0\left(\frac{kb}{\gamma}\right) + c_3(k)I_0\left(\frac{kb}{\gamma}\right) = d(k) \tag{C.50}$$

$$-i\gamma\frac{\beta}{c}\left(-c_2(k)K_1\left(\frac{kb}{\gamma}\right) + c_3(k)I_1\left(\frac{kb}{\gamma}\right)\right) = -d(k)\frac{k}{\beta\lambda c}\left(1+\frac{\lambda^2}{k^2}\right)\ . \tag{C.51}$$

For the coefficients $c_1(k)$, $c_2(k)$, $c_3(k)$ and $d(k)$ we obtain

$$c_1(k) = -\frac{ik}{2\pi\epsilon_0\gamma^2}q\tilde{\lambda}(k)K_0\left(\frac{ka}{\gamma}\right) \tag{C.52}$$

$$c_2(k) = -\frac{ik}{2\pi\epsilon_0\gamma^2}q\tilde{\lambda}(k)I_0\left(\frac{ka}{\gamma}\right) \tag{C.53}$$

$$c_3(k) = \left(d(k) + \frac{ik}{2\pi\epsilon_0\gamma^2}q\tilde{\lambda}(k)I_0\left(\frac{ka}{\gamma}\right)K_0\left(\frac{kb}{\gamma}\right)\right)/I_0\left(\frac{kb}{\gamma}\right) \tag{C.54}$$

$$d(k) = \frac{\beta}{2\pi\epsilon_0 b}q\tilde{\lambda}(k)\frac{I_0\left(\frac{ka}{\gamma}\right)}{I_0\left(\frac{kb}{\gamma}\right)}\frac{1}{\left(i\gamma\beta\frac{I_1\left(\frac{kb}{\gamma}\right)}{I_0\left(\frac{kb}{\gamma}\right)} - \frac{1}{\beta}\left(\frac{k}{\lambda}+\frac{\lambda}{k}\right)\right)}\ . \tag{C.55}$$

The fields $\tilde{E}_z$, $\tilde{E}_r$ and $\tilde{B}_\theta$ are obtained both in the vacuum and the metal by introducing these coefficients into Eq. (C.30)–(C.32). We obtain for the vacuum solution

$$\begin{aligned}\tilde{E}_z(k,r) = \frac{ik}{2\pi\epsilon_0\gamma^2}q\tilde{\lambda}(k)&\left\{\begin{array}{l} -K_0\left(\frac{ka}{\gamma}\right)I_0\left(\frac{kr}{\gamma}\right),\ r<a \\ -I_0\left(\frac{ka}{\gamma}\right)K_0\left(\frac{kr}{\gamma}\right),\ r>a \end{array}\right\} \\ &+\left[d(k)+\frac{ik}{\gamma^2}q\tilde{\lambda}(k)I_0\left(\frac{ka}{\gamma}\right)K_0\left(\frac{kb}{\gamma}\right)\right]\frac{I_0\left(\frac{kr}{\gamma}\right)}{I_0\left(\frac{kb}{\gamma}\right)}\end{aligned} \tag{C.56}$$

$$\tilde{E}_r(k,r) = \frac{k}{2\pi\epsilon_0\gamma} q\tilde{\lambda}(k) \left\{ \begin{array}{l} -K_0\left(\frac{ka}{\gamma}\right) I_1\left(\frac{kr}{\gamma}\right), \; r < a \\ I_0\left(\frac{ka}{\gamma}\right) K_1\left(\frac{kr}{\gamma}\right), \; r > a \end{array} \right\} \\ -i\gamma\left[d(k) + \frac{ik}{\gamma^2} q\tilde{\lambda}(k) I_0\left(\frac{ka}{\gamma}\right) K_0\left(\frac{kb}{\gamma}\right)\right] \frac{I_1\left(\frac{kr}{\gamma}\right)}{I_0\left(\frac{kb}{\gamma}\right)} \tag{C.57}$$

and $\tilde{B}_\theta = \beta/c\tilde{E}_r$.

(4) The Ultra-relativistic Limit

For high particle energies, the argument of the modified Bessel-functions will tends to zero and an approximate expression for the electromagnetic fields can be derived. For $x \ll 1$

$$I_0(x) \approx 1 \tag{C.58}$$
$$I_1(x) \approx \frac{x}{2} \tag{C.59}$$
$$K_0(x) \approx -\left(\ln\left(\frac{x}{2}\right) + 0.5772\right) \tag{C.60}$$
$$K_1(x) \approx \frac{1}{x} \tag{C.61}$$

Vacuum Chamber of Infinite Conductivity: Inserting the approximate expression for the small argument modified Bessel functions into Eq. (C.27)–(C.29) we obtain

$$\tilde{E}_z(k,r) = \lim_{\gamma\to\infty} \frac{-ik}{2\pi\epsilon_0\gamma^2} q\tilde{\lambda}(k) \left\{\log\left(\frac{kr}{2\gamma}\right) + \log\left(\frac{kb}{2\gamma}\right)\right\} = 0 \tag{C.62}$$
$$\tilde{E}_r(k,r) = \lim_{\gamma\to\infty} \frac{k}{2\pi\epsilon_0\gamma} q\tilde{\lambda}(k) \left\{\frac{\gamma}{kr} + \log\left(\frac{kb}{2\gamma}\right)\right\} = \frac{q\tilde{\lambda}(k)}{2\pi\epsilon_0}\frac{1}{r} \tag{C.63}$$
$$\tilde{B}_\theta(k,r) = \frac{\beta}{c}\tilde{E}_r(k,r)\,. \tag{C.64}$$

The fields of Eq. (C.62)–(C.64) are now identical to the fields evaluated by a steady-state coasting beam approach [80].

Vacuum Chamber of Finite Conductivity: Inserting the approximations (C.58) - (C.61) into Eq. (C.54) and (C.55) yields the following result for $\gamma \to \infty$

$$d(k) = \frac{q\tilde{\lambda}(k)}{2\pi\epsilon_0 b} \frac{1}{\frac{ikb}{2} - \left(\frac{k}{\lambda} + \frac{\lambda}{k}\right)} \tag{C.65}$$
$$c(k) = d(k)\,. \tag{C.66}$$

In the ultra-relativistic limit the coefficients $c(k, r_s)$ and $d(k, r_s)$ become equal. The electromagnetic fields simplify to

$$\tilde{E}_z = d(k) \tag{C.67}$$

$$\tilde{E}_r = \frac{q\tilde{\lambda}(k)}{2\pi\epsilon_0 c}\frac{1}{r} - \frac{ik}{2}d(k)r \tag{C.68}$$

$$\tilde{B}_\theta = \frac{q\tilde{\lambda}(k)}{2\pi\epsilon_0 c}\frac{1}{r} - \frac{ik}{2c}d(k)r\ . \tag{C.69}$$

Notice that the longitudinal field components do not vanish even for infinitely high beam energies. These fields, called longitudinal wake fields, originating from resistive wall of the vacuum chamber influence the energy spread of short electron bunches. These wake fields become stronger for a smaller radius of the vacuum chamber b, for shorter bunches σ_z and for a smaller conductivity σ of the beam pipe. The bunch length dependence of Eq. (C.67)–(C.69) is hidden in the Fourier transformation of the longitudinal charge distribution $\tilde{\lambda}(k)$ (see Eq. (D.24) and (D.25). Longitudinal wake fields are important for the understanding of the longitudinal charge profile determination as presented in chapter 6.

Source dimension of Coherent Transition Radiation from a Uniform Charge Distribution: The integration of Eq. (C.28)–(C.29) weighted with a transverse uniform charge distribution yields the source dimensions of coherent transition radiation on the radiation boundary. The following calculation considers only the radial component of the electric field, because it dominates over the longitudinal component and is related to the azimuthal magnetic field by β/c. The coordinates are chosen such that a denotes the radius of the ring charge distribution and r the radius at which the field is evaluated. A transverse uniform charge distribution $\bar{\lambda}(a)$ can be composed of a set of ring charge distributions. The integral over a,

$$\begin{aligned}\tilde{E}_r = \frac{k}{2\pi\epsilon_0\gamma}q\tilde{\lambda}(k)\Bigg\{ &- \int_0^r d\phi\, da\, aK_0\left(\frac{ka}{\gamma}\right)\bar{\lambda}(a)I_1\left(\frac{kr}{\gamma}\right) + \\ &\int_r^\infty d\phi\, da\, aI_0\left(\frac{ka}{\gamma}\right)\bar{\lambda}(a)K_1\left(\frac{kr}{\gamma}\right) + \\ &\int_0^\infty d\phi\, da\, aI_0\left(\frac{ka}{\gamma}\right)\bar{\lambda}(a)\frac{K_0\left(\frac{kb}{\gamma}\right)}{I_0\left(\frac{kb}{\gamma}\right)}I_1\left(\frac{kr}{\gamma}\right)\Bigg\}\ .\end{aligned} \tag{C.70}$$

is solved for a uniform transverse charge distribution of radius R

$$\bar{\lambda}(a) = \frac{1}{\pi R^2}\left\{\begin{array}{ll} 1\,, & a < R \\ 0\,, & a > R \end{array}\right\}\ . \tag{C.71}$$

We obtain

$$\begin{aligned}\tilde{E}_r = \frac{k}{2\pi\epsilon_0\gamma}\frac{q\tilde{\lambda}(k)}{\pi\sigma_r^2}\Bigg\{ &\int_0^r d\phi\, da\, aK_0\left(\frac{ka}{\gamma}\right)I_1\left(\frac{kr}{\gamma}\right) + \\ &\int_r^R d\phi\, da\, aI_0\left(\frac{ka}{\gamma}\right)K_1\left(\frac{kr}{\gamma}\right) + \\ &\int_0^R d\phi\, da\, aI_0\left(\frac{ka}{\gamma}\right)\frac{K_0\left(\frac{kb}{\gamma}\right)}{I_0\left(\frac{kb}{\gamma}\right)}I_1\left(\frac{kr}{\gamma}\right)\Bigg\}\ .\end{aligned} \tag{C.72}$$

The integrals can be evaluated analytically using [79]

$$\int_0^z dt\, t^\nu I_{\nu-1}(t)dt = z^\nu I_\nu(z) \tag{C.73}$$

$$\int_0^z dt\, t^\nu K_{\nu-1}(t)dt = -z^\nu K_\nu(z) + 2^{\nu-1},\,(z) \tag{C.74}$$

where ν denotes an integer. We obtain

$$-\int_0^r da\, aK_0\left(\frac{ka}{\gamma}\right) = \frac{\gamma r}{k}K_1\left(\frac{kr}{\gamma}\right) - \frac{\gamma^2}{k^2} \tag{C.75}$$

$$\int_0^r da\, aI_0\left(\frac{ka}{\gamma}\right) = \frac{\gamma r}{k}I_1\left(\frac{kr}{\gamma}\right) \tag{C.76}$$

$$\int_0^R da\, aI_0\left(\frac{ka}{\gamma}\right) = \frac{\gamma R}{k}I_1\left(\frac{kR}{\gamma}\right)\,. \tag{C.77}$$

The radial electric fields of a uniform bunch charge distribution moving with velocity v in straight line uniform motion is

$$\tilde{E}_r(k,r) = \frac{q\tilde{\lambda}(k)}{\pi\epsilon_0 R^2}\left[\left\{\begin{array}{ll} \frac{\gamma}{k}I_1\left(\frac{kr}{\gamma}\right), & r<R \\ RI_1\left(\frac{kR}{\gamma}\right)K_1\left(\frac{kr}{\gamma}\right), & r>R \end{array}\right\} + RI_1\left(\frac{kR}{\gamma}\right)\frac{K_0\left(\frac{kb}{\gamma}\right)}{I_0\left(\frac{kb}{\gamma}\right)}I_1\left(\frac{kr}{\gamma}\right)\right]\,. \tag{C.78}$$

The electric field of a uniform charge distribution projected onto the transition radiation screen is rising proportional to $I_1(kr/\gamma)$ towards R. At radii larger than R, the field drops proportional to $K_1(kr/\gamma)$. The vacuum chamber adds to the final electric field by a term proportional to $I_1(kr/\gamma)$.

Longitudinal Space Charge Forces: The longitudinal space charge forces can be evaluated by Eq. C.28. To derive Eq. (2.3) in chapter 2 we consider a point charge, hence $r_s = 0$ and $\lambda(\zeta) = \delta(\zeta - \zeta_0)$, yielding

$$\tilde{\lambda} = \frac{1}{2\pi}\exp(-ik\zeta_0)\,. \tag{C.79}$$

Equation (C.28) then reduces to

$$\tilde{E}_z = \frac{ik}{4\pi^2\epsilon_0\gamma^2}qK_0\left(\frac{kr}{\gamma}\right)\exp(-ik\zeta_0)\,. \tag{C.80}$$

In time-domain we obtain

$$E_z = \frac{q}{4\pi^2\epsilon_0\gamma^2}\int_{-\infty}^{\infty} dk\, ikK_0\left(\frac{kr}{\gamma}\right)\exp(ik\,(\zeta-\zeta_0)) \tag{C.81}$$

$$= \frac{q}{4\pi^2\epsilon_0\gamma^2}\frac{d}{d\zeta}\left[\int_{-\infty}^{\infty} dk\, K_0\left(\frac{kr}{\gamma}\right)\exp(ik\,(\zeta-\zeta_0))\right] \tag{C.82}$$

$$= \frac{q}{4\pi^2\epsilon_0\gamma^2}\frac{d}{d\zeta}\frac{1}{\left(\left(\frac{r}{\gamma}\right)^2 + (\zeta-\zeta_0)^2\right)^{\frac{1}{2}}} \tag{C.83}$$

$$= \frac{q}{4\pi^2\epsilon_0\gamma^2}\frac{(\zeta-\zeta_0)}{\left(\left(\frac{r}{\gamma}\right)^2 + (\zeta-\zeta_0)^2\right)^{\frac{3}{2}}} \tag{C.84}$$

Equation (2.3) in chapter 2 is obtained by setting $r = 0$

$$E_z = \frac{q}{4\pi^2\epsilon_0\gamma^2}\frac{1}{(\zeta - \zeta_0)^2} \tag{C.85}$$

Appendix D

Space Charge Forces

A linear expression for the space charge forces experienced by a test particle in a uniform and a Gaussian charge distribution can be evaluated using Eq. (C.29) describing the radial electric field of a ring charge distribution of radius a traveling in uniform motion with velocity v along a straight line. Neglecting the wall effects of the beam pipe we obtain

$$\tilde{E}_r(k,r) = \frac{k}{2\pi\epsilon_0\gamma} q\tilde{\lambda}(k) \left\{ \begin{array}{ll} -K_0\left(\frac{ka}{\gamma}\right) I_1\left(\frac{kr}{\gamma}\right) & , \quad r < a \\ I_0\left(\frac{ka}{\gamma}\right) K_1\left(\frac{kr}{\gamma}\right) & , \quad r > a \end{array} \right\} . \tag{D.1}$$

where a denotes the radius of the ring charge distribution and r the radius where the field is evaluated. To describe the field travelling together with a transverse charge distribution $lam\bar{b}da$, Eq. (D.1) has to be wighted with $\bar{\lambda}$. The integral yields

$$\begin{aligned} \tilde{E}_r = \frac{k}{2\pi\epsilon_0\gamma} q\tilde{\lambda}(k) \left\{ - \int_0^r d\phi\, da\, a K_0\left(\frac{ka}{\gamma}\right) \bar{\lambda}(a) I_1\left(\frac{kr}{\gamma}\right) + \right. \\ \left. \int_r^\infty d\phi\, da\, a I_0\left(\frac{ka}{\gamma}\right) \bar{\lambda}(a) K_1\left(\frac{kr}{\gamma}\right) \right\} . \end{aligned} \tag{D.2}$$

Uniform Charge Distribution

For a uniform charge distribution

$$\bar{\lambda}_U(a) = \frac{1}{\pi R^2} \left\{ \begin{array}{ll} 1\,, & a < R \\ 0\,, & a > R \end{array} \right\} \tag{D.3}$$

Eq. (D.2) yields

$$\tilde{E}_r^U = \frac{k}{2\pi\epsilon_0\gamma} \frac{q\tilde{\lambda}(k)}{\pi R^2} \left\{ - \int_0^r d\phi\, da\, a K_0\left(\frac{ka}{\gamma}\right) I_1\left(\frac{kr}{\gamma}\right) + \int_r^R d\phi\, da\, a I_0\left(\frac{ka}{\gamma}\right) K_1\left(\frac{kr}{\gamma}\right) \right\} \tag{D.4}$$

$$= \frac{q\tilde{\lambda}(k)}{\pi\epsilon_0 R^2} \left\{ \begin{array}{ll} \frac{\gamma}{k} I_1\left(\frac{kr}{\gamma}\right) & , \quad r < R \\ R I_1\left(\frac{kR}{\gamma}\right) K_1\left(\frac{kr}{\gamma}\right) & , \quad r > R \end{array} \right\} . \tag{D.5}$$

A small argument approximation of Eq. (D.5) is obtained by inserting the small argument approximation of the modified Bessel functions Eq. (C.58)–(C.60)

$$\tilde{E}_r^U(k,r) = \frac{q\tilde{\lambda}(k)}{\pi\epsilon_0 R^2} \left\{ \begin{array}{ll} \frac{r}{2} & , \quad r < R \\ \frac{R^2}{2r} & , \quad r > R \end{array} \right\} . \tag{D.6}$$

The field is increasing linearly until the edge of the uniform charge distribution. For larger radii it decreases proportional to $1/r$.

Gaussian Charge Distribution

To describe a Gaussian charge distribution, Eq. (D.1) has to be weighted with a transverse Gaussian distribution

$$\bar{\lambda}_G(a) = \frac{1}{2\pi\sigma_r^2}\exp\left(-\frac{a^2}{2\sigma_r^2}\right). \tag{D.7}$$

Integral (D.2) yields

$$\tilde{E}_r^G = \frac{k}{2\pi\epsilon_0\gamma}\frac{q\tilde{\lambda}(k)}{2\pi\sigma_r^2}\left\{-\int_0^r d\phi\, da\, aK_0\left(\frac{ka}{\gamma}\right)\exp\left(-\frac{a^2}{2\sigma_r^2}\right)I_1\left(\frac{kr}{\gamma}\right) + \int_r^\infty d\phi\, da\, aI_0\left(\frac{ka}{\gamma}\right)\exp\left(-\frac{a^2}{2\sigma_r^2}\right)K_1\left(\frac{kr}{\gamma}\right)\right\}. \tag{D.8}$$

The second integral is split into two components. Applying partial integration we obtain

$$\int_0^\infty da\, a\, I_0\left(\frac{ka}{\gamma}\right)\exp\left(-\frac{a^2}{2\sigma_r^2}\right) = \sigma_r^2 + \frac{\sqrt{2\pi}k\sigma_r^3}{\gamma}\exp\left(\frac{k^2R^2}{4\gamma^2}\right)I_{1/2}\left(\frac{k^2\sigma_r^2}{4\gamma^2}\right) \tag{D.9}$$

and

$$-\int_0^r da\, a\, I_0\left(\frac{ka}{\gamma}\right)\exp\left(-\frac{a^2}{2\sigma_r^2}\right) = \sigma_r^2\left(I_0\left(\frac{kr}{\gamma}\right)\exp\left(-\frac{r^2}{2\sigma_r^2}\right) - 1\right) - \frac{k\sigma_r^2}{\gamma}\int_0^r da\, I_1\left(\frac{ka}{\gamma}\right)\exp\left(-\frac{a^2}{2\sigma_r^2}\right). \tag{D.10}$$

where

$$\int_0^\infty dt\exp\left(-a^2t^2\right)I_\nu(bt)\,dt = \frac{\sqrt{\pi}}{2a}\exp\left(\frac{b^2}{8a^2}\right)I_{\nu/2}\left(\frac{b^2}{8a^2}\right) \tag{D.11}$$

has been used [79]. The expressions (D.9) and (D.10) have to be evaluated for small transverse dimensions r, i. e. close to the center of the Gaussian charge distribution where we expect a linear characteristic of the space charge force. Using the small argument approximations of the modified Bessel functions and the polynomial expansion of the exponential function we obtain a linear contribution from Eq. (D.10) yielding

$$\begin{aligned}
\tilde{E}_r^I &= -\frac{k}{2\pi\epsilon_0\gamma}\frac{q\tilde{\lambda}(k)}{2\pi\sigma_r^2}2\pi\sigma_r^2\left\{I_0\left(\frac{kr}{\gamma}\right)\exp\left(-\frac{r^2}{2\sigma_r^2}\right) - 1\right\}K_1\left(\frac{kr}{\gamma}\right) && \text{(D.12)}\\
&= -\frac{1}{2\pi\epsilon_0}q\tilde{\lambda}(k)\left\{1 - \frac{r^2}{2\sigma_r^2} - 1\right\}\frac{1}{r} && \text{(D.13)}\\
&= \frac{q\tilde{\lambda}(k)}{4\pi\epsilon_0\sigma_r^2}r\,. && \text{(D.14)}
\end{aligned}$$

The two missing integrals bound by 0 and r are evaluated for small radii. We obtain

$$\frac{k\sigma_r^2}{\gamma}\int_0^r da\, I_1\left(\frac{ka}{\gamma}\right)\exp\left(-\frac{a^2}{2\sigma_r^2}\right) \approx \frac{k\sigma_r^2}{\gamma}\int_0^r da\,\frac{ka}{2\gamma}\left(1 - \frac{a^2}{2\,\sigma_r^2}\right) \quad \text{and} \tag{D.15}$$

$$-\int_0^r da\, aK_0\left(\frac{ka}{\gamma}\right)\exp\left(-\frac{a^2}{2\sigma_r^2}\right) \approx -\int_0^r da\left(-\ln\left(\frac{ka}{\gamma}\right)-0.58\right)\left(a-\frac{a^3}{2\sigma_r^2}\right) \tag{D.16}$$

Equation (D.15) yields a term linear in r

$$\tilde{E}_r^{II} = -\frac{k}{2\pi\epsilon_0\gamma}\frac{q\tilde{\lambda}(k)}{2\pi\sigma_r^2}\frac{2\pi k^2\sigma_r^2}{\gamma^2}\frac{r^2}{2}K_1\left(\frac{kr}{\gamma}\right) \tag{D.17}$$

$$\approx -\frac{k^2}{4\pi\epsilon_0\gamma^2}q\tilde{\lambda}(k)r\,. \tag{D.18}$$

The evaluation of integral (D.16) yields lowest order terms of $\mathcal{O}(r)$. The lowest order of the radial electric field is then of the order of $\mathcal{O}(r^2)$ because $I_1(kr/\gamma) \approx kr/2\gamma = \mathcal{O}(r)$.

The electric and magnetic fields close to the center of a transverse Gaussian charge distribution are in linear approximation

$$\tilde{E}_r^G \approx \frac{q\tilde{\lambda}(k)}{4\pi\epsilon_0\sigma_r^2}r - \frac{k^2}{4\pi\epsilon_0\gamma^2}q\tilde{\lambda}(k)r \approx \frac{q\tilde{\lambda}(k)}{4\pi\epsilon_0\sigma_r^2}r \tag{D.19}$$

The second term of Eq. (D.19) is small compared to the first term because of the factor $1/\gamma^2$ and can therefore be neglected. The linear approximation of the fields of a Gaussian bunch charge distribution is a valid approximation for radii $r \leq \sigma_r$.

Forces and Transverse Kicks

The electromagnetic force $\tilde{F}$ can be evaluated using

$$\tilde{F}_r = e\left(\tilde{E}_r - v\tilde{B}_\theta\right) = e\tilde{E}_r\left(1-\beta^2\right) = \frac{e\tilde{E}_r}{\gamma^2} \tag{D.20}$$

where e indicates a test charge. The linearized space charge force has to be inserted into the equation of motion. To do so, the force $\tilde{F}_r$ has to be transformed into an acceleration d^2r/dz^2 with respect to the longitudinal position z in an accelerator. For the acceleration we obtain

$$\frac{d^2r}{dz^2} = \frac{1}{\beta^2c^2}\frac{d^2r}{dt^2} = \frac{1}{\beta^2c^2}\frac{\tilde{F}_r}{m\gamma} = \frac{q\tilde{E}_r}{\beta^2c^2m\gamma^3}\,. \tag{D.21}$$

The special case of a uniform and a Gaussian charge distribution yields

$$\left.\frac{d^2r}{dz^2}\right|_U = \frac{Ne^2\tilde{\lambda}(k)}{4\pi\epsilon_0m\beta^2c^2\gamma^3R^2} = \frac{2Nr_e\tilde{\lambda}(k)}{\beta^2\gamma^3R^2}r \tag{D.22}$$

$$\left.\frac{d^2r}{dz^2}\right|_G = \frac{Ne^2\tilde{\lambda}(k)}{4\pi\epsilon_0m\beta^2c^2\gamma^3\sigma_r^2}r = \frac{Nr_e\tilde{\lambda}(k)}{\beta^2\gamma^3\sigma_r^2}r \tag{D.23}$$

where $q = Ne$ and N denote the number of particles per bunch. $\tilde{\lambda}(k)$ denotes the Fourier transformation of the longitudinal bunch charge distribution. The kick a test charge experiences close to the center of a uniform charge distribution is twice the kick close to a Gaussian distribution of equal total charge.

A longitudinal Gaussian charge distribution can be expressed in terms of the wave number k

$$\tilde{\lambda}(k) = \exp\left(-\frac{k^2}{2\sigma_k^2}\right). \tag{D.24}$$

The Fourier transformation yields

$$\lambda(\zeta) = \int_{-\infty}^{\infty} \tilde{\lambda}(k)\exp(ik\zeta)dk = \frac{1}{\sqrt{2\pi\sigma_z^2}}\exp\left(-\frac{\zeta^2}{2\sigma_z^2}\right) \tag{D.25}$$

where σ_z denotes the bunch length. For Gaussian distributions the rms width in time and frequency are related by $\sigma_z = 1/\sigma_k$. The coordinate $\zeta = z - \beta ct$ takes into account that the fields travel along with the bunch at a velocity v.

The resulting transverse space charge kick is

$$k_r = \frac{2Nr_e}{\sqrt{2\pi}}\frac{1}{\beta^2\gamma^3R^2\sigma_z} \quad , \quad k_r = \frac{Nr_e}{\sqrt{2\pi}}\frac{1}{\beta^2\gamma^3\sigma_r^2\sigma_z} \tag{D.26}$$

for a uniform and a Gaussian charge distribution, respectively. Equations (D.26) are written for the central slice of the bunch ($\zeta = 0$).

Equations (D.26) describe the linearized space charge forces for a bunch of cylindrical symmetry. Using an elliptical integration path a more general situation, where the horizontal σ_x and vertical σ_y beam dimensions are different, can be evaluated. The result of this calculation yields for a Gaussian transverse charge distribution [81]

$$k_x = \frac{2Nr_e}{\sqrt{2\pi}}\frac{1}{\sigma_x(\sigma_x+\sigma_y)\,\sigma_z\beta^2\gamma^3} \quad , \quad k_y = \frac{2Nr_e}{\sqrt{2\pi}}\frac{1}{\sigma_y(\sigma_x+\sigma_y)\,\sigma_z\beta^2\gamma^3}\,. \tag{D.27}$$

Equation (D.27) is used for the evaluation of linearized space charge forces in chapter 4. For the special case of $\sigma_x = \sigma_y$, Eq. (D.26) is obtained.

Appendix E

Hilbert Transform Spectroscopy

This appendix outlines the theory of Hilbert transform spectroscopy for Josephson junctions obeying the so-called RSJ-model. The response of the junction without incident radiation (autonomous case), with incident monochromatic radiation and with an incident radiation spectrum will be treated.

E.1 Current-Voltage Characteristic without Radiation

A Josephson junction obeying the RSJ model is described by Equation (8.3)

$$I_0 = I_c \sin\phi + \frac{\hbar}{2eR}\frac{d\phi}{dt}.$$

A constant dc current $I_0 > I_c$ is applied. In the following we use dimensionless quantities

$$i_0 = I_0/I_c, \qquad u = U/RI_c, \qquad \tau = t\omega_c, \qquad \omega_c = \frac{2eRI_c}{\hbar}\ . \tag{E.1}$$

Equation (8.3) then transforms to

$$\frac{d\phi}{d\tau} = i_0 - \sin\phi(\tau)\ . \tag{E.2}$$

For $I_0 > I_c$, i.e. $i_0 > 1$, one gets $d\phi/d\tau = i_0 - \sin\phi(\tau) \neq 0$ so we can separate variables:

$$\frac{d\phi}{i_0 - \sin\phi} = d\tau\ . \tag{E.3}$$

Integration gives

$$\frac{2}{\sqrt{i_0^2 - 1}} \arctan\left(\frac{i_0 \tan(\phi/2) - 1}{\sqrt{i_0^2 - 1}}\right) = \tau + \text{const} \tag{E.4}$$

or

$$\tan(\phi/2) = \frac{1}{i_0} + \frac{\sqrt{i_0^2 - 1}}{i_0} \tan\left(\frac{\sqrt{i_0^2 - 1}}{2}\,\tau + \chi\right) \tag{E.5}$$

where χ is an arbitrary phase. Then ϕ is

$$\phi(\tau) = 2\arctan\left(\frac{1}{i_0} + \frac{\sqrt{i_0^2-1}}{i_0}\tan(\frac{\sqrt{i_0^2-1}}{2}\tau + \chi)\right) \ . \tag{E.6}$$

The normalized voltage is $u(\tau) = d\phi/d\tau$:

$$\begin{aligned} u(\tau) &= i_0 - (i_0^2-1)\frac{1+\tan^2\left(\frac{\sqrt{i_0^2-1}}{2}\tau+\chi\right)}{i_0+\frac{1}{i_0}\left(1+\sqrt{(i_0^2-1)}\tan\left(\frac{\sqrt{i_0^2-1}}{2}\tau+\chi\right)\right)^2} \\ &= (i_0^2-1)\frac{1}{i_0+\frac{1}{i_0}\left(\cos\left(\sqrt{i_0^2-1}\,\tau+2\chi\right)+\sqrt{(i_0^2-1)}\sin\left(\sqrt{i_0^2-1}\,\tau+2\chi\right)\right)}. \end{aligned} \tag{E.7}$$

The last expression can be simplified by substituting $\sin\theta = 1/i_0$ (remember that $I_0 > I_c$, so $i_0 > 1$). Then $\cos\theta = \sqrt{1-\sin^2\theta} = \frac{1}{i_0}\sqrt{i_0^2-1}$ and

$$u = \frac{(i_0^2-1)}{i_0+\sin\left(\sqrt{i_0^2-1}\,\tau+2\chi+\theta\right)}. \tag{E.8}$$

The constant χ is determined by the initial conditions. For the following calculations χ is chosen such that

$$u = \frac{(i_0^2-1)}{i_0-\cos\left(\sqrt{i_0^2-1}\,\tau\right)} \ . \tag{E.9}$$

Returning to unnormalized quantities we get Equation (8.4). The dc voltage measured across the junction is the time-average of u(τ):

$$\overline{u} = \frac{1}{\tau_0}\int_0^{\tau_0}\frac{i_0^2-1}{i_0-\cos\left(\sqrt{i_0^2-1}\,\tau\right)}d\tau \ . \tag{E.10}$$

Here $\tau_0 = 2\pi/\sqrt{i_0^2-1}$ is the period of oscillation. The integral yields

$$\overline{u} = \frac{2}{\tau_0}\left[\arctan\left(\frac{(i_0-1)\tan\left(\sqrt{i_0^2-1}\,\frac{\tau}{2}\right)}{\sqrt{i_0^2-1}}\right)\right]_{\tau=0}^{\tau=\tau_0} \ . \tag{E.11}$$

The argument of the tangent function is zero at the lower boundary and π at the upper boundary. The arctan function advances by π between two successive zeros of its argument. Therefore we obtain the simple formula

$$\overline{u} = \frac{2}{\tau_0}\pi = \sqrt{i_0^2-1} \ . \tag{E.12}$$

The result can be summarized by

$$\overline{u} = \left\{\begin{array}{ll} 0 & \text{for} \quad |i_0| \le 1 \\ \sqrt{i_0^2-1} & \text{for} \quad |i_0| > 1 \end{array}\right\} \tag{E.13}$$

and corresponds to Equation (8.5) in unnormalized quantities.

E.2 Current-Voltage Characteristic with Radiation

Incident radiation is modeled by an additional sinusoidal current with amplitude I_s and frequency ω_s, which has to be superimposed on the dc bias current I. In normalized quantities, the differential Equation (8.7) becomes

$$i + i_s \sin(\Omega\tau) = \sin\phi(\tau) + \frac{d\phi}{d\tau} \tag{E.14}$$

with

$$i_s = \frac{I_s}{I_c} \quad \text{and} \quad \Omega = \frac{\omega_s}{\omega_c} \,. \tag{E.15}$$

Equation (E.14) has no analytical solution. The radiation-induced current can be regarded as a small perturbation since $i_s \ll 1$ [66]. In the following calculation we determine the change in the dc bias current while keeping the time-averaged voltage $\overline{u}$ constant (compare figure 8.3). The dc current i and the phase ϕ are expanded into powers of the ac-current amplitude i_s

$$i = i_0 + \sum_{k=1}^{\infty} a_k i_s^k \quad \text{and} \quad \phi = \phi_0 + \sum_{k=1}^{\infty} b_k i_s^k \,. \tag{E.16}$$

The $\sin\phi$ term in Equation (E.14) is expanded into a second-order Taylor series

$$\sin\left(\phi_0 + \sum_{k=1}^{\infty} b_k i_s^k\right) \approx \sin\phi_0 + b_1 \cos\phi_0 \; i_s + \left(b_2 \cos\phi_0 - \frac{b_1^2}{2}\sin\phi_0\right) i_s^2 \,. \tag{E.17}$$

Equations (E.16) and (E.17) are introduced into the differential Equation (E.14). Sorting for powers of i_s we get

$$\frac{d\phi_0}{d\tau} + \sin\phi_0 = i_0 \tag{E.18}$$

$$\frac{db_1}{d\tau} + b_1 \cos\phi_0 = a_1 + \sin(\Omega\tau) \qquad \text{for} \quad k = 1 \tag{E.19}$$

$$\frac{db_2}{d\tau} + b_2 \cos\phi_0 = a_2 + \frac{b_1^2}{2}\sin\phi_0 \qquad \text{for} \quad k = 2 \,. \tag{E.20}$$

Equation (E.18) describes the characteristic of the junction without radiation and is solved by (E.6). Equations
(E.19) and (E.20) are of the form

$$\frac{db_k}{d\tau} + b_k \cos\phi_0 = f_k(\tau) \,. \tag{E.21}$$

The general solution of this equation is

$$b_k = \exp\left(-\int^{\tau} \cos\phi_0 \, d\tau'\right)\left(\int^{\tau} \exp\left(\int^{\tau'} \cos\phi_0 \, d\tau''\right) f_k(\tau')\, d\tau'\right) \,. \tag{E.22}$$

An expression for $\cos\phi_0$ can be derived from (E.2). Taking the derivative with respect to the normalized time

$$\frac{d^2\phi_0}{d\tau^2} + \frac{d\phi_0}{d\tau}\cos\phi_0 = 0$$

one obtains

$$\cos\phi_0 = -\frac{\ddot{\phi}_0}{\dot{\phi}_0} = -\frac{d\ln\dot{\phi}_0}{d\tau} \ . \tag{E.23}$$

Inserting Equation (E.23) into (E.22) the latter equation yields

$$b_k = \dot{\phi}_0 \int^{\tau} \frac{f_k(\tau')}{\dot{\phi}_0(\tau')}\, d\tau' \ . \tag{E.24}$$

We are now looking for the change in the dc current at a fixed value of the time-averaged voltage:

$$\overline{u} = \overline{\dot{\phi}_0} + \overline{\dot{b}_1} + \overline{\dot{b}_2} + ... = \overline{\dot{\phi}_0} \ . \tag{E.25}$$

This is fulfilled if

$$\overline{\dot{b}_k} = 0 \quad \text{for all} \quad k > 0 \ . \tag{E.26}$$

A consequence is that the integrand in Equation (E.24) is not allowed to have a dc component. This can be seen as follows. We form the long-term time average of $\dot{b}_k$

$$\overline{\dot{b}_k} = \lim_{T\to\infty} \frac{1}{T}\int_0^T \dot{b}_k d\tau = \lim_{T\to\infty} \frac{1}{T}(b_k(T) - b_k(0)) \ . \tag{E.27}$$

Assume now that the integrand in Equation (E.24) had a dc component, say A. Then $b_k(T) - b_k(0)$ would be of the form $A \cdot T$ plus a bounded term due to the ac components of the integrand in (E.24). From the condition $\overline{\dot{b}_k} = 0$ follows immediately $A = 0$, i.e. the dc component is indeed zero.
The condition $\overline{\dot{b}_1} = 0$ implies

$$\overline{(a_1 + \sin(\Omega\tau))\,\dot{\phi}_0^{-1}} = 0 \tag{E.28}$$

or

$$\overline{(a_1 + \sin(\Omega\tau))\,(i_0 - \cos(\overline{u}\tau))} = 0 \tag{E.29}$$

where $f_1(\tau) = a_1 + \sin(\Omega\tau)$ has been inserted. Keeping in mind that a_1 describes a pure dc current component, Equation (E.29) can be solved for a_1:

$$a_1 = \frac{1}{i_0}\overline{\sin(\Omega\tau)\cos(\overline{u}\tau)} \quad \Rightarrow \quad a_1 = 0 \quad \text{for} \quad \Omega \neq \overline{u} \ . \tag{E.30}$$

From Equation (E.30) follows directly that there is no first-order dc current component is introduced by the small ac current[1]. The first-order phase correction $b_1(\tau)$ can now be calculated from Equation (E.24) setting $a_1 = 0$. It follows

$$b_1 = \dot{\phi}_0 \int^{\tau} \frac{\sin(\Omega\tau')}{\dot{\phi}_0} d\tau' = \frac{1}{i_0 - \cos(\overline{u}\tau)} \int^{\tau} (i_0 - \cos(\overline{u}\tau'))\sin(\Omega\tau')\, d\tau' \tag{E.31}$$

or

$$b_1 = -\frac{1}{i_0 - \cos(\overline{u}\tau)} \left(\frac{i_0\cos(\Omega\tau)}{\Omega} - \frac{\cos((\Omega - \overline{u})\,\tau)}{2\,(\Omega - \overline{u})} - \frac{\cos((\Omega + \overline{u})\,\tau)}{2\,(\Omega + \overline{u})} \right) \ . \tag{E.32}$$

[1] A finite value is obtained for a_1 if $\Omega = \overline{u}$. This special case is excluded by taking the principal value of the integral in Equation (E.41)

The next step is the solution of Equation (E.20) with the condition $\overline{\dot{b}_2} = 0$. The absence of a dc component in the integrand in (E.24) means for $k = 2$:

$$\overline{\left(a_2 + \frac{b_1^2}{2}\sin\phi_0\right)\left(i_0 - \cos\left(\overline{u}\tau\right)\right)} = 0 \tag{E.33}$$

An expression for $\sin\phi_0$ can be derived from Equations (E.9) and (E.2).

$$\dot{\phi}_0 = \frac{\overline{u}^2}{i_0 - \cos\left(\overline{u}\tau\right)} = i_0 - \sin\phi_0 \tag{E.34}$$

and therefore

$$\sin\phi_0 = \frac{1 - i_0\cos\left(\overline{u}\tau\right)}{i_0 - \cos\left(\overline{u}\tau\right)} \; . \tag{E.35}$$

Inserting the latter expression into Equation (E.33) and solving for the second-order correction a_2 of the dc current we find

$$a_2 = -\frac{1}{2i_0}\overline{\left(1 - i_0\cos\left(\overline{u}\tau\right)\right)b_1^2} \; . \tag{E.36}$$

Now expression (E.32) has to be substituted for b_1 and with the identity

$$\frac{1 - i_0\cos\left(\sqrt{i_0^2 - 1}\,\tau\right)}{\left(i_0 - \cos\left(\sqrt{i_0^2 - 1}\,\tau\right)\right)^2} = -2\sum_{k=1}^{\infty}\frac{k\cos\left(k\sqrt{i_0^2 - 1}\,\tau\right)}{\left(i_0 + \sqrt{i_0^2 - 1}\right)^k} \tag{E.37}$$

the following expression for the second-order dc current is found

$$a_2 = \overline{\frac{1}{a_0}\sum_{k=1}^{2}\frac{k\cos\left(k\sqrt{i_0^2 - 1}\,\tau\right)}{\left(i_0 + \sqrt{i_0^2 - 1}\right)^k}\left(\frac{i_0\cos\left(\Omega\tau\right)}{\Omega} - \frac{\cos\left(\left(\Omega - \overline{u}\right)\tau\right)}{2\left(\Omega - \overline{u}\right)} - \frac{\cos\left(\left(\Omega + \overline{u}\right)\tau\right)}{2\left(\Omega + \overline{u}\right)}\right)^2} \; .$$

Note that only the first two terms ($k = 1, 2$) of the sum are included in taking the time average. Three terms have to be evaluated

$$\begin{aligned}
T_1 &= \frac{1}{\tau}\int^{\tau}\frac{1}{i_0(i_0 + \overline{u})}\left(\frac{-a_0\cos^2\left(\Omega\tau'\right)\cos^2\left(\overline{u}\tau'\right)}{\Omega\left(\Omega - \overline{u}\right)}\right)d\tau' \\
T_2 &= \frac{1}{\tau}\int^{\tau}\frac{1}{i_0(i_0 + \overline{u})}\left(\frac{-a_0\cos^2\left(\Omega\tau'\right)\cos^2\left(\overline{u}\tau'\right)}{\Omega\left(\Omega + \overline{u}\right)}\right)d\tau' \\
T_3 &= \frac{1}{\tau}\int^{\tau}\frac{2}{i_0\left(i_0 + \overline{u}\right)^2} \\
&\quad \left(\frac{\left(\cos^2\left(\overline{u}\tau'\right)\cos^2\left(\Omega\tau'\right) - \sin^2\left(\overline{u}\tau'\right)\sin^2\left(\Omega\tau'\right)\right)\left(\cos^2\left(\overline{u}\tau'\right) - \sin^2\left(\overline{u}\tau'\right)\right)}{2\left(\Omega^2 - \overline{u}^2\right)}\right)d\tau' \; .
\end{aligned}$$

The integrations are straight forward and lead to

$$a_2 = T_1 + T_2 + T_3 = -\frac{1}{4i_0\left(\Omega^2 - \overline{u}^2\right)} \; . \tag{E.38}$$

The important result is that in second order a non-zero dc current component remains after the integration. This leads to a resonance-type correction of the dc current-voltage characteristic of the Josephson junction. In terms of currents, the final result can be stated as

$$\Delta i = a_2 i_s^2 = -\frac{i_s^2}{4i_0\,(\Omega^2 - \overline{u}^2)} \quad \text{for} \quad \overline{u} \neq \Omega\ . \tag{E.39}$$

Returning to unnormalized quantities we get Equation (8.8). The current correction in second order Δi is proportional to the square of the perturbing radiation amplitude i_s^2 and is sensitive to its frequency ω_s. The first property implies that the Josephson junction acts as a "quadratic detector", i. e. the detector response is proportional to the incident radiation power.

The generalization of Equation (E.39) to a continuous radiation spectrum is straight forward. The response of the Josephson junction to monochromatic perturbation has to be convoluted with the normalized continuous power spectrum $\overline{s}(\Omega)$. Equation (E.39) then becomes

$$\Delta i = -\frac{1}{4i_0}\int_{-\infty}^{\infty} \frac{i_s^2\,\overline{s}(\Omega)}{\Omega^2 - \overline{u}^2}\,d\Omega = -\frac{1}{4i_0}\int_{-\infty}^{\infty} \frac{s(\Omega)}{\Omega^2 - \overline{u}^2}\,d\Omega \tag{E.40}$$

where $s(\Omega) = \overline{s}(\Omega)\,i_s^2$. Returning to unnormalized quantities and setting $S(\Omega) = s(\Omega)/I_c$ we get Equation (8.11).

Equation (E.40) has to be solved for the power spectrum $s(\Omega)$. Consider

$$\begin{aligned}
\int_0^{\infty} \frac{s(\Omega)2\overline{u}}{\Omega^2 - \overline{u}^2}\,d\Omega &= \int_0^{\infty} \frac{s(\Omega)(-\Omega + \overline{u})}{\Omega^2 - \overline{u}^2}\,d\Omega + \int_0^{\infty} \frac{s(\Omega)(\Omega + \overline{u})}{\Omega^2 - \overline{u}^2}\,d\Omega \\
&= \int_{-\infty}^{0} \frac{s(\Omega)(\Omega + \overline{u})}{\Omega^2 - \overline{u}^2}\,d\Omega + \int_0^{\infty} \frac{s(\Omega)(\Omega + \overline{u})}{\Omega^2 - \overline{u}^2}\,d\Omega \\
&= \int_{-\infty}^{\infty} \frac{s(\Omega)}{\Omega - \overline{u}}\,d\Omega
\end{aligned}$$

where $s(\Omega) = s(-\Omega)$ is assumed. The latter integral diverges for $\Omega = \overline{u}$. A correct mathematical treatment, however, demands for a principal value integral, denoted by $\mathcal{P}$, to exclude the pole. Hence

$$\Delta i = -\frac{1}{8i_0\overline{u}}\,\mathcal{P}\int_{-\infty}^{\infty} \frac{s(\Omega)}{\Omega - \overline{u}}\,d\Omega. \tag{E.41}$$

Equation (E.41) corresponds to Equation (8.12) in the text. The principal value integral (E.41) is related to the Hilbert transform, a well defined integral transform. The Hilbert transformation is derived from Fourier theory in Appendix E.3.

E.3 The Hilbert Transform

In this section the Hilbert transformation will be derived from Fourier theory. The Fourier integral is written in the following way [82]:

$$f(x) = \int_0^{\infty} (a(y)\cos xy + b(y)\sin xy)\,dy \tag{E.42}$$

where

$$a(y) = \frac{1}{\pi}\int_{-\infty}^{\infty} f(u)\cos yu\, du \tag{E.43}$$

$$b(y) = \frac{1}{\pi}\int_{-\infty}^{\infty} f(u)\sin yu\, du \tag{E.44}$$

Inserting Equation (E.43) and (E.44) into (E.42) we obtain

$$f(x) = \frac{1}{\pi}\int_0^{\infty} dy \int_{-\infty}^{\infty} f(u)\cos\left(y(u-x)\right) du \tag{E.45}$$

or written in complex form

$$f(x) = \mathrm{Re}\,\frac{1}{\pi}\int_0^{\infty} dy \int_{-\infty}^{\infty} f(u)\exp\left(iy(u-x)\right) du = \mathrm{Re}\;\Phi. \tag{E.46}$$

Calculating the imaginary part of Φ instead we obtain

$$g(x) = \mathrm{Im}\;\Phi = \frac{1}{\pi}\int_0^{\infty} dy \int_{-\infty}^{\infty} f(u)\sin\left(y(u-x)\right) du \tag{E.47}$$

or

$$g(x) = \int_0^{\infty} \left(b(y)\cos xy - a(y)\sin xy\right) dy\ . \tag{E.48}$$

The integral (E.48) is called the allied integral of Fourier's integral [83]. The allied integral is obtained by replacing $a(y)$ by $b(y)$ and $b(y)$ by $-a(y)$ in (E.42). The twice repeated formation of the allied Fourier integral leads to the negative of the original.

According to Equation (E.48) the Fourier coefficient $a(y)$ and $b(y)$ can be written in a different way:

$$a(y) = -\frac{1}{\pi}\int_{-\infty}^{\infty} g(u)\sin yu\, du \tag{E.49}$$

$$b(y) = \frac{1}{\pi}\int_{-\infty}^{\infty} g(u)\cos yu\, du\ . \tag{E.50}$$

Formally we obtain from Equation (E.47)

$$g(x) = \frac{1}{\pi}\lim_{\lambda\to\infty}\int_0^{\lambda} dy \int_{-\infty}^{\infty} f(u)\sin\left(y(u-x)\right) du\ . \tag{E.51}$$

Integration of the outer integral leads to

$$g(x) = \frac{1}{\pi}\lim_{\lambda\to\infty}\int_{-\infty}^{\infty} f(u)\frac{1-\cos\left(\lambda(u-x)\right)}{u-x}\, du. \tag{E.52}$$

For $\lambda\to\infty$, however, the term $\cos\left(\lambda(u-x)\right)$ averages to zero. Hence

$$g(x) = \frac{1}{\pi}\,\mathcal{P}\int_{-\infty}^{\infty}\frac{f(u)}{u-x}\, du \tag{E.53}$$

where $\mathcal{P}$ denotes the principal value at $u=x$.

The inversion of Equation (E.53) is derived by inserting (E.49) and (E.50) into (E.42) following

$$f(x) = -\frac{1}{\pi}\int_0^\infty dy \int_{-\infty}^\infty g(u)\sin\left(y(u-x)\right)\,du. \tag{E.54}$$

Following the previous steps we obtain

$$f(x) = -\frac{1}{\pi}\lim_{\lambda\to\infty}\int_{-\infty}^\infty g(u)\frac{1-\cos\left(\lambda(u-x)\right)}{u-x}\,du. \tag{E.55}$$

The $\cos\left(\lambda(u-x)\right)$ term can be neglected for $\lambda \to \infty$ and the following expressions have been derived

$$g(x) = \frac{1}{\pi}\,\mathcal{P}\int_{-\infty}^\infty \frac{f(u)}{u-x}\,du, \qquad f(x) = -\frac{1}{\pi}\,\mathcal{P}\int_{-\infty}^\infty \frac{g(u)}{u-x}\,du \tag{E.56}$$

The reciprocity expressed by (E.56) was first discovered by Hilbert. The Hilbert transformation can also be derived from Cauchy's integral theorem.

Appendix F

Acceptance Measurement of the Pyroelectric Detectors

The spectral acceptance of the pyroelectric detectors has been measured at the TU Munich using GaAs Read-type IMPATT diodes [61, 84]. The output power of the oscillators, shown by Tab. F.1, is calibrated using a calorimetric measurement.

	W-band				D-band		G-band			
f [GHz]	78.0	82.3	88.2	101.9	123.4	128.5	156.0	164.8	176.0	203.2
P_{rf} [mW]	46.8	37.1	37.1	15.1	1.2	1.0	5	4	3.6	1.1

Table F.1: Output power and frequency of the radiation sources. An isolator between the oscillator and the horn antenna has been used with the W-band and G-band sources.

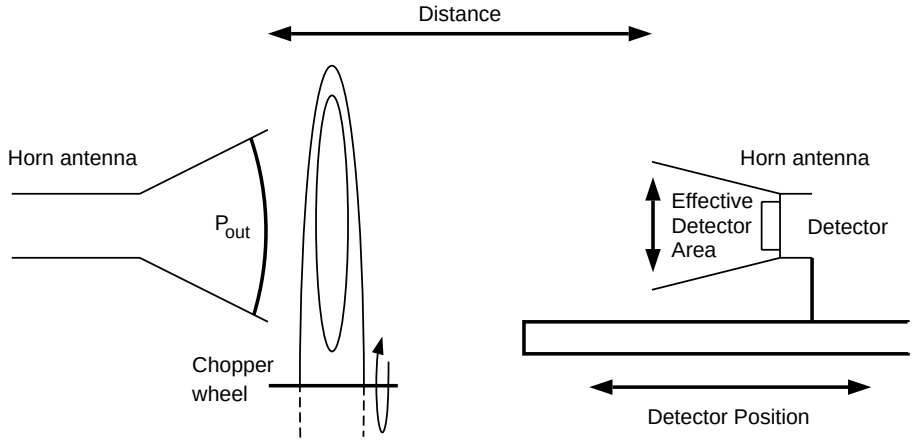


Figure F.1: Spectral acceptance measurement of the pyroelectric detectors with power calibrated dc diodes sources. The diode is connected to an isolator and a horn antenna. The emitted GHz radiation propagates freely to the detector. A chopper in front of the source is used to impose an harmonic variation on the radiation signal. The pyroelectric detector equipped with a horn antenna is mounted opposite to the source. The detector is mounted on a rail to vary the distance between the source and the detector.

An isolator between the horn antenna has been used with the W-band and G-band sources. The isolator prevents reflected rf power from traveling back to the oscillator. The attenuation caused by the use of the isolator is 1.9 dB. The W-band horn antenna has an opening of 36.5×27.5 mm and a length of 61.5 mm. The D-band horn antenna opening is 24.5×18.5 and the length is 43 mm. The attenuation of the horn antenna is determined by a calorimetric measurement and yields 3.1 dB at 101.9 GHz and 1.85 dB at 78.0 GHz. The measurement agrees well with numerical simulations performed by [85] yielding

f [GHz]	78.0	82.3	88.2	101.9	123.4	128.5
Δ [dB]	1.97	2.19	2.51	3.33	1.56	1.69

Table F.2: Attenuation Δ evaluated for the source horn antennas.

The calibration measurements of the pyroelectric detectors have been performed using the assembly shown in Fig. F.1 (W-band, D-band). The oscillator, the isolator and the horn antenna are mounted on an optical table. The GHz radiation propagates freely from the horn antenna to the detector. A chopper wheel is used to impose an harmonic variation on the radiation signal. The pyroelectric detector equipped with a cylindrical horn antenna is mounted opposite to the source on a rail to vary the distance between the source and the detector.

During the calibration measurement the detector signal is recorded at different distances from the source with and without radiation in order to subtract the background from the signal. The measurement is repeated for each of the five pyroelectric detectors. The left graph of Figure F.2 shows the resulting signal amplitude for the 78 GHz source as

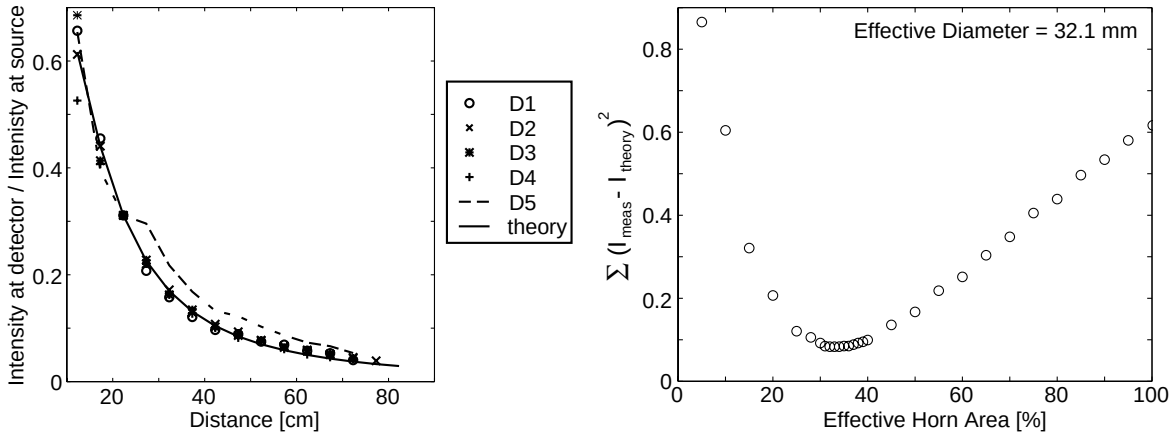


Figure F.2: Left graph: detector response caused by the 78 GHz radiation source as a function of the distance between source and detector. D1–D5 denote five different pyroelectric detectors. The solid curve shows the theoretical prediction by diffraction calculations. Right graph: theory is fitted to the measurement by varying the effective diameter of the detector horn antenna. The sum of the quadratic differences between theory and measurement (see left graph for best adaption) is plotted versus the effective diameter of the horn antenna.

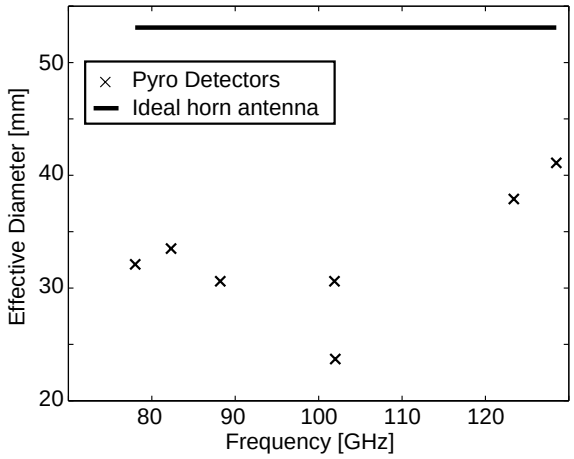


Figure F.3: Effective diameter of the pyroelectric detector equipped with the horn antenna. Data is shown as markers in the frequency range of 78 GHz to 128.5 GHz. The solid line indicates the theoretical expectation of an ideal horn antenna.

a function of the distance between the source and the detector horn antennas. The five pyro detectors are indicated as D1–D5 and the theoretical prediction is depicted as solid curve. The theoretical prediction is evaluated from a diffraction calculation of the freely propagating radiation wave. The electric field distribution in an rectangular horn antenna can be evaluated by solving Maxwell's equations [86] yielding

$$E = E_0 \cos\left(\frac{\pi x}{2a}\right) \exp\left(-ik\left(\frac{x^2}{2l_E} + \frac{y^2}{2l_H}\right)\right) \tag{F.1}$$

where x and y denotes the coordinates of the aperture dimension and l_E and l_H the slant heights of the horn. Effects at the outer rim of the horn antenna are not considered. The field distribution of Eq. (F.1) is propagated to the detector horn antenna by superimposing spherical wavelets according to the Huygens-Fresnel principle which was outlined in chapter 7. A numerical simulation is used to compute the field intensity at the opening of the detector horn antenna. The detector signal is assumed to be proportional to the integral of the intensity distribution. The theoretical prediction is adapted to the measured data by varying the effective diameter of the detector horn antenna. The right graph of Fig. F.2 shows the sum of the quadratic differences $\sum_i (I^i_{\text{meas}} - I^i_{\text{theory}})^2$ of the intensity measurement and the intensity simulation at distances d_i between the source and the detector. The optimum horn antenna diameter is 32.1 mm. The left graph of Fig. F.2 shows the comparison of the measurement and the computation for the optimum horn antenna diameter.

The effective diameter of the detector horn antenna is shown in Fig. F.3 in the frequency range of 78 GHz to 128.5 GHz. An effective diameter of 30–35 mm in the W-band range and of about 40 mm in the D-band range has been evaluated. Measurements in the G-band were not possible because of a change of the experimental setup. The solid line indicates the true diameter of the horn antenna (55.9 mm).

The G-band measurements have been performed using an optical setup which is depicted

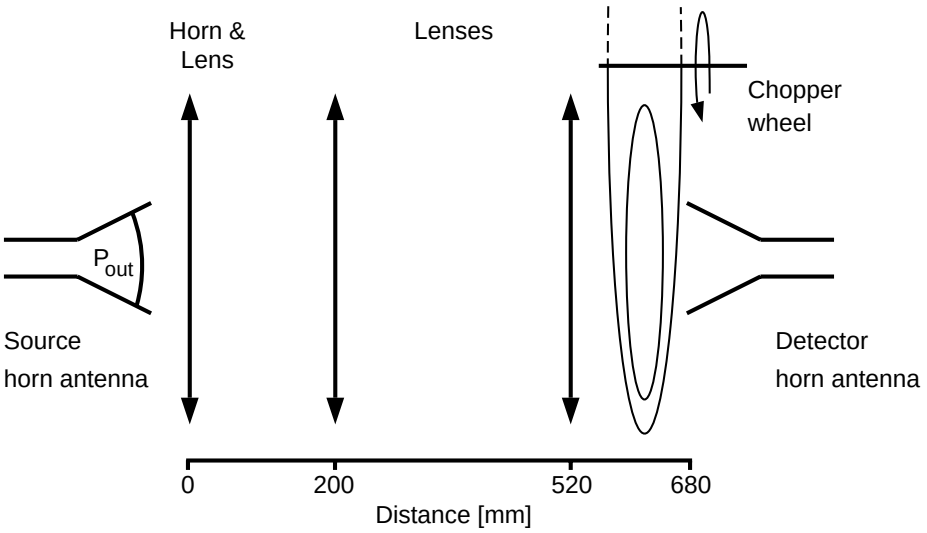


Figure F.4: Quasi-optical setup to determine the detector acceptance in the G-band range. Frequency-doubled W-band sources are used. Radiation is emitted through a horn antenna, collected and transfered by an assembly of lenses and focused onto the detector horn antenna.

in Fig. F.4. The Gigahertz radiation is generated by frequency-doubled W-band sources and is emitted through an isolator and a horn antenna. The radiation is collected, transfered and focused on the detector horn antenna by an assembly of teflon lenses. The beam transfer can be computed using the transformation laws applied for the propagation of Gaussian beams outlined in chapter 7. The transverse dimension of the GHz radiation pulse behind the third teflon lens is computed by assuming a symmetric radiation envelope in between lens #2 and #3, which was the design specification of the optical beam line. The detector is positioned at the waist of the radiation beam which is the longitudinal position where the largest signal is detected. The damping of the optical setup, which is a function of radiation frequency, has been measured and the radiation power behind the third teflon lens is listed in Tab. F.3.

f [GHz]	156.0	164.8	176.0	203.2
P_{rf} [dBm]	15.7	14.7	12.1	10.0

Table F.3: Expected radiation power behind the third lens of the quasi-optical setup.

The maximum detector signal is recorded and compared to the radiation power reaching the horn antenna. The transverse power distribution is given by the properties of a Gaussian beam.

The detector acceptance is the ratio of the recorded detector signals and the radiation intensity reaching the detector horn antenna. The result is shown in Fig. F.5. The detector acceptance is increasing rapidly between 100 and 130 GHz, reaches a maximum at $f = 156$ GHz and decreases towards larger frequencies. The error bars originate from

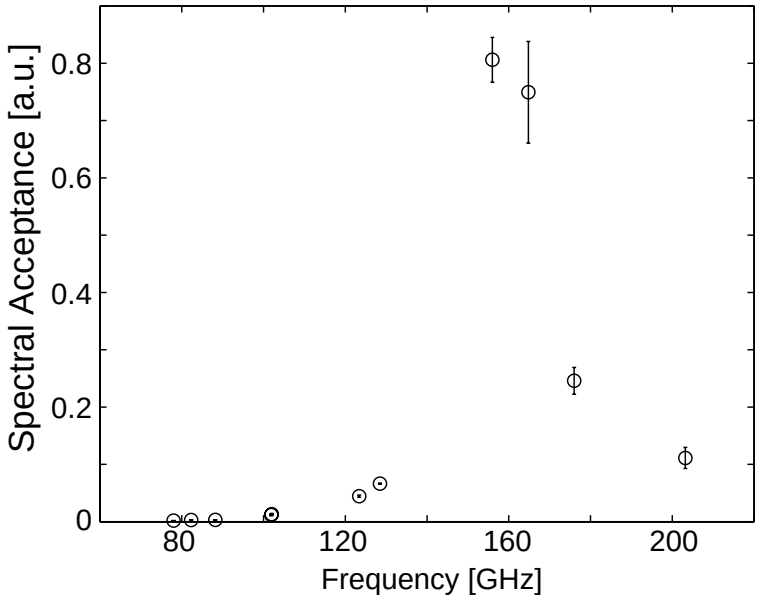


Figure F.5: Calibration measurement of the pyroelectric detectors. The acceptance is increasing rapidly at frequencies larger than $f = 130\,\mathrm{GHz}$. A maximum is at $f = 156\,\mathrm{GHz}$ and the acceptance is decreasing towards higher frequencies. The decrease is explainable by destructive interference of the radiation between the front and the back side of the $100\,\mu\mathrm{m}$ thick pyroelectric crystal.

read-out errors of a digital oscilloscope, uncertainties of the computed attenuation of the horn antenna and uncertainties of the radiation transfer in the optical setup.

Bibliography

[1] T. Garvey et. al., *First Beam Tests of the TTF Injector*, in *Proceedings of the Particle Accelerator Conference 1997*, (Vancouver, Canada, 1997).

[2] TESLA Collaboration, *TESLA Test Facility Linac – Design Report*, TESLA Report **95-1** (1995) 58–92.

[3] B. Mouton, Parmela Implementation Version 5.00.

[4] K. L. Brown, F. Rothacker, D. C. Carey, Ch. Iselin, *Transport – A Computer Program for Designing Charged Particle Beam Transport Systems*, CERN **80-04** (1980).

[5] S. Schreiber et. al., *First Running Experience with the RF Gun based Injector of the TESLA Test Facility Linac*, in *Proceedings of the FEL Conference 1999*, (Hamburg, 1999).

[6] I. Will et. al., *The TTF Photocathode Laser*, in *Proceedings of the FEL conference 1999*, (Hamburg, 1999).

[7] TESLA Collaboration, *TESLA Test Facility Linac – Design Report*, TESLA Report **95-1** (1995) 92–113.

[8] M. Geitz et. al., *Determination of the Longitudinal Phase Space Distribution produced with the TTF Photo Injector*, in *Proceedings of the FEL conference 1999*, (Hamburg, 1999).

[9] D. Sertore et. al., *First Operation of Cesium Telluride Photocathodes in the TTF Injector RF Gun*, in *Proceedings of the FEL Conference 1999*, (Hamburg, 1999).

[10] B. E. Carlsten, *New Photoelectric Injector Design for the Los Alamos National Laboratory XUV FEL Accelerator*, NIM **A285** (1989) 313–319.

[11] F. I. Sacherer, *The effect of space charge in beam transfer lines*, IEEE Trans. Nucl. Sci. **18** (1971) 1066–1067.

[12] K. J. Kim, *Rf and Space-Charge Effects in Laser-Driven RF Electron Guns*, NIM **A275** (1989) 201–218.

[13] A. Gamp et. al., *Experience with the Control of the Vector Sum at the TESLA Test Facility Linac*, in *Proceedings of the European Particle Accelerator Conference 1998*, (Stockholm, 1998).

[14] M. Geitz, A. Kabel, T. Limberg, G. Schmidt, *TTF Bunch Compressor 2*, in *Proceedings of the Particle Accelerator Conference 1999*, (New York, USA, 1999).

[15] H. Schlarb, *Collimation of the electron beam at the TESLA Test Facility Linac*, in *Proceedings of the FEL Conference 1999*, (Hamburg, 1999).

[16] J. Pflueger, *Undulators for SASE FEL's*, in *Proceedings of the FEL Conference 1999*, (Hamburg, 1999).

[17] T. Winkler, *XBEAM – A First Order Interactive Beam Transport Calculation*, Diploma Thesis, Institut für Kernphysik, TH Darmstadt, Darmstadt, 1993.

[18] TESLA Collaboration, *TESLA Test Facility Linac – Design Report*, TESLA **95-01** (1995) 48.

[19] J. Rosenzweig, L. Serafini, *Transverse Particle Motion in Radio-Frequency Linear Accelerators*, Phys. Rev. **E 49** (1994) 1599–1602.

[20] C. Hawkes, M. J. Lee, *Recent Upgrading of the Modelling Program COMFORT*, SLAC **CN-342** (1986) 1–7.

[21] W. Brefeld, P. Castro, T. Limberg, H. Schlarb, *Optics for TTF-FEL*, TESLA-FEL **99-06** (1999).

[22] K. Ricci, *Sub-Picosecond Electron Bunch Profile Measurements using Magnetic Longitudinal Dispersion and Off-Phase RF Acceleration*, in *Proceedings of the AIP Conference 1998.*

[23] V. L. Ginzburg, V. N. Tsytovich, *Several Problems of the Theory of Transition Radiation and Transition Scattering*, Physics Reports **49/1** (1979) 1–89.

[24] Computar Company, CCTV Equipment Catalogue, p. 38–39, 1998.

[25] M. L. Ter-Mikaelian, *High-Energy Electromagnetic Processes in Condensed Media*, (Wiley Interscience, New York, 1972).

[26] A. Chao, *Physics of Collective Beam Instabilities in High Energy Accelerators*, (Wiley, New York, 1993).

[27] H. Schlarb, *Resistive wall wake fields*, Diploma Thesis, University of Hamburg, Hamburg, 1997.

[28] M. Castellano et. al., *Spatial Resolution in optical transition radiation (OTR) beam diagnostics*, LNF **98/017(P)** (1998) 1–20.

[29] E. Hecht, *Optics*, (Addison-Wesley, Reading, Ma, 1989).

[30] E. B. Blum et. al., *Observation of Coherent Synchrotron Radiation at the Cornell Linac*, Nucl. Instr. Meth. **A 307** (1991) 568–576.

[31] T. Nakazato et al., *Coherent Synchrotron Radiation*, Part. Accel. **33** (1990) 141–146.

[32] T. Takahashi et. al., *Coherent Transition Radiation at Submillimeter and Millimeter Wavelengths*, Phys. Rev. **E 48** (1993) 4674.

[33] H. Liehn et. al., *Measurement of Subpicosecond Electron Pulses*, Phys. Rev. **E 53/6** (1996) 6413–6418.

[34] C. Settakorn et. al., *Subpicosecond Electron Bunch Length Measurement*, SLAC PUB **7586** (1997) 1–4.

[35] O. R. Sander, G. N. Minerbo, R. A. Jameson, D. D. Chamberlin, *Beam Tomography in Two-Dimensions and Four-Dimensions*, in *Proc. of the Linear Accelerator Conference*, (Montauk, USA, 1979).

[36] G. N. Minerbo, O. R. Sander, R. A. Jameson, *Four-Dimensional Beam Tomography*, IEEE Trans. Nucl. Sci. **28** (1981) 2231–2233.

[37] J. Radon, *Über die Bestimmung von Funktionen durch ihre Integralwerte längs gewisser Mannigfaltigkeiten, Ber. Verh. Saechs. Akad. Leipzig*, Math. Phys. Kl. **69** (1917) 262.

[38] D. W. Townsend, M. Defrise, *Image Reconstruction Methods in Positron Tomography*, CERN Yellow Report **93-02** (1993) 1–43.

[39] G. T. Herman, *Image Reconstruction from Projections: the Fundamentals of Computerized Tomography*, (Academic Press, New York, 1980).

[40] F. Natterer, *The Mathematics of Computerized Tomography*, (Teubner, Stuttgart, Germany, 1986).

[41] R. A. Brooks, *Principles of Computerized Tomography (CAT) in radiographic and radioisotopic imaging*, Phys. Med. Biol. **21** (1976) 689.

[42] The Mathworks Inc. , Matlab Version 4.2c, 1994.

[43] C. B. McKee, P. G. O'Shea, J. M. J. Maday, *Phase Space Tomography of Relativistic Electron Beams*, Nucl. Instr. Meth. **A 358** (1995) 264–267.

[44] S. Hancock, A. Jansson, M. Lindroos, *Tomographic Reconstruction of Transverse Phase Space from Turn-By-Turn Profile Data*, CERN-PS **99-029-OP** (1999) 1.

[45] M. Castellano, *Resolution of the TTF Optical Diagnostics System*, in *Presentation at the TTF collaboration meeting 1999*, (DESY, 1997).

[46] M. Castellano, Technical Drawing: Targhetta Rettangolare TTF .01.03, INFN, (1995).

[47] S. Schreiber et. al., *Measurement of the Transverse Emittance in the TTF injector*, in *Proceedings of the FEL conference 1999*, (Hamburg, 1999).

[48] J. P. Carneiro et. al., *Beam transport, acceleration and compression studies in the Fermilab high brightness photoinjector*, Fermilab Conf. **98-329** (1998).

[49] K. Ricci, *Direct Observation of Electron Beam Micro-bunching in a Free-Electron Laser Oscillator*, in *Proceedings of the FEL Conference 1999*, (Hamburg, 1999).

[50] B. Leissner, *Strahluntersuchung am TESLA-Linearbeschleuniger*, Diploma Thesis, RWTH Aachen, Aachen, 1998.

[51] Molectron Company, Data sheet of the pyroelectric detector PI-45.

[52] D. H. Martin, *Polarizing Martin-Puplett Interferometric Spectrometers for the Near- and Submillimeter Spectra*, Infrared and Millimeter Waves **6** (1982).

[53] W. G. Chambers, C. L. Mok, T. J. Parker, *Theoretical studies on the frequency response of some far-infrared interferometers with wire-grid beam deviders*, J. Phys **D 13** (1980) 515–526.

[54] W. G. Chambers, T. J. Parker, A. E. Costley, *Freestanding Fine-wire Grids for Use in Millimeter- and Submillimeter-Wave Spectroscopy*, Infrared and Millimeter Waves **16** (1986).

[55] W. G. Chambers, C. L. Mok, T. J. Parker, *Theory of the scattering of electromagnetic waves by a regular grid of parallel cylindrical wires with circular cross-section*, J. Phys **A 13** (1980) 1433–1441.

[56] P. C. Waterman, *Computer Techniques for Electrodynamics*, (Oxford Pergamon, Oxford, 1973).

[57] P. W. Barber, *Resonance Electromagnetic Absorption by Non-spherical Dielectric Objects*, IEEE Trans. **MTT-25** (1977) 373–81.

[58] I. Wilke et. al., *Surface Resistance of YBCO thin films at THz-frequencies*, in *Proceedings of the European Conference of Applied Superconductivity 1999*, (Barcelona, Spain, 1999).

[59] G. Herziger, Laser Technik I – Lectures at the RWTH Aachen 1994.

[60] H. Loos, private communication.

[61] M. Tschernitz, J. Freyer, *140 GHz GaAs double-Read IMPATT diodes*, Electronic Letters **31-7** (1995) 582–583.

[62] R. Lai, A. J. Sievers, *On using the coherent far IR radiation produced by a charged-particle bunch to determine its shape: I Analysis*, NIM **A 397** (1997) 221–231.

[63] Gi. Schneider, M. G. Billing, R. Lai, A. J. Sievers, *Comparison of electron bunch asymmetry as measured by energy analysis and coherent transition radiation*, Phys. Rev. **E 56** (1997) 3780–3783.

[64] K. Hanke, *Beam Diagnostics using Coherent Transition Radiation at the TESLA Test Facility Linac*, PhD Thesis, University of Hamburg, Hamburg, 1997.

[65] G. Orlandi, *Misura della lunghezza del pacchetto di elettroni dell'acceleratore lineare superconduttivo TTF con la radiazione di transizione e diffrazione*, PhD Thesis, University of Rome "Tor Vergata", Roma 2000, Rome, 1999.

[66] K. K. Likharev, *Dynamics of Josephson Junctions and Circuits*, (Gordon and Breach, New York, 1996).

[67] H. Kanter, F. L. Vernon, *High-frequency Response of Josephson Point Contacts*, J. Appl. Phys. **43** (1972) 3174.

[68] J. H. Hinken, *The Josephson Junction as a Spectral Detector, in Superconducting Quantum Electronics, Ed. V. Kose*, (Springer, Berlin, 1989).

[69] Y. Y. Divin, O. Y. Polyanski, A. Y. Shul'man, *Incoherent Radiation Spectroscopy based on the AC Josephson Effect*, IEEE Trans. Magn. **19** (1983) 613.

[70] Y. Y. Divin, H. Schulz, U. Poppe, N. Klein, K. Urban, P. Shadrin, I. M. Kotelyanski, E. A. Stepantsov, *Josephson effects in $YBa_2Cu_3O_{7-x}$ grain-boundary junctions on (001) $NdGaO_3$ bicrystal substrates*, Physica **C 256** (1996) 149.

[71] A. V. Andreev, Y. Y. Divin, V. N. Gubankov, I. M. Kotelyanski, V. B. Kravchenko, S. G. Zybtsev, E. A. Stepantsov, *$YBa_2Cu_3O_{7-x}$ thin-film Josephson junctions on $2 \times 12^\circ$ bicrystal (110) $NdGaO_3$ substrates*, Physica **C 226** (1994) 149.

[72] Y. Y. Divin et. al., *Millimeter-wave Hilbert-transform spectroscopy with high-T_c Josephson junctions.*, Appl. Phys. Lett. **68** (1996) 1561.

[73] J. Menzel, *Hilbert-transformationsspektroskopie an der TESLA Test Anlage*, Diploma Thesis, RWTH Aachen, Aachen, 1999.

[74] F. Ludwig, PhD thesis in preparation.

[75] P. Schmüser, *Basic Course on Accelerator Optics*, DESY M **93-02** (1993) 1–71.

[76] S. C. Hartmann, J. B. Rosenzweig, *Ponderomotive Focusing in Axisymmetric RF Linacs*, Phys. Rev. **E 47** (1993) 2031.

[77] H. Panofsky, *Classical Electricity and Magnetism*, (Addison-Wesley, London, 1955).

[78] L. D. Landau, E. M. Lifshitz, *Theoretische Physik Bd. 8*, (Akademie Verlag, Berlin, 1976).

[79] M. Abramowitz et. al., *Handbook of mathematical functions with formulas, graphs and mathematical tables*, (National Bureau of Standards, Applied Mathematical Series 55, Washington, 1966).

[80] K. H. Schindl, *Space Charge*, CERN-PS **99-012-DI** (1998) 1–25.

[81] K. Bongardt, *Linacs*, in *Lectures given at the CERN Accelerator School 1997*, (Gjovik, Norway, 1997).

[82] I. N. Bronstein, K. A. Sememdjajew, *Taschenbuch der Mathematik*, (Teubner, Leipzig, 1979).

[83] E. C. Titchmarsh, *Introduction to the Theory of Fourier Integrals*, (Clarendon Press, Oxford, 1962).

[84] M. Tschernitz, J. Freyer, H. Grothe, *GaAs Read-type IMPATT diodes for D-band*, Electronic Letters **30-13** (1994) 1070–1071.

[85] E. H. Braun, *Some Data for the Design of Electromagnetic Horns*, IEEE Trans. Antennas Propagat. **AP-4** (1956) 29–31.

[86] E. H. Braun, *Gain of Electromagnetic Horns*, Proc. IRE **41** (1953) 109–115.

Acknowledgments

Without the great support and assistance I was given, both during the experimental phase of my work and during the evaluation of my data, this thesis would not have been completed.

I want to thank Prof. Dr. P. Schmüser for his effort and enthusiasm in advising my PhD thesis. He supported the formation of this thesis by fruitful discussions and constructive ideas.

I show my gratitude to Priv. Doz. Dr. M. Tonutti, who excited my curiosity about the TESLA project. I thank Dr. Tonutti, Prof. Dr. Ch. Berger and R. Siedling for the construction of the beautiful Martin-Puplett interferometer and for making many measurements possible.

Special thanks to Dr. H. Weise who introduced me into the technology of the TTF linac and made it possible for me to learn how to operate the accelerator. I enjoyed working with him and learned a lot from his experience with superconducting linacs.

I want to thank Priv. Doz. Dr. M. Leenen for the possibility to present my work at international workshops and conferences and for getting the chance to meet and to interchange ideas with experienced scientists.

I thank Dr. Y. Divin and Dr. U. Poppe for spending several weeks at DESY and for the introduction into Hilbert-transform spectroscopy. I want to thank Dr. I. Wilke and M. Khazan to measure the spectral transmission of the wire grids and the vacuum window. I furthermore acknowledge the help of Dr. J. Freyer and his collaborators to make acceptance measurements of the pyroelectric detectors possible.

I am much obliged to express my thanks to all the members of the TESLA collaboration for the opportunity to take part in their discussions and to learn from their activities. I had helpful discussions with Priv. Doz. J. Rossbach, Dr. G. Schmidt, Dr. S. Schreiber, Dr. S. Roth, H. Schlarb and F. Ludwig. I thank the diploma students B. Leissner and J. Menzel for supporting my scientific investigations. Soft- and hardware problems I discussed with and obtained a lot of help from K. Rehlich, O. Hensler, Dr. K. Mess and P. Albrecht. I want to thank Dr. M. Castellano and L. Catani to profit from the optical diagnostics system, Dr. S. Simrock, M. Hüning and G. v. Walter for supporting the radio frequency system.

For technical support I want to thank B. Sparr, O. Peters, J. Holz, T. Plawski and B. Sarau and the workshops of the RWTH Aachen, the University of Hamburg and DESY.

I finally thank my girlfriend Dr. E. M. Jaeckel for her moral support and understanding for being up working many whole nights and weekends to collect the data presented in this thesis.